This is to certify that the
dissertation entitled

Response of Restrained Steel Beams Subjected to Fire
Induced Thermal Gradients

presented by

Mahmoud M. S. Dwaikat

has been accepted towards fulfillment
of the requirements for the

Doctoral degree in Civil Engineering

Major Professor's Signature

6/10/2010

Date

RESPONSE OF RESTRAINED STEEL BEAMS SUBJECTED TO FIRE INDUCED THERMAL GRADIENTS

By

Mahmoud M. S. Dwaikat

A DISSERTATION

Submitted to
Michigan State University
in partial fulfilment of the requirements
for the degree of

DOCTOR OF PHILOSOPHY

Civil Engineering

2010

ABSTRACT

Response of Restrained Steel Beams Subjected to Fire Induced Thermal Gradients

By

Mahmoud M.S. Dwaikat

Structural steel is frequently used in high rise building construction due to its low weight-to-strength ratio and high ductility characteristics. However, steel suffers fast degradation of its strength and stiffness properties at elevated temperature, and hence, steel structural members are to be provided with a certain level of fire protection to achieve required fire resistance. The current approaches for evaluating fire resistance of steel members have many limitations and do not take into consideration critical factors governing fire response. For instance, a restrained steel beam develops significant fire induced restraint forces when exposed to fire and these forces transform the behavior from beam to that of a beam-column. However, current design provisions do not take into consideration the effect of fire induced restraint forces, and thus beams are continued to be designed for flexural capacity only under fire conditions.

To obtain test data on the influence of thermal gradients on steel beam-columns, fire resistance tests on four beam-columns were conducted as part of this study. The test variables included magnitude and direction of thermal gradients, load level, insulation scheme, and fire scenarios. Results from the fire tests show that beam-columns develop significant thermal gradients under uneven fire exposure and these gradients alter the failure mode from that predicted using conventional P-M curves.

Test data were utilized to validate finite element models created using ANSYS for tracing thermal and structural response of beam-columns under fire conditions. The finite element models account for various critical factors, namely high temperature material properties, fire induced restraints and thermal gradients, and the different strain components (including high temperature creep), that have significant influence on the fire response of steel beam-columns. Once validated, the models were used to carry out detailed parametric studies to quantify the influence of critical parameters, such as load, end restraints, and fire scenario, on the fire response of beam-columns. Results from the parametric study showed that fire resistance of restrained steel beams is adversely affected by increasing load ratio and fire severity, while fire resistance gets enhanced by increasing axial and rotational restraint stiffnesses.

Results from the parametric studies and from fire experiments were utilized to develop two simplified calculation methodologies at sectional and global levels for tracing the response of steel beam-columns under fire. At sectional level, a simple methodology for adjusting the conventional plastic P-M diagrams to account for the effect of fire induced thermal gradients is derived. At global level, an engineering methodology is developed for evaluating the fire response of restrained steel beams utilizing equilibrium and compatibility principles. The proposed approach accounts for load, boundary conditions, fire scenarios, and beam geometry, and can be applied for evaluating fire resistance of restrained steel beams utilizing either deflection or strength limit state.

A comparison of results show that the proposed approaches provide better fire resistance estimates of restrained beams than that predicted by current provisions in codes and standards. The simplicity of the proposed approaches makes them attractive for undertaking a rational fire design under a performance-based environment. Application of these rational approaches in the design process of beam-columns will contribute to reliable and cost effective fire response predictions.

DEDICATION

To the grace and pleasure of G-d,
the soul of my mother,
and my father.

ACKNOWLEDGMENT

I would like to sincerely thank my advisor Prof. Venkatesh Kodur for the encouragement, guidance, and support he provided me throughout the 4.5 years of research I spent with him. Also, special thanks to the distinguished faculty members who served on my committee: Professors Ronald Harichandran, Rigoberto Burgueño, and Alejandro Diaz. Thanks to all my committee members for their support, patience, encouragement, and useful suggestions and guidance.

Sincere and warm thanks to my friends who supported me during the course of my research, particularly Monther Dwaikat and Saskia Polder-Verkiel, and the rest of my friends and colleagues in the CEE department.

Thanks to the faculty and personnel in the CEE department for their support and help, especially the manager of the Civil Infrastructure Laboratory Mr. Siavosh Ravanbakhsh, and the rest of the personnel.

I and my advisor also wish to acknowledge the support of National Institute of Standards and Technology (through Building and Fire Research Laboratory Fire Grant # 60NANB7D6120), National Science Foundation (through Award# CMMI 0652292).

TABLE OF CONTENT

CHAPTER THREE

CHAPTER FOUR

CHAPTER FIVE

CHAPTER EIGHT

LIST OF TABLES

LIST OF FIGURES

CHAPTER ONE

INTRODUCTION

1.1 GENERAL

In high-rise buildings, steel is often the material of choice for structural framing consisting of beams and columns. Steel structures are to be designed to withstand various loads including effects arising due to fire accidents. Fire incidents and laboratory experiments have shown that fire is one of the most severe hazards to which structures are subjected during their life time. Thus, the provision of appropriate fire safety measures is an important aspect of building design in order to enhance the safety of the occupants and to control the spread of fire (NIST 2005). Fire safety can be achieved through active and passive fire safety systems. Active systems are generally activated once the fire has started and they include fire detectors, smoke control systems and sprinklers. Passive fire protection systems, which include fire resistance, are those inherent in the structure and do not require specific operation to get activated in the event of a fire. The rationale for passive fire safety systems is that structural integrity is the last line of defense when other measures for resisting fire fail. Fire resistance is defined as the duration during which a structural member (system) exhibits resistance with respect to structural integrity, stability, and temperature transmission under fire conditions (Buchanan 2002). Typical fire resistance requirements for specific building members are specified in building codes. Fire resistance issues play a crucial role in the performance of buildings and infrastructure in the event of a fire as seen in the collapse of the WTC twin towers and the damage to the Eurotunnel.

Beams and columns are primary load carrying members in a framed structure. When exposed to fire, not only does steel loses its strength and stiffness at accelerated rates, but beams and columns also develop significant internal forces that transform their behavior from beams or columns into beam-columns. Limited guidance is provided in codes and standards for the design of restrained steel members to resist fire conditions. There are two main approaches through which such design is carried out, namely; prescriptive- and performance-based approaches. While the prescriptive approach is based on empirical relations that are derived from fire tests carried out under standard conditions, the performance-based approach focuses on the performance of the structural system under given load, fire, and boundary conditions.

The implementation of a performance-based approach in fire design of structural members is a recent development, and therefore, most provisions provided by performance-based codes (such as the Eurocode (EC3 2005)) are an extension of room-temperature design equations. In the Eurocode for instance, the ambient temperature design equations are used to check for load-bearing capacity of the structural members under fire, but with the replacement of the material properties by those of high temperature properties. Based on this methodology, beams under fire are still structurally treated as beams under ambient temperature. The influence of fire and boundary conditions on the fire response of such structural members is not explicitly treated.

Three critical issues are neglected when fire design is based on ambient temperature design equations with the material properties reduced as a function of temperature. These critical issues are the change of fire response, the change of failure mode, and the change of failure criterion. The fire response of a beam within a framed structure is different from its ambient temperature response. For instance, a beam at room temperature generally carries the applied load through flexure, however, under later stages of fire exposure; the same beam within a framed structure carries the load through a cable (catenary) mechanism. Further, as the beam at ambient temperature may fail either by flexure, shear, or buckling; under fire temperature the same beam is more likely to fail by tension or by developing excessive deflection. Also, while failure at ambient temperature is generally based on strength limit state for steel beams, deflection limit state becomes more realistic for assessing the failure of steel beams under fire conditions (Skowronski 1988 and 1990).

When exposed to fire, strength and stiffness properties of steel degrade rapidly with the rise of temperature, leading to deterioration in the behavior of steel structural members and systems. Also, due to the effect of end restraints, significant forces can develop in a steel beam or column. In current design practice, these fire induced restraint forces are usually not taken into consideration because they do not exist at room temperature. Nevertheless, these fire-induced forces transform the behavior of a beam or column into that of a beam-column and alter the fire response of a structural system (Kodur and Dwaikat 2009).

1.2 FIRE RESPONSE OF BEAMS AND COLUMNS

Under fire conditions, temperatures attained in steel lead to both degradation in material properties and generation of additional internal forces that do not exist at room temperature. These fire induced restraint forces (*P* & *M*), which can often reach 30% of the room-temperature capacity, transfer the behavior of the beam (or column) to that of a beam-column (Kodur and Dwaikat 2009). Generally, beam-columns are defined as members that are subjected to an axial load (*P*) and a bending moment (*M*). At room temperature, the applied forces (*P* and *M*) are assumed to remain constant and can be computed directly from the applied loads (gravity, snow, wind, or seismic loads). However, under fire conditions, the fire induced restraint forces (P and M) are a function of a number of factors including the characteristics of the beam (or column), and type of fire exposure, and the magnitude and duration of these forces vary with time.

The response of a beam-column primarily depends on the interaction between bending moment (*M*) and axial force (*P*). The combination of *P* & *M* affects the load carrying capacity of beam-columns which is generally expressed, in codes and standards, using the following relationship at ambient conditions:

$$c_1 \frac{P}{\Phi P_n} + c_2 \frac{M}{\Phi M_n} \leq 1.0 \qquad [1.1]$$

where *c1* and *c2* are interaction coefficients, and *ΦMn* and *ΦPn* are the moment and axial capacities, respectively. Since there are no validated expressions or methodologies for computing the fire-induced *P* & *M* acting on restrained beams (or columns), Eq. [1.1] cannot be applied under fire conditions. Therefore, one of the main objectives in this research is to quantify the critical values for the *P* & *M* that emerge as a result of fire exposure.

Another aspect is the development of fire-induced thermal gradients across the cross-section of a beam-column due to 1-, 2-, or 3-sided fire exposure, as shown in Fig. 1.1(*a*). Generally, 4-sided fire exposure leads to nearly uniform temperature within the cross section, while 1-, 2-, or 3- sided fire exposure tends to generate thermal gradients in the cross section. For example, a restrained column subjected to a thermal gradient (as in perimeter columns exposed to fire from one side) develops a bending moment in addition to the axial force. Similarly, a restrained beam subjected to a thermal gradient (since beams generally support a concrete slab and thus fire exposure is from 3 sides) develops an axial force in addition to the bending moment. These fire induced thermal gradients can severely distort the plastic P-M diagram (*Pn* and *Mn* in Eq. [1.1]) due to varying strength and stiffness properties of steel across the depth of the section. This "*nonhomogeneity*" within the steel section produces a distorted P-M interaction diagram that is different from that of a "*homogenous*" steel section at room temperature (Garlock and Quiel 2008).

Further, the type of fire scenario has a significant influence on the development of restraint forces in beam-columns. Much of the current knowledge is based on fire resistance tests on restrained columns or beams where the exposure is typically assumed to be that of a standard fire. However, in buildings the fire exposure is likely to be different and dependent on fuel load and ventilation characteristics in the fire compartment (Buchanan 2002). Fig. 1.1(b), illustrates the difference between standard fire and realistic (design) fire scenarios. The main difference between the two is that in standard fire exposure, the temperature of the fire is assumed to increase without any decaying (cooling). However, fires in buildings die down after reaching a peak temperature, and the compartment enters a cooling phase as a result of exhaustion of fuel and/or ventilation (oxygen). This decay phase results in cooling of steel and thus development of tensile stresses due to the shrinkage of steel. This aspect of the cooling phase has significant influence on the fire response of structural members, especially on restrained members such as beam-columns. There is a very limited number of studies on the effect of this cooling phase of fire on the structural response of steel members in general (Li and Guo 2006 and 2008), and beam-columns in particular.

1.3 CURRENT APPROACHES OF FIRE RESISTANCE EVALUATION

There are many drawbacks in the current approach for evaluating fire resistance of beam-columns. The fire resistance of a restrained beam is evaluated by a mere reduction in strength properties and without any consideration to restraint forces that develop under fire conditions. This is mainly due to the lack of methodologies for quantifying the internal forces that develop in restrained beams (or columns). In addition, the current fire resistance approaches for steel beams and columns are based on fire tests which were carried out on specimens of standard sizes under service loads, simply supported end (unrestrained) conditions, and standard fire exposure which does not reflect reality. Furthermore, in the current approaches, the failure is often based on a thermal (prescriptive) criterion, which assumes a member to fail once steel reaches a "*critical*" temperature, regardless of loading, restraint conditions, or fire scenario. Further, the effect of fire induced restraints on steel members is not fully accounted for in current code provisions. Therefore, the current prescriptive approaches for evaluating fire resistance do not represent realistic fire, loading, and restraint scenarios as encountered in practice. This makes the current design approaches inapplicable for use under the recently introduced performance-based codes that seek to facilitate innovative, cost-effective and rational designs.

In a performance-based environment, the response of beam-columns is based on realistic performance criteria (Wang and Kodur 2000). The failure criteria may vary depending on the function of the steel member. For example, for a restrained beam under fire, a deflection limit state may be more critical than achieving full yield capacity, while for a column, a strength (or buckling) limit state can be more critical. Excessive deflection can not only severely affect the structural integrity; it can also accelerate the spread of fire to other compartments.

Another limitation of the current design approaches lies in the evaluation of the capacity of beam-columns. The ultimate capacity of beam-columns is assessed using P-M interaction diagrams. These interaction diagrams are generated based on the assumption of uniform temperature. This means that a constant yield stress, *Fy*, is assumed through the depth of the section when predicting the capacity of beam-columns (e.g., AISC 2005, EC3 2005). However, under real fire exposure, thermal gradients are likely to emerge and they can alter the shape of the P-M interaction diagram. These gradients are significant in the case of beams and columns under 1-, 2-, or 3-side exposure (See Fig. 1.1(*a*)).

Figure 1.2 illustrates the plastic P-M interaction curve for a W24x76 beam section under different thermal gradients. The average temperature of the section (across the depth) is maintained at 500°C, while the thermal gradient was increased from zero to 150°C. The interaction curves are computed through direct integration of ultimate stresses across the cross section for each case of thermal gradient. The values of the moment and axial force are normalized to the plastic moment and axial capacities of the section at each case of thermal gradient. It can be seen from Fig. 1.2 that: 1) Using *constant minimum Fy* (constant *maximum T* of 650°C) may be overly conservative as seen by comparing this yield surface to the true yield surfaces at different thermal gradients; and 2) the *true plastic P-M interaction curve* (that considers variable *Fy* through the section as a result of thermal gradient) shifts and departs from the shape of the curve considering constant average *Fy*. This shift and distortion of the P-M diagram depends on the level of thermal gradient in the section. Fig. 1.2 also shows that the assumption of *constant* (i.e. uniform) *average Fy* ($\Delta T = 0$) through the depth of the section can be conservative in some cases and nonconservative in other cases.

The response of beam-columns was closely examined in WTC twin towers collapse studies. Based on these investigations it was recommended that the behavior of steel beam-columns is an urgent research need since they are critical components of structural frames in high rise buildings and other built infrastructures (NIST 2005). The limited studies undertaken in literature on fire response of beam-columns did not properly account for many important factors, such as the fire scenario, thermal gradient, restraint configuration, and high-temperature properties. Also, there is a lack of understanding of the interaction between fire induced internal forces and capacities, such as between bending moment and axial force and the respective capacities. Knowledge of such interactions is critical for the proper design of beam-columns under fire conditions.

1.4 RESEARCH OBJECTIVES

From the above discussion, it is clear that there is a considerable lack of knowledge of the fire response of steel beam-columns under realistic fire, loading, and restraint scenarios. To address this knowledge gap, it is proposed to undertake a comprehensive study of the structural response of restrained steel beams under fire conditions with the ultimate objective of developing a rational methodology for evaluating the fire resistance of restrained steel beams. The specific objectives of the research are:

- Conduct a detailed state-of-the-art review on the fire response of restrained steel beams. The comprehensive review will cover experimental and numerical studies, provisions in codes and standards, and high temperature material properties.

- Model the thermal and structural response of restrained steel beams under realistic fire, loading, and failure conditions. The models for thermal and structural analysis will account for nonlinear high temperature material properties, various strain components and fire induced restraint effects.
- Conduct fire resistance tests on steel beam-columns under realistic fire, loading and restraint scenarios to generate data for the validation of the models.
- Verify the computational models using data from fire resistance tests on steel beam-columns.
- Carry out parametric studies to quantify the influence of various factors on the fire resistance of restrained steel beams.
- Develop a rational design methodology, using data from fire tests and parametric studies, for evaluating the response of restrained steel beams under realistic fire, load, restraint, and failure limit states.

1.5 SCOPE

The research, undertaken to address the above objectives, is presented in eight Chapters. Chapter 1 gives a general background to the fire response of steel beam-columns and presents the objectives of this study. Chapter 2 provides a state-of-the-art review on the behavior of steel beam-columns exposed to fire. The review includes a summary of experimental and analytical studies, as well as the fire design provisions for restrained steel beams in current codes of practice. A review of the high temperature material properties and associated constitutive relationships for structural steel is also presented in Chapter 2.

Chapter 3 deals with fire resistance experiments on four steel beam-columns under realistic fire, loading and restraint scenarios. Results from these fire tests are used to discuss the response of steel beam-columns under these realistic conditions. Chapter 4 presents details of finite element modeling of the fire response of steel beam-column beams. The validation of the finite element models (thermal and structural) is also presented in Chapter 4, where predictions from the model are compared with available test data from literature, and also with results from the fire tests presented in Chapter 3.

Parametric studies are presented in Chapter 5. The definitions and ranges of parameters governing the fire resistance of restrained steel beams are described in Chapter 5, followed by a discussion of the results from the parametric studies. In Chapter 6, a methodology for evaluating the P-M diagrams of steel beam-column under fire induced thermal gradients is presented. In Chapter 7, simplified equations for predicting the response of restrained steel beams under fire are developed. The proposed equations in Chapter 6 and 7 are verified using results from fire resistance tests and from the parametric studies. Finally, Chapter 8 summarizes the main findings arising from the current study and lays out recommendations for further research.

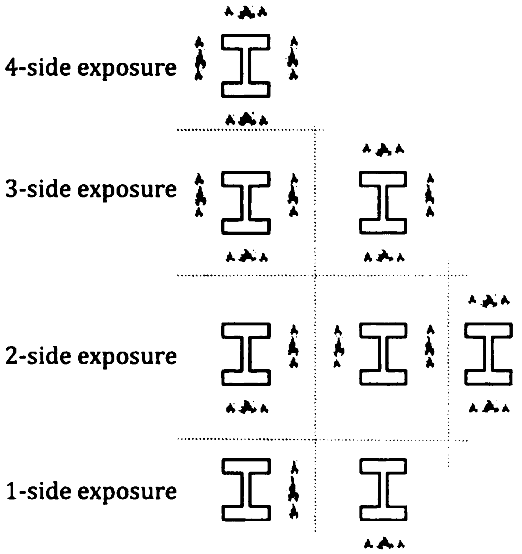

(a) Fire exposure types

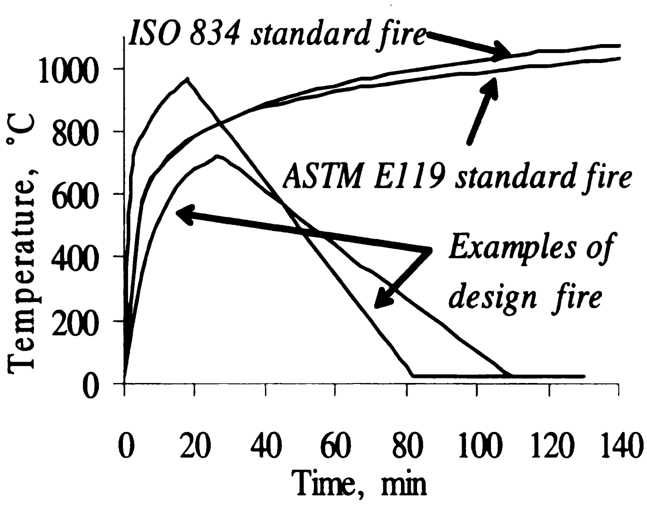

(b) Fire scenarios

Fig. 1.1: Types of fire exposure and fire scenario commonly encountered in buildings

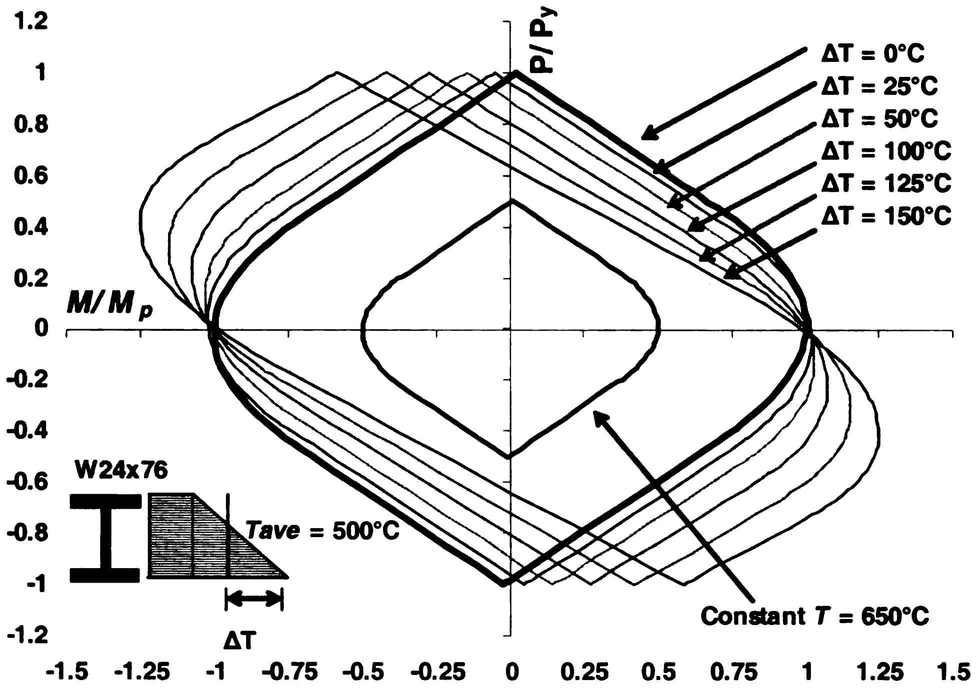

Fig. 1.2: Transformation of the P-M interaction diagram under thermal gradients

C

2.

A

sig

th

ne

no

be

20

ha

ma

mo

sta

fre

firs

sta

exp

cla

thi

CHAPTER TWO

STATE-OF-THE-ART REVIEW

2.1 GENERAL

A restrained beam in a framed steel structure, when exposed to fire, can develop significant internal forces that transform its behavior to that of a beam-column. This change in behavior and resulting failure patterns of restrained beams is often neglected in the design and analysis. Current provisions in codes and standards do not address this change in behavior under fire conditions, and therefore, restrained beams in a framed structure are often treated as simply supported beams (AISC 2005, EC3 2005, ASCE 1992). Since 1960's, few experimental and numerical studies have shown that the fire resistance of steel structures is critically influenced by a number of important factors, including load, fire, and restraint conditions. While most of these studies focused on individual beam or column responses, very limited studies addressed the more likely *beam-column* behavior. In this chapter, the typical fire behavior of steel beam-columns, with emphasis on restrained steel beams, is first discussed, followed by a critical review of design provisions in codes and standards for evaluating their fire resistance. Also, a summary of previous experimental and analytical studies on the fire performance of restrained beams or columns is presented. Further, since high temperature properties are critical for understanding fire response of steel structures, the variation of high temperature material properties of structural steel in material property tests and in constitutive relationships are also discussed.

2.2 FIRE RESPONSE OF RESTRAINED STEEL BEAMS

The behavior of steel structures under fire is quite different from that at room temperature (Kodur and Dwaikat 2009). This may be attributed to many factors that influence the response under fire conditions. Beams are primary load-bearing members typically used in a steel framed structure, and are often restrained from free expansion. This restraint condition of the steel beams under fire leads to generation of significant internal forces that are nonexistent at ambient temperature. Combined with the degradation in steel strength and stiffness as temperature increases, the effect of restraint under fire generally transforms the structural response of a steel beam to that of a beam-column.

To illustrate the development of fire-induced forces in a restrained beam (or column), a steel frame as shown in Fig. 2.1(*a*) is exposed to fire. In current fire design practice, this type of structure is modeled as a simply supported beam (or column) (Fig. 2.1(*b*)). However, due to the restraint offered by the adjacent members, the beams and columns are likely to behave as restrained members (Fig. 2.1(*c, d*)). When the beam (or column) expands under increasing temperatures, the adjacent members impose both axial and rotational restraints (*Ka* and *Kr*) on the beam (or column) that prevent it from free expansion. This generates axial force (*P*) and bending moment (*M*) as seen in Fig. 2.1 (*c, d*). Also, with the increase of temperature, steel loses its strength and stiffness properties. Therefore, both the midspan deflection (Δ) and the end-rotation (θ) of the beam (or column) gradually increase with the increase in steel temperature. Further, the fire induced axial force (P) causes additional bending moment on the beam (or column) due to P-Δ effect, as seen in Fig. 2.1(*c, d*). The increase in the bending moment (M) produces additional deflections and hence further deterioration in the response of the beam (or column) under fire. Furthermore, the increasing temperature and stress in steel accelerate the development of high temperature creep deformations leading to rapid increase in deflection and ultimately failure of the member.

The general discussion presented above can be illustrated specifically for a restrained steel beam exposed to fire. The fire response of a restrained steel beam generally undergoes three distinct stages, as shown in Fig. 2.2. In Stage I, elastic response dominates the behavior wherein the beam expands as a result of continuous heating, and compressive axial force and bending moment develop due to the effect of end-restraints. Fire-induced internal forces and deflections continue to increase until yielding or buckling occurs in the beam. For the purpose of illustration, the behavior shown in Fig. 2.2 is for the case where no buckling occurs in the beam, and therefore, elasto-plastic response dominates the behavior in Stage II, as shown in Fig. 2.2(b). As steel temperature continues to increase with fire exposure time, softening of steel causes larger deflections and rotations until the first plastic hinge develop in the beam. The plastic hinge, which forms at the location of maximum bending moment in the beam, causes further increase in deflection as shown in Fig. 2.2(c), which leads to a gradual transformation of the fire induced axial force from compressive to tensile force. The beam enters a catenary phase in

Stage III when the fire-induced compressive axial force vanishes as shown in Fig. 2.2(b). In the catenary phase, tensile force develops in the beam and the load bearing mechanism gradually changes form flexural to cable (tensile) until failure occurs by rupture of the beam (or in the connections). As the beam undergoes the above three stages, it is assumed that the connections continue to perform elastically. Therefore, fire-induced forces and rotations in the beam must not exceed the connections capacity. During the above process, the magnitude of response of the beam (fire induced deflection and restraint forces) is affected by many factors and is quite different than the response at room temperature.

The beam-column response of either restrained steel beam or restrained steel column under fire is affected by three main aspects, namely; *a*) the development of fire induced restrained forces (*P* & *M*), *b*) the influence of thermal gradient, and *c*) the influence of fire scenario. The three aspects are discussed in the following paragraphs.

2.2.1 Beam-Column Response

The fire induced restraint forces (*P* & *M*) in a beam-column, can often reach 30% of the room-temperature capacity of either the beam or the column, and these forces transfer the behavior of the beam (or column) to that of a beam-column (Kodur and Dwaikat 2009). At room temperature, the applied forces (*P* and *M*) are assumed to remain constant and can be computed directly from the applied loads (gravity, snow, wind, or seismic loads). However, under fire conditions, the fire induced restraint forces (*P* and *M*) vary as a function of a number of factors including the geometry of the beam (or column), the boundary conditions, applied load and fire characteristics.

The response of the beam-column primarily depends on the interaction between bending moment (*M*) and axial force (*P*). The combination of *P* & *M* affects the load carrying capacity of beam-columns which is generally expressed using the following relationship at ambient conditions:

$$c_1 \frac{P}{\Phi P_{cr}} + c_2 \frac{M}{\Phi M_{cr}} \leq 1.0 \qquad [2.1]$$

where *c1* and *c2* are interaction coefficients, and *Mcr* and *Pcr* are the moment and axial critical capacities, respectively. The applied forces (*P & M*) in Eq. [2.1] are generally the second order values that result due to geometric nonlinearities. However, Eq. [2.1] cannot be applied as is under fire conditions since there are no validated expressions or methodologies for computing the fire-induced *P* & *M* acting on restrained beams (or columns). Also, Eq. [2.1] is valid for uniform temperature (uniform strength stresses) distribution in the beam-column. As it will be explained in the following section, Eq. [2.1] does not properly account for the influence of thermal gradient across the cross section of the beam-column.

2.2.2 Thermal Gradient

When a beam-column is exposed to fire, significant thermal gradients can develop across the cross-section due to 1-, 2-, or 3-sided fire exposure, as shown in Fig. 2.3 (*a*). Generally, 4-sided fire exposure produces nearly uniform temperature, while 1-, 2-, or 3- sides of fire exposures can generate thermal gradients in the section. For example, a restrained column subjected to a thermal gradient (as in perimeter columns exposed to fire from one side) develops a bending moment in addition to the axial force. Similarly, a restrained beam subjected to a thermal gradient (since beams generally support a concrete slab and thus fire exposure is from 3 sides) develops an axial force in addition to the bending moment.

The influence of thermal gradients is partially considered in some codes of practice by carrying out cross-sectional analysis. The Eurocode (EC3 2005) accounts for thermal gradient by applying numerical integration (sectional analysis) for the axial and moment plastic capacities of the section only. However, the influence of thermal gradient on the shape of the interaction equation [2.1] is not addressed at all.

Due to uneven heat distribution in the section, strength and stiffness properties of steel vary across the depth of the section. This variation of strength and stiffness of steel leads to an eccentricity between the center of stiffness and center of geometry of the cross section. Because of this gradient-induced shift in the center of stiffness, the axial force (*P*) will act eccentrically on the section, and thus generates bending moment. This bending moment can cause a shift in the plastic P-M diagram. Therefore, this migration of center of stiffness causes a distortion in the plastic P-M interactive diagram.

Figure 2.4 illustrates the plastic P-M interaction curve for a W24x76 beam section under different thermal gradients. The average temperature of the section (across the depth) is maintained at 500°C, while the thermal gradient was increased from zero to 150°C. The interaction curves are computed through direct integration of ultimate stresses across the cross section for each case of thermal gradient. The values of the moment and axial force are normalized to the plastic moment and axial capacities of the section at each case of thermal gradient. It can be seen from Fig. 2.4 that: 1) Using *constant minimum Fy* (constant *maximum T* of 650°C) may be overly conservative as seen by comparing this yield surface to the true yield surfaces at different thermal gradients; and 2) the *true plastic P-M interaction curve* (that considers variable *Fy* through the section as a result of thermal gradient) shifts and departs from the shape of the curve considering constant average *Fy*. This shift and distortion of the P-M diagram depends on the level of thermal gradient in the section. Figure 2.4 also shows that the assumption of *constant* (i.e. uniform) *average Fy* ($\Delta T = 0$) through the depth of the section can be conservative in some cases and unconservative in other cases.

In a similar fashion, thermal gradient can also cause a shift in the shear center of the section, and this shift influences the lateral torsional buckling capacity of steel beams exposed to realistic fire exposures. This issue of shifting center of stiffness, which can have a significant influence on beam-column equation, is not treated in almost all design codes or standards.

2.2.3 *Fire Scenario*

The type of fire scenario has a significant influence on the evolution of steel temperature and on the development of restraint forces in beam-columns. Much of the current knowledge is based on fire resistance tests on restrained columns or beams where the exposure is typically assumed to be that of a standard fire. However, in buildings the fire exposure is likely to be different and dependent on fuel load and ventilation characteristics in the fire compartment (Buchanan 2002). Fig. 2.3(b), illustrates the difference between standard fire and realistic (design) fire scenarios. The main difference between the two is that in standard fire exposure the temperature of the fire is assumed to increase without any decaying (cooling). However, fires in buildings die down and the compartment enters a cooling phase as a result of exhaustion of fuel and/or ventilation (oxygen). This aspect of cooling phase has significant influence on the fire response of structural members, specially restrained members such as beam-columns.

While under standard fire steel properties continue to deteriorate due to increasing temperature, the decay phase of a design fire leads to a recovery of strength and stiffness in steel as a result of decreasing temperature in steel. Also, the decay phase of a design fire leads to cooling and contracting of steel and this contraction causes an increase in tensile stresses in the beam and thus leads to recovery of some of the deformations in the beam. The total recovered deformation in the beam depends on the stress state of steel prior to the start of cooling of the beam. There is a lack of information on the behavior of steel in the cooling phase under realistic fires. There is a very limited number of studies on the effect of this cooling phase of fire on the structural response of steel members in general (Li and Guo 2006 and 2008), and beam-columns in particular.

2.3 CURRENT APPROACHES FOR EVALUATION OF FIRE RESISTANCE

Generally, there are two broad approaches through which the fire resistance of steel members is evaluated, namely; prescriptive- and performance-based approaches. A brief discussion on these two broad approaches is presented below.

2.3.1 Prescriptive Approach

In this approach, the fire resistance is evaluated based on standard fire tests. The purpose of the standard fire test is to determine the failure time (fire resistance) at which the structure/assembly loses its load bearing and/or compartmentation ability to withstand fire exposure. Generally, in standard fire tests, the failure is based on a thermal (prescriptive) criterion, which assumes a member to fail once steel reaches a "*critical*" temperature, regardless of loading, restraint conditions, or fire scenario. The critical temperature as per ASTM E119 is defined as the temperature at which *steel* loses 50% of its room-temperature yield strength (ASTM E119a 2008). Therefore, standard fire tests are a comparative tests and do not reflect actual performance of the member.

Standard fire resistance tests are generally carried out on building elements such as walls, floors, beams, or columns in accordance with national standards such as ASTM E119a (2008) and ISO 834 (1975). Test specimens are constructed in a similar manner as the building elements in practice. ASTM E119 specifies the dimensions of the test specimen and the size of the furnace being used for the standard fire test. Further, the furnace chamber is heated by liquid fuel or gas such that the average temperature in the furnace follows the specified standard temperature-time curve shown in Fig. 2.3(b).

During the fire test, load bearing members, such as a steel beam, are loaded with service loads (dead load + live load). A common practice in standard fire tests is to apply a service load level (about 50% of the room temperature capacity) on the tested member. The test continues until failure occurs by exceeding the critical temperature or when the structural member is no longer able to sustain the applied load.

Based on these standardized tests, tabulated data or empirical relations are derived for fire resistance. Therefore, the current prescriptive approaches that are based on standard tests do not account for realistic fire, loading, and restraint scenarios as encountered in practice. This makes the prescriptive design approaches in conflict with the recently introduced performance-based codes as it will be explained in the following section.

2.3.2 Performance Based Approach

In recent years, there has been an increased focus on moving towards performance-based fire safety design from the current prescriptive-based approaches (Meacham and Custer 1992, Kodur 1999, and Wang and Kodur 2000). This is mainly due to cost-effective and rational fire safety solutions that can be arrived at through performance-based design approach. One of the key aspects in any performance-based design is the fire resistance design of structural members. At present, there is limited information or tools (design equations) that can be applied for performance-based fire safety design of restrained steel beams. This is due to the lack of both experimental and analytical studies on the fire response of restrained steel beams. In the development of the performance-based approach for evaluating the fire resistance of steel beams, three main factors must be considered, namely, (1) fire scenario, (2) loading conditions and (3) failure criteria (Kodur 1999). These three factors are discussed in the following sections.

2.3.2.1 Fire Scenarios

The development of a fire scenario in a building compartment, which is commonly referred to as "a room fire" involves three stages; namely, growth, burning, and decay stages as shown in Fig. 2.5. In the growth stage, the temperature of the fire gradually increases and the fire spreads slowly over combustible surfaces within the room. Generally, in this stage, the structural integrity is not significantly influenced because the fire temperature does not reach high levels. However, once the fire temperature reaches about 600°C, flashover occurs and the fire enters the intense burning stage, where the temperature may exceed 1000°C. In the burning stage, the temperatures and the radiant heat flux are so high within the room that all exposed surfaces will ignite and burn. The structural integrity may be severely damaged at this stage. Fires that pass the flashover threshold are commonly referred to as "post flashover" fires. Eventually, the fire enters the decay stage where the fire temperature drops once the fuel burns out or there is a lack of ventilation (oxygen) (Buchanan 2002). Often, for structural analysis, the fire growth is idealized through time-temperature relationships, as shown in Fig. 2.3(b) and Fig. 2.5.

The development of a fire scenario is quite complex since it is dependent on a number of factors. For ease of calculation, a standard time temperature curve is often used to represent a room fire scenario in various standards (ASTM E119a 2008, EC1 2002, ISO 834 1975). Such standard fires are used to define the temperature profile that is generally used in standard fire tests as discussed earlier. While standard fire resistance tests are useful benchmarks to establish the relative performance of different steel members under the standard fire condition, they should not be relied upon to determine the survival time of steel members under realistic fire scenarios. Nor does the standard heating condition bear any relation to the often less severe heating environments encountered in real fires.

Figure 2.3(b) illustrates the time-temperature curves for a standard and two realistic design fire scenarios. In the standard fire (ASTM E119a 2008), the fire size is the same (irrespective of compartment characteristics), temperature increases with time throughout the fire duration, and there is no decay phase. This standard fire does not represent an actual fire scenario in a building.

While the temperature in a standard fire continues to increase indefinitely with time, a natural room-fire starts to gradually cool down as shown in Fig. 2.5. Room-fires are generally expressed in terms of "design or realistic" fires. A typical design fire can be mathematically represented by a parametric time-temperature curve that is dependent on the fuel and ventilation characteristics of fire compartment. Examples of these parametric fires are those specified in Eurocode (EC1 2002) and one of them is shown in Fig. 2.5. In the Eurocode, the heating phase of a design fire is specified parametrically in terms of the factor Γ which is dependent on the ventilation characteristics and thermal inertia of fire compartment. For $\Gamma = 1.0$ the heating phase of a parametric fire represents the ISO 834 standard fire. Higher the value of Γ represents more severe fire conditions with faster rise of temperature in fire compartment. In these idealized parametric fires, the decay phase is typically linear with a constant decay rate that is also dependent on the ventilation characteristics, as shown in Fig. 2.3 (b) and Fig. 2.5.

2.3.2.2 Loading Conditions

The current provisions in codes of practice for evaluating fire resistance are generally based on a load ratio of about 50%. Load ratio is defined as the ratio of the applied load on the beam under fire conditions to the strength capacity of the beam at room temperature. The load ratio depends on many factors including the type of occupancy of the building, dead-load-to-live-load ratio, safety factors (load and capacity factors) used for design under both room temperature and fire conditions. The loads that are to be applied on a steel beam, in the event of fire, can be estimated based on the guidance given in design codes. The ASCE-07 (2005) and Eurocode (EC1 2004) have different specifications for the critical load combination under fire conditions (wf), and these are:

$$\{\text{ASCE-07 2005}\}: \; wf = 1.2 \text{ dead load} + 0.5 \text{ live load} \qquad [2.2a]$$

$$\{\text{EC1 2004}\}: \; wf = 1.0 \text{ dead load} + 0.5 \text{ live load} \qquad [2.2b]$$

Different combinations are specified for different cases of load types. Based on these guidelines for load combinations, and for typical dead-load-to-live-load ratios (in the range of 2 to 3), the actual load ratio typically found under fire conditions ranges between 50% and 70%.

2.3.2.3 Failure Criteria

The conventional prescriptive approach of evaluating fire resistance (defining failure under fire conditions) is based on thermal and/or strength failure criteria as specified in ASTM E119a (2008). Accordingly, the thermal failure of a steel beam is said to occur when at least one of the following criteria is met:

- The average temperature in steel exceeds the critical temperature, which is 538° C (1000° F) for ASTM A36 structural steel.
- The beam is unable to resist the applied service load (50% of ambient temperature capacity).

The deflection and rate of deflection play a crucial role on the response of steel beams exposed to fire. In fact, a deflection limit is often applied to check the status of steel beams (serviceability limit state) at ambient conditions (AISC 2005 and EC3 2005). This criterion should be considered to determine failure under fire conditions. This is because generally, strength failure in a steel beam exposed to fire is reached after undergoing large deflections. The resulting deflections in fire scenarios are generally higher than those at room temperature due to deterioration of member stiffness and also due to temperature-induced creep. The British Standard (BS 476 1987) contains deflection and rate of deflection criteria for defining failure of steel beams tested in a furnace. Although these deflection limit states might have been set to limit damage to the furnace during fire tests, deflection and rate of deflection can be important under certain fire conditions. This is because the integrity of the structural member cannot be guaranteed with excessive deformations. Moreover, fire resistance based on limiting deflection will help to facilitate the safety of fire fighters and also to safely evacuate occupants prior to structural collapse. According to BS 476, failure is assumed to occur when:

- The maximum deflection (Δ) of the beam exceeds $L/20$ (or $L/30$ in some cases) at any fire exposure time, or
- The rate of deflection ($\frac{d\Delta}{dt}$) exceeds the limit given by the following expression:

$$\frac{d\Delta}{dt} = \frac{L^2}{9000d} \text{ (mm/min)} \qquad [2.3]$$

where L = span length of the beam (mm), and d = effective depth of the beam (mm).

2.3.3 Provisions in Codes and Standards

Provisions for evaluating the fire resistance of steel members are generally specified in codes and standards such as American Institute for Steel Construction (AISC 2005) or American Society of Civil Engineers (ASCE 1992), or the Eurocode Standards (EC3 2005). Based on the two broad approaches described earlier, the current provisions in codes and standards can be split into two main categories, namely; prescriptive- and performance-based provisions. While the prescriptive approach is predominantly used in the American standards, the European standards use a performance-based procedure for evaluating fire resistance. There is still extensive research taking place for transforming the current design provisions into purely performance-based approach.

2.3.3.1 Prescriptive-Based Fire Design

Most of the provisions in codes and standards share a common strategy of computing a critical temperature of steel member, and use that critical temperature for evaluating fire resistance. The critical temperature is defined as the temperature at which *steel* loses 50% of its room-temperature yield strength. According to ASTM E119, critical temperature of 538°C (1000°F) is generally used in for structural steel. Based on this definition of critical temperature, empirical relations are derived from standard fire tests for computing fire resistance of various steel sections with various insulation schemes. These prescriptive-based relations are derived from standardized fire tests and sectional seizes and generally depend on the sectional geometry and insulation scheme. An example of such relations is the following formula provided by the International Building Code (IBC 2000) section 720.5.1.3 for evaluating fire resistance of I-shaped steel columns insulated with spray applied fire proofing material:

$$t_F^{IBC} = \left[C_1 \left(\frac{A_p}{V_p} \right) + C_2 \right] \times t_p \qquad [2.4]$$

where t_F^{IBC} is the fire resistance (in minutes) according to IBC equation, *Ap/Vp* is the ratio of the heated perimeter (*Ap*) to the cross sectional area (*Vp*) of the steel section, and *tp* is the insulation thickness. *C1* and *C2* are regression coefficients.

Equation [2.4] is used to either evaluate fire resistance, or the required insulation thickness for achieving a specific fire resistance rating. Such equations are too simplistic and are based on critical temperature obtained from standard fire tests with standard test conditions.

Due to its simplicity, the prescriptive design approach continues to be used in codes adopting performance-based approach such as the Eurocode (EC3 2005), New Zealand Standards (SNZ 1997), and Japanese Building Code (Harada et al. 2004). In these codes and standards, the concept of critical temperature has been slightly modified to be the average temperature at which steel *member* (rather than steel *material*) loses 50% of its room-temperature capacity. Empirical or semi-empirical formulas are provided in these codes to evaluate the critical temperature. For instance, Eurocode 3, New Zealand and Japanese steel design codes provide the following relations for computing the critical temperature (*Tcr*) of steel beams:

$$T_{cr}^{EC3} = 39.19 \ln\left[\frac{1}{0.967 \times r^{3.833}} - 1\right] + 482 \qquad [2.5a]$$

$$T_{cr}^{SNZ} = 905 - 690 \times r \qquad [2.5b]$$

$$T_{cr}^{JBC} = 700 - 375 \times r \qquad [2.5c]$$

where the load ratio (*r*) is defined as the ratio between the bending moment (*Mo*) resulting from reduced load during fire to the room-temperature plastic moment capacity of the steel beam (*Mp*). Obviously, in these equations and the like, the influence of restraint conditions and fire is not properly accounted for.

2.3.3.1 Performance-Based Fire Design

The advanced calculation methods in codes adopting performance-based approach evaluate the fire resistance based on strength criteria. The implementation of performance-based approach in fire design of structural members is recent, and therefore, most fire design provisions are based on the room-temperature design equations. In the Eurocode for instance, the ambient temperature design equations are used to check for load-bearing capacity of the structural members under fire but by updating steel properties as a function of steel temperature. For example, for fire design of a steel beam according to EC3, the designer must ensure that the temperature-dependent bending capacity ($M_{cr,T}^{EC3}$) of the steel section is greater than the imposed action (*M*) on the beam due to loading, i.e.:

$$M_{cr,T}^{EC3} \geq M \qquad [2.6]$$

In the relation above, $M_{cr,T}^{EC3}$ is generally evaluated by using the same room-temperature design equations but with reduced steel properties. The imposed action (*M*) is also evaluated based on reduced load combination at the event of fire. Based on this methodology, beams at ambient temperature are treated structurally as beams under fire. The influence of fire and boundary conditions on the fire response of such structural members is not considered.

Generally, three critical issues are neglected when the fire design is based on using ambient temperature design equations, but with updated reduced steel properties.

These critical issues are the change of structural response, the change of failure mode, and the change of failure criterion.

Change in structural response occurs due to the development of fire induced forces in the restrained steel beams or columns within framed structure. For instance, a beam at room temperature generally carries the applied load through flexure, however, under fire conditions; the same beam in a framed structure (where it is very likely to be restrained) carries the load through either arching or tensile catenary mechanisms at later stages of fire exposure.

Change in failure mode can occur due to the effect of restraint conditions. For instance, a beam at ambient temperature may fail either by flexure, shear, or buckling (global or local), while under fire conditions the same beam is more likely to fail by tension or by developing excessive deflection.

Change in failure criterion results as a direct consequence of the change in structural response and in failure mode mentioned above. While at ambient temperature, strength failure is considered as an ultimate limit state, however, under fire conditions, and due to high ductility of steel, strength failure is an impractical ultimate limit state criterion since strength failure is reached after undergoing very large deflection. Thus, an ultimate limit state based on deflection might be a better assessment for restrained beams under fire. Most fire tests and actual fire incidents have shown that fire resistance of restrained beams is generally governed by deflection criteria rather than strength criteria (Skowronsky 1990 and 1988, Kirby 1997, Newman et al. 2000, Wang and Kodur 2000, Wang 2000). Large deflection in steel beams can cause severe damage to structural integrity of the framed building and thus may hinder evacuation of people and facilitate the spread of fire.

2.3.4 Summary

The fire resistance of steel members is currently evaluated through prescriptive-based approaches that are derived based on standard fire tests and thus have limited application. Realistic fire resistance assessment can be obtained through a performance-based approach in which fire scenario, load level, restraint effects, and failure criteria, can be accounted for based on actual (rather than standard) scenarios. Presently, there is lack of design approaches for undertaking performance-based fire design of restrained steel beams. The aim of the current study is to develop rational guidelines for fire design of restrained steel beam under realistic load, fire and end conditions.

2.4 PREVIOUS STUDIES ON STEEL BEAM-COLUMNS UNDER FIRE

A review of the literature indicates that limited experimental and numerical studies have been undertaken on the fire response of beam-columns. This section provides an overview of experimental and analytical studies that were undertaken to study the fire performance of restrained steel beams or columns.

2.4.1 Experimental Studies

There have been few experimental studies that have been performed on steel beam-columns. In these experiments, attempts have been made to simulate fire-induced thermal gradients and axial and rotational restraint effects. The following is a summary of reported relevant fire tests.

The effect of fire induced restraint in beams was studied by Bletzacker at The Ohio State University (OSU) for the American Iron and Steel Institute (AISI) (Bletzacker, 1966). This research was initiated to establish criteria termed as *"restrained rating criteria"* by which steel beams in slab-beam assemblies can be identified as restrained or unrestrained under fire.

The experimental program consisted of twelve slab-beam assemblies consisting of 4-in. thick structural concrete slab on 22-gauge steel floor units supported by a W12×27 steel beam. The beam and floor deck were protected with a spray-applied cementitious fire protection material. A representative floor construction of 3 ft wide and the full length (16.75 ft) of the beam was assembled and loaded uniformly. The parameters considered in the test program included connection types, composite action between beam and concrete slab (noncomposite, partially composite, and fully composite action), axial and rotational restraints through the application of various levels of axial thrust and end moment, and the applied vertical load on the critical temperature of the beams.

Results from OSU fire tests showed that any increase of the stiffnesses of end restraints beyond a certain limit does not improve fire resistance of beams (Bletzacker, 1966). In the tests, as the magnitude of restraining stiffness was increased the flanges and/or the web of beams became more susceptible to local buckling. This is because the larger the restraining stiffness, the larger the fire induced axial force in the beam. Also, test results showed that composite action can enhance fire resistance of beams by providing additional restraint (especially rotational restraint near the supports) in conjunction with the restraint provided by the beam-to-column connections. It was also found that the higher the load levels the lower will be the fire resistance, regardless of whether the beam is restrained or not.

The generated test data from the OSU fire tests were studied extensively (Iding et al. 1988) and many numerical models were created (IITRI, FASBUS I & II) to simulate the effect of restraint on the fire response of beam-slab assemblies. However, these studies were of a commercial nature and were not used to develop an understanding of the fire response of restrained beams. The effects of critical factors such as thermal gradient, fire scenario, or failure criteria on fire response of restrained beams were not considered. The main purpose of these studies was to highlight that ASTM fire ratings (which are prescriptive in nature) are generally conservative for use in actual practice, since these ratings are based on unrestraint fire tests, employ thermal failure criteria, and are conducted under service load conditions.

The OSU fire tests and related numerical studies culminated in the development of descriptive criteria for classification of restrained steel assemblies. These qualitative and simple criteria were later adopted by the ASTM E119 standard, Table X3.1 (ASTM 2008) and are used for assigning fire ratings to assemblies. This table classifies the construction types into "*restrained*" or "*unrestrained*" beam-slab assemblies based on some "rules of thumb". There were no detailed or specific guidelines as how to rationally design such restrained steel members (which become beam-columns due to interaction with fire).

During 1995 and 1996, large-scale fire tests were conducted on an eight-story, steel-framed office building at the Cardington Large Building Test Facility (LBTF) by the Building Research Establishment in the United Kingdom (Newman 1999). The purpose of these tests was to study the behavior of full scale structural systems (frames) under realistic fire and loading conditions, and to generate data for developing computer models that are capable of analyzing framed structures under fire. The steel frame building was five bays long (148 ft) by 3 bays wide (69 ft) and 8 stories (108 ft) high. The beams in most of the tests were designed as simply supported members acting compositely with a concrete slab cast on metal deck. Columns were protected (insulated) up to the underside of the floor slab, but the beams, deck and floor slab in this unsprinklered building were unprotected.

A total of eight fire tests were undertaken on this steel framed building, including two fire tests on restrained beams that were unprotected and directly exposed to a design fire through a special furnace built around the beams. Results from these fire tests confirmed the OSU observations, and it was noted that for restrained beams, catenary tensile membrane action can significantly improve fire resistance. Also, it was observed that the weakest link in a steel construction under fire were the columns, because of the severe local buckling that occurred in the column near the connection. Thermal gradients induced significant bending moments during these full-scale structural-fire tests (Bailey et al. 1999) but the effect of these thermal gradients on the load carrying capacity of beam-columns was not investigated.

Some of the recent experimental studies focused on the influence of end restraints on the fire response of beam-columns. Li et al. (2000) conducted a fire test on axially restrained steel beams and found noticeable axial forces building up in the beam. Ali et al. (1998), Rodrigues et al. (2000), Ali and O'Connor (2001), Yang et al. (2006), and Tan et al. (2007) conducted a series of fire tests on axially and rotationally restrained steel columns under monotonic uniform heating. The main findings from these experiments were that increasing the axial restraint lead to earlier failure of the column and this corresponds to a lower critical temperature in steel. Wang and Davies (2003) tested columns that developed thermal gradients across the sections. They inferred that the thermal gradients produced additional bending moments in the columns. There were no attempts to quantify these fire induced bending moments.

Axially restrained steel beams, with fire induced thermal gradients, were tested by Liu et al. (2002) and Li and Guo (2008). Based on these fire tests, the authors concluded that the restraint effect and catenary action significantly influence the behavior of a beam under fire conditions. However, in their experimental studies, the effect of thermal gradient on the fire response was not explicitly measured or even discussed.

2.4.2 Analytical Studies

There have been a limited number of analytical studies on the fire behavior of beam-columns. Most of these studies presented results from finite element analysis, and in the analysis a number of assumptions were made to reduce the complexity of the problem. These studies did not yield simple design tools that can aid the designer to properly and efficiently account for fire effects

Usmani et al. (2001) presented a discussion of the basic principles that govern fire response of restrained steel beams. The analytical study focused on axially and rotationally restrained beams subjected to linear thermal gradient over the cross section. The study was based on simplified assumptions for the strains arising due to fire exposure. Further, the study did not include material nonlinearities or transient material characteristics such as strain hardening, high-temperature creep and fire scenarios. Moreover, geometric nonlinearities, such as large deflections were not addressed in this study.

Tan and Huang (2005) investigated the development of fire-induced restraint forces in steel beams using one dimensional single span beams. The effect of slenderness ratio, load utilization factor, thermal gradient across the steel section and axial and rotational restraints on the fire response of steel beams was evaluated. In the analysis, the failure of the beam was said to occur when the steel section reaches the critical temperature. The critical temperature was redefined as the temperature at which steel member loses 50% of its room temperature strength. Results from the analysis indicated that the axial restraint reduces the critical temperature, while the rotational restraint increases it. The effects of local buckling of the steel beam and the different fire scenarios were not considered in this study.

Yin and Wang (2003) applied a finite-element method to study the behavior of restrained steel beams under fire conditions. Results generated from these numerical studies were used by Wang and Yin (2006) to develop a method for predicting the fire behavior of restrained steel beams. However, the method is applicable for a narrow range of situations due to the nature of the assumptions the method is based on. For example, the method requires the user to assume a deflected profile of the entire beam, which makes the method case-specific since the deflected profile is a function of the load shape. Local buckling, high-temperature creep and fire scenarios, which influence the fire response of restrained steel beams, were not included in these studies

A closer examination of the previous studies reveals that the location of the fire induced axial restraint was assumed to remain at the geometrical centroid of the beam. In actual practice, the location of the axial restraint can vary depending on the type and configuration of the connection between the beam and the column. The literature review reveals that the effect of varying the location of the axial restraint on the fire response of restrained beams has not been investigated (Dwaikat and Kodur 2009). For a simply supported beam, assuming the restraint location to be at the geometric centroid results in the fire induced axial force not generating any moment around the beam center. However, if the location of the axial restraint is not at the centroid of the section, then a significant bending moment might develop at supports due to the eccentricity of the fire induced restraint force. This generated bending moment can affect the fire response of a beam-column (Dwaikat and Kodur 2009).

2.5 HIGH TEMPERATURE STEEL PROPERTIES

Knowledge of high-temperature properties of steel is critical for evaluating fire resistance using numerical models. In most previous studies, researchers have either used material models specified by codes and standards such as the Eurocode or ASCE manual of practice (EC3 2005, ASCE 1992), or they devised their own material models (Poh 2001, Anderberg 1988, William-Leir 1983) for evaluating fire resistance of steel structures. In this section, a review of the high temperature properties of steel is presented and the sources for the variations between the different steel material models will be highlighted.

Steel has excellent strength properties at ambient temperature, however, like other materials; steel loses its strength and stiffness with rise of temperature. The temperature dependent properties that are important for modeling the fire response of steel structures include thermal, mechanical, and deformation properties. These properties vary with temperature and are also dependent on a number of other parameters. Much of the current knowledge on the high-temperature properties of steel is based on limited material property tests. Also, most of the current information on high temperature material properties of structural steel is suitable for the heating phase of fires. This is because most (if not all) material tests were conducted under either transient or steady state tests with increasing temperature. However, there is lack of data on how properties of steel vary during the cooling phase of fire.

The response of a steel structure exposed to fire is governed by: (a) thermal (b) mechanical and (c) deformation properties. Thermal properties determine the temperature profile in the steel sections resulting from exposure to fire, while the mechanical properties govern the loss of strength and stiffness as a function of temperature. Deformation and mechanical properties determine the extent of deformation of the steel member under fire conditions.

Until recently there were no standard test methods for evaluating high temperature mechanical properties. This has led to researchers using their own test methods to measure the high temperature properties of steel. Due to differences in test methods, heating conditions, and data collection techniques, there is a noticeable variation in the different sets of data available in the literature. Thus, there are considerable variations in the different constitutive relationships presented in different codes and standards for many of the high-temperature properties of steel (Kodur and Harmathy 2002).

2.5.1 Thermal Properties

The main thermal properties that influence the temperature rise in steel are thermal conductivity and specific heat (often expressed in terms of heat capacity). Figs. 2.6(a) and (b) plot the available data on thermal conductivity, and specific heat of steel as a function of temperature, respectively. Relationships from codes and standards (EC3 2005, ASCE 1992), as well as published test data were used to compile Figs. 2.6(a) and (b) (Rempe and Knudson 2008, Bentz and Prasad 2007, Touloukian 1972, Powel and Tye 1960, and Yawata 1969).

It can be seen in Fig. 2.6(a) that thermal conductivity decreases with temperature in an almost linear fashion, and there is little variation between the models presented in ASCE manual and Eurocode. On the contrary, specific heat models vary considerably between 700°C and 800°C, as can be seen in Fig. 2.6(b). In general, the specific heat of steel increases with an increase in temperature with a large spike occurring around 750°C. The spike in the specific heat at around 750°C is due to the phase change that occurs in steel in which the atoms transition from a face centered cubic "FCC" to a body centered cubic "BCC" structure. In overall assessment, for high temperature thermal properties of steel, minor variations exist in the specified models in design codes and standards. This process absorbs considerable energy (heat), thus accounting for the spike around 750°C seen in Fig. 2.6(b).

The variation between the test data and the models shown in Fig. 2.6 is partly due to the fact that the majority of the existing data on specific heat originates from studies carried out on iron and non-structural steel alloys. Additionally, the maximum temperature reached in these studies on iron and non-structural steel was below 750°C, thus not capturing the full range of temperatures observed in fire conditions.

2.5.2 Mechanical Properties

A review of the literature indicated that there have been more studies on high-temperature mechanical properties of steel than that on thermal properties. Tests for high temperature strength properties are conducted mainly in two ways: transient- and steady-state tests. In transient-state tests, the test specimen is subjected to a constant load and then exposed to uniformly increasing temperature.

Temperature and strain are continuously recorded under constant stress. Thermal strain (evaluated from a separate test) is then subtracted from the total measured strain (Outinen 2007). In the transient-state tests, the heating rate has a great influence on the strain rate and thus different heating rates produce different strain rates. The heating rate of steel depends on the nature of the fire as well as on the thermal protection (insulation) and geometry of the cross section. Generally, for a typical beam with 2-hour fire rated protection (i.e. at least 2 hours to reach critical temperature of the steel), the heating rate of steel can be in the range between 3-7°C/min. However, for unprotected steel sections, the heating rate can be in the range between 25-40°C/min. In the literature, (Outinen 2007) transient mechanical property tests were conducted at heating rates ranging between 10 to 50°C/min. This heating rate can be suitable for unprotected steel members, but not for protected members with slow heating rates.

Steady-state tests are generally faster and easier to conduct than the transient-state tests. In steady-state tests, the test specimen is heated to a specific temperature and after that a tensile test is carried out. Stress and strain values are recorded continuously under constant temperature. The test can be either load-controlled (loading rate is constant) or strain-controlled (strain rate is constant) (Outinen 2007, Anderberg 1988). Despite the fact that strain rate has a significant effect on the test results, a large amount of test data on conventional steel is published without the information on strain rates (Outinen 2007, Anderberg 1988, and Cooke 1988).

2.5.2.1 Yield Strength and Elastic Modulus

As mentioned earlier, different test regimes were used to obtain yield strength and elastic modulus of steel at elevated temperatures. The variations in test parameters resulted in different test measurements, thereby leading to differences in constitutive relationships presented in different codes and standards. Generally, tensile tests are conducted to obtain elastic modulus and yield strength of steel. There is lack of experiments for steel modulus under compression. This is because in tensile tests, complications that may arise due to geometric instabilities and confinement of specimens are eliminated. However, it is generally assumed that the modulus of elasticity for steel derived based on tensile tests is the same under compression.

Figs. 2.7(a) and 2.7(b) show the yield strength and modulus of elasticity of steel as a function of temperature respectively. The test data plotted in the figures are compiled from various high temperature property tests as shown on the figures. Both the yield strength and elastic modulus decrease as temperature increases. This decrease can be attributed to the nucleus of the iron atoms in steel moving farther apart due to rising temperature in steel, leading to decreased bond strength, which in turn reduces the yield strength and elastic modulus.

It can be seen in the figures that there is significant variation in test data on yield strength and modulus of elasticity at temperatures above 300°C. This variation can be attributed to many factors, primarily variable heating and strain/load rates during the test. For example, when the heating rate of the stressed specimen is small, the specimen will be subjected to stress at elevated temperatures for longer time duration, therefore, other factors, such as high-temperature creep (time-dependent plastic strain under constant stress and temperature), can influence the resulting temperature-stress-strain curves of the tested specimen.

The yield strength and elastic modulus constitutive relationships from ASCE manual, Eurocode, and those proposed by Poh (2001) are also shown in Figs. 2.7(a) and 2.7(b) respectively.

As is the case with test data, there is also a considerable variation in the constitutive models for yield strength and modulus of elasticity. These variations in constitutive models are due to the large variation in the test data used to compile the respective constitutive models. A review of the models shows that the Eurocode model predicts less reduction in yield strength of steel with temperature as compared to the ASCE or Poh models. However, the Eurocode model provides a higher reduction in elastic modulus of steel with temperature as compared to the ASCE and Poh constitutive models as shown in Fig. 2.7(b).

Also, up to 400°C, the Eurocode model assumes no reduction in steel yield strength; however, ASCE and Poh models assume a loss of 30% and 40%, respectively, at 400°C, as shown in Fig. 2.7(b). This major difference between Eurocode and other constitutive models can be attributed to the fact that Eurocode distinguishes between two limits on the temperature-stress-strain curves, namely, the proportionality limit (*Fp*), and the yield limit (*Fy*). The proportionality limit in the Eurocode is the end of the linear portion of the stress-strain curve, after which point the stress-strain relation becomes plastic and nonlinear (ellipsoidal shape). The yield limit in Eurocode is the defined as the end point of the inelastic portion of the stress-strain curve. This feature of the stress-strain in Eurocode does not exist in either ASCE or Poh models which both assume a sharp point as a limit between linear-elastic and inelastic material response. The theory behind introducing proportionality limit in the Eurocode stress-strain curves at high temperatures is to capture visco-elastic behavior that is partly due to creep effect. The nonlinearity after the proportionality limit indicates that stress causes more strain after this point than in the linear elastic range. This simplification enables the stress-strain curves of the Eurocode to partly account for creep strains at elevated temperature.

2.5.2.2 Temperature-Stress-Strain Relationships

Figures 2.8(a) and 2.8(b) show the temperature-stress-strain curves from Eurocode 3, ASCE manual, and as proposed by Poh (2001) at room temperature and at 600°C, respectively. The y-axis represents normalized stress and the x-axis represents normalized strain. Originally, the Eurocode temperature-stress-strain curves were derived based on transient-tests under slow heating rates (Twilt 1991 and Anderberg 1988). Therefore, when used in the fire resistance analysis, the Eurocode constitutive relationships generally produce slightly more flexible response as compared to ASCE or Poh constitutive models. This is attributed to the fact that in the transient-state tests, adopted by the Eurocode, part of high temperature creep is included in the resulting temperature-stress-strain curves (Anderberg 1988, Buchanan 2002). However, less information is known about the test data that were used to derive ASCE temperature-stress-strain curves of steel. On the other hand, Poh (2001) developed generalized temperature-stress-strain relations for structural steel based on a large set of experimental data. These relations account for specific features, such as the yield plateau and the effect of strain hardening. These temperature-stress-strain relations have been validated against the specified relationships in codes and standards, and they have been shown to give more realistic predictions of fire resistance when used in conjunction with high temperature creep model.

2.5.3 Deformation Properties

The deformation properties that influence the fire response of steel structures are thermal strain and high-temperature creep. The following sections discuss the variations in deformation properties of steel at elevated temperatures.

2.5.3.1 Thermal Strain

There have been many tests to characterize thermal strain of steel at elevated temperatures, results from some of which are compiled in Fig. 2.9 (Outinen 2000, Cooke 1988, Anderberg 1988, and Stirland 1980,). As seen in Fig. 2.9, thermal strain of steel increases with temperature up to nearly 750°C, at which point a phase change takes place (as discussed previously) and the thermal strain becomes nearly constant up to 800°C, after which point thermal strain starts to increase again.

Variation of thermal strain models as specified in ASCE and EC3 are also plotted in Fig. 2.9. Minimal differences exist between the Eurocode and ASCE models for thermal strain of steel up to 700°C. However, in the temperature range of 700°C-850°C the ASCE model assumes a continuously increasing thermal strain while the Eurocode model accounts for the phase change that occurs in steel in this tem

foll

2.5

Cre
tem
is n
is l
con
tem
spe
mo
ana
mai
ass
exp
and
The
stre
Gen
400
effec
(Hua

temperature range by assuming a constant thermal strain from 750°C to 850°C, followed by an increasing thermal strain up to 1000°C (See Fig. 2.9).

2.5.3.2 High Temperature Creep

Creep is defined as the time-dependent plastic strain under constant stress and temperature. The influence of high temperature creep on the response of structures is much more pronounced at elevated temperatures than at room temperature. This is because at elevated temperatures steel becomes less viscous and thus the continuous deformations under constant stress and temperature, referred to as high temperature creep, become more significant. The codes and standards are not specific about how to incorporate creep into fire analysis, and the choice of creep models is often left to the user (Kodur et al. 2009). At present, most fire resistance analyses are carried out using Harmathy's high temperature creep model that is mainly based on Dorn's theory (Dorn 1954; Harmathy 1967). Dorn's creep theory assumes constant stress ($d\sigma_S / dt = 0$). However, in the case of beam-columns exposed to fire, the fire induced stresses vary considerably and rapidly with time and temperature, and these conditions are not captured by Dorn's theory. Therefore, an alternate high temperature creep model that can capture variable stress scenarios is required to account for these extreme conditions.

Generally, creep deformations in steel become noticeable at temperatures above 400°C. However, it was found experimentally that when the stress level is high, the effect of creep becomes significant in steel members even at temperatures of 300°C (Huang et al. 2006, and Huang and Tan 2003). Creep tests (Kirby and Preston 1988, Harmathy and Stanzak 1970, and Dorn 1954) were generally conducted for steel and metal alloys with variable chemical compositions, and very little information is available on the effect of high temperature creep on the structural response. Contradictions also exist in codes of practice when it comes to high temperature creep. Eurocode states that "*the effects of transient thermal creep need not be given explicit consideration*" (Clause 4.3.3(4) of EC3 2005). However, the ASCE manual of practice states that high temperature creep should be accounted for in fire resistance analysis through one of two options. The first option is to use "*effective*" temperature-stress-strain curves derived from transient-state tests at relevant heating and strain rates (ASCE 1992 and Buchanan 2002), while the second option is to use specific high temperature creep models developed for structural steel. As such, it is generally left to the user to choose which creep model to use.

2.6 SUMMARY

The state-of-the art review clearly indicates that there is a lack of knowledge with respect to a number of key areas that are critical for developing a holistic approach for the fire safety design of beam-columns. The following are some of the key factors that need to be considered for developing such design guidelines:

- No fire resistance experiments have been performed on beam-columns that develop thermal gradients. Data from fire experiments are needed to validate finite element models.
- The effect of fire scenario on the response of beam-columns was not investigated in previous studies. Fire scenario can vary from a standard fire

curve (with no decay phase) to a design fire (with decay phase). The decay phase can result in cooling of steel in a restrained beam and thus leads to generation of tensile forces due to the shrinkage of steel. The development of these tensile forces was not investigated in previous work.

- Evaluating and quantifying fire induced forces in beam-columns. The fire induced axial force and bending moment have a significant influence on the performance of the beam-columns themselves and on beam-to-column connections. For example, simple shear connections are not designed to resist tensile forces that develop due to fire induced catenary action or due to shrinkage of steel in cooling phase of a design fire. Generally, these fire induced forces are not accounted for in fire design due to lack of tools for evaluating them. Simple expressions for evaluating these fire induced forces become a necessity for proper fire design of beam-columns.
- There is a large variation in high temperature properties of steel presented in different codes. For example, the Eurocode states that high temperature creep can be neglected, while ASCE manual of practice states that high temperature creep must be included in the analysis. This led the researchers to either use the discrepant code-specified material models or devise their own material models.
- Accounting for the response of beam-columns is quite complex and has to be carried out using sophisticated finite element analysis. Such analysis requires a large amount of input data and also produces a huge amount of numerical results that are not easy to analyze. To avoid all these complexities,

simplified design tools need to be developed based on intensive numerical studies that take into account all of the previously mentioned factors.

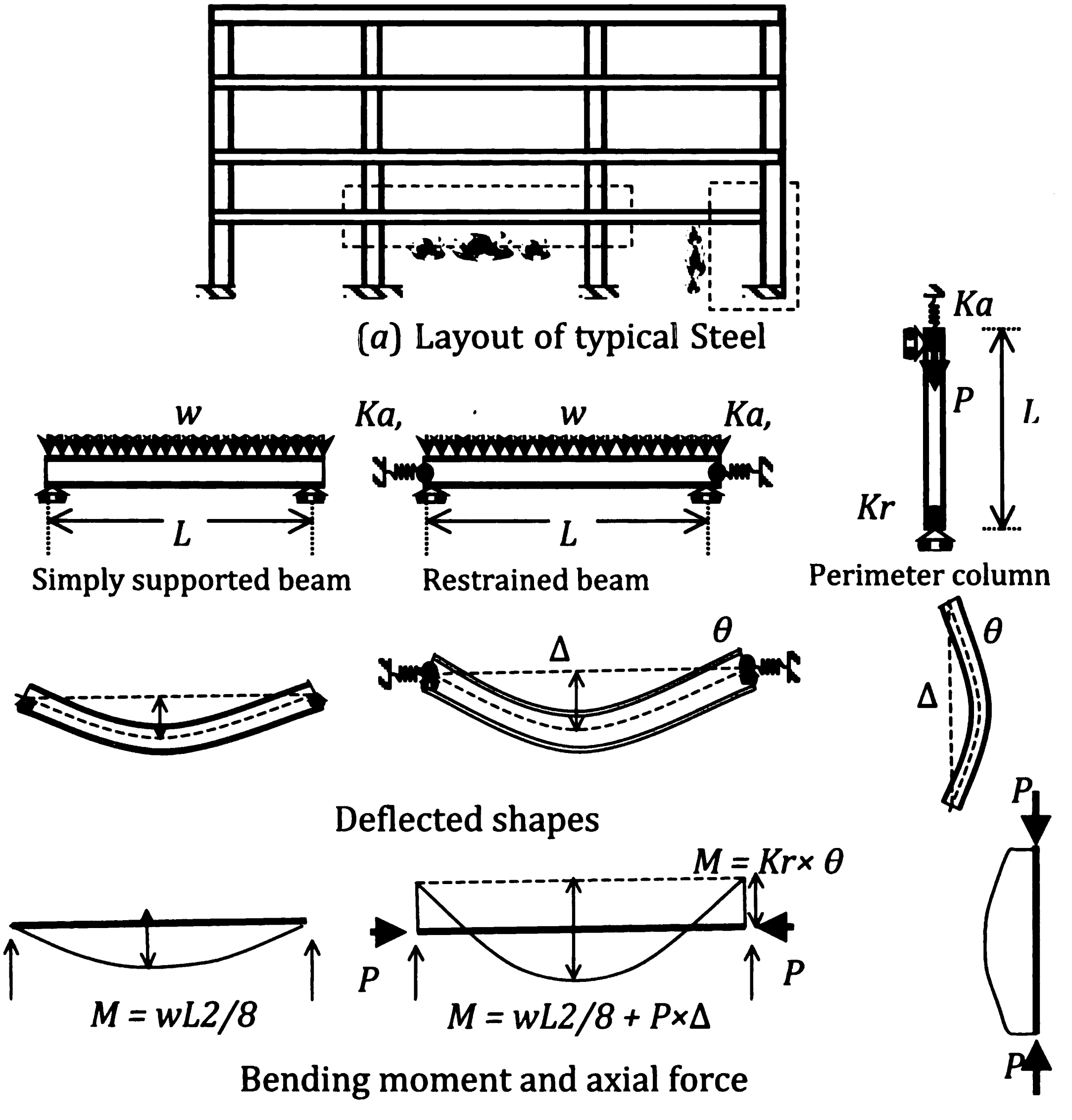

(b)Simply supported (c) Restrained beam (d)Restrained column-beam

Fig. 2.1: Development of fire induced restraint forces in restrained steel beams and columns.

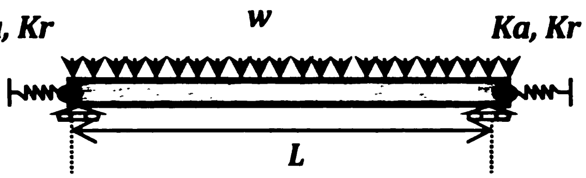

a) Layout of restrained steel beam

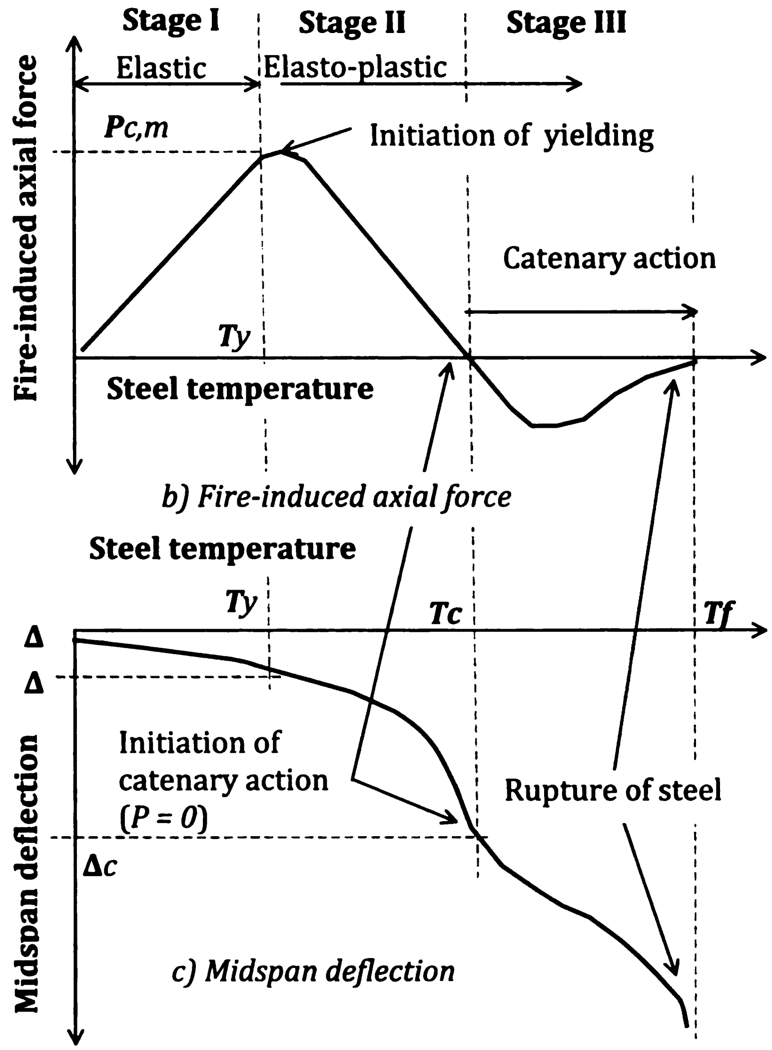

b) Fire-induced axial force

c) Midspan deflection

Fig. 2.2: Typical fire response of a restrained steel beam that fails by yielding

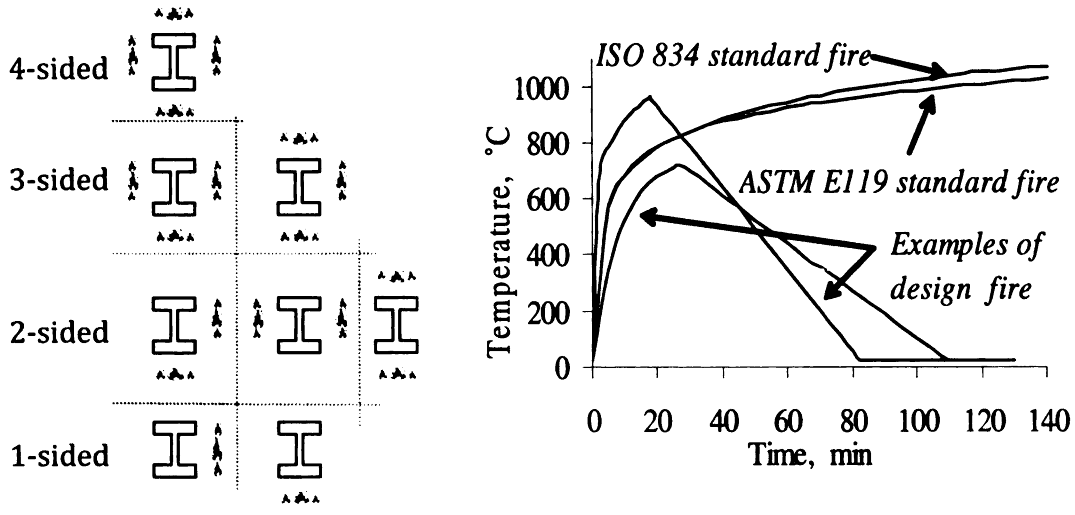

(a) Fire exposure types

(b) Fire scenario

Fig. 2.3: Types of (a) fire exposure and (b) fire scenario

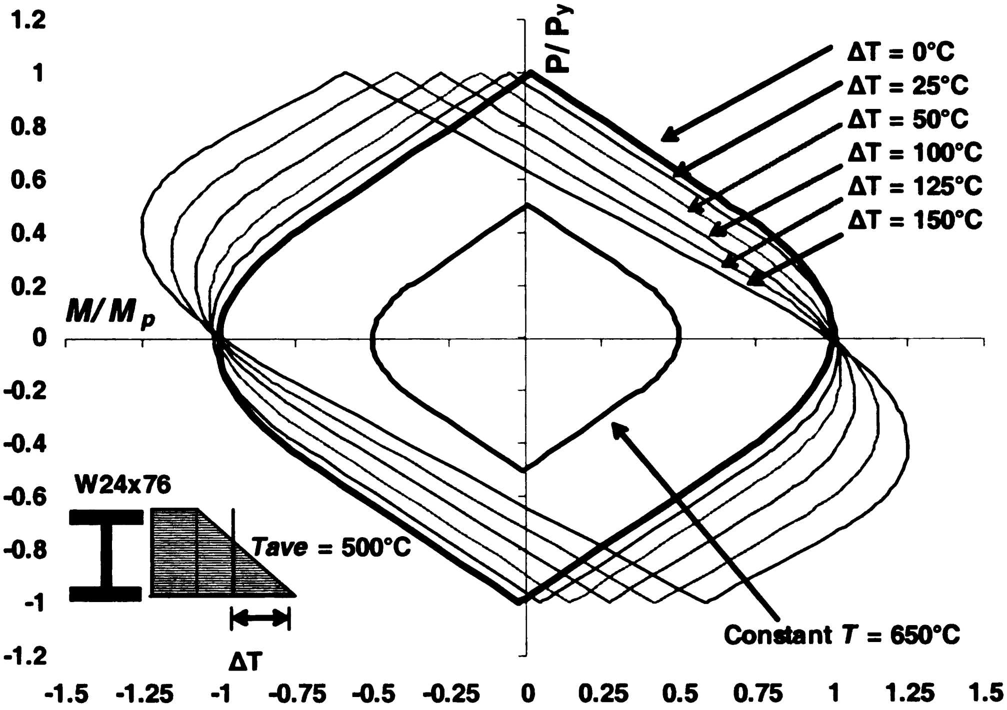

Fig. 2.4: Changes in the shape of the P-M interaction diagram under the influence of thermal gradients

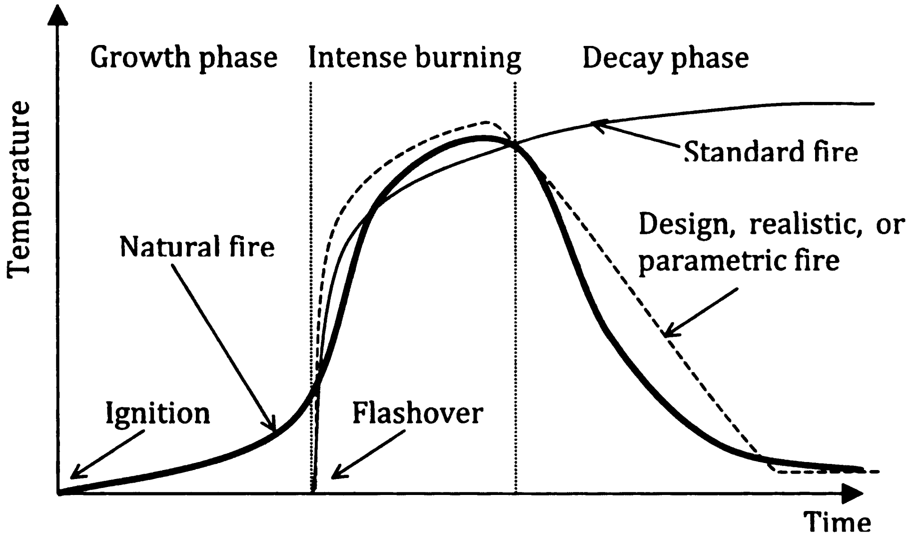

Fig. 2.5: Various Stages of Fire in a Typical Compartment with common idealization

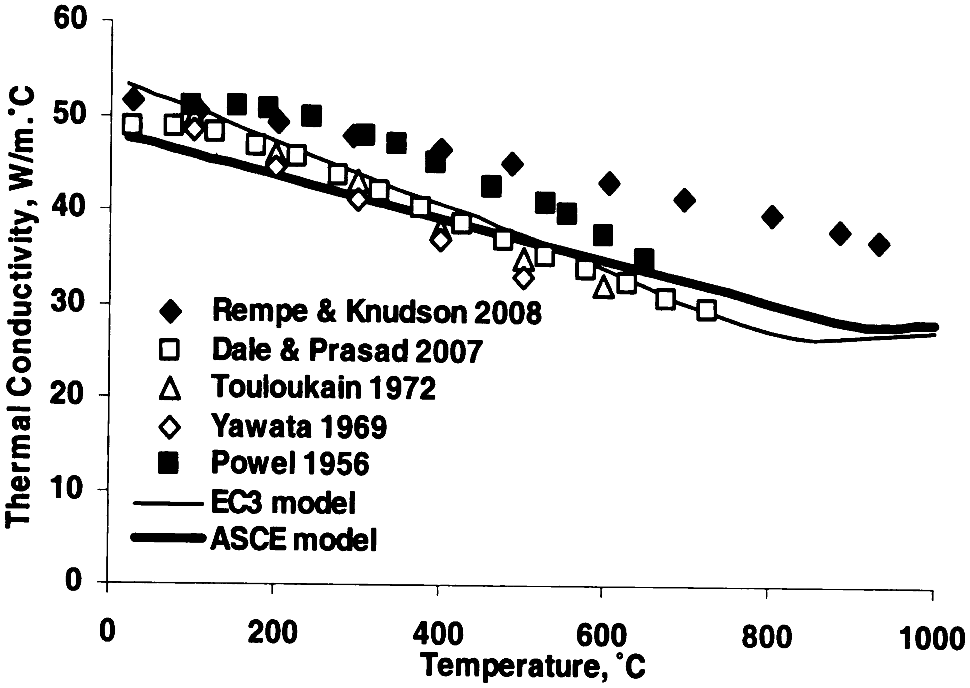

(a) Thermal conductivity

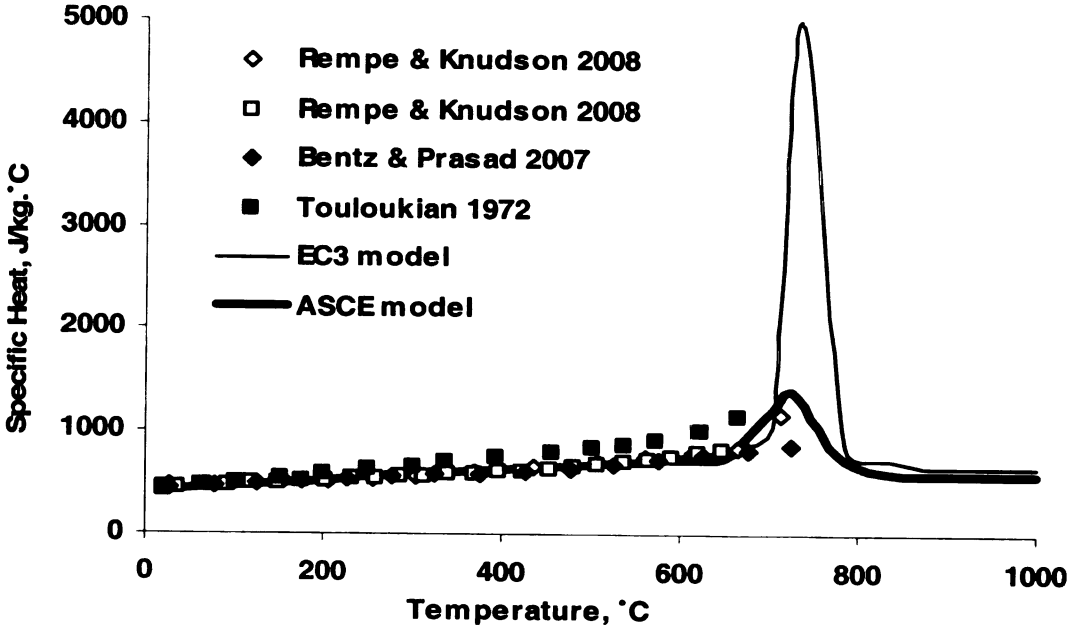

(b) Specific heat

Fig. 2.6: Thermal properties of steel as predicted by different models and as measured in different test programs

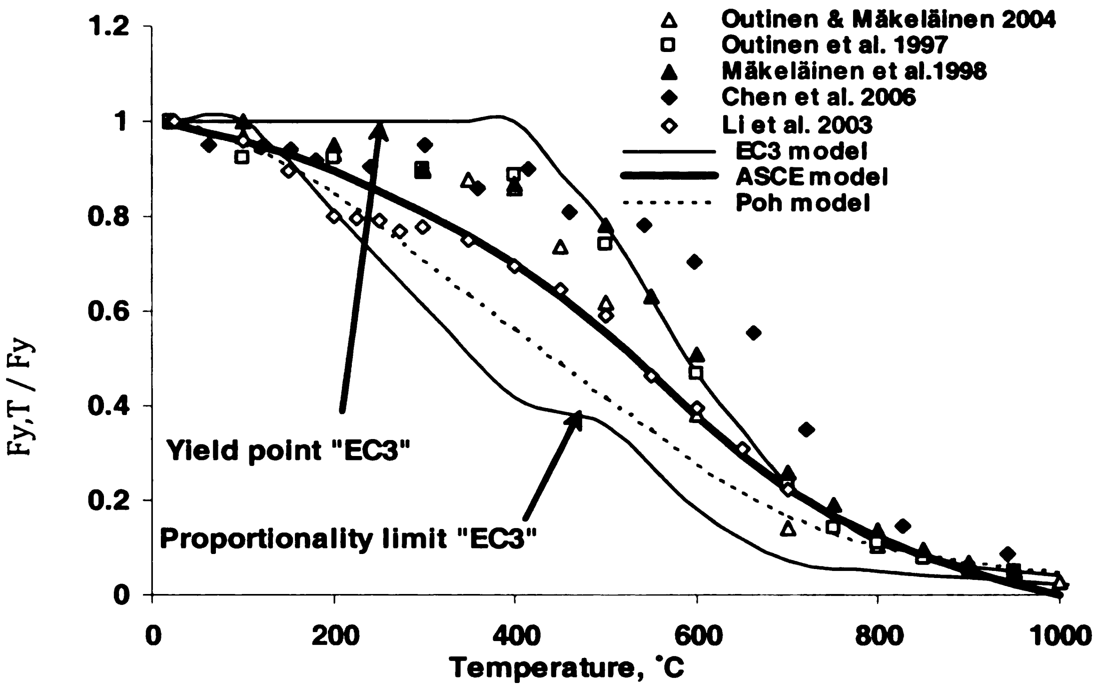

(a) Yield strength

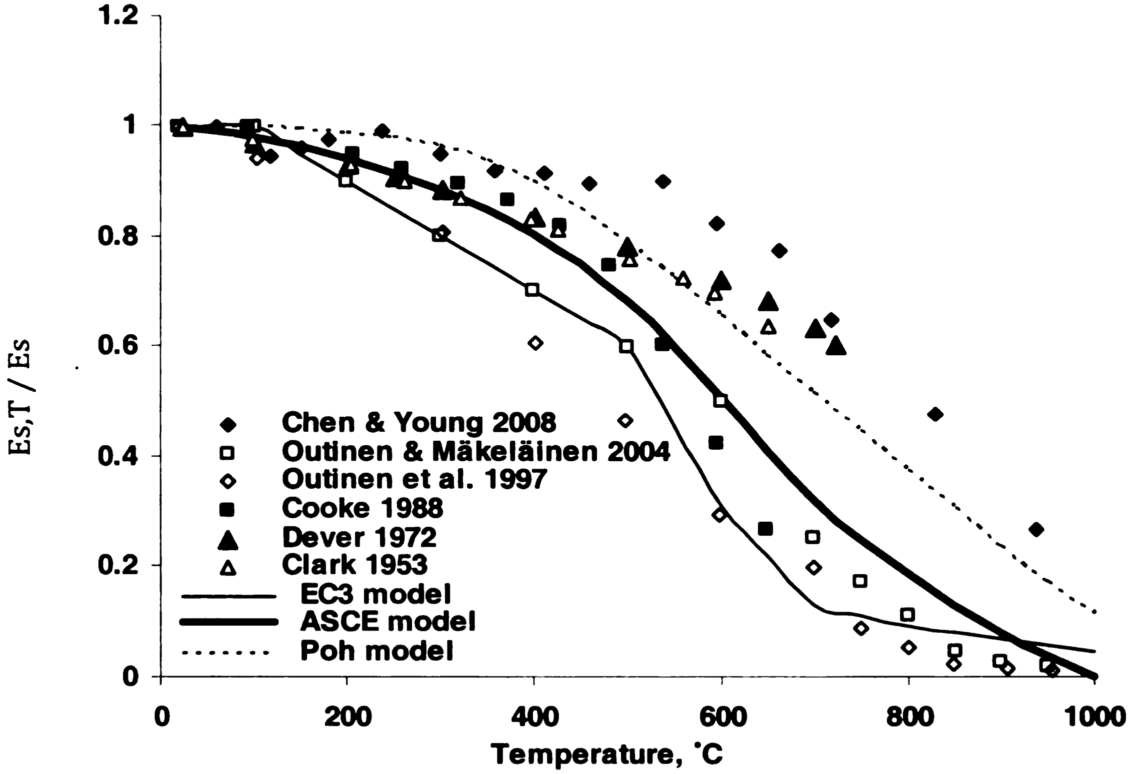

(b) Elastic modulus

Fig. 2.7: Yield strength and elastic modulus of steel as predicted by different models and as measured in different tests

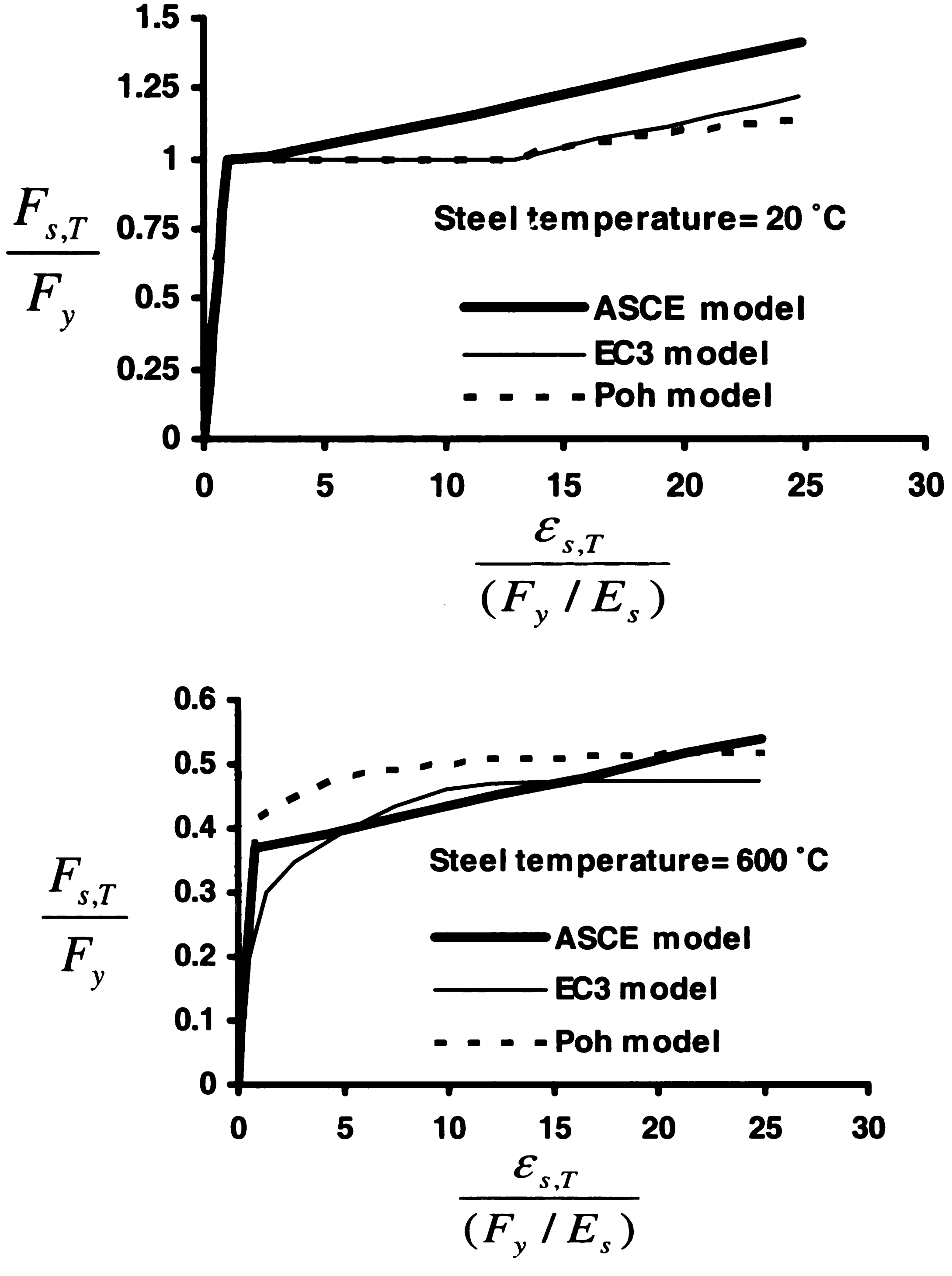

Fig. 2.8: Temperature-stress-strain relationships for structural steel as per ASCE, Eurocode and Poh models

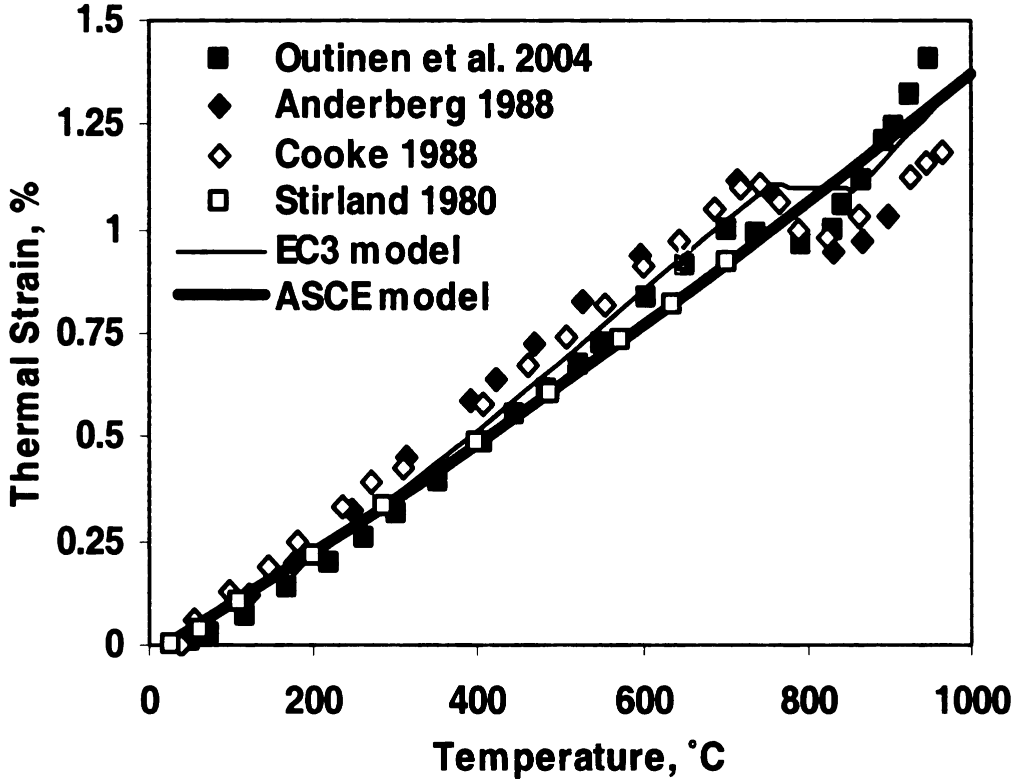

Fig. 2.9: Thermal strain of steel as predicted by different models and as measured in different tests

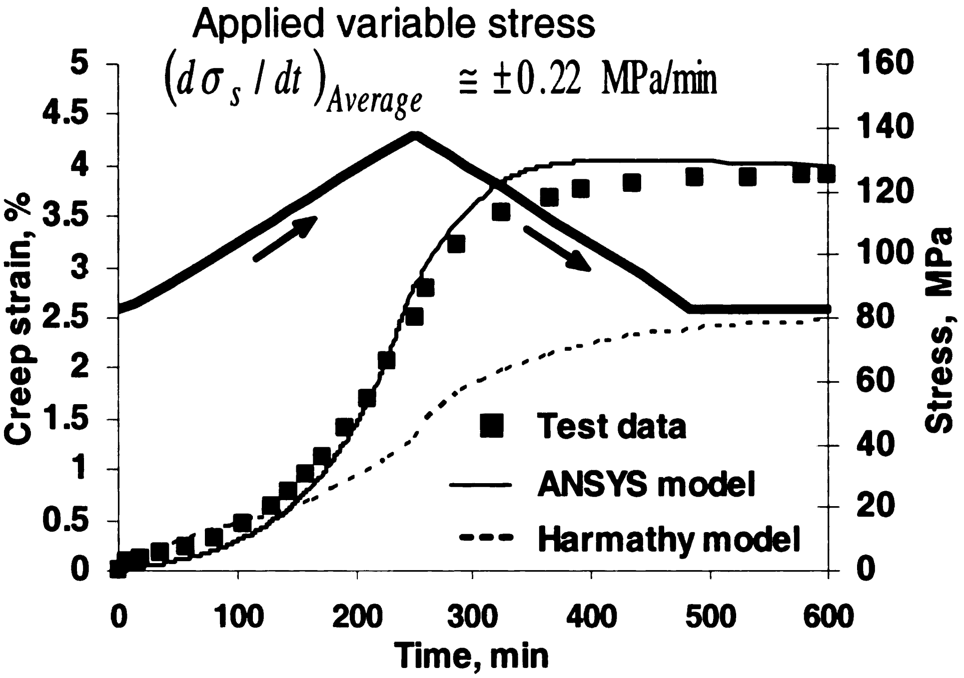

dσs/dt ≠ 0, Ts=550°C

Fig. 2.10: Comparison of measured and predicted (using ANSYS and Harmathy models) creep strains

CHAPTER THREE

FIRE RESISTANCE EXPERIMENTS

3.1 GENERAL

The state-of-the-art review indicates that there is a lack of fire tests on beam-columns subjected to realistic conditions, such as thermal gradients and design fire scenarios. There have been few fire tests conducted on restrained steel beams subjected to thermal gradients and realistic fires. However, almost all of the reported fire tests on steel columns were carried out under standard fire exposure and under uniform heating. Because of the lack of fire tests on steel columns subjected to thermal gradients, four steel columns subjected to thermal gradients were tested under realistic conditions. The main purpose of these tests is to investigate the effect of thermal gradient on the beam-column response of the restrained columns and to generate test data for validation of finite element models. Full details of the fire experiments, including specimens' instrumentation, fire tests procedure and measured parameters are presented in this chapter.

3.2 TEST APPARATUS

The fire resistance tests on steel columns were carried out using the structural fire testing furnace recently commissioned at MSU (Dwaikat et al. 2009). The test furnace, shown in Fig. 3.1, has been specially designed to produce conditions, such as temperature, loads and heat transfer, to which a structural member might be exposed during a fire. The furnace consists of a steel framework supported by four steel columns, with a fire chamber that is 2.44 m wide, 3.05 m long, and 1.78 m high. The maximum heat power the furnace can generate is 2.5 MW. Six natural gas burners located within the furnace provide thermal energy, while six thermocouples, distributed throughout the test chamber, monitor the furnace temperature during a fire test. Two small view ports on either side of the furnace wall are provided for visual monitoring of the fire-exposed specimens during a test. Vertical pressure actuators with individual capacities of 2400 kN were used to apply axial load to the top of each column. The furnace can accommodate two columns to be tested at a time, and different load levels can be applied for each column with the two separate vertical actuators.

3.3 TEST SPECIMENS

The experimental program consisted of fire resistance tests on four steel columns designated C1-S, C1-W, C2-S, and C2-W. All specimens used a W8x48 cross-section with A992 Grade 50 steel (*Fy* = 345 MPa) and were fabricated to a length of 3.3 m. The classification of each column was based on the direction of thermal gradient in the section. Columns C1-S and C2-S experienced a thermal gradient along the strong axis, while columns C1-W and C2-W experienced a thermal gradient along the weak axis. The C1 columns were tested simultaneously during the same fire test, and likewise for the C2 columns. Since the beam-columns are exposed to fire from the four sides, insulation was removed in certain location so as to generate thermal gradient in the required direction, as shown in Fig. 3.2.

The average measured dimensions of each specimen are shown with their corresponding insulation scheme in Fig. 3.2. Initially, each specimen was insulated with spray-on fire resistive material (SFRM) on all four sides along the majority of its length. As shown in Fig. 3.2(a), the top and bottom ends of each specimen, which were not to be exposed to fire, were left unprotected. The sections dimensions and average insulation thickness for each column is reported in Fig. 3.2(b). The insulation material that was used is CAFCO 300 with a specified thermal conductivity of 0.078 W/m-K and a density of 240 kg/m3 at room temperature (Isolatek International 2008).

The insulation was applied by a contractor so as to simulate the conditions actually found on a construction site. During the application of the insulation, special care was taken to measure the SFRM thickness at various locations on the specimens to ensure reasonable agreement with nominal specifications. The insulation was left for three weeks to allow the insulation to adequately dry prior to testing and develop thermal resistance properties realistic to actual building construction.

Since the columns were exposed to fire from four sides, the insulation was removed in specific locations, as shown in Fig. 3.2(b), to allow a thermal gradient in the desired direction. These insulation schemes simulated the thermal gradients that would realistically emerge in perimeter columns and floor beams due to three-sided heating.

3.4 INSTRUMENTATION

The test specimens were instrumented with thermocouples, strain gauges, and displacement transducers to monitor their thermal and mechanical response during the fire test. Steel temperatures were measured using Type-K Chromel-alumel thermocouples, 0.91 mm thick, installed at four cross sections along the length of each column, as shown in Fig. 3.3. The furnace temperature was monitored using six thermocouples distributed spatially inside the furnace. Five high-temperature strain gages were attached closer to the base of every column at section D-D to directly measure the total strains. Vertically and horizontally oriented linear variable displacement transducers (LVDT's) were attached at three distinct locations at the top of each member in order to calculate axial and lateral displacements and top-end rotations. The pressure in the vertical actuators was also recorded as a measure of applied axial load.

3.5 TEST CONDITIONS AND PROCEDURE

Two fire tests were performed, each with two steel columns placed vertically inside the furnace as shown in Fig. 3.1(b). A length of 1775-mm over the middle of the 3300-mm long column was directly exposed to fire. The columns were fixed to a very thick steel base plate at the bottom by the use of four 100x150x12.5-mm steel angles and 25.4-mm diameter high strength bolts (see Fig. 3.4(a)). Heavy steel plate (300x300x50 mm) was placed at the top of each column to ensure a uniform distribution of the applied axial load (see Fig. 3.4(b)). There was no bolted or welded connection between the heavy steel plate and the vertical actuator's loading piston (i.e. only bearing), and horizontal sway at the top end was not fully restrained. Restraint to axial elongation was provided by the loading frame. These boundary conditions simulated realistic restraint experienced by a fire-exposed perimeter column and allowed for the development of bending moments and increased axial load due to restraint of thermal effects.

The fire exposure and loading details for each of the four specimens are shown in Table 3.1. As mentioned previously, the columns were exposed to fire on four sides. Columns C1-S and C1-W were tested under ASTM E119 standard fire exposure (ASTM, 2008), while columns C2-S and C2-W were tested under a design fire scenario. The design fire included a growth phase simulating the ASTM E119 standard fire for about 90 minutes and then underwent a rapid cooling phase. The fire scenarios used in the two tests are shown in Fig. 3.5.

All columns were tested with axial loads applied at their top end by the vertical actuators. Columns C1-S and C1-W were subjected to an initial axial load of 650 kN, which is equal to 25% of the columns' yield capacity at room temperature. Columns C2-S and C2-W were subjected to an initial axial load of 1430 kN, 45% of the columns' yield capacity at room temperature. The load was applied in average increments of 200 kN for 10 minutes until full load was applied. The total applied load was maintained for approximately 30 minutes before the start of the fire test and was maintained until a condition was reached at which no further increase of the axial deformation of the columns could be measured. This was selected as the initial condition for measuring the axial deformation of the columns. During the test, the columns were exposed to heat controlled in such a way that the average temperature in the furnace followed, as closely as possible, the targeted time temperature curve. The load was kept constant throughout the test. The columns were considered to have failed and the tests were terminated when the columns suffered strength failure and could no longer carry the load.

3.6 EXPERIMENTAL RESULTS

Data generated from the fire tests were used to study the overall performance of steel beam-columns under fire induced thermal gradients. Thermal response, structural response, and failure patterns were compared to evaluate the effect of thermal gradient orientation, load level, and type of fire exposure.

3.6.1 Thermal Response

The temperatures recorded during the fire tests at location B-B in each column are shown in Fig. 3.5. Section B-B consistently recorded the highest temperatures because it had the most direct exposure to the burners due to its position (center of column) in the furnace (see Fig. 3.3). Thermocouples across the section at D-D recorded nearly uniform temperatures that did not exceed 100°C, and therefore temperature effects at this location were negligible.

Each plot in Fig. 3.5 shows a steel temperature plateau at about 100°C that can be primarily attributed to the evaporation of residual water in the insulation that remained following curing. This reaction consumed a significant amount of energy and initially slowed the transfer of heat from the hot gases through the insulation to the steel. Once the residual water was dispelled, steel temperature increased with fire exposure and a thermal gradient developed due to the strategic removal of the insulation. This effect is more pronounced for the C1 columns as shown in Figs. 3.5(a) and (b).

Columns C1-S and C1-W, exposed to ASTM E119 standard fire as shown in Figs. 3.5(a) and (b), experienced increasing temperature until the end of the test at t = 240 minutes. The average rate of temperature increase for these columns was approximately 3.5°C/min. Columns C2-S and C2-W, exposed to the design fire shown in Figs. 3.5(c) and (d), experienced increasing temperature until t = 90 minutes when a rapid decay phase was invoked. During the decay phase, the temperature in these columns decreased as heat was exchanged with the now cooler ambient environment. The average rate of steel temperature increase prior to the decay phase for these columns was approximately 7°C/min, and the average rate of temperature decrease during the decay phase was approximately 3°C/min. The difference in heating rate between the C1 and C2 specimens is primarily attributed to the difference in insulation thickness (44 mm for the C1 columns, and 38 mm for the C2 columns). In addition, the C2 columns had bare steel exposed to the fire at the locations of insulation removal shown in Fig. 3.2, as opposed to the C1 columns which had a trace (~2.5 mm) of remaining SFRM on its stripped areas. Column C2-S also had a wider insulation gap than C1-S, thus allowing more heat transfer directly to the steel. The plots in Fig. 3.5 show that each section experienced the largest temperature increase at the location nearest the gap in insulation with temperatures decreasing with distance from the gap.

Since the insulation was applied by a contractor, the SFRM thickness had variations that would be realistically seen on site, and these variations affected the thermal response. Pre-test measurements of insulation thickness taken at section B-B of column C1-W are shown in Fig. 3.6(a), and the location of WTC6 had 20% less insulation thickness than that of WTC5. Therefore, this location of WTC6 developed higher temperatures than that of WTC5 for column C1-W as shown in Fig. 3.5(b). Column C1-S experienced a similar effect, as seen in Fig. 3.5(a), and the temperature of its web and bottom flange are almost always equal. Fig. 3.6(b) shows that the insulation on this specimen's web was nearly 30% thicker than on the rest of the section (due to pooling when the insulation was spray-applied), causing a slower growth of web temperature relative to that of the flanges.

Fig. 3.5 shows the development of thermal gradients as represented by the difference in temperature at the various locations through the depth of the section. The magnitude of these gradients undergo a rapid initial increase followed by a slight and gradual decrease as the section begins to approach thermal equilibrium during the later stages of the fire growth. As shown in Figs. 3.5(a) and (c), the strong axis gradients are significant because heat transfer from the hotter flange (with the insulation gap) to the cooler flange is slowed due to their separation by the thin web plate. Columns C1-W and C2-W developed less severe thermal gradients about the weak axis (Figs. 3.5(b) and (d)) because the gradient now forms along the width of the flanges (which represent the majority of the sections' thermal mass) and heat can be transferred more readily across the thicker flange plate.

In the case of columns exposed to design fire, Figs. 3.5(c) and (d) show that the thermal gradients began to reverse direction once the decay phase initiated. During the decay phase of the fire, the portions of the section with less insulation (i.e. at the insulation gaps) cooled at a faster rate while fully insulated regions lost heat more slowly to the cooler ambient environment. The plots in Figs. 3.5(c) and (d) also reveal that during the decay phase, column C2-W experienced faster reversal in the direction of its thermal gradient as compared to that of C2-S. This phenomenon can be attributed to the fact that in the case of column C2-W, the uninsulated tip surfaces of the flanges have a higher emissivity factor when compared to the insulation gap on the flange of column C2-S. The adopted insulation schemes for C2-S with the insulation removed from the middle of the flange (as shown in Fig. 3.2) makes the exposed flange "less visible" to the surrounding thermal environment, and therefore it will have less heat loss compared to C2-W.

3.6.2 Structural Response

The structural performance of the column specimens was monitored using the deformations and strains recorded during the fire tests, and that data is reflected in Fig. 3.7. The axial displacement and top-end rotation curves shown in Figs. 3.7(a) and 3.7(b) were calculated using vertical displacement data recorded by the three vertical LVDT's attached to the top of each member. Axial displacement was calculated as an average of these three data points, and rotations were calculated by analyzing the orientation of the plane between the three LVDT displacements. The experimental axial loads shown in Fig. 3.7(c) were calculated by multiplying the recorded changes in loading pressure in the vertical actuator by the cross-sectional area of the actuator's piston.

Bending moments shown in Fig. 3.7(d) were calculated using strain data recorded using strain gauges at section D-D. Because the temperature at D-D did not exceed 50°C, the experimental moment can therefore be calculated by multiplying the strain gradient, Φ, through the depth of the section by the bending stiffness at room temperature ($M = EI\,\Phi$). Sign conventions for deflection and rotation are shown in Fig. 3.8. Positive axial force denotes compression, and positive bending moment corresponds to added compression on the hotter face of the column.

During the fire tests, each column experienced thermal expansion upward against the restraint of the loading frame due to increasing temperature, which in turn generated a corresponding increase in axial load. Figs. 3.7(a) and 3.7(c) show that reduction in strength and stiffness eventually lead to a rapid decrease in both axial displacement and axial load as the column approached failure. This decrease initiated once the average temperature in the column's hottest regions begin to exceed about 600-700°C, as shown in Fig. 3.5. The C1 columns take nearly three times longer to reach this point than the C2 columns because they have 25% more insulation thickness, less significant insulation gaps, and less than half the initially applied axial load.

As the column cross-sections heated unevenly and developed a thermal gradient, the columns initially developed a positive bending moment due to the rotational restraint of the end connections (i.e. the hotter face of the section became more compressed in response to the gradient). At the same time, the effective centroid (i.e. the center of stiffness) of each section began to migrate toward the cooler face of the section as the gradient generated non-uniform stiffness (i.e. a non-uniform distribution of E) through the section. Axial loads applied about the section's geometric centroid via the vertical actuator now generated a bending moment because the axial force resultant was eccentric to the center of stiffness. This moment is opposite in direction to that caused by restraint of thermal bowing even though the direction of the thermal gradient has not changed. Fig. 3.7(d) shows that the eccentric moments in each column eventually became larger than the thermal bowing moments, reversing the moment-time curve from positive to negative until the specimen reached its plastic capacity. The strong axis specimens experienced larger bending moments than the weak axis specimens due to their larger moment of inertia in the direction of bending (i.e. in the direction of the gradient). Fig. 3.7(b) shows that rotations of the top end of the beam-columns increased with the increase of fire exposure time, but then the rotations decrease at later stages of fire exposure. The initial increase of top-end rotations can be attributed to the development of thermal gradients, which produce thermal curvatures in the beam-columns. However, as the center of stiffness of the cross section is moving towards the cooler side, and with spread of plasticity in the hotter regions of the sections at later stages of fire exposure, the top end rotations start to reduce and switch direction, as shown in Fig. 3.7(b).

In the later stages of fire exposure, differences in behavior between C2 and C1 columns were caused by the presence of decay phase in the C2 fire test. The C2 columns continued to expand under exposure to the growth phase of the design fire, and then the columns yielded through their full depth a few minutes before entering decay phase of the design fire. At this point, the loaded columns underwent severe deformation similar to that of the C1 columns until the decay phase initiated. During the decay phase, steel temperature in the C2 columns started to decrease, allowing the steel to regain some of its strength and stiffness and therefore reducing their rate of deformation as seen in Fig. 3.7(a).

3.6.3 Failure Pattern and Fire Resistance

The failure times for the four tested columns are shown in Table 3.1. Failure is defined as the time when the columns cannot maintain the applied load (i.e. when the sudden decrease in axial load and moment shown in Figs. 3.7(c) and 3.7(d) initiates). There were no incidents of sudden global or local instability observed during the fire test. Validation studies using computer models show that failure is reached via full section yielding as discussed in Chapter 4. Fig. 3.9 shows the failed shape of each column, with the location of plastic hinge marked as a distance from the bottom of the member. The time to reach failure from the start of fire exposure is defined as fire resistance. This definition of failure contrasts with the traditional prescriptive-based approach in which failure is often assumed to occur when steel attains its critical temperature regardless of loading level or thermal gradients.

The beam-columns failed by developing full plastic response. It can be seen from Fig. 3.9 that the location of the plastic failure for every specimen is nearly in the hottest region (at the center) of the beam-columns far from the base. This failure trend can be explained by referring to the distorted P-M diagrams of the beam-columns. This failure pattern will be explained with full details in Chapter 6.

3.7 SUMMARY

Fire tests were conducted to study the behavior of axially loaded steel columns that develop thermal gradients through their depth. Thermal gradients were created by removing part of insulation on one side of the specimen thus simulating the thermal response of a three-sided heating scenario such as a column on the perimeter of a building frame. The column specimens developed significant bending moments in response to these gradients and therefore they behaved as beam-columns. Thermal gradients also produced a change in plastic capacity to combinations of axial load (P) and moment (M). All four specimens failed by plastic yielding under the effect of combined axial force and bending moment.

The location at which failure occurred was where the temperature was the largest and the moment was the smallest (the latter due to the effects of the thermal gradients on the combined P and M demand and capacity). Results of the tests showed that load level, fire scenario, and the magnitude and the direction of the thermal gradient (i.e. along the strong or weak axis) had a significant influence on the fire response of these beam columns.

Table 3.1: Matrix of fire test parameters.

Specimen	Fire Exposure	Axis Orientation	Insulation Thickness (mm)	Initial $\frac{P}{P_y}$	Recorded time of failure (min.)
C1-S	ASTM E119	strong	44	0.25	220
C1-W	ASTM E119	weak	44	0.25	215
C2-S	design fire	strong	38	0.45	90
C2-W	design fire	weak	38	0.45	93

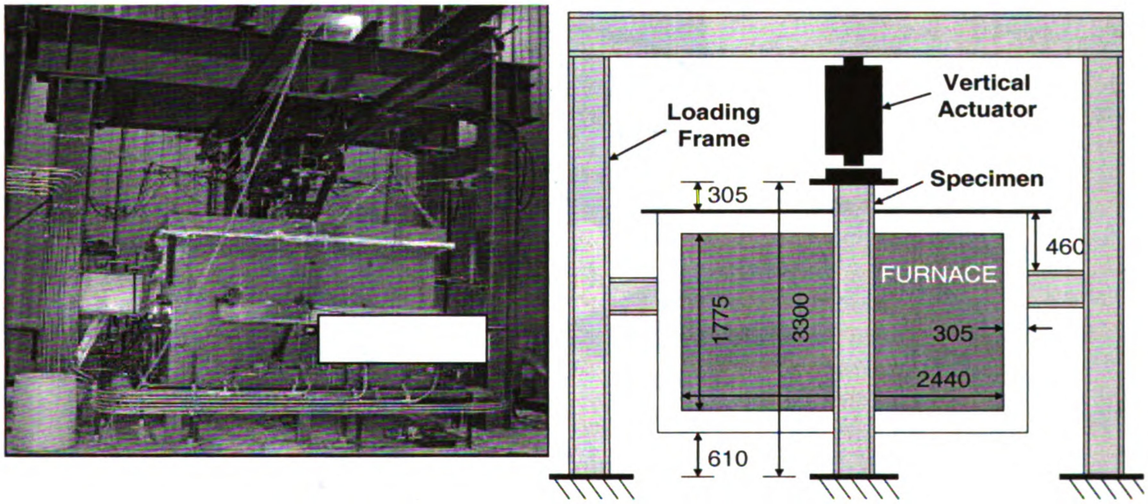

(a) Furnace and loading frame

(b) Schematic for furnace front view

Fig. 3.1: Structural-fire test furnace at MSU's Civil and Infrastructure Laboratory (dimensions shown in mm)

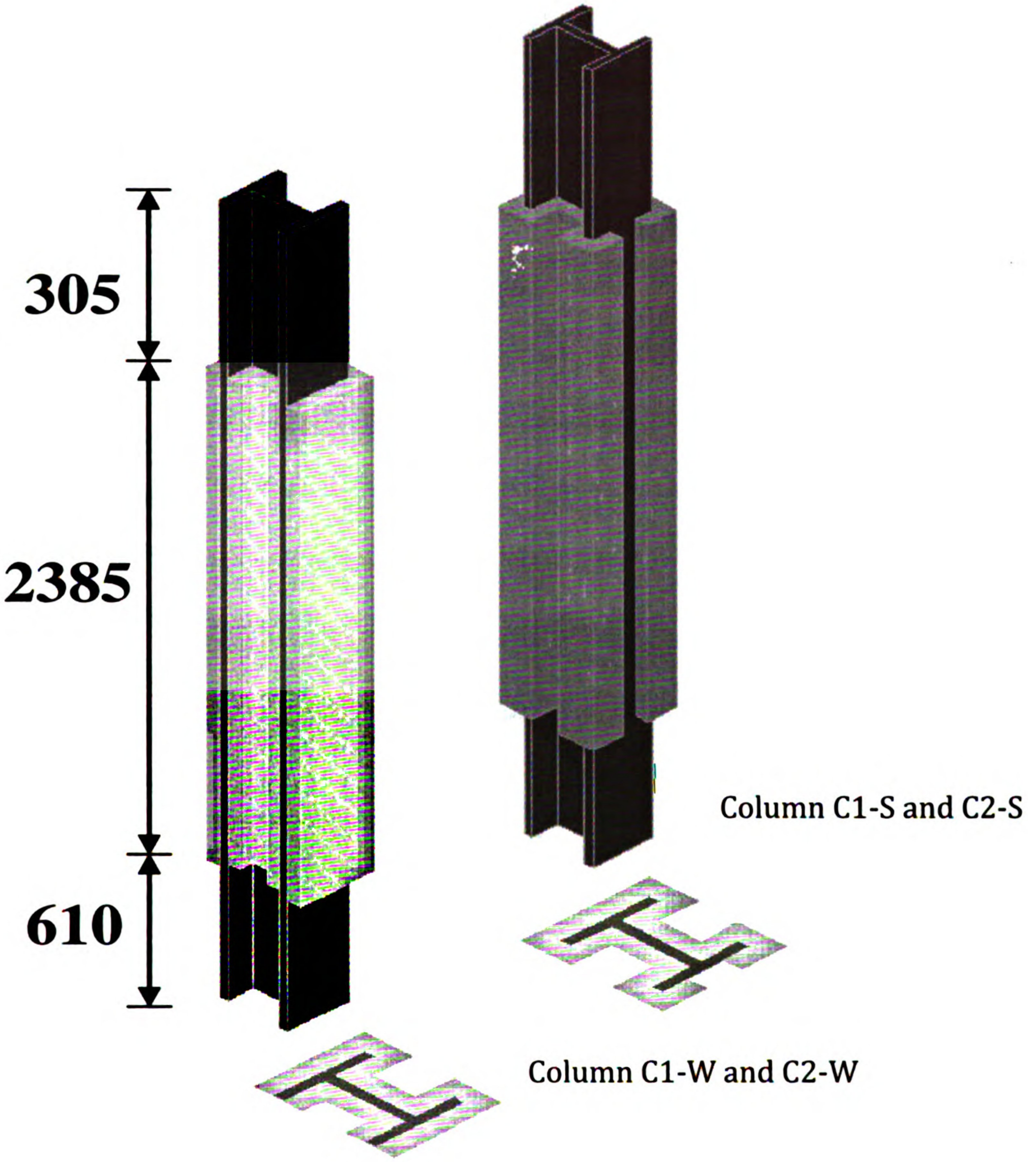

Column C1-S and C2-S

Column C1-W and C2-W

Fig. 3.2: Insulation schemes for the beam-column specimens

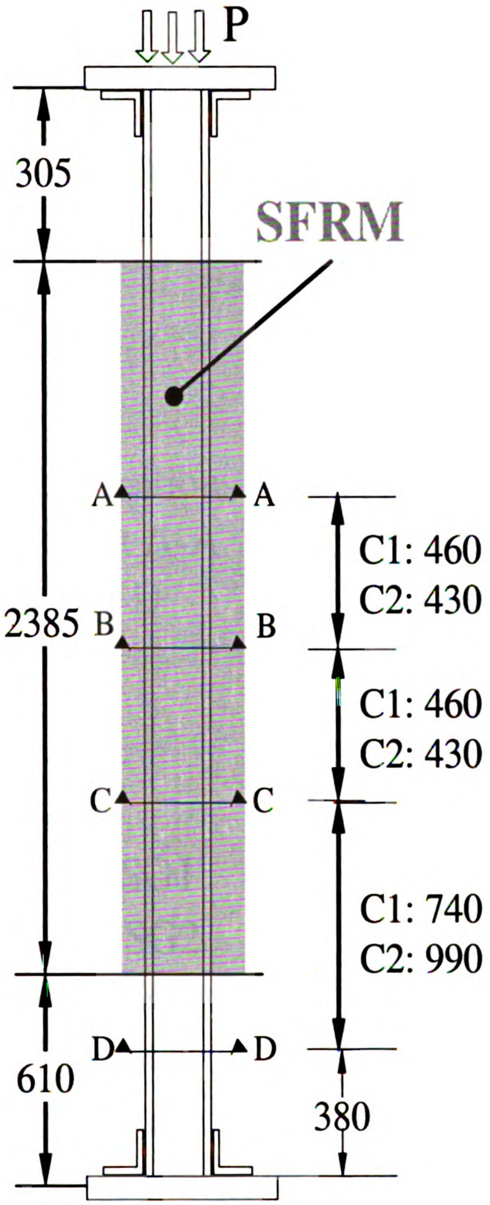

Fig. 3.3: Instrumentation mapping for the tested specimens (dimensions shown in mm)

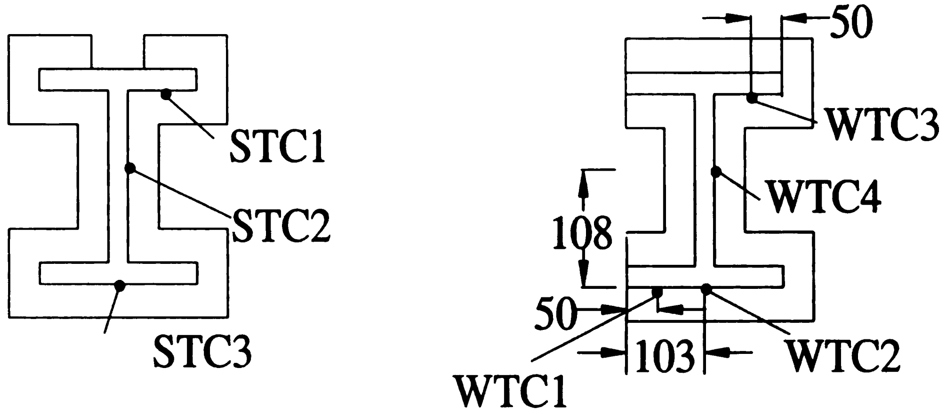

(a) Thermocouple locations for C1-S and C2-S at A-A, B-B, C-C and D-D

(b) Thermocouple locations for C1-W and C2-W at A-A, B-B, C-C and D-D

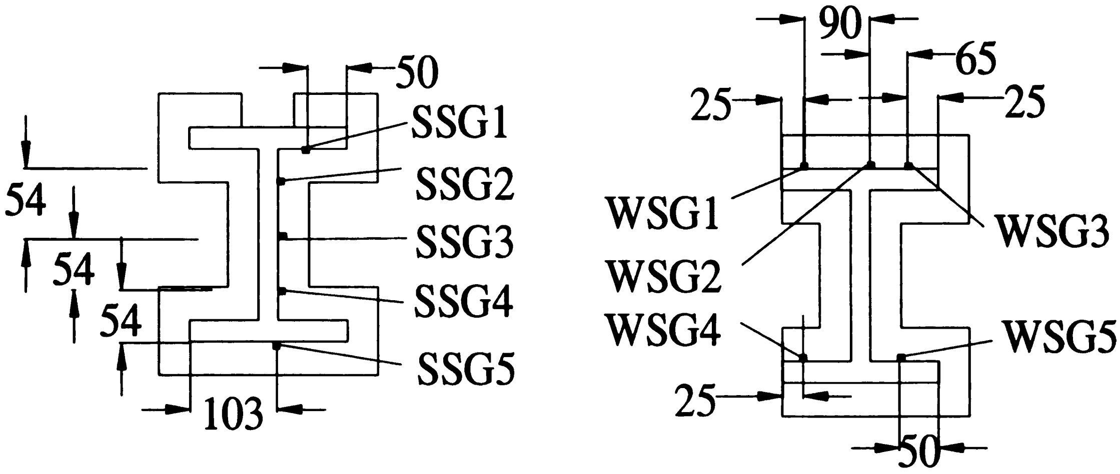

(c) Strain gauges at D-D for C1-S and C2-S

(d) Strain gauges at D-D for C1-W and C2-W

Fig. 3.4: Instrumentation mapping for the tested specimens (dimensions shown in mm)

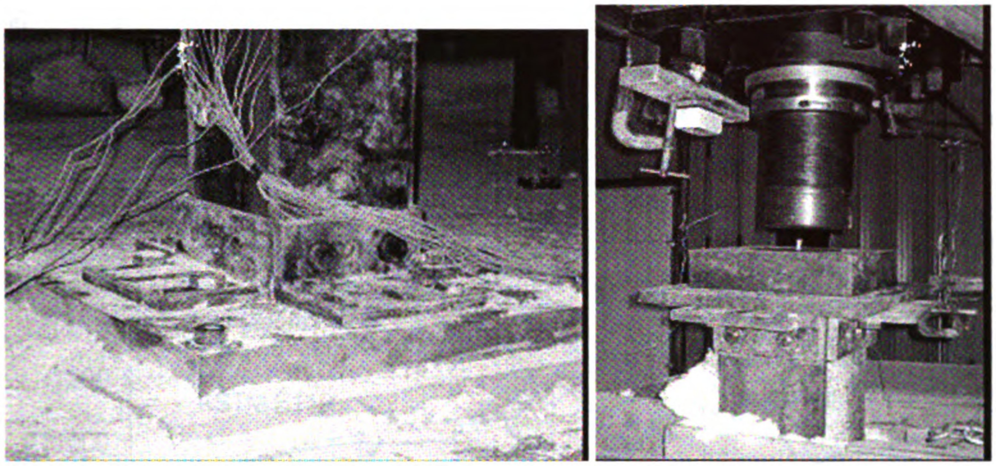

a) Base fixation *b) Top end*

Fig. 3.5: Photos of the boundary conditions for the tested beam-columns

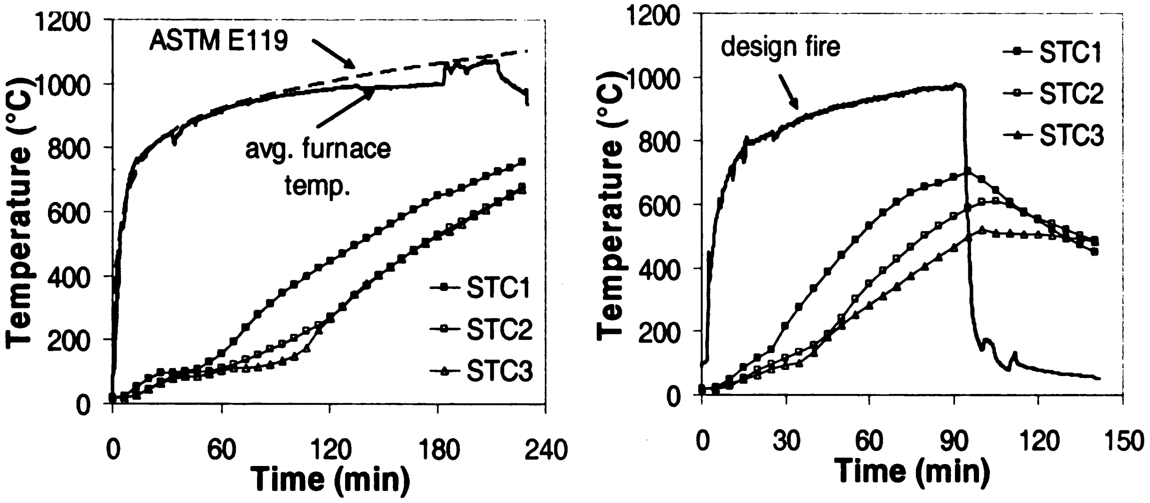

(a) Column C1-S

(b) Column C2-S

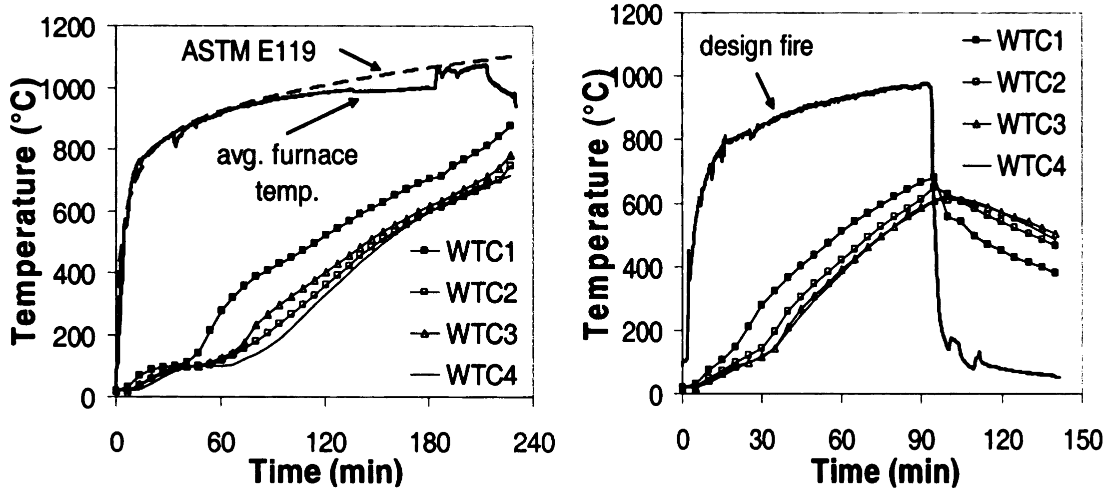

(c) Column C1-W

(d) Column C2-W

Fig. 3.6: Temperatures recorded at section B-B for beam-columns

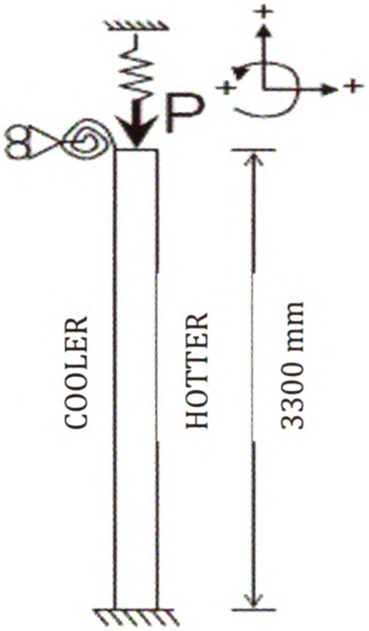

Fig. 3.7: Sign convention adopted for the fire induced restraint forces in beam-columns

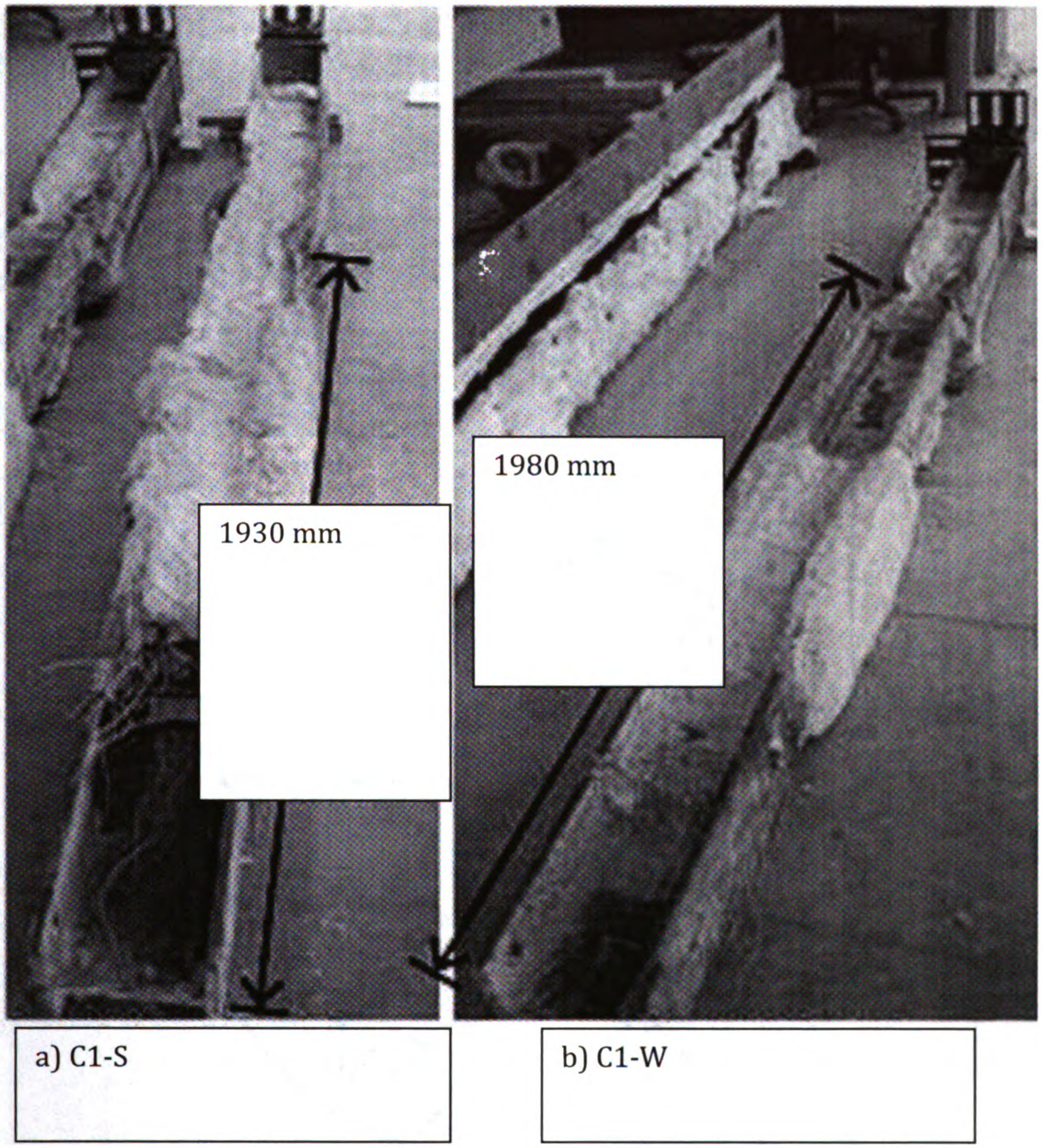

a) C1-S

b) C1-W

Fig. 3.8: Failed shape of each beam-column, shown with failure locations

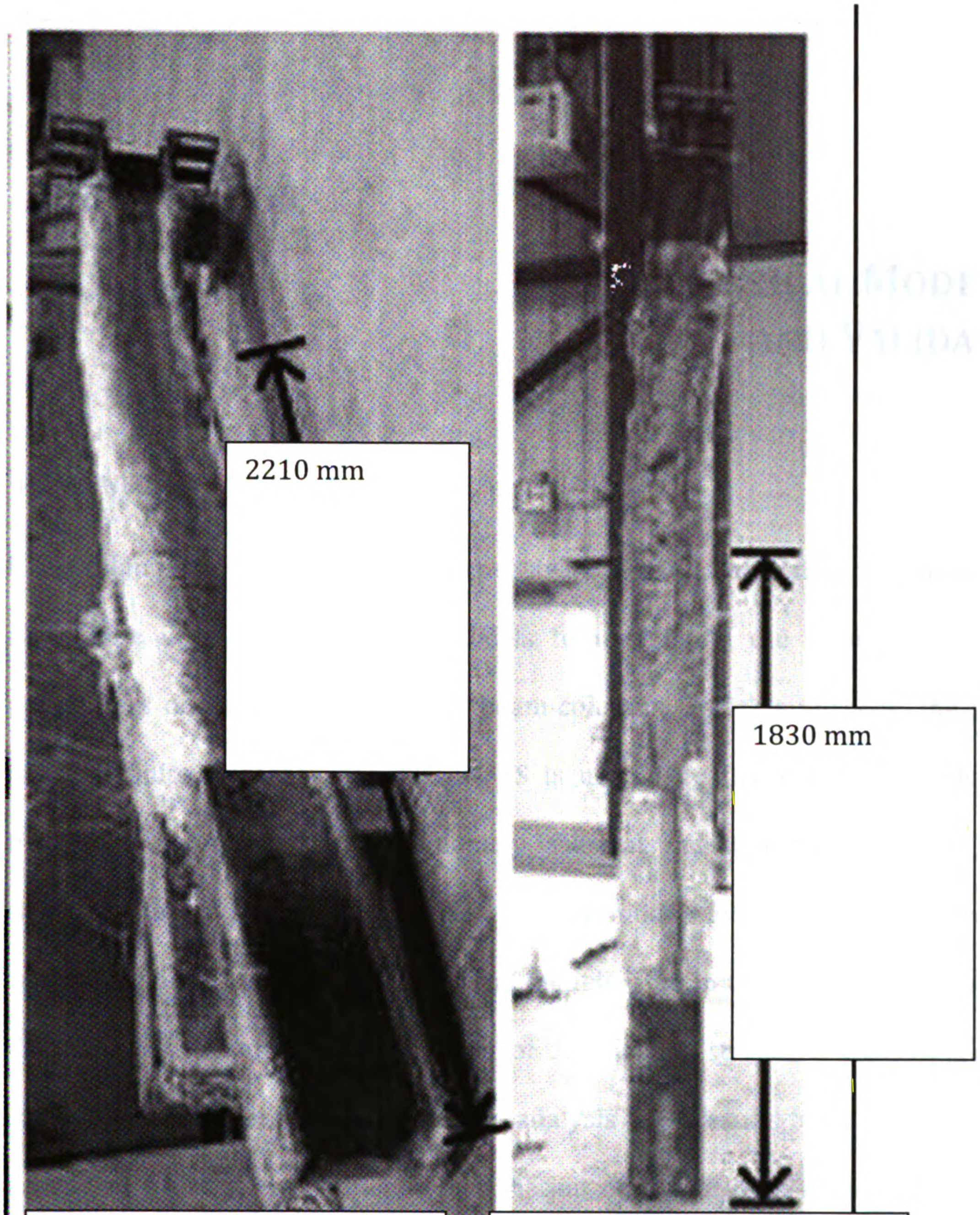

c) C2-S

d) C2-W

Fig. 3.8: Continued

CHAPTER FOUR

NUMERICAL MODELING AND VALIDATION

4.1 GENERAL

Undertaking fire tests is quite expensive, complex, and time consuming. An alternative is to use numerical models to investigate the influence of critical parameters on the fire response of beam-columns. For this purpose, the general purpose finite element program ANSYS is used. The fire response is evaluated through two stages of analysis, namely, thermal and structural analysis. In this chapter, the development of finite element model for thermal and structural analyses is presented. Also, the material models used in the analysis are described. Validation of the finite element models for thermal and structural analysis is carried out by comparing predictions from the analysis with results from fire tests. In the validation process, the influence of variation of constitutive models of structural steel on the predictions of fire response is carefully examined.

4.2 SELECTION OF FINITE ELEMENT PROGRAM

Undertaking detailed parametric studies requires the use of a numerical model. The general-purpose finite element program ANSYS (ANSYS 2007) was chosen to carry out the numerical studies because of its diverse capabilities. ANSYS has the ability to efficiently model highly sophisticated material and geometrical nonlinearities, and allows the user to specify temperature-dependent thermal and mechanical properties of almost any material. Also, ANSYS provides a wide range of high temperature creep models in addition to any user-specified high temperature creep model. ANSYS contains an optimization tool that can be used effectively for automating parametric studies. Further, ANSYS contains a rich library of diverse categories of elements that are well suited for simulating various structural systems. ANSYS has been used by various researchers for undertaking fire resistance analysis of steel structures (NIST 2005).

The analysis was carried out by incorporating all significant parameters, such as material and geometrical nonlinearities, end restraints, fire scenarios, and thermal gradients. Details on the finite element analysis are provided in the following sections.

4.3 FINITE ELEMENT MODELING

4.3.1 General Approach

The fire resistance analysis is generally carried out through two stages, namely; thermal and structural analyses. The purpose of the thermal analysis is to obtain the evolution of temperature in a structural member as a function of fire exposure time. The purpose of the structural analysis is to obtain the deformations and stresses resulting due to fire exposure. For practical cases of analysis, the following assumptions are adopted while carrying out structural fire analysis:

- Fire characteristics are independent of both thermal and structural analysis results.
- Thermal analysis is independent of the structural analysis.
- Temperature distribution is uniform along the beam span length.

The fire scenarios that are typically used in structural fire engineering can be grouped under two categories. Standard fire scenarios; where fire continues to increase indefinitely, and realistic, natural, or design fire scenarios where fire temperature undergoes a decay phase. Examples of standard fire scenarios are ASTM E119 and ISO 834 standard fire exposures. The fire temperature (Tf in °C) as a function of time (t in minutes) for the standard fire curves are expressed as:

ASTM E119: $$T_f = 20 + 750\left(1 - \exp\left(-3.79553\sqrt{t/60}\right)\right) + 170.41\sqrt{t/60} \quad [4.1]$$

ISO 834: $$T_f = 20 + 345\log(8t + 1) \quad [4.2]$$

In case of a design or "realistic" fire, a decay phase follows after reaching a maximum fire temperature. Unlike standard fire curves that are function of time only, the growth and decay phases of design fires are dependent on the compartment geometry and fuel and ventilation characteristics. Examples of design fires are the Swedish fire curves and the parametric fire curves specified in the Eurocode (EC1 2002).

Generally, the rise of fire temperature is dependent on geometric, fuel and ventilation characteristics of the compartment. Computational fluid dynamics (CFD) models are required to compute the evolution of fire in a certain enclosure. Since this kind of analysis is beyond the scope of this study, fire characteristics are reduced to time-temperature relationships and are taken from the specified design fire curves in codes.

The fire resistance analysis, with its thermal and structural phases, is carried out via ANSYS finite element program using the following general procedure:

- Thermal analysis: Fire exposure time is incremented and temperature distribution in the beam cross section is obtained at every time step and for the entire fire exposure history.
- Room-temperature structural response: Static structural analysis is performed on the entire structural model of the beam to obtain the room-temperature structural response (deformations and stresses).
- Structural fire analysis: Fire exposure time is incremented and the temperature distribution obtained from the thermal analysis is applied, at each time step, on the room-temperature deformed model of the beam.

In the following sections, more details are given about the thermal and structural analyses.

4.3.1 Thermal Analysis

Since the temperature along the beam span length is assumed to be uniform, heat transfer in the beam is reduced to a two-dimensional problem. Thus, the governing partial differential heat transfer equation within the beam cross section can be written as (Purkiss 2007):

$$\rho c \frac{dT}{dt} = \nabla \cdot (k \nabla T) \qquad [4.3]$$

where k = conductivity matrix, ρc = heat capacity, T = temperature, t = time, and ∇ = is the spatial gradient operator.

At the fire-beam interface, heat is transferred through radiation and convection. The heat flux on the boundary due to convection and radiation can be given by the following equation:

$$q_b = (h_{con} + h_{rad})(T - T_f) \qquad [4.4]$$

where *hrad* and *hcon* are the radiative and convective heat transfer coefficients, and are defined as:

$$h_{rad} = 4\sigma\varepsilon(T^2 + T_f^2)(T + T_f) \qquad [4.5]$$

Tf = temperature of the atmosphere surrounding the boundary (in this case it is the fire temperature),

σ = Stefan-Boltzman constant = 5.67×10-8 (W/m2.°K4), and

ε = emissivity factor and it is related to the "visibility" of the surface to the fire.

The heat flux and temperature gradient are related through Fourier's Law of conduction:

$$q = -k\nabla T \qquad [4.6]$$

Using Fourier's Law, the governing heat transfer equation on the boundary of the beam can be expressed as:

$$k\left(\frac{\partial T}{\partial y}n_y + \frac{\partial T}{\partial z}n_z\right) = -q_b \qquad [4.7]$$

where

ny and *nz* = components of the vector normal tc the boundary in the plane of the cross-section. The right hand side of Eq. [4.7] is dependent on the type of boundary condition. Since the beam is exposed to fire from three sides, there are two types of boundaries:

- Fire exposed boundaries where the heat flux is governed by:

$$q_b = -h_f\left(T - T_f\right) \qquad [4.8]$$

- Unexposed boundary where the heat flux equation is given by:

$$q_b = -h_0\left(T - T_0\right) \qquad [4.9]$$

where *hf* and *h0* are heat transfer coefficient of the fire side and the cold side, respectively. *Tf* and *T0* = fire and cold side temperatures, respectively.

By relating nodal temperatures through proper shape functions matrix {N} such that:

$$T = \{N\}^T \cdot T_e \qquad [4.10]$$

the heat transfer equation (Eq.[4.3]) subjected to the boundary conditions (Eq. [4.7]) can be discretized as (ANSYS 2007):

$$C_e^t \dot{T}_e + K_e^t T_e = Q_e \qquad [4.11]$$

C_e^t is the specific heat matrix. K_e^t is the thermal "stiffness" matrix and is the sum of conductivity and convection matrices. *Qe* is the applied nodal thermal load and is composed of the convective and radiative heat fluxes. **Te** is the nodal temperatures.

The cross section of the beam is meshed using two types of elements, namely PLANE55 and SURF151. Figure 4.2 shows the two elements and the typical discretization of steel cross section for thermal analysis for different cases of exposures.

PLANE55 is used as a solid plane element with two-dimensional thermal conduction capability. The element has four nodes with a single degree of freedom, temperature, at each node. This element is applicable to a two-dimensional, steady-state or transient thermal analysis. The temperature within PLANE55 element is interpolated from the degrees of freedom (*Te* = *Ti,j,k,l*) using the following isoparametric function (ANSYS 2007):

$$T = \frac{1}{4}\begin{bmatrix} T_i & T_j & T_k & T_l \end{bmatrix} \cdot \begin{bmatrix} (1-s)(1-t) \\ (1+s)(1-t) \\ (1+s)(1+t) \\ (1-s)(1+t) \end{bmatrix} \qquad [4.12]$$

where *s* and *t* are the isoparametric locus of a point in the element domain. To carry out the numerical integrations, 2x2 integration points are used in PLANE55.

The SURF151 element is generally used for various load and surface effect applications. The one-dimensional SURF151 is overlaid onto the face of PLANE55 2D thermal solid element to simulate the effect of both thermal radiation and heat convection from the surrounding environment to the boundaries of the steel section (see Eq. [4.4]).

Heat convection load was applied around the section, and a convection coefficient of *hcon* = 25 W/(m2 .°C) was assumed in the analysis. The ambient (bulk) temperature on the node K of SUR151 element was assumed to be equal to either the fire temperature (*Tf*) in case the boundary is exposed to fire, or to room-temperature, in case the boundary is not exposed to fire. SURF151 uses linear interpolation function and two integration points for numerical integration.

4.3.2 Structural Analysis

According to the principle of virtual work, any virtual change of the internal strain energy must be balanced by a change in the external work due to the applied loads.

$$\delta U = \delta V \tag{4.13}$$

where *U* is the strain energy and *V* is the external work. Variation of strain energy (δU) can be expressed as:

$$\delta U = \int_{vol} \{\delta \varepsilon\} \sigma dvol \tag{4.14}$$

Under fire conditions, the strain vector (ε) is the sum of mechanical (εm), thermal (εth), and creep (εcr) strains in steel, i.e.:

$$\varepsilon = \varepsilon_m + \varepsilon_{th} + \varepsilon_{cr} \qquad [4.15]$$

Variation of the external work (δV) due to the applied nodal forces (F_e^n) can be computed by assuming a variation of nodal displacement $\{\delta u\}$ as:

$$\delta V = \{\delta u\}^{\mathrm{T}} \{F_e^n\} \qquad [4.16]$$

By relating nodal displacements (ue) of the finite elements to the displacement field (u) through shape functions matrix $\{N\}$ as follows:

$$u_e = \{N\}^T \cdot u \qquad [4.17]$$

the virtual work equation (Eq. [4.13]) can be rewritten in matrix form as (ANSYS 2007):

$$K_e u_e - F_e^{th} = F_e^n \qquad [4.18]$$

where Ke is the element stiffness matrix, and F_e^{th} is the element thermal load vector

The finite element analysis is carried out using 8-noded SHELL93 element in ANSYS. Figure 4.3(a) shows the main features of the SHELL93 element while Fig. 4.3(b) shows the discretization of a beam-column for structural analysis. SHELL93 element is suitable for analyzing slender to moderately thick beam-column members, and it accounts for material and geometric nonlinearities, non-uniform temperature distribution over either the length of the element and/or the cross-section of the element. Material nonlinearities include nonlinear temperature-stress-strain curves, high temperature creep, and temperature-dependent thermal strain. Geometric nonlinearities include large deformations and large rotations with bending capabilities in and out of the plane of the element.

4.3.3 Modeling End Restraints

Restraint conditions on the boundary of the steel beams arise due to adjacent structural members. Rotational restraint (generally in the plane of bending) is a function of many factors including the continuity of the beam (to adjacent spans), rotational stiffness offered by the supporting columns, rotational stiffness of the beam-to-column connection, and the extent of composite action that develops between concrete slab and steel beam. The axial restraint is also a function of a number of factors including the continuity of the beam, lateral stiffness of the supporting columns, and the composite interaction between concrete slab and steel beam. The computation of these restraint stiffnesses (axial and rotational) at room temperature can be carried out using conventional methods of analysis for indeterminate structures that can be found in structural analysis textbooks (Ghali et al. 2003). In this study, we assume that the axial and rotational restraints on the ends of the beam are elastic, constant, and symmetric as shown in the illustration in Fig. 4.4.

Further, the location of the axial restraint force can vary depending on the type and configuration of the connection between the beam and the column as shown in Fig. 4.5(b). The axial restraint stiffness may not pass through the centroidal axis of the cross section, but may be eccentric by a distance y from the center of geometry of the section. In almost all previous studies, the location of axial restraint stiffness was always assumed to be in the centroid of the section.

In order to account for the above factors, axial and rotational restraints are modeled using a set of three axial springs on each end of the beam. The three springs are arranged such that both axial and rotational restraint can be imposed on the beam as shown in Fig. 4.6. The top and bottom springs have an axial stiffness of *ks,1* while the middle spring has an axial stiffness of *ks,2*.The linear springs were modeled using COMBIN39 spring element available in ANSYS. It is assumed that these three springs has constant elastic stiffness properties

Using the configuration shown in Fig. 4.6, the axial restraint stiffness (*Ka*) and rotational restraint stiffness (*Kr*) are obtained as (Dwaikat and Kodur 2010):

$$K_a = k_{s,1} + 2 \times k_{s,2} \qquad [4.19]$$

$$\begin{aligned} K_r &= \frac{M}{\theta} = \frac{F_T \times (d/2 + y) + F_B \times (d/2 - y)}{1^{Rad}} \\ &= 2k_{s,1} \tan(1^{Rad}) \left[(d/2)^2 + y^2 \right] \end{aligned} \qquad [4.20]$$

where *ks,1* and *ks,2* are the stiffnesses of the spring elements, *y* is the eccentricity of the axial restraint stiffness from the geometric centroid of the section. *FT* and *FB* are the forces in the top and bottom axial springs as illustrated in Fig. 4.6. By changing the values of *ks,1* and *ks,2*, different values of axial and rotational restraint can be imposed on the beam.

In order to use the 3-axial spring approach for modeling rotational and axial restraints, the three spring elements must act on a rigid diaphragm. Therefore, to simulate this effect, the following kinematic constraints equations are imposed on the restrained ends of the beam (Dwaikat and Kodur 2010):

$$(u_x)_n = (u_x)_m + (z_n - z_m)(\theta_y)_m \quad [4.21]$$

$$(\theta_y)_n = (\theta_y)_m \quad [4.22]$$

where *ux* represents the translational degree of freedom in the X axis, and θ_y is the rotational degree of freedom about the Y axis. Z is the coordinate of the node. Figure 4.7 shows a schematic of this kinematic constraint condition where the subscript *n* refers to the nodes that are located on the end of the beam, and the subscript *m* refers to the master node. These constraint equations (Eq. [4.21] and [4.22]) force all the nodes on the restrained edge of the beam to follow the master node that is represented by the roller in Fig. 4.7, and hence results in a rigid diaphragm condition on that end.

4.4 SELECTION OF MATERIAL MODELS

It was shown in Chapter 2 that significant variations exist among different constitutive models for high temperature properties of structural steel. These variations can lead to differences in predicted response of the restrained beams. Therefore, it is important to decide on the material models for use in finite element models.

In the following sections, the selected constitutive models, for thermal and structural analyses, will be presented. The selection of the constitutive models that will be used in the analysis is based on comparing the experimental results to numerical results obtained from using different constitutive models for thermal and structural analysis. The results of the comparison are presented in the validation section (Section 4.5).

4.4.1 Thermal Properties

The main thermal properties that influence the temperature rise in steel are thermal conductivity and specific heat. As previously illustrated in the literature review on high temperature material properties, there is not significant variation in the thermal properties as specified in different codes and standards. Therefore, high-temperature thermal properties and thermal expansion of steel specified in the Eurocode (EC3 2005) are used as input parameters to both thermal and structural analysis in ANSYS.

4.4.2 Mechanical Properties

The literature review (Chapter 2) showed that there is a high variation in the high temperature mechanical properties of structural steel as specified in different codes and standards. Also, the mechanical properties specified in codes and standards are mainly derived from "old" test data and there is lack of information on the methodologies through which these tests were conducted. For example, transient effect of high temperature creep is not treated properly in most design codes and standards, despite the fact that it influences the response of steel members under elevated stresses and temperatures (Kodur and Dwaikat 2009, Kodur et al. 2009). It is not clear how and to what extent high temperature creep is included in the temperature-stress-strain relations for structural steel as specified in codes and star

reco

ana

give

to i

ste

use

Fig

ter

cur

sta

col

to

cle

20

Ba

ch

exp

tra

fre

hea

stre

standards (e.g. ASCE 1992, AISC 2005, EC3 2005). For example, while ASCE manual recommends explicit consideration of high temperature creep in the structural analysis, the Eurocode states that "*the effects of transient thermal creep need not be given explicit consideration*" (Clause 4.3.3(4) of EC3 2005). Therefore, in an attempt to isolate the contribution of high-temperature creep to the response of restrained steel beams, temperature-stress-strain relations recommended by Poh (2001) were used in the analysis.

Figure 4.8 shows the stress-strain model of the structural steel at elevated temperatures as proposed by Poh. The generalized temperature-stress-strain curves developed by Poh were based on an intensive experimental program and on statistical studies. These curves were used to predict fire response of tested steel columns and found to be sufficiently accurate (Poh 1995 and 2001). Also, contrary to the confusion regarding the treatment of creep in codes and standards, Poh clearly states that his stress-strain curves do not include the effect of creep (Poh 2001).

Based on a comparison between the constitutive models that will ensue in this chapter, temperature-stress-strain curves of Poh are used (in conjunction with an explicit high temperature creep model) in the structural analysis in case of a transient structural analysis is carried out, such as exposure to a design or standard fire time-temperature curve. However, when the analysis is not concerned with heating rate (i.e. when temperature is applied monotonically), the temperature-stress-strain curves of Eurocode 3 (EC3 2005) will be used in the analysis. This is because Eurocode curves partially account for the transient effect of creep as will be demonstrated later in this chapter.

4.4.3 High Temperature Creep

At present, most fire resistance analyses are carried out using Harmathy's high temperature creep model that is mainly based on Dorn's theory (Dorn 1954; Harmathy 1967). Dorn's creep theory assumes constant stress ($d\sigma_s / dt = 0$). However, in the case of restrained beams exposed to fire, the fire induced stresses vary considerably and rapidly with time and temperature, and these conditions are not captured by Dorn's theory. Therefore, an alternate high temperature creep model that can capture variable stress scenarios is required to account for these extreme conditions.

4.4.3.1 ANSYS Creep Model

ANSYS provides 13 creep models that can be fitted empirically. Also, ANSYS provides nonlinear regression tools for fitting creep models to experimental creep test data. Implicit creep model number 11 is selected because it can model both the primary and secondary creep, and is capable of predicting creep strain regardless of any coupling between time and either stress or temperature of steel. The fundamental theory for this creep model is based on the work of Zienkiewicz and Cormeau (1974) on unified theory on plasticity and creep strains. The model is presented in simplified format in ANSYS theoretical manual.

The selected ANSYS high-temperature creep model is given in a simplified format, as (ANSYS 2007, Kodur and Dwaikat 2009*b*):

$$\Delta\varepsilon_{eq}^{creep} = \varepsilon_{\text{primary}} + \varepsilon_{\text{secondary}} = \frac{\left(c_1\sigma_s^{c_2} t^{c_3+1}\right) e^{-c_4/T_s}}{c_3+1} + \left(c_5 t \sigma_s^{c_6}\right) e^{-c_7/T_s} \qquad [4.23]$$

where *c1* through *c7* are coefficients that are dependent on type of steel and are obtained through nonlinear regression analysis to high temperature creep test data; with c1 = 6x10-6 per minute, c2 = 6.95, c3 = - 0.4, c4 =16500°C, c5 = 6.0x10-6 per minute, c6 = 6x10-5, c7 = 5x10-3°C, t = time at end of sub step (min), *σs* = steel stress (MPa), *Ts* = steel temperature (°C), and $\Delta\varepsilon_{eq}^{creep}$ = modified creep strain increment.

ANSYS calculates creep strain in incremental form in which creep strain increment is dependent on the creep strain at a given time step (*t*). First, the modified total strain vector at time step (*t*) is computed using the creep strain vector of the previous time step (*t* - 1) as:

$$\boldsymbol{\varepsilon}_t^{\text{mod}} = \boldsymbol{\varepsilon}_t^{total} - \boldsymbol{\varepsilon}_t^{plastic} - \boldsymbol{\varepsilon}_t^{thermal} - \boldsymbol{\varepsilon}_{t-1}^{creep} \qquad [4.24]$$

The modified total strain ($\boldsymbol{\varepsilon}_t^{\text{mod}}$) is then used to compute the equivalent modified total strain as:

$$\varepsilon_{eq}^{\text{mod},total} = \frac{1}{\sqrt{2}(1+\nu)}\left[\begin{array}{l}\left(\varepsilon_{t,x}^{\text{mod}} - \varepsilon_{t,y}^{\text{mod}}\right)^2 + \left(\varepsilon_{t,y}^{\text{mod}} - \varepsilon_{t,z}^{\text{mod}}\right)^2 + \left(\varepsilon_{t,z}^{\text{mod}} - \varepsilon_{t,x}^{\text{mod}}\right)^2 + \\ + \frac{3}{2}(\gamma_{t,xy}^{\text{mod}})^2 + \frac{3}{2}(\gamma_{t,yz}^{\text{mod}})^2 + \frac{3}{2}(\gamma_{t,zx}^{\text{mod}})^2\end{array}\right]^{\frac{1}{2}} \qquad [4.25]$$

The equivalent modified total strain ($\varepsilon_{eq}^{\mathrm{mod},total}$) is used to compute the equivalent stress (σ_{eq}) as

$$\sigma_{eq} = \mathbf{E}\varepsilon_{eq}^{\mathrm{mod},total} \tag{4.26}$$

where **E** is the temperature-dependent young modulus of steel, and ν is Poisson's ratio.

This equivalent stress is used to compute the equivalent creep strain increment ($\Delta\varepsilon_{eq}^{creep}$) as a scalar quantity using ANSYS model for creep (Eq. [4.23]) and employing temperature at current time step (*t*). The scalar equivalent creep strain increment ($\Delta\varepsilon_{eq}^{creep}$) is then converted to a full creep strain tensor as follows:

$$\begin{bmatrix} \Delta\varepsilon_{x}^{creep} \\ \Delta\varepsilon_{y}^{creep} \\ \Delta\varepsilon_{z}^{creep} \\ \Delta\varepsilon_{xy}^{creep} \\ \Delta\varepsilon_{xz}^{creep} \\ \Delta\varepsilon_{yz}^{creep} \end{bmatrix} = \left(\frac{\Delta\varepsilon_{eq}^{creep}}{2(1+\nu)\varepsilon_{eq}^{\mathrm{mod},total}} \right) \cdot \begin{bmatrix} 2 & -1 & -1 & 0 & 0 & 0 \\ -1 & 2 & -1 & 0 & 0 & 0 \\ -1 & -1 & 2 & 0 & 0 & 0 \\ 0 & 0 & 0 & 3 & 0 & 0 \\ 0 & 0 & 0 & 0 & 3 & 0 \\ 0 & 0 & 0 & 0 & 0 & 3 \end{bmatrix} \begin{bmatrix} \varepsilon_{t,x}^{\mathrm{mod}} \\ \varepsilon_{t,y}^{\mathrm{mod}} \\ \varepsilon_{t,z}^{\mathrm{mod}} \\ \gamma_{t,xy}^{\mathrm{mod}} \\ \gamma_{t,xz}^{\mathrm{mod}} \\ \gamma_{t,yz}^{\mathrm{mod}} \end{bmatrix} \tag{4.27}$$

where $\Delta\varepsilon_{x}^{creep}, \Delta\varepsilon_{y}^{creep}, \Delta\varepsilon_{z}^{creep}, \Delta\varepsilon_{xy}^{creep}, \Delta\varepsilon_{xz}^{creep}$, and $\Delta\varepsilon_{yz}^{creep}$ are the final creep strain increments in *x*, *y*, *z*, *xy*, *xz*, and *yz*, respectively.

Next, the elastic strains ($\varepsilon_{x,t}^{elastic}$) and the total creep strains ($\varepsilon_{x,t}^{creep}$) are calculated as follows, using the example of the *x*-component:

$$\varepsilon_{x,t}^{elastic} = \varepsilon_{x,t}^{\mathrm{mod}} - \Delta\varepsilon_{x}^{creep} \qquad [4.28]$$

$$\varepsilon_{x,t}^{creep} = \varepsilon_{x,t-1}^{creep} + \Delta\varepsilon_{x}^{creep} \qquad [4.29]$$

Comparison between ANSYS creep model and existing Dorn-based creep models will be carried out in the following section. As a representative for Dorn-based models, Dorn-Harmathy modified model will be used to demonstrate the effect of non-trivial stress rate development ($d\sigma_S / dt \neq 0$) on high temperature creep strain of steel.

4.4.3.2 Calibration of ANSYS Creep Model

High temperature creep test data is required to generate the seven coefficients (*c1,...,c7*) of ANSYS creep model. Nonlinear regression fitting tool is available in ANSYS finite element software, and this fitting tool is dedicated for fitting creep test data in order to obtain the coefficients of the creep model.

Performing creep tests at high temperature is very complex and time consuming. Therefore, there is a lack of creep test data in literature. However, two independent sets of high-temperature creep test data were used to fit the ANSYS creep model (Kodur and Dwaikat 2009*b*). The first set of high temperature creep test data, shown in Fig. 4.9(a), is published by Nippon Steel Corporation (NKK 1989) for structural steel SM50A (equivalent to A992 in American designation, or S355 in European norms). The second set of high-temperature creep test data, shown in Fig. 4.9(b), is from tests carried out by Kirby and Preston (1988) for A36 (S275) steel.

The first set of high temperature creep test data is from transient tests wherein temperature is increased at a rate of 10°C/min, while stress is kept constant. The second set is from steady state tests wherein temperature is kept constant at 550°C, while stress is kept constant. For both sets of test data, different values of applied stress were used as shown in Fig. 4.9.

The results of the calibration is plotted in Figure 4.9, which shows the comparison of high-temperature creep strain computed using Equation [4.23] with that of test data for various stress levels. The model shows good agreement with the test data for both types of A36 and Grade 50 steel. It can be seen from Figure 4.9(b) that creep strain can become very significant at high temperatures and increased stress levels. The calibrated creep model of ANSYS was integrated into the finite element structural model.

4.4.3.3 Comparison with Other Creep Models

Calibrated ANSYS creep model is compared against Dorn-based creep models. Dorn's creep theory assumes constant stress ($d\sigma_s / dt = 0$), and states that creep strain is a function of temperature (*TR*), stress (*σs*), and time (*t*). Creep strain in Dorn is derived using the following creep strain rate equation (Dorn 1954):

$$\frac{d\varepsilon_{cr}}{dt} = \left[S\Phi(\sigma_s)\right] \cdot e^{-Q/T_R}, \qquad \left(\frac{d\sigma_s}{dt} = 0\right) \qquad [4.30]$$

where the compound function *SΦ*(*σs*) is dependent on stress and temperature, and is given as (Dorn 1954):

$$S\Phi(\sigma_s) = \begin{cases} S' e^{B\sigma_s} & B\sigma_s \geq 1.4 \\ S'' \sigma_s^n & B\sigma_s > 1.4 \end{cases} \qquad [4.31]$$

where *B*, *n* and *Q* are constants that depend on the type of steel. It should be noted that the above equations, as proposed by Dorn, were essentially devised from material tests of metal alloys under constant stress ($d\sigma_s / dt = 0$) and constant temperature increments ($dT_R / dt = 0$).

Harmathy extended Dorn's approach and proposed a revised creep model for structural steel (Harmathy 1967). Harmathy-Dorn modified creep theory is given as:

$$\frac{d\varepsilon_{cr}}{dt} = Z \cdot \coth^2(b_H / \varepsilon_\circ) \cdot e^{-Q/T_R} \quad \text{for } d\sigma_s / dt = 0 \qquad [4.32]$$

$$b_H = \begin{cases} 3\,tZ \cdot e^{-Q/T_R} & \text{(time hardening rule)} \\ \sum \left| \mathrm{d}\varepsilon_{cr} / \mathrm{dt} \right| \cdot \Delta t & \text{(strain hardening rule)} \end{cases} \qquad [4.33]$$

where (*Z*) is the Zener-Hollomon experimental parameter and is given for A36 steel as:

$$Z = \begin{cases} 0.026\sigma_s^{4.7} & \sigma_s \leq 15000 \text{ psi} \\ 1.23 \times 10^{16} \times e^{0.0003\sigma_s} & 15000 < \sigma_s \leq 45000 \text{ psi} \end{cases} \qquad [4.34]$$

Where $\varepsilon_{\circ} = 1.7 \times 10^{-10} \sigma_s^{1.75}$, $Q = \Delta H/R$, ΔH is the activation energy of creep, and R is the universal gas constant.

A critical review of Eq. [4.34] indicates that in the case of strain hardening creep, Harmathy model becomes implicit [4.34] and requires rigorous solving techniques, which can pose difficulties in the convergence. Also, since Harmathy-Dorn modified creep theory assumed a constant stress, Harmathy (1967) himself expressed doubts on the validity of his creep model when $d\sigma_s / dt$ becomes significant.

Fig. 4.10 shows a comparison of ANSYS and Harmathy-Dorn modified (1967) creep models with test data. The two creep models (ANSYS and Harmathy) were compared for two cases, namely; when the stress rate was held constant ($d\sigma_s / dt = 0$) and when the stress rate is variable ($d\sigma_s / dt \neq 0$). In the first case (Fig. 4.10(a)), creep test data from Nippon Steel Corporation tests (NKK 1989) on structural steel at a constant temperature of 550°C and at different (but constant) stress levels were used. In the second case (Fig. 4.10(b)), test data from an experiment reported by Harmathy (1967) and Harmathy and Stanzak (1970) were used. Harmathy tested A36 steel rods under constant temperature of 550°C, but with varying stress levels in three phases. In the first phase, the stress was increased stepwise at an average rate of 0.22 MPa/min; in the second phase, the stress was decreased at the same rate; in the third phase the stress was maintained constant as shown in Fig. 4.10(b).

It can be seen in Fig. 4.10(a) that for the three cases of constant stress (49 MPa, 73.6 MPa, and 98 MPa) and constant temperature (550°C), ANSYS and Harmathy models predict creep strains with acceptable accuracy as compared to test data. For the case of varying stress with time (Fig. 4.10(b)), Harmathy creep model diverges from test data, specifically at high stress levels, whereas the ANSYS model predictions compare well with the test data. This is due to the fact that Harmathy creep model is based on Dorn's theory which does not account for a variable stress state.

4.5 MODEL VALIDATION

The finite element model created in ANSYS was validated by comparing the predictions from the analysis with the results from fire tests (Dwaikat et al. 2009). The validation process covered both thermal and mechanical analysis. Since variation in material properties can cause variations in predicted thermal and structural responses, different material models are used in the validation process and the results are compared. The following sections provide details on the validation process.

4.5.1 Validation of Thermal Response

Two cases of validation are carried out for the thermal analysis. First case is unprotected steel sections, and second case is a section with applied fire proofing material. The case of unprotected steel provides better comparison for the influence of thermal properties of steel since the effect of insulation is neutralized.

4.5.1.1 Unprotected Steel

To validate the thermal analysis, recorded temperatures in four bare steel sections tested by Wainman and Kirby (1988 and 1989) are compared in Fig. 4.11 to predictions from the finite element analysis. In the tests, unprotected steel sections were exposed to ISO 834 standard fire from 3 sides, with the forth (top) surface being covered by a concrete slab. The temperatures plotted in Fig. 4.11are the temperature at the geometrical center of every plate. Emissivity factors used in the thermal analysis varied between 0.9 for directly exposed surfaces (such as the bottom surface of the bottom flange) to 0.5 for the "hidden" areas in the section (such as the corners where the web and flanges meet). The convective heat coefficient (*hcon*) was assumed to be equal to 25 W/m.°K. Overall, Fig. 4.11 shows that the predictions from the finite element model are in good agreement with the recorded temperatures for different types of steel sections.

In order to compare the influence of using different thermal property models on the results of the thermal analysis a steel beam tested by Li and Guo (2008) was analyzed. The unprotected steel beam in the experiment was exposed to fire from four sides with the top flange being insulated by 3 mm thick ABK ceramic fiber insulation to simulate a three-side fire exposure. The temperature dependent thermal properties of the ceramic fiber can be found in Gumen et al. (2001). The thermal conductivity of the fiber insulation ranged from 0.053 W/m.°C at room temperature to 0.12 W/m.°C at 800°C. In the experiment, the beam was exposed to a design fire scenario and the same was studied in the analysis.

Figure 4.12 shows the fire temperature and the resulting steel temperatures as measured in the test and as predicted using the ASCE and Eurocode thermal properties (models). The measured and predicted temperatures in top and bottom flanges are compared. It is evident that the differences in the predicted and measured temperatures are insignificant. Further, the results show that the predicted temperatures based on ASCE thermal properties are slightly higher than the predictions based on Eurocode thermal properties when the temperature is above 700°C. This is due to the fact that, above 700°C, the specific heat of steel according to ASCE is significantly lower than that in the Eurocode as shown in Fig. 2.6. Therefore, at temperatures above 700°C, the rise in steel temperature is slightly higher when the ASCE model is used. However, these variations in temperature predictions based on the two models are very minor and can be ignored from a design point of view.

4.5.1.2 Protected Steel

For the second case of analysis, a protected steel section is compared. There is a lack of fire test data on the thermal response of protected steel members under thermal gradients. Therefore, data form the fire tests on beam-columns (Dwaikat et al. 2009) that were conducted at Michigan State University (MSU) is used for validating the thermal response predictions from finite element program. These fire resistance tests were conducted on four insulated beam-columns of W8x48 sections and were designated C1-S, C1-W, C2-S, and C2-W. Figure 4.13 shows schematic for the tested beam-columns and location of thermocouples. Full details on the fire resistance experiments on these beam-columns, including test procedures, instrumentations, and detailed measurements details on these tested beam-columns are presented in Chapter 3.

Comparison between measured steel temperature and that predicted by finite element is shown in Fig. 4.14 for the strong (C1-S) and weak (C1-W) axis orientation, respectively. The B-B cross-section was selected for this comparison because it consistently recorded the highest temperatures for each specimen, due to its location in the middle of the furnace, and therefore represents the worst case scenario for temperature increase. The comparison presented in Fig. 4.14 shows good agreement between measured temperatures in test and as predicted by finite element analysis in the section plates. Figure 4.14 show that the predicted temperatures for columns C1-S and C1-W are initially conservative because the ANSYS thermal model does not account for the evaporation of the insulation's residual water near 100°C, which slowed the initial increase of temperature. The slight variations between the computational and experimental temperatures may also have been caused by variation in the actual SFRM thickness as compared to the idealized constant 45 mm thickness used for computational thermal analysis. Also, slight variation in heat transfer parameters, such as emissivity and convection coefficients (especially near the gaps in insulation), may have contributed to temperature variations to some extent Overall, the comparison shows that the thermal model in ANSYS is capable of predicting steel temperatures within sufficient accuracy.

4.5.2. Validation of Structural Response

The structural analysis is also validated by comparing predictions from the finite element model with test results of two cases of beam-columns. First case represents a restrained beam tested by Li and Guo (2008), while the second case represents restrained columns (beam-columns) tested under fire at MSU civil and infrastructure laboratory. In both cases, the beam-columns were subjected to fire-induced thermal gradients. The following sections provide details about the validation process

4.5.2.2 Li and Guo Tests

Fire tests on restrained steel beam carried out by Li and Guo (2008) was selected for validation of the structural analysis. The tested beam was of cross section H250x250x8x12 and had a clear span length of 4500 mm. This axially-restrained beam was tested under a design fire scenario, with the top flange covered with 3 mm thick ceramic insulation to simulate three-side fire exposure (Refer to Section 4.5.1.1 on the thermal analysis of this beam). Two point loads, 130kN each, were applied at two-third points of the beam prior the exposure to fire, and the this loading generated maximum bending moment that corresponded to almost 70% of the plastic bending moment capacity if the beam. Figure 4.15 shows the schematics of the test setup and the final result of the structural fire analysis on the beam.

The fire test was simulated through two approaches. First approach is through modeling the entire loading frame including the beam exposed to fire, as shown in Fig. 4.15(b). 8-noded shell elements were used to model the assembly with mesh size of 35mmx35mm (4 elements per plate width). The connections between the beam and the columns were assumed rigid. The second approach is through modeling only the beam exposed to fire. The boundary conditions in this case were modeled as axial and rotational springs as was illustrated in Section 4.3.3. The values of the axial and rotational restraint stiffnesses (*Ka* and *Kr*) were computed based on the setup and members dimensions of the loading frame and. For estimating *Ka* and *Kr* the columns in the loading frame were assumed to be fixed at top end but free to move on the end where the beam is attached. Based on these computations, the values for restraint stiffnesses were estimated as 39kN/mm and 54kN.m/milirad for axial and rotational restraints, respectively. In both approaches of the modeling, temperatures obtained from the thermal analysis are applied on the corresponding locations of the nodes in the structural mesh of the beam.

Figure 4.15(c and d) compares the actual deflected shape of the beam after fire test with that obtained from analysis. The occurrence of local buckling in the fire test (Fig. 4.15(c)) is well captured in the structural analysis (Fig. 4.15(d)).

Measured deflections and axial restraint forces are also compared in Figs. 4.16(a, b) with predictions from ANSYS model of the entire test setup. Three different constitutive models for structural steel were used in the analysis, namely: Eurocode 3, ASCE, and Poh temperature dependent stress-strain curves. The thermal strain as per Eurocode 3 (2005) was used in conjunction with Poh model since the latter does not have a constitutive relationship for thermal strain. It is clear from Fig. 4.16(a, b) that the mid-span deflection and axial force predicted based on the three models are less than that reported in test data. This can again be attributed to the fact that high-temperature creep is not considered in ASCE and Poh models while it is partially considered in Eurocode constitutive model.

The results also indicate that using Eurocode stress-strain constitutive models lead to better prediction of the response compared to using ASCE constitutive models. This is mainly attributed to the fact that the Eurocode stress-strain relationships partly account for high temperature creep. Since accounting for high temperature creep in the structural fire analysis is quite laborious and computationally expensive, Eurocode constitutive relationships are a preferred choice if creep effects are to be explicitly neglected.

In Fig. 4.16(c and d), Poh stress-strain constitutive model is used in the analysis with the incorporation of ANSYS high-temperature creep. Two creep models were incorporated, namely ANSYS creep model and Dorn-Harmathy modified creep model. Harmathy creep model is incorporated in ANSYS as a user-defined subroutine, an option that is readily available in ANSYS program. It can be seen in Fig. 4.16(c and d) that creep has significant influence on the resulting deflections and the restraint forces in the beams. As can be seen in Fig. 4.16(c), neglecting high temperature creep effect leads to much lower deflections, especially towards the later stages of fire exposure. When Harmathy's creep model is used, the comparison is slightly better, as shown in Fig. 4.16(c). However, when ANSYS creep model is included in the analysis, the resulting deflection and restraint force match well with measured test data. This is because ANSYS creep model takes into consideration the high stress rate ($(d\sigma_s / dt)_{average} \cong 3.5\ \text{MPa/min}$) resulting in the beam from fire induced restraint effect. However, the predictions using Harmathy's creep model did not match with test data and this can be attributed to the fact that the model is based on invariant stress state. Overall, predictions from the model compare well with test data when high-temperature creep is included in the analysis. When the creep effect is not included, the predicted deformations and restraint forces are under-estimated in the later stage of fire exposure. Therefore, neglecting high-temperature creep in the analysis may not lead to realistic predictions of both deflection and fire induced restraint force.

4.5.2.1 MSU Fire Tests

The beam-columns tested at MSU, and presented in Chapter 3, are used here for the validation of the structural analysis. Fig. 4.3(b) shows the mesh that was used to discretize the tested beam-columns.

The base of the column is assumed to be fully fixed, while the top of the column is assumed to have partial rotational and axial restraints with no horizontal movement. Stiffnesses of axial and rotational restraints were estimated to be 25000 kN/m and 2500 kN-m/rad, respectively, by examining the vertical and rotational stiffnesses recorded during the experiments (Dwaikat et al. 2009, Quiel et al. 2009). The axial load is applied as distributed nodal force on the boundaries of the shell elements at the top end of the beam-column.

Two cases of structural fire analysis were carried out. First case, the partial simulation case, is carried out using the experimentally measured temperature distribution in the steel sections for each of the tested beam-column. Fig. 4.13(a) shows the temperature zones that were used in the analysis for the first case. In each temperature zone shown in Fig. 4.13(a), the temperature is assumed to be uniform along the length of that zone. The temperature in the transition zones as assumed to decrease gradually from the measured temperature (in Zone A-A or C-C) to room-temperature away from the furnace.

The second case, the full simulation case, the analysis is carried out using nodal temperature obtained from thermal analysis of the column cross section. Steel temperature at every nodal location of the discretized mesh is obtained for each time step through thermal analysis. Then these temperatures were applied on the corresponding nodes of the shell elements at one cross section of the meshed column. The nodal temperature loads were then replicated along the entire heated length of the column (see Fig. 4.3(b)). And finally, nonlinear finite element analysis is carried out to obtain the total structural response of the beam-column under fire exposure.

The results of structural analysis for the case of partial simulation (using experimentally obtained temperatures) and the case of full simulation (using numerically obtained temperatures) are compared to experimental data for all four columns in Figs. 4.17 through 4.20. The figures show axial deformation and bending moment measured at section D-D as a function of time. Figs. 4.17(a) through 4.20(a) show that the axial deformation trends of the computational models are similar to those for all four tested specimens. Furthermore, both models provide a conservative estimate compared to values recorded during the fire tests. Computational axial displacements are roughly 20-30% greater than experimental values, most likely due to the use of Eurocode high temperature properties to model the structural behavior of steel. This can be attributed to the fact that the Eurocode (as a design code) provides a conservative model for coefficient of thermal expansion of structural steel, and this likely contributed to the overestimation of axial displacement in Figs. 4.17(a) through 4.20(a).

Figs. 4.17(b) through 4.20(b) show the moment curves for each of the two computational models as well as the experimental moments. These plots show similar moment trends for both computational models and the experimental data among all four specimens. All data sets show an initial increase in positive moment due to restraint of thermal bowing, followed by a shift of the effective centroid (i.e the center of stiffness) which produces a moment reversal. For columns C1-S and C2-W (Figs. 4.17(b) and 4.20(b)), the moments at D-D obtained from the direct validation model show close agreement with those obtained from experimental data. This correlation indicates not only that the strain gauge data for these specimens is reliable but also that the structural analysis performed with partial simulation model is able to accurately predict the development of bending moment caused by the experimentally measured thermal gradient. The moment obtained through full simulation (with numerically obtained temperature) for C1-S also shows similar magnitudes of positive and negative bending moment as the direct validation model and experimental data.

The full simulation of specimen C2-W (Fig. 4.20(b)) shows similar trends in overall moment and similar magnitudes of negative moment but a different magnitude of positive moment. This variation is caused by a difference in thermal gradient over the thru-furnace length of the column between the experiment/partial simulation cases and the full simulation case. Since the experimental specimen and the partial simulation model have a shorter zone length with a significant gradient, they developed smaller magnitudes of positive bending moment in response to thermal bowing. Likewise, both the experimental and partial simulation cases also experienced a smaller moment reversal than the full simulation model because they have a shorter zone length over which the effective centroid has shifted. However, when the negative moments that cause the reversal are added to the positive moments, the end result, which is the maximum negative moments at failure, is the same for all cases.

For specimens C1-W and C2-S (Figs. 4.18(b) and 4.19(b)), the trend of moments at D-D is similar for all three data sets. However, only the two computational models show overall agreement in magnitude. Experimental moments for C1-W, though reaching similar values of negative moment, experienced positive moments up to three times smaller than that of the computational models. Positive experimental moments for C2-S showed a similar variation, and negative moments were up to two times greater in magnitude. Since the two computational models showed reasonable overall agreement, it is possible that the strain gauge data is not reliable for these specimens. For example, there may have been slip at the interface of the gauges and the steel, mechanical problems with the gauges, or experimental error.

4.6 EFFECT OF VARIATION OF CONSTITUTIVE MATERIAL MODELS

The effect of the different constitutive relationships on fire resistance predictions is investigated through fire resistance analysis on two types of beams, namely restrained and simply supported beams. Three constitutive material models are used in the analysis, namely, Eurocode, ASCE and Poh models for structural steel. The results of the comparison on the restrained beam are presented in Section 4.5.2.2. The results of the comparison on simply supported beams are presented here.

Thirteen simply supported (axially unrestrained) steel beams tested under standard fire exposure were used to study the differences in predictions using different constitutive models. Beams 1 to 12 were tested in the U.K. (Wainman and Kirby 1988 and 1989), while the data for Beam #13 was reported by Thor (1973). The load ratio applied to the beams is defined as the ratio of moment due to applied load under fire conditions to the room temperature capacity of the beam. A summary of the parameters and properties of the tested beams is presented in Table 4.1.

In addition, Table 4.1 shows the recorded (in fire tests) and predicted (from current analysis) fire resistances of the thirteen beams. The beams were tested under the ISO-834 standard fire exposure (ISO 1975) from three sides. Beams 1 to 11 were unprotected, and beams 12 to 13 were protected with insulation. These tests were terminated when the deflections of beams reached a limiting value of *L*/20. The structural fire response of the beams was simulated using ANSYS structural model, with recorded temperature applied directly on the structural model. Three different constitutive models for structural steel were used in the analysis, namely: Eurocode

3, ASCE, and Poh temperature dependent stress-strain curves. The thermal strain as per Eurocode 3 (2005) was used in conjunction with Poh model since the latter does not have a constitutive relationship for thermal strain.

Results in Table 4.1 show that in case of higher load ratios (above than 40%), other factors, such as effect of creep that is partly accounted for in Eurocode, and effect of strain hardening that is neglected in Eurocode for temperatures above 400°C, play an important role in predicting fire resistance. This aspect is causing more plastic deformations when using Eurocode material constitutive model, and hence smaller fire resistances that is closer to the measured values. However, when compared to ASCE and Poh models, the Eurocode model generated predictions closer to the test results. This is clearly evident for the case of protected steel beams (Beam # 12 and #13). These variations in predictions can be attributed to the fact that the Eurocode temperature-stress-strain relationships partly account for high-temperature creep (Buchanan 2002). However, in the ASCE and Poh models, high-temperature creep is not included in the temperature-stress-strain relationship, thus leading to un-conservative fire response predictions. This is due to the fact that high-temperature creep causes additional deformations under fire conditions, thus less time is needed to reach the failure (deflection) limit state.

Fire resistance predictions for eleven beams (the unprotected beams) are plotted in Fig. 4.21 for comparison. The results shows, for all load ratios, that fire resistance predictions using ASCE mechanical properties are generally less than those predicted using Eurocode material properties. However, both provide unconservative predictions with the case of using ASCE being closer to the measured fire resistances of the beams. The reason can be attributed to the differences between material property reduction factors and nature of stress-strain relationships adopted by both ASCE and Eurocode. For example, as per Eurocode, reduction in yield strength starts in steel at temperatures above 400°C. While according to ASCE, reduction in yield strength with temperature starts from just above 20°C. Therefore, with rise of temperature, plastic deformations using ASCE can be achieved faster than when using Eurocode. Consequently, using ASCE material properties leads to faster yielding and shorter fire resistance times when compared to Eurocode.

To further illustrate the effect of varying material mechanical models on the fire resistance predictions, the mid-span deflections of Beam # 13 (with insulation) are plotted in Fig. 4.22 as a function of fire exposure time. Beam # 13 was selected because it was insulated and thus underwent long duration under fire. The long duration under fire conditions is expected to better reveal the influence of high temperature creep on the fire response. The figure shows that at early stages of fire exposure, mid-span deflection increases slightly and there is little variation in the predicted deflections based on the different constitutive models. However, at later stages of fire exposure, variation in predicted deflections based on different models become significant, as seen in Fig. 4.22. This can be attributed to the fact that at high temperatures the constitutive models vary considerably and the effect of creep plays a major role. Also, the comparison in Fig. 4.22 shows that inclusion of creep strain results in conservative predictions using all of the models, with the Eurocode predictions being slightly more conservative than those obtained from ASCE or Poh models. Poh model, when creep is included, produced deflections that match very well with the test data. However, including creep in the Eurocode model produced overly conservative predictions. This can be mainly attributed to the fact that the Eurocode constitutive models account partially for high temperature creep (Buchanan 2002), therefore, adding additional creep strains results in over-predicted deflections.

4.7 SUMMARY

This chapter presents the development and validation of numerical model for tracing the response of restrained steel beams exposed to fire. The numerical model, created via ANSYS, incorporates thermal and structural finite element submodels. The three stages associated with fire resistance analysis, namely, fire growth, thermal, and structural analysis, are explained. The developed model accounts for high temperature material properties, various fire scenarios, fire induced axial restraint effects, geometrical nonlinearity, and various strain components including high temperature creep.

The validity of the thermal and structural models is established by comparing the analysis results to data generated from fire resistance tests. During the validation process, the influence of material constitutive models on the predictions is carefully examined.

This validation indicates that ANSYS is capable of tracing the fire response of restrained beam-columns and thus can be used for undertaking numerical studies.

In the next chapter, ANSYS will be utilized to carry out numerical studies to quantify the influence of critical parameters governing fire response of beam-columns.

Table 4.1: Comparison of measured fire resistance with that obtained from numerical simulations using ASCE, Eurocode and Poh constitutive relationships.

Beam #	Beam section	Length m	Load ratio %	Fire resistance (min.)				
				Test	Model			
					EC3 model	ASCE model	Poh model	
							Without creep	With creep
1	UB305x165x54(S)	4.5	35	23	26	23	25	21
2	UB305x165x46(S)	4.5	35	22	25	23	24	22
3	UB406x178x60(S)	4.5	35	23	26	24	25	20
4	UB356x171x67(S)	4.5	35	25	27	26	28	24
5	UB254x146x43(S)	4.5	35	27	32	28	29	25
6	UB254x146x43(S)	4.5	44	21	23	26	26	21
7	UB254x146x43(S)	4.5	45	22	24	26	26	20
8	UB254x146x43(S)	4.6	46	23	21	25	25	20
9	UB356x171x67(S)	4.5	51	29	28	38	39	27
10	UB254x146x43(S)	4.6	53	20	20	25	25	20
11	UB356x171x67(S)	4.5	56	27	32	35	35	25
12	UB254x146x44(S)	4.5	67	93	112	117	119	91
13	HE220B(S)	3.2	55	122	130	139	139	118
14	H250x250x8x12(R)	4.5	70	16	19	NF	NF	16

Notes: S: Simply supported; R: Axially restrained; NF: Deflection limit state (*L/20*) is not reached, creep model used is ANSYS high temperature creep model

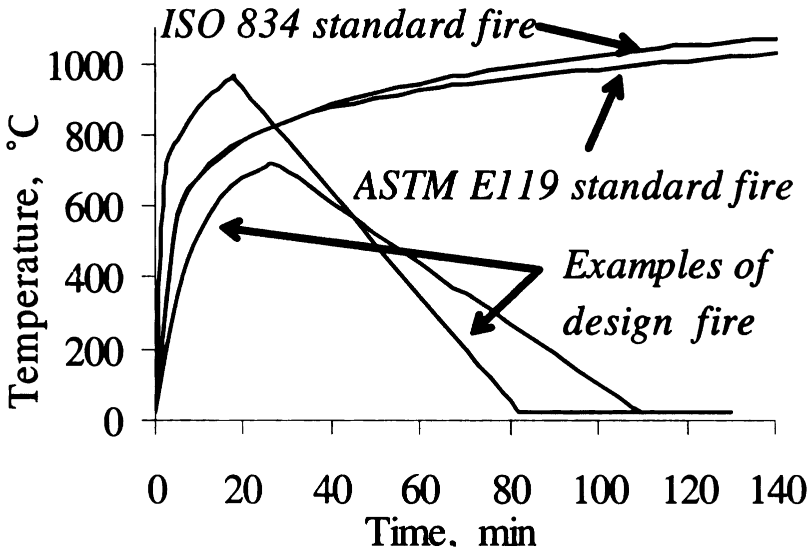

Fig. 4.1: Standard and design fire scenarios

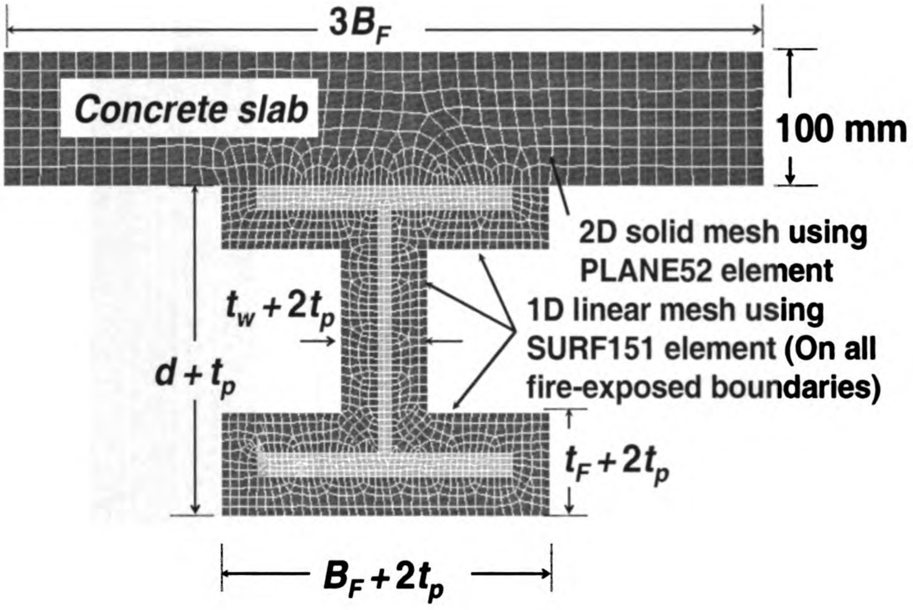

b) Composite beam

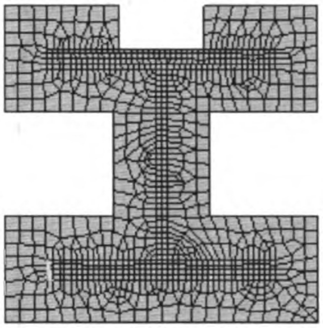

c) Column with special insulation (See C1-S column in Chapter 3)

Fig. 4.2: Discretization of steel sections for thermal analysis

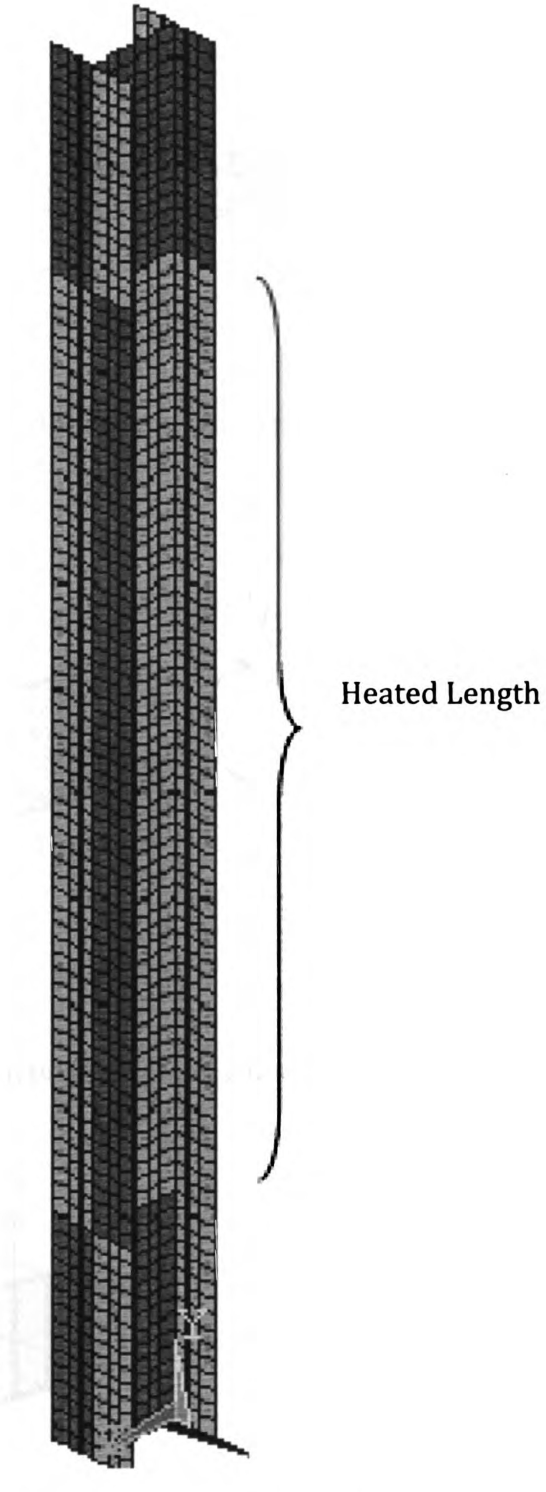

Typical mesh used for structural analysis

Fig. 4.3: Elements and meshes that are used for discretization structural analysis

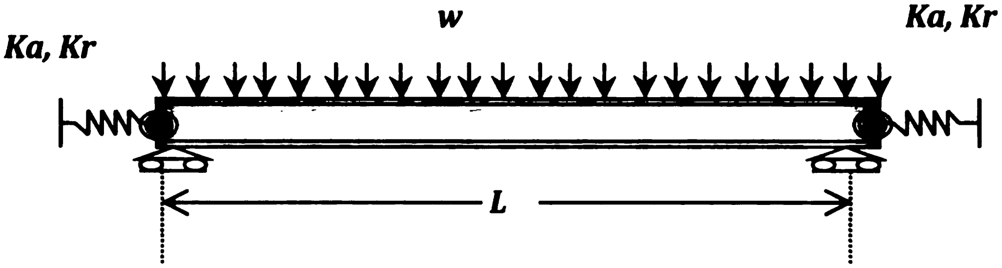

Fig. 4.4: Restrained beam with symmetric restraint conditions

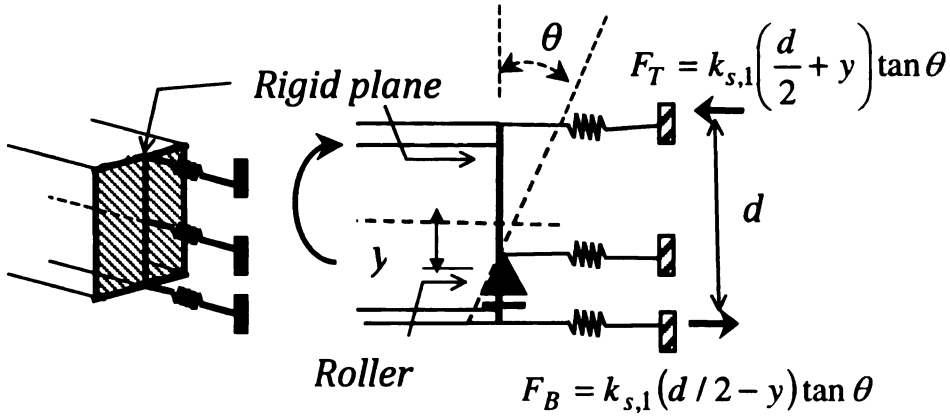

Fig. 4.5: Structural discretization and modeling of end restraint

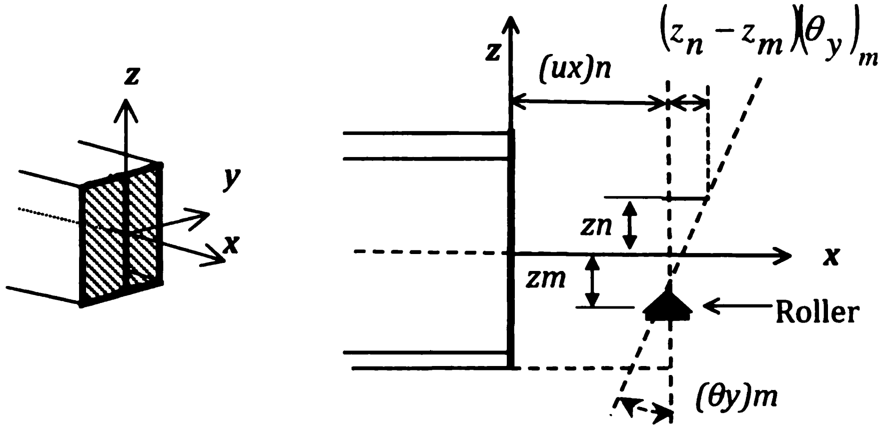

Fig 4.6: Kinematics for simulating end restraint in a beam

Fig.

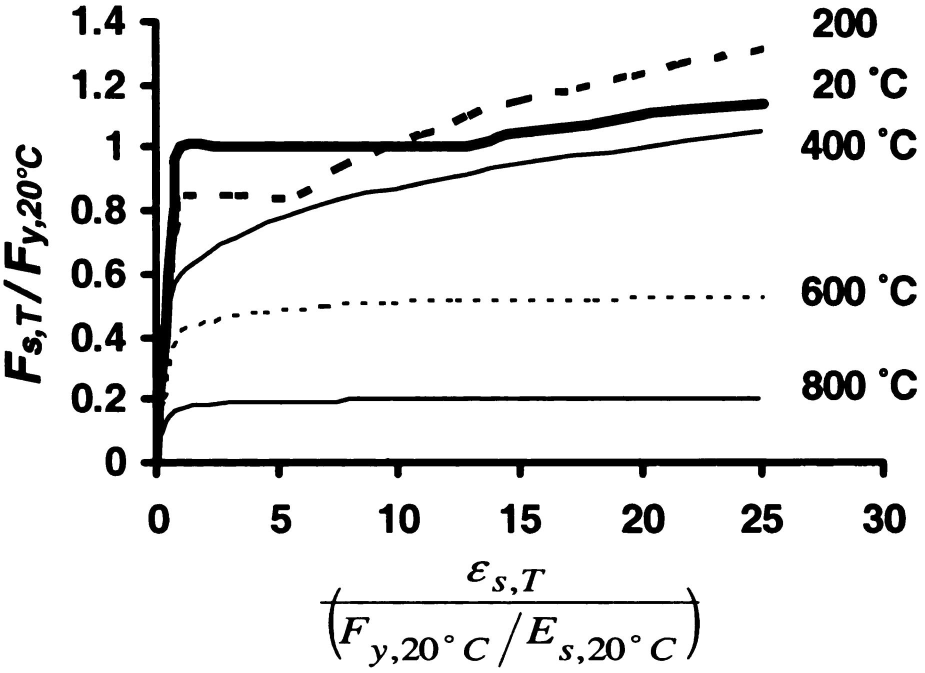

Poh model (2001)

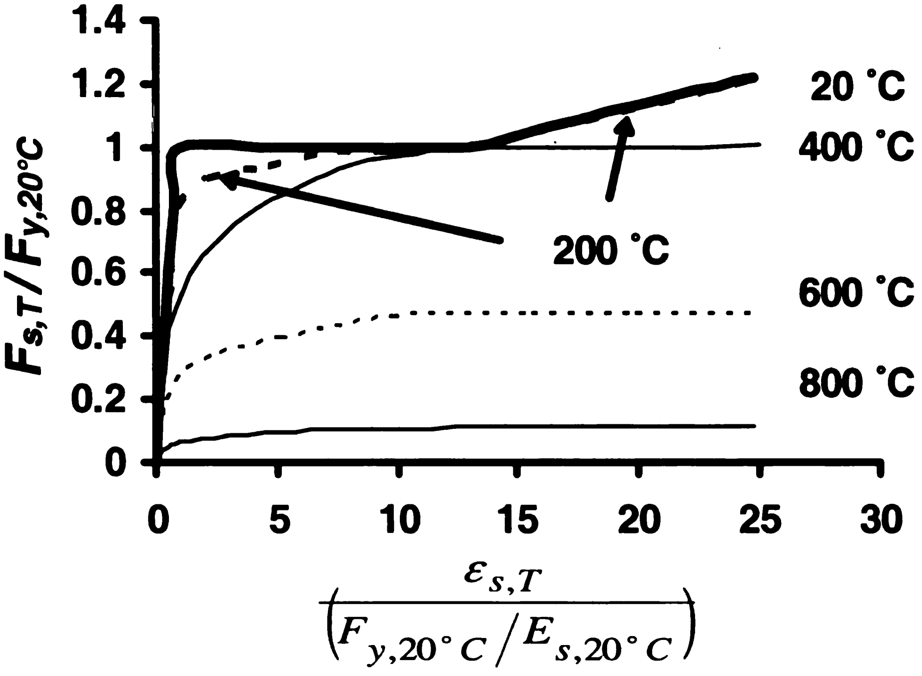

Eurocode 3 model

Temperature-stress-strain curves

Fig. 4.7: Stress-strain relationships adopted for structural fire analysis

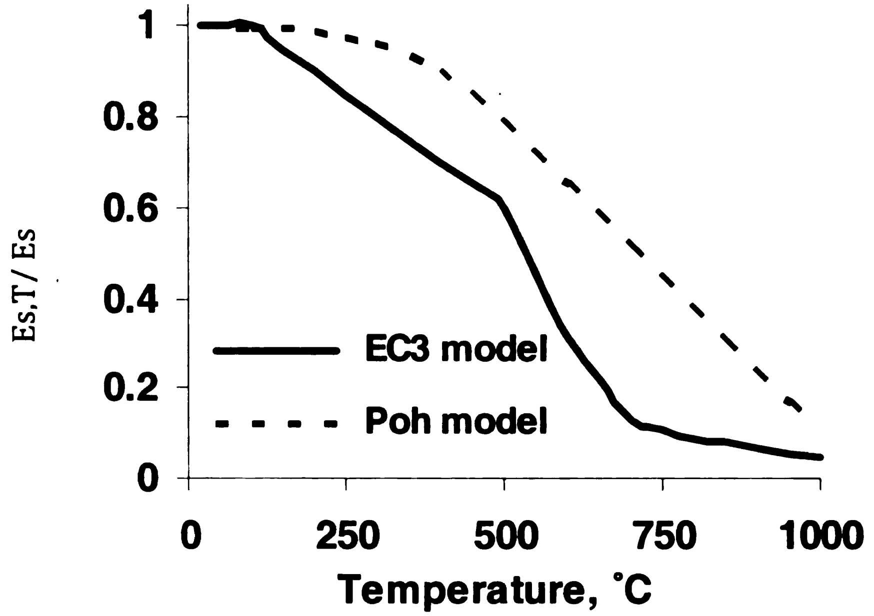

Young elastic modulus

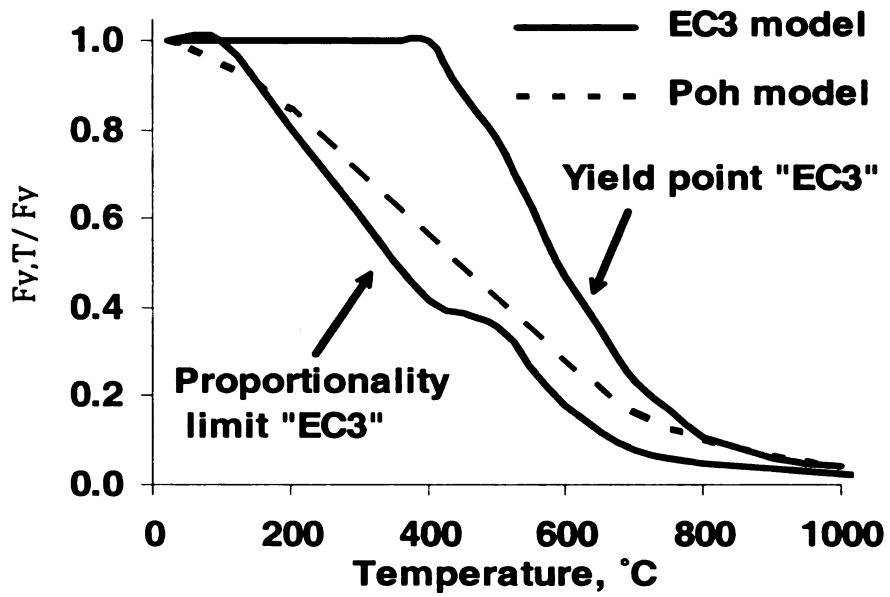

Yield stress
Temperature-dependent reduction factors

Fig. 4.8: Stress-strain relationships adopted for structural fire analysis

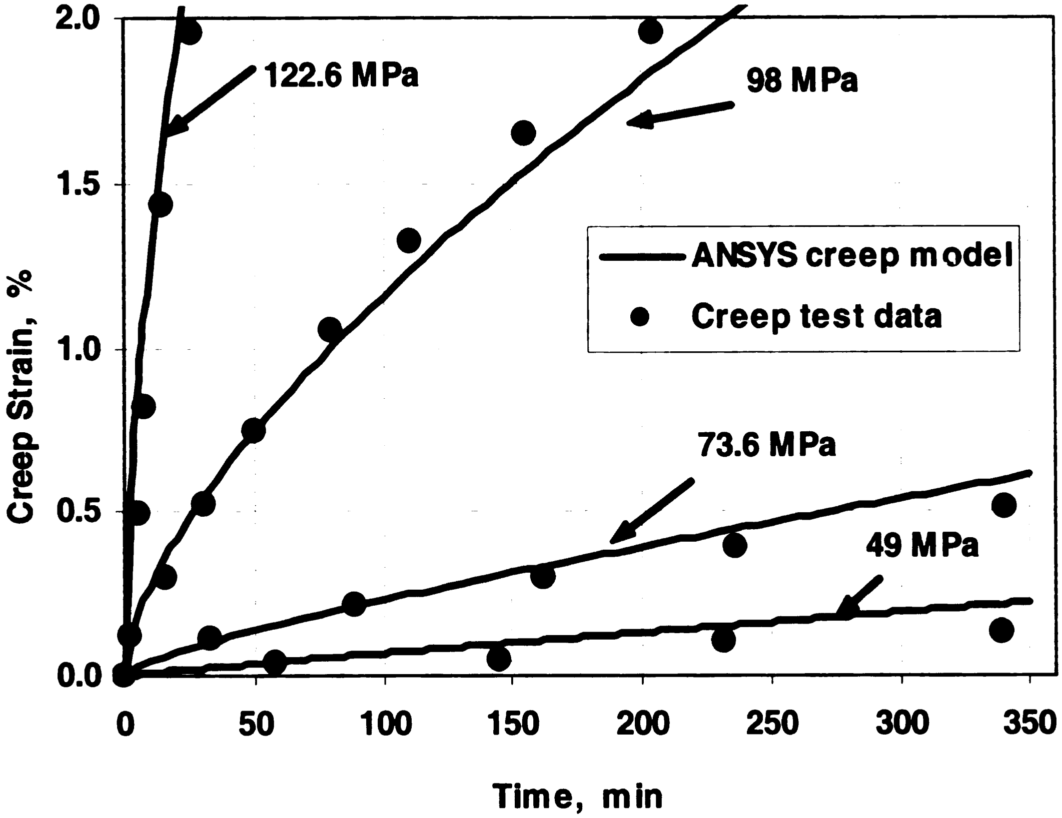

(a) Calibrating using Nippon creep test data (T=550°C)

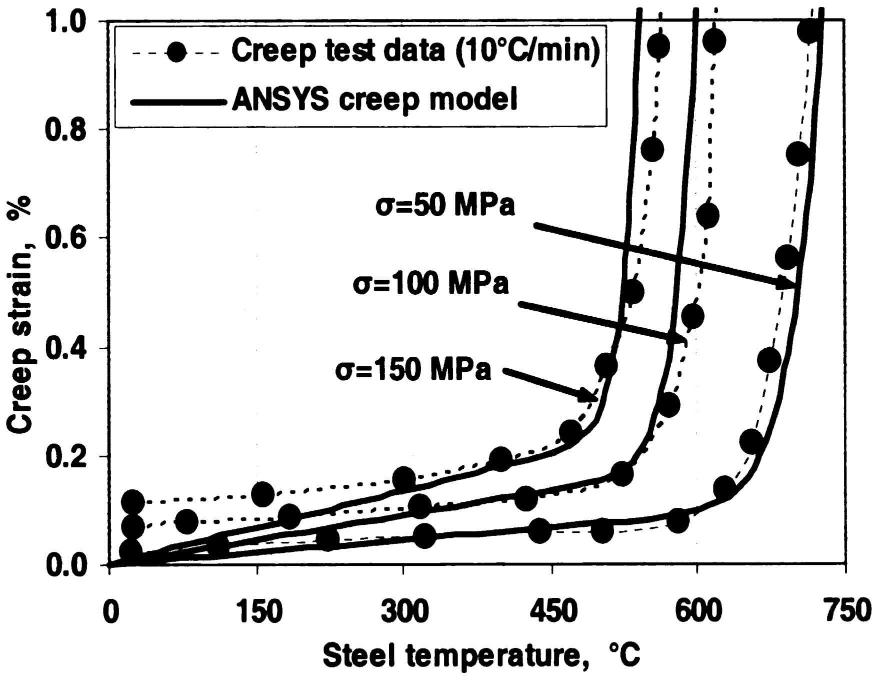

(b) Calibrating using Kirby and Preston creep test data

Fig. 4.9: Calibration of ANSYS high-temperature creep model for structural steel

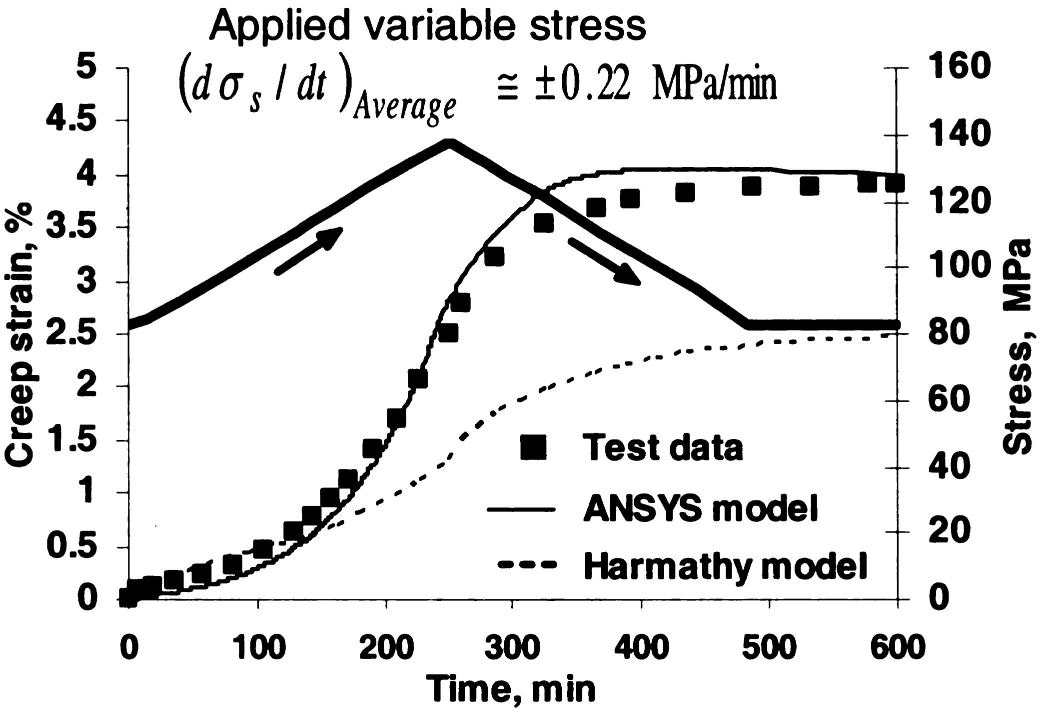

dσs/dt ≠ 0, Ts=550°C

Fig. 4.10: Creep strains predicted using ANSYS and Harmathy models compared to test data

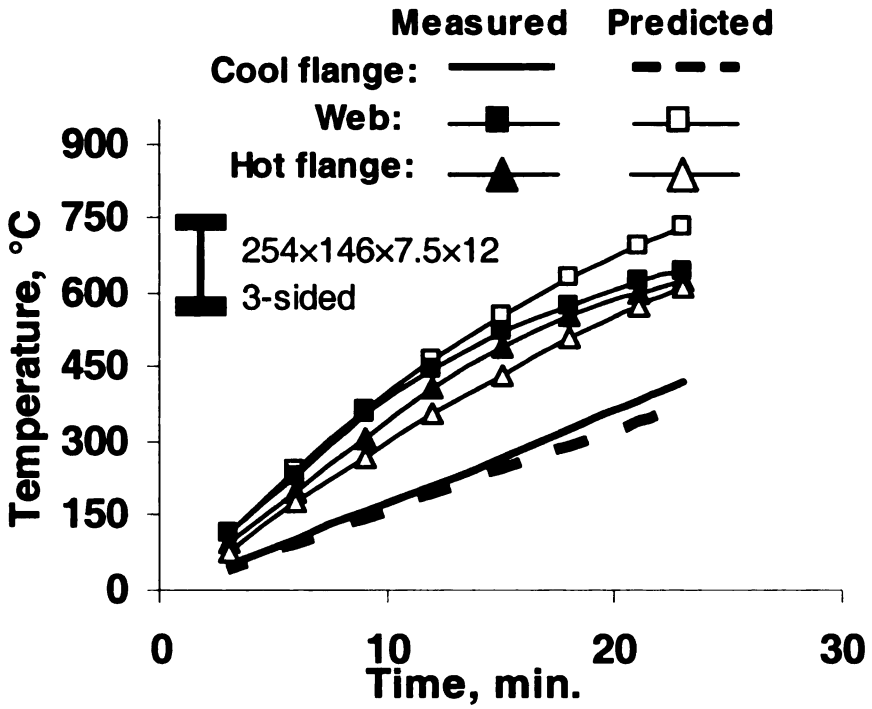

(a) Section 254x146x7.5x12

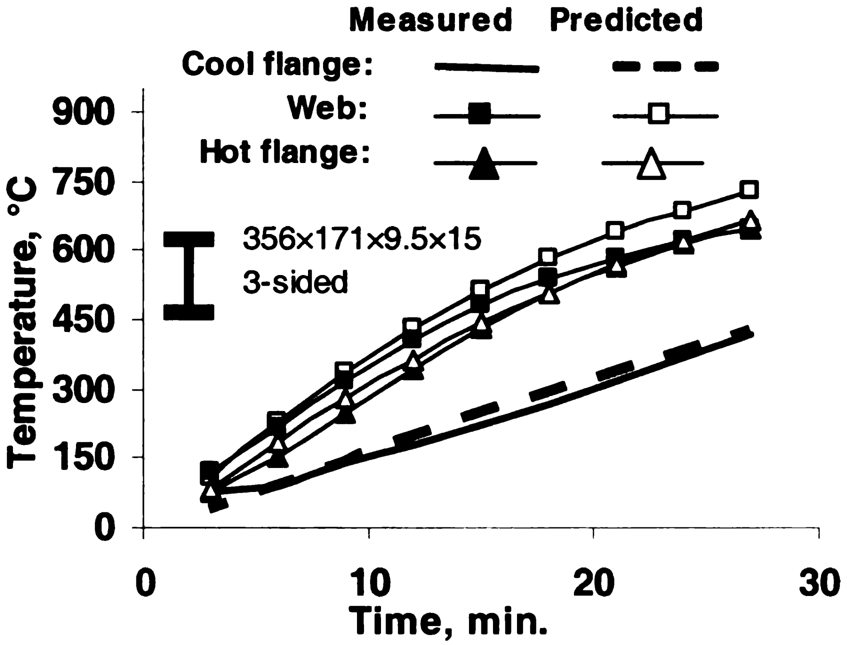

(b) Section 356x171x9.5x15

Fig. 4.11: Comparing predicted steel temperatures with measured values from fire tests

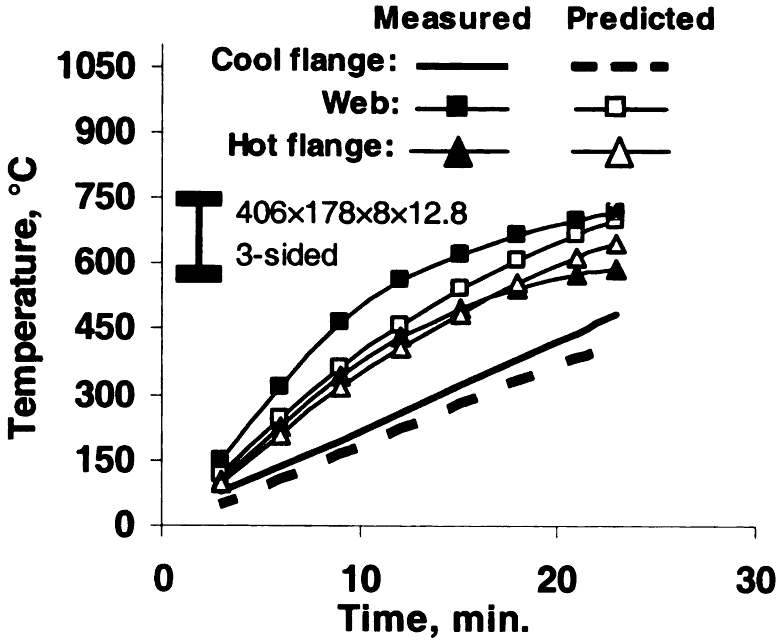

(c) Section 406x178x8x12.8

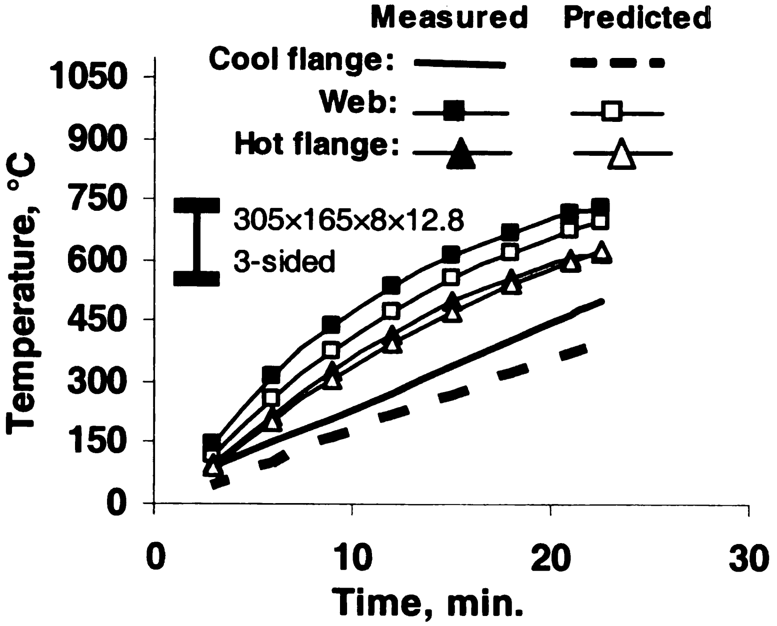

(d) Section 305x165x8x12.8

Fig. 4.11: Continued

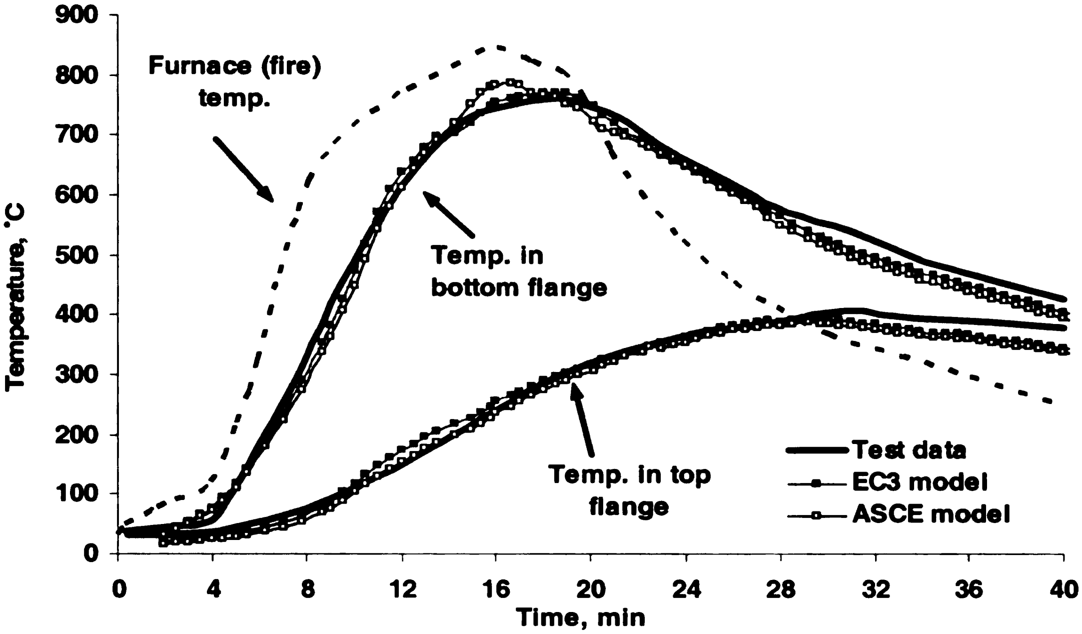

Fig. 4.12: Predicted and measured temperatures in the steel beam tested by Li and Guo (2007)

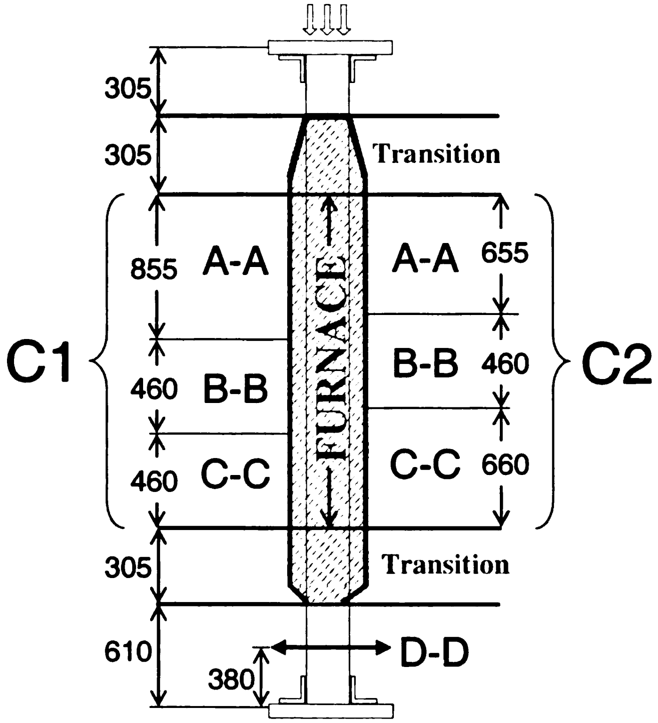

Fig. 4.13: Temperature zones for the validation and thermocouple locations

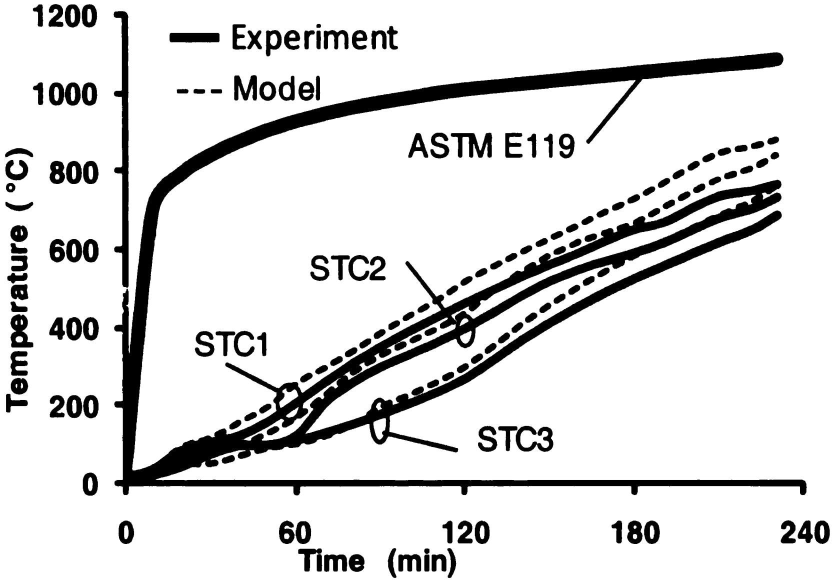

(a) C1-S column

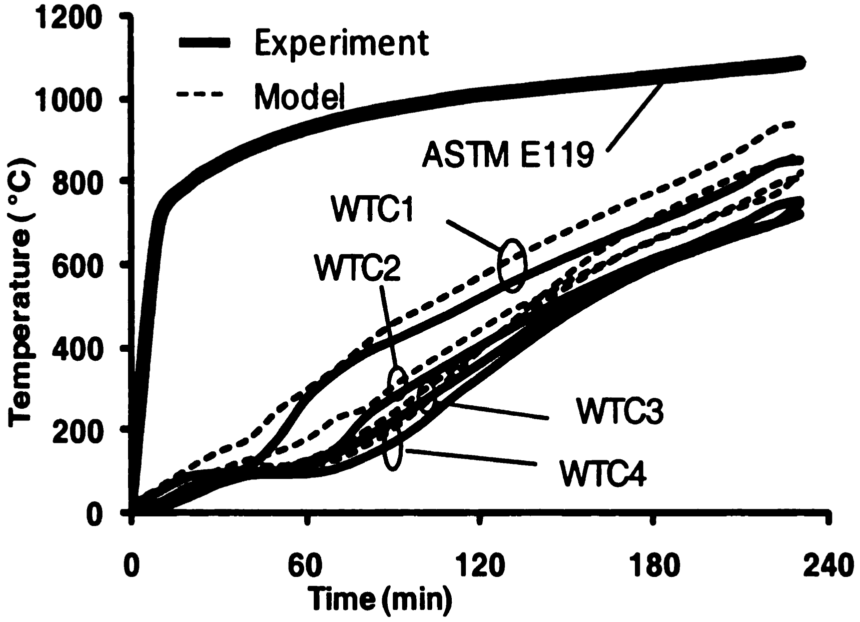

(b) C1-W column

Fig. 4.14: Recorded and predicted temperatures of tested columns (section B-B)

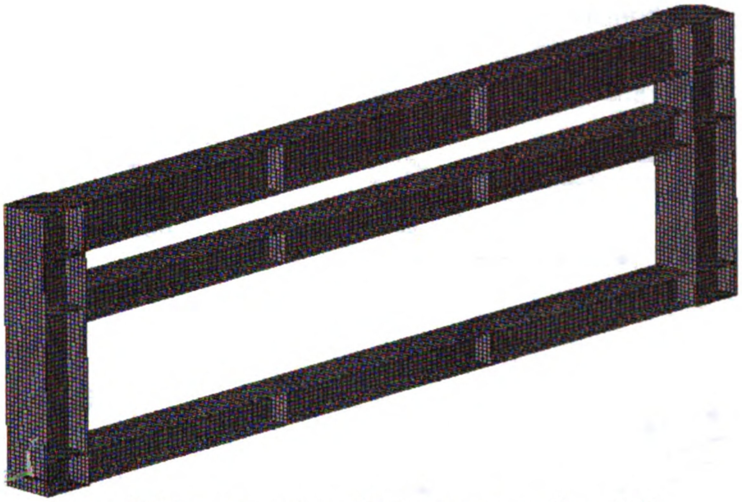

a) Discretization of the structural model

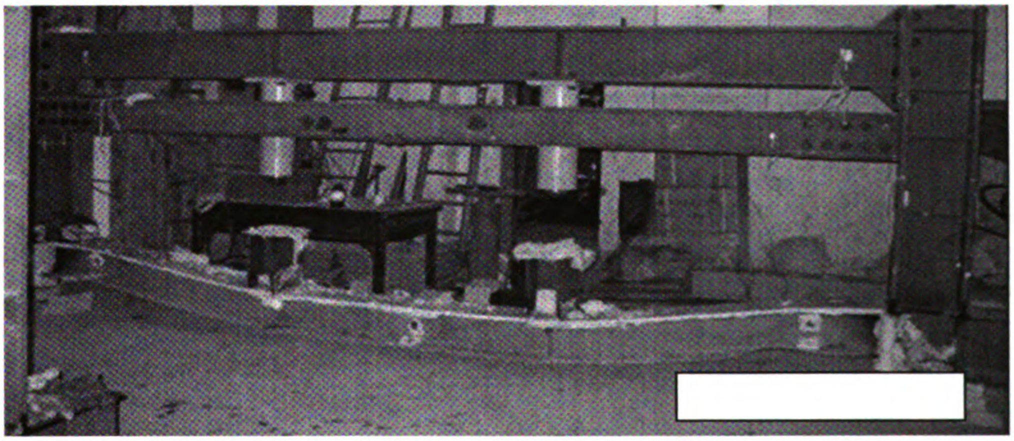

b) Deformed shape of the beam after test

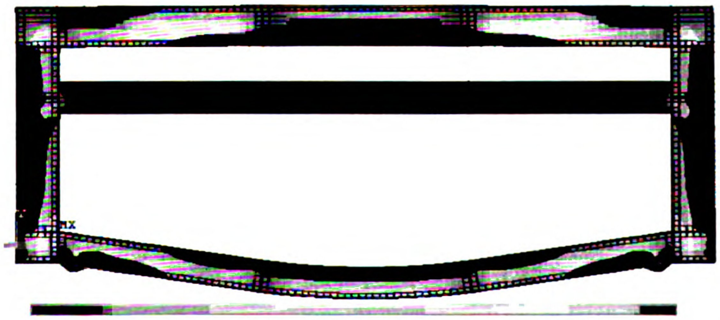

c) Deformed shaped of the model (First principal stress)

Fig. 4.15: Simulation of fire resistance test on restrained beam

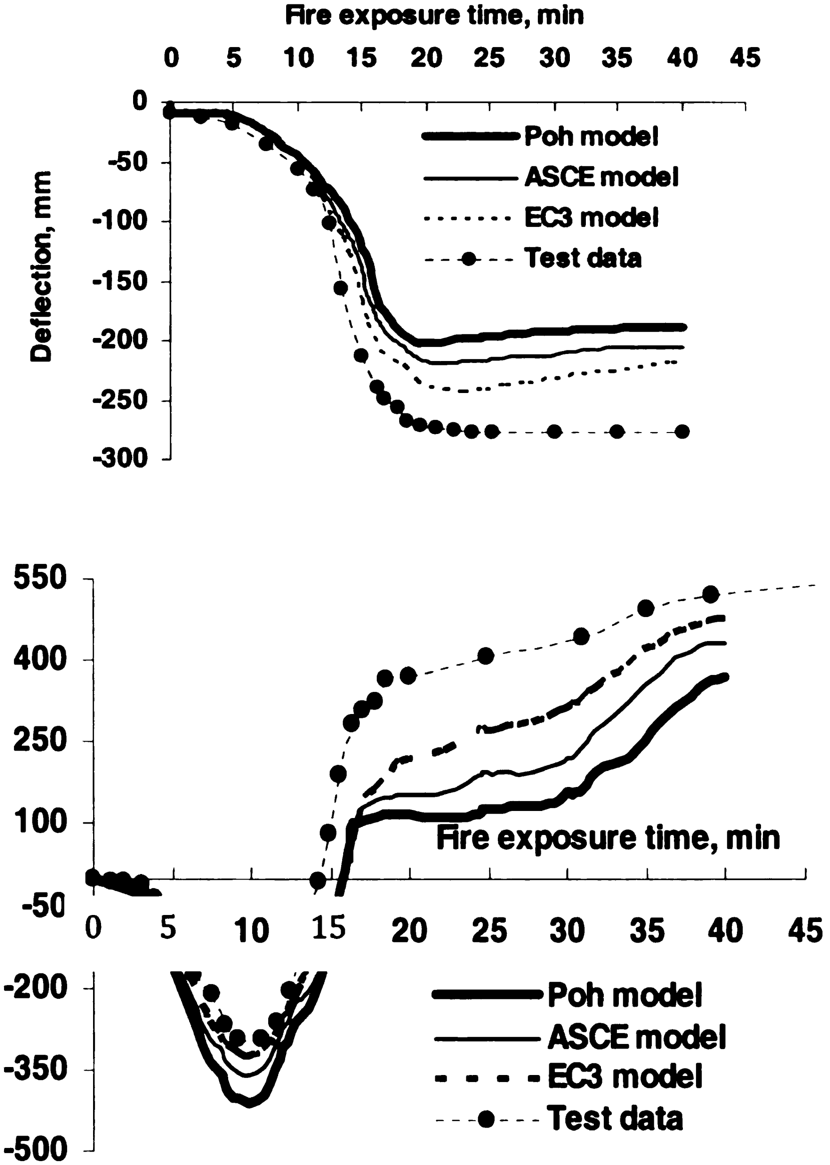

(a,b) Predictions using Poh (2001), ASCE and Eurocode temperature-stress-strain models

Fig. 4.16: Recorded and predicted deflection and restraint force as a function of fire exposure time

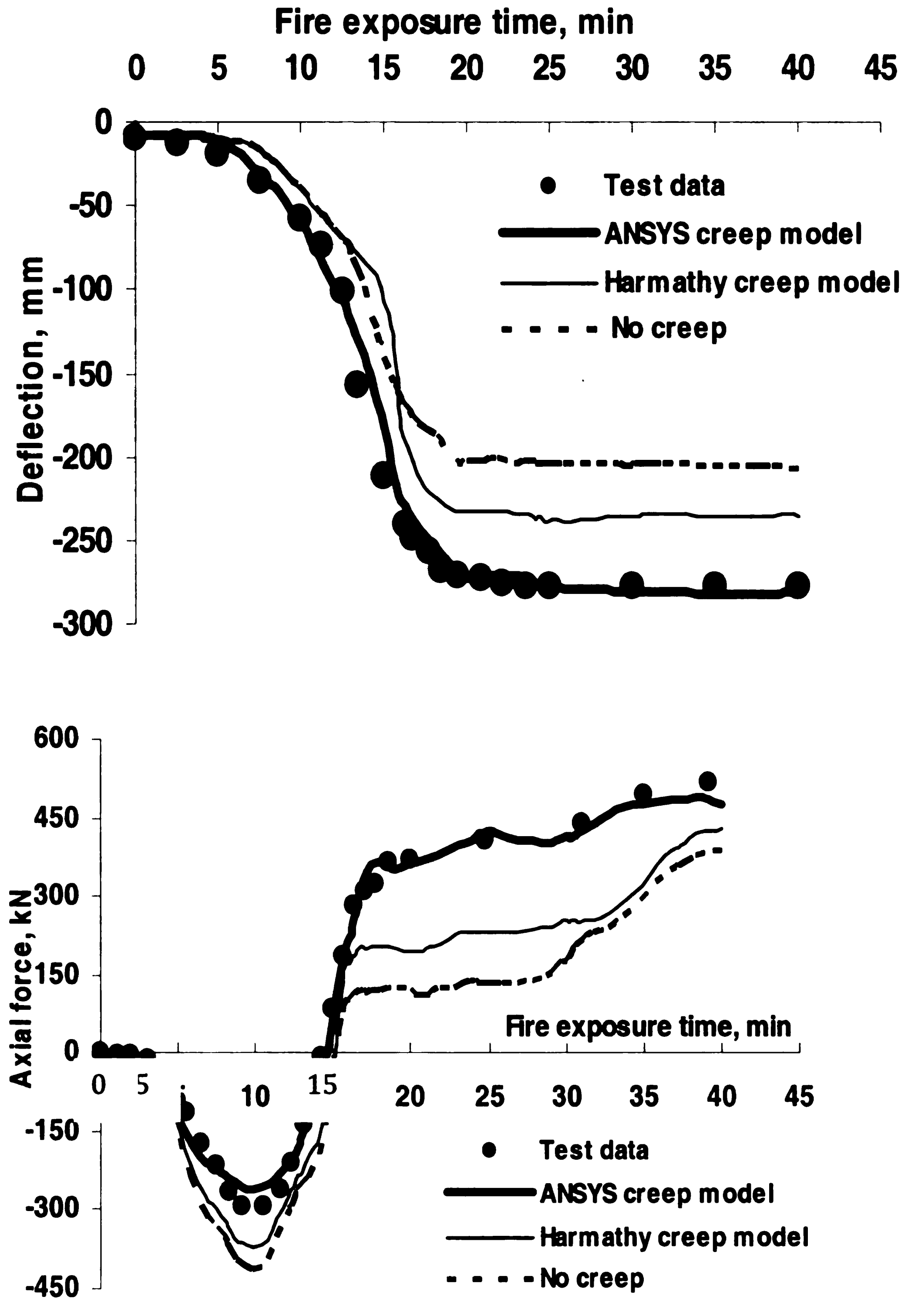

(c,d) Effect of high-temperature creep on predictions (using Poh constitutive model)

Fig. 4.16: Continued

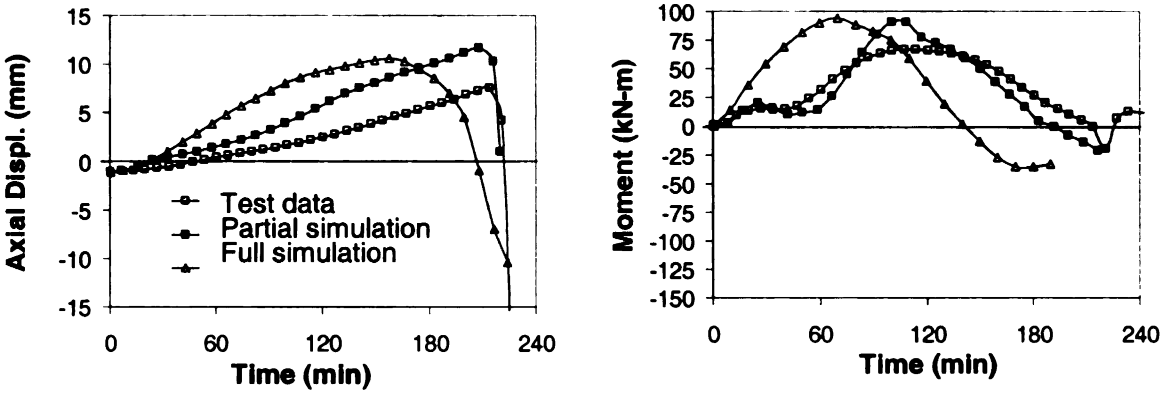

a) Axial deformation *b) Bending moment (at D-D)*

Fig. 4.17: Predicted and measured axial deformation and moment for beam-column C1-S

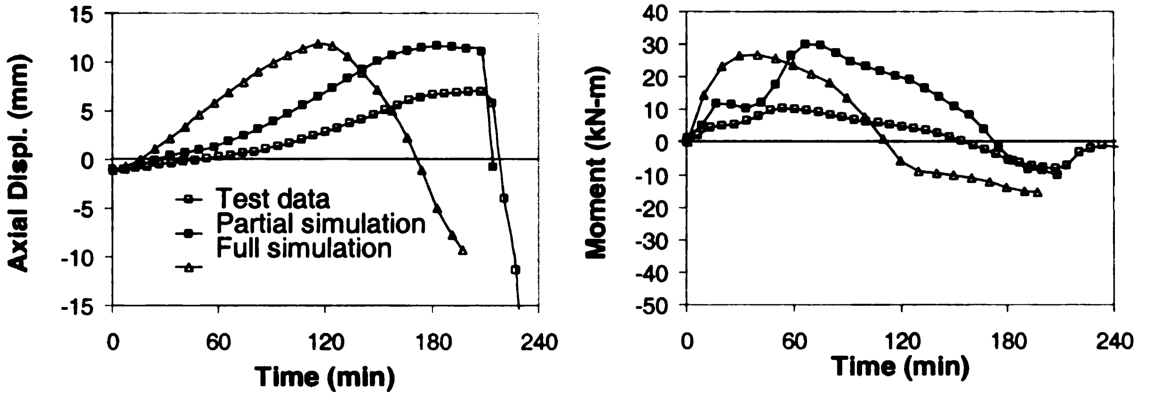

a) Axial deformation *b) Bending moment (at D-D)*

Fig. 4.18: Predicted and measured axial deformation and moment for beam-column C1-W

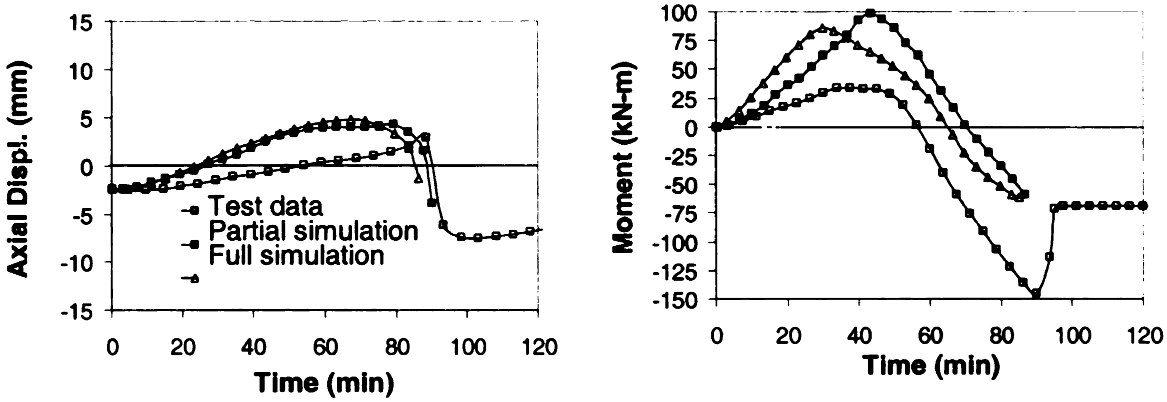

a) Axial deformation *b) Bending moment (at D-D)*

Fig. 4.19: Predicted and measured axial deformation and moment for beam-column C2-S

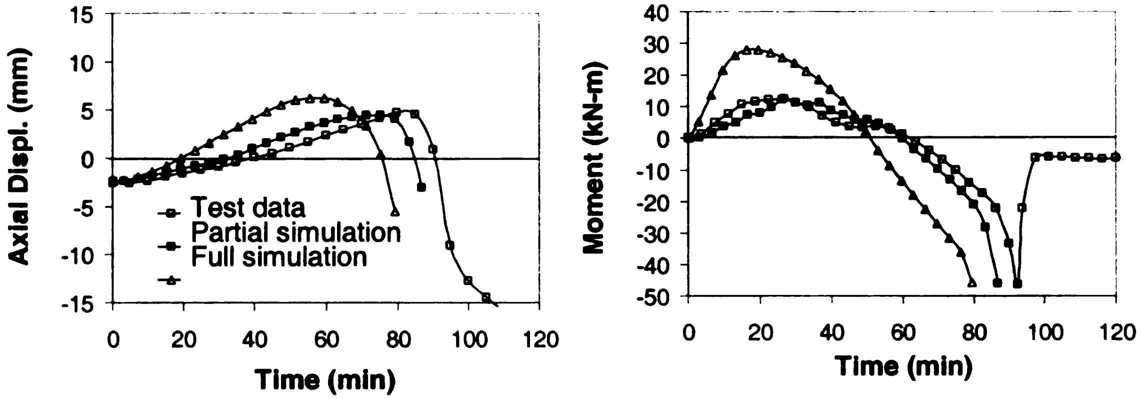

a) Axial deformation *b) Bending moment (at D-D)*

Fig. 4.20: Predicted and measured axial deformation and moment for beam-column C2-W

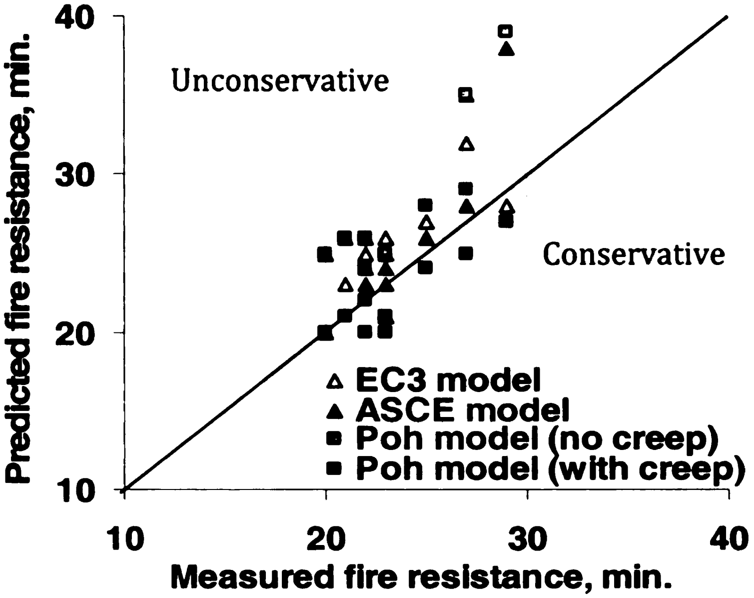

Fig. 4.21: Effect of using different material constitutive models on fire resistance

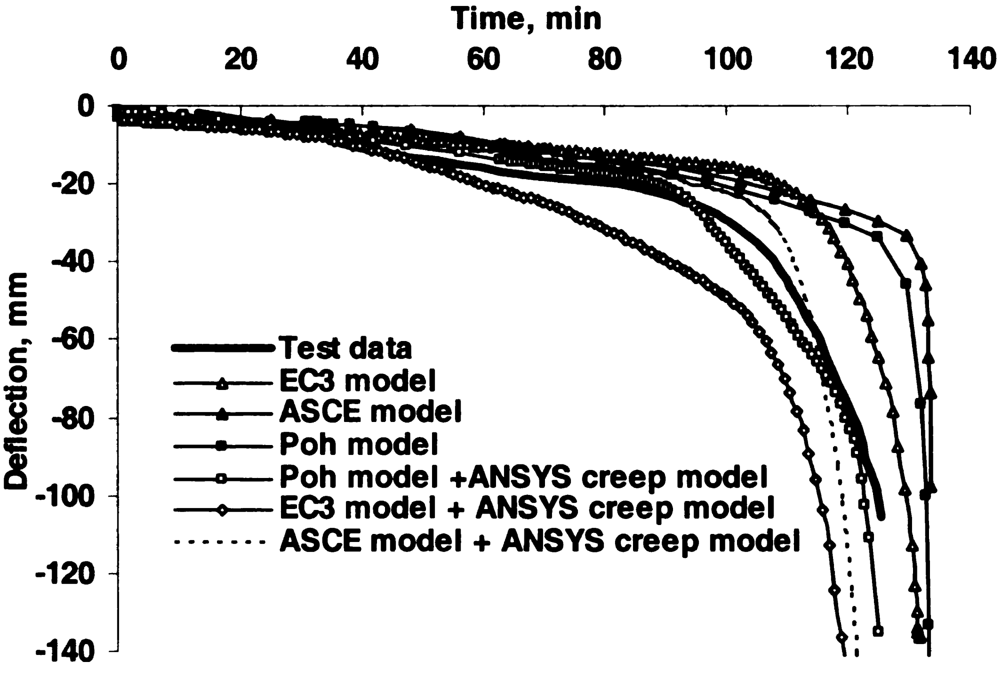

Fig. 4.22: Effect of using different constitutive models on fire response of Beam # 13

CHAPTER FIVE

PARAMETRIC STUDIES

5.1 GENERAL

The numerical model presented in Chapter 4 is applied to study the effect of various parameters on the fire response of restrained steel beams. The varying parameters included: load level, axial and rotational restraint stiffnesses, location of axial restraint force, thermal gradient, and fire scenario.

The fire resistance analysis is generally coupled in one direction, i.e.; the results of thermal analysis affect the structural response, but the effect of structural response on the thermal analysis is neglected. Based on this, in the parametric study, the temperature will be applied on the steel beams without reference to time, i.e. rate-independent monotonic heating. The only exception is when the influence of fire scenario is studied, and thus heating is rate-dependent. In the analysis where heating is rate-independent, the Eurocode high temperature mechanical properties of structural steel are used in the structural analysis. This is because the temperature-stress-strain relationships of steel in the Eurocode partially account for high temperature creep in a form of additional stress-dependent plastic strains. However, in the case where heating is rate-dependent (i.e. in case of exposure to a fire scenario), high temperature mechanical properties as per Poh constitutive model are used in conjunction with ANSYS creep model. The reason for using two different stress-strain curves is to avoid convergence complexities that arise due to the use of high-temperature creep models in the finite element analysis. In all cases of analysis, high temperature thermal properties of structural steel specified in Eurocode are used in the analysis. Results from the parametric studies on the structural fire response of restrained beams are presented in this chapter.

5.2 FACTORS INFLUENCING FIRE RESISTANCE

A state-of-the-art review clearly indicates that several factors govern the fire response of restrained steel beams. It was shown through qualitative parametric studies (Kodur and Dwaikat 2009, Dwaikat and Kodur 2009) that the main factors influencing the fire response of steel beam-columns beams are:

- Load ratio
- Rotational restraint stiffness
- Axial restraint stiffness
- Location of axial restraint
- Thermal gradient
- Fire scenario

Detailed parametric studies were conducted to quantify the influence of each of the above factors on the fire resistance of restrained steel beams and the results are presented in Section 5.4.

5.3 DEFINITION AND RANGE OF PARAMETERS

In this section, the parameters influencing fire response of restrained steel beams are introduced and defined. Realistic range of these parameters is also discussed.

5.3.1 Load Ratio

The load ratio (*LR*) is a measure of stress level in the beam just prior to fire exposure. *LR* is defined as the ratio between the maximum bending moment (*Mmax*) induced in the beam due to gravity load to the unfactored plastic bending capacity of the beam at room temperature, i.e.

$$LR = \frac{M_{\max}}{F_y Z_x} \times 100\% \qquad [5.1]$$

Since fire is a rare incident, the critical load combination is less than the ultimate load used for the room-temperature design of the beams. For a live-to-dead load ratio of 2, the critical load combination at fire conditions reaches 70% of the room-temperature capacity. Therefore, the *LR* was varied from 30% to 70% as shown in Table 5.1.

5.3.2 End Restraints

The end restraint conditions are modeled using spring combinations as was described in Section 4.3.3. The resultant axial and rotational spring stiffnesses of the spring configurations (*Ka* and *Kr*) were varied independently so as to study the influence of both axial and rotational restraint conditions on the fire response. The axial restraint ratio (*AR*) is defined as the ratio between the resultant axial restraint stiffness applied on the beam to the beam axial stiffness, i.e.:

$$AR = \frac{K_a}{E_s A_s / L} \qquad [5.2]$$

In the same fashion, the rotational restraint ratio (*RR*) is defined as:

$$RR = \frac{K_r}{E_s I_x / L} \qquad [5.3]$$

It will be shown through the parametric study that as the value of the applied *AR* and *RR* increases, the change in the fire response of the beam diminishes. For practical cases of steel framed buildings, the value of *AR* and *RR* acting on the beam range between 10% and 20% (Purkiss 2007, Wang 2002). Therefore, the values of *AR* and *RR* that are used in the parametric study were varied according to Table 5.1. The axial and rotational restraints are assumed in this study to be elastic and constant. Also, the restraint stiffnesses are assumed to be invariable with respect to time of fire exposure. This assumption is justified for the cases where the beam-to-column connection and the columns are well insulated against fire exposure, and/or the adjacent frames (to which the beam extends) are not exposed to fire. The real and assumed behavior for the case of rotational restraint for a typical connection is compared in Fig. 5.1. The restrained beam within a framed structure (Fig. 5.1(a)) is idealized to a beam with end restraints as shown in Fig. 5.1(b). As observed in special tests on different connections under fire (Al-Jabri et al. 2005), the rotational stiffness of the connection remains elastic until yielding (or local buckling) occurs in the connection, which in turn causes a reduction in the rotational stiffness of the connection, as shown in Fig. 5.1(d). In case of extended plate shear connections (Fig. 5.1(c)), the rotation increases until the bottom flange of the beam hits the flange of the supporting column and this leads to further increase in the rotational stiffness of the connection, as shown in Fig. 5.1(d). However, in this study, the connection is assumed to be isolated from fire exposure and thus the variation in connection stiffness is not considered. Similarly, the axial stiffness mainly depends on the adjacent frames and supporting columns. If the adjacent frame is under fire, its lateral resistance will deteriorate and the lateral stiffness will decrease, as shown in Fig. 5.1(e and f). However, if the adjacent frames are not under fire, the lateral stiffness will experience minimum variation and thus it can be assumed to be constant with time, as shown in Fig. 5.1(d and f).

5.3.3 Location of Axial Restraint

The literature review revealed that in all previous studies the location of the fire induced axial restraint was assumed to be at the geometrical centroid of the beam. Location of axial restraint force can vary depending on the type and configuration of the connection between the beam and the column. For a simply supported beam, assuming the restraint location to be at the geometric centroid results in the fire induced axial force not generating any moment around the beam center. However, if the location of the axial restraint is not at the centroid of the section, then a significant bending moment might develop at supports due to the eccentricity of the fire induced restraint force. This generated bending moment can affect the response of the beam-column under fire.

The assumption that the line of thrust is along the centroidal axis is valid if the beam-to-column connection is similar to the type shown in Fig. 5.2(a) and the rotation of the connection is not large. If the rotation of the connection is large enough, the bottom flange of the beam will touch the flange of the column and this will generate higher compressive stresses in the bottom flange of the beam. In such a situation, the resultant line of thrust of the axial force will be shifted towards the bottom flange, where stress concentration is large. Other types of connections can cause a shift in the line of thrust of the fire induced axial force. An example is shown in Fig. 5.2(b), where "welded angle seat" connections are used to support the beam. Therefore, the lint of action of the fire induced axial force (at the support section) can vary depending on the connection configuration. For this purpose of study, the location of axial restraint force (y) was varied from zero (centroidal axis) to $d/2$ (parallel to the bottom flange).

5.3.4 Thermal Gradient

Generally fire induced thermal gradients in steel beams (due to 1, 2, or 3-sided exposure) are nonlinear and vary depending on the geometric properties of the cross section and insulation schemes. However, thermal gradients can be approximated linearly without significant loss of their actual influence on the fire response of steel beams (Dwaikat and Kodur 2009). Figure 5.3 shows the linearization of the thermal gradient in steel sections exposed to fire. The average temperature of the top and bottom steel flanges of the section in the linearized thermal gradient profile are computed as follows:

$$T_{top,L} = \frac{T_{av,s} + T_{top,NL}}{2} \qquad [5.4]$$

$$T_{bot,L} = \frac{3T_{av,s} - T_{top,NL}}{2} \qquad [5.5]$$

where the average temperature in the entire section is computed as:

$$T_{av,s} = \frac{\int T_s dA}{\int dA} = \frac{\sum T_{av,i} A_i}{A_s} \qquad [5.6]$$

where *Tav* and *As* are the average temperature and the cross sectional area of the entire steel section, respectively. *Tav,i* and *Ai* are the average temperature and cross sectional area of the *i*-th steel plate of the cross section. The subscripts *NL* and *L* refer to nonlinear and linear temperature profile in the section, respectively. The notations in the above equations are illustrated in Fig. 5.3.

The linearization of thermal gradient is applied on a typical steel section (W24x76) exposed to a standard fire from three sides. The nonlinear and linear thermal profiles are compared in Fig. 5.4(a and c) for case of no insulation applied, and in Fig. 5.4 (b and d) when the section is protected by 1- inch spray applied fire proof material.

The results in Fig. 5.4 show that the maximum thermal gradient can be as high as 150°C between the top and bottom flanges of the section. Also, as seen in Fig. 5.4(d), the linearization of thermal gradient is better approximation in the case when fire protection is applied as compared to unprotected section. It will be shown in the parametric study that using the linearized thermal profile will result in a conservation prediction of fire response.

5.3.5 Fire Scenario

Fire scenarios used for structural fire design are generally grouped under two categories, namely; standard and design fire scenarios. The first type assumes a nearly constant or increasing heat flux from the fire to the exposed structural elements throughout the duration of fire exposure, while the second type represents an increasing heat flux first and then a decreasing heat flux from the fire to the structural members, and thus gradual reduction of fire temperature after achieving a maximum value. The first type of fires requires continuous supply of fuel and oxygen, while the second type can be either fuel or ventilation controlled or both. In this study, the first type of fire is represented by ASTM E119 standard fire curve, while for the second type of fires scenarios; the parametric fire curves specified in Eurocode 1 (EC1 2005) are used. ASTM E119 scenario, which does not have a decay phase, represents a baseline case for comparing the response of the steel beam under different fire scenarios. Two parametric fires will be used; fire scenario I, representing a severe fire condition compared to ASTM E119, and fire scenario II, representing a mild fire severity. The time-temperature curves for the three fire scenarios are shown in Figure 5.5. The time-temperature curves of fire scenarios are assumed to include the effect of heat radiation and convection from the ambient air and surrounding walls of the compartment. It is beyond the scope of this study to investigate the development of these fire scenarios.

The design fires, I and II, were selected to represent different cases of fire severity. Fire I represents a typical fire scenario that can occur in a compartment with the following characteristics: Total area of compartment = 320m2, opening area = 10 m2, floor area =100m2, average opening height = 1.5m, thermal inertia "*b* factor" = 500 J/ m2s0.5K, fire load density = 500 MJ/ m2. For the mild fire scenario (fire II), the same compartment characteristic (of fire I) were assumed with the only change is in the value of thermal inertia "*b*" factor, changed to 1500 J/ m2s0.5K. The thermal inertia factor "*b*" is a measure of how much heat is absorbed by the compartment boundaries, and this is dependent on the thermal properties of the material of walls, ground, and ceiling (Buchanan 2002). Smaller values of "*b*" indicate that smaller amount of fire generated heat flux is absorbed by the boundaries, and thus, greater amount of heat flux goes to increasing the temperature of the atmosphere of the compartment, and hence increasing the fire severity.

5.4 RESULTS OF PARAMETRIC STUDY

Results from the parametric studies are presented in Figures 5.6 to 5.16 where time-deflection (or temperature-deflection) curves for the analyzed beams are plotted in addition to the fire-induced axial force. The effect of the studied parameters on the thermal response of the beam is not presented here because many of these parameters such as load ratio and restraint conditions do not influence the thermal response of the beams. The effect of each of the parameters on the fire response is discussed bellow.

5.4.1 Effect of Load Ratio

To investigate the effect of load on fire resistance, the beams were analyzed under three load ratios, namely, LR = 30%, 50% and 70%. Figure 5.6 shows the effect of load ratio on the response of a simply supported beam exposed to uniform temperature. Generally, higher load ratio results in higher deflection, and this is due to higher stresses developed the beam prior to fire exposure, and this causes earlier spread of plasticity in the beam compared to the cases with lower load ratio.

The influence of load ratio on the response of restrained steel beam is presented in Fig. 5.7. The fire induced axial force, due to restraint effect (shown in Fig. 5.7(b)) has a direct influence on the midspan deflection as shown in Fig. 5.7(a). Since the beam is restrained form expanding, compressive axial force develops in the beam, and this causes a reduction in the overall geometric stiffness of the beam. Also, as the axial force increases, the stresses in the beam increase until plasticity is initiated in the beam and this occurs at the moment of the peak value of the compressive fire restraint force. Plasticity causes a severe reduction in the beam stiffness which leads to higher deflection that in turn leads to increased midspan bending moment due to increased P-delta effect on the beam. This continues until the deflection in the beam is so large that the fire induced force switches from compression to tensile force. The peak value of the fire induced force is smaller for higher load ratios. Since this peak value of the restraint force corresponds to the initiation of plasticity in the beam (no local buckling in elastic range), the beam with higher load ratio (higher initial stress level prior to fire) will experience plasticity at earlier stages of fire exposure.

As expected, higher load levels produce larger downward deflections in the restrained steel beam. On the other hand, the detrimental compressive axial force, which develops due to thermal expansion of the steel beam, reduces with the increased load level. However, the increasing load level produces larger deflection, which makes the beam go into catenary action at earlier stages of fire exposure. Hence higher tensile forces develop in the restrained steel beam under catenary action as the load level is increased.

5.4.2 Effect of Rotational Restraint

To investigate the effect of rotational restraint on the fire resistance, the beams were analyzed under four rotational restraint ratios, namely, *RR* = 0, 10%, 30% and infinity. Two sets of results are presented here, first set is for beams with no axial restraint (*AR* = 0), while the second set of results is for beams with *AR* = 10%. Results from two cases are plotted in Fig. 5.8 and 5.9, respectively, as function of steel temperature.

The increase in rotational restraint leads to a change in the shape of room-temperature bending moment diagram. To compensate for this change in bending moment along the span of the beam, the value of the actual applied load (*w*) was varied such that load ratio (*LR*) remains constant under different rotational restraint ratios (*RR*). For the two sets of results shown in Fig. 5.8 and 5.9, the load ratio was maintained at 50%.

The results shown in Fig. 5.8 indicate that higher rotational restraint ratio leads to improved performance under fire. This can be attributed to the fact that higher rotational restraint stiffness leads to greater overall stiffness of the beam. The results also show that it requires small value of rotational restraint (*RR* = 30%) to cause a significant improvement in fire response.

The effect of increasing rotational restraint on the fire response of axially restrained beam is shown in Fig. 5.9. Similar to the trend of results in Fig. 5.8, the improvement of fire response is also observed in the results plotted in Fig. 5.9. The occurrence of local buckling in the post-yield stage in the bottom flange of the support section slightly affects the response of the rotationally restrained beams as shown in Fig. 5.9(a). The increase in *RR* does not affect the fire induced axial force in the elastic range, however, higher values of *RR* lead to lower tensile catenary forces in the beam, as seen in Fig. 5.9(b). For small values of *RR*, the failure mode in the beam results from a combination of tensile and flexural failures. However, as the value of *RR* increases, the failure mode becomes more related to flexure and the beam fails by developing simultaneous plastic hinges at midspan and support sections, rather than by reaching full tensile capacity as in the case of a beam with axial restraint only, as it will be described in the following section.

5.4.3 Effect of Axial Restraint

Figure 5.10 shows the mid-span deflection of a restrained beam as a function of fire exposure time for different values of axial restraint (*AR*) stiffness, i.e. *AR* = 0, 10%, 30%, and infinity. The *AR* was varied for two cases, first with no rotational restraint (*RR* = 0), and second with *RR* = 25%.

It can be seen in Fig. 5.10 in the elastic range of fire response, increasing *AR* leads to insignificant increase in midspan deflection as seen in Fig. 5.10(a). However, with the buildup of compressive force, as shown in Fig. 5.10(b), plasticity starts to spread in the section and larger deflection is induced in the beam by higher values of *AR*. The increased deflection in this stage is mainly attributed to softening of steel, P-delta effect, and the negative influence the compressive fire induced axial force on the flexural stiffness of the beam. Despite the relatively larger midspan deflection in the beam that is caused by increasing *AR*, the ultimate bearing capacity of the restrained beam is greatly enhanced due to restraint effect as seen in Fig. 5.10(a). This enhanced response is mainly due to the development of tensile catenary action which leads to increased overall stiffness of the beam. Similar pattern of the influence of *AR* on the rotationally restrained beams is observed in the results plotted in Fig. 5.11.

The plastic tensile capacity profile of the beam (*ky(T)* × *Fu* × *As*) is also shown on figures that plot the fire induced axial force as a function of fire exposure time. This profile represents the maximum tensile axial force that can possibly be attained by the beam. As shown in Fig. 5.10(b), the beams failed when the fire induced axial force almost reached the maximum plastic axial capacity of the beam (*ky(T)* × *Fu* ×

As). In the case of rotationally unrestrained beams (*RR* = 0, Fig. 5.10), the development of plastic hinge in the mid span of the beam did not cause failure and the load bearing mechanism changed from flexural to cable mechanism. And therefore, failure occurred in the beams when the catenary tensile force reached the maximum plastic axial capacity of the beam (*ky(T)* × *Fu* × *As*). However, in the case of rotational restrained (*RR* ≠ 0, Fig. 5.11), the failure occurred before developing full plastic tensile capacity of the beam in the catenary phase. This is because for rotationally unrestrained beam, strength failure requires the development of three plastic hinges simultaneously. The strength failure of these rotationally restrained beams occurred when the combined effect of tension and bending (on the support section) exceeded the combined plastic axial and moment capacity of the section.

It is worth noting that in both cases (Fig. 5.10 and 5.11) the occurrence of local buckling has minor influence on fire response of the restrained beams. The occurrence of local buckling leads to either a slight increase in the midspan deflection, or a change in the rate of deflection due to localized reduction of flexural rigidity of the beam near support. Also, occurrence of local buckling leads to a drop in the fire induced axial force due to relaxation effect. As repeatedly observed in fire tests and actual fire incidents (discussed in Chapters 2 and 3), occurrence of local buckling at the bottom flange of the beam near support does not lead to failure in the restrained beams.

5.4.4 Effect of Location of Axial Restraint

To investigate the influence of varying the position of fire induced axial restraint force on the response of beams; the location of axial restraint force was varied from the mid-height of the web ($y = 0$) to the mid-height of the bottom flange ($y = d/2$). Two sets of results are presented in Fig. 5.12 and 5.13; first set is for uniform heating, while the second is for a linear thermal gradient of 200°C.

Trends of results in Fig. 5.12(a) indicate that the fire response of a restraint beam improves when the axial restraint is located at the bottom flange (case $y = d/2$). The improvement in fire response can be attributed to the development of additional hogging moment at the support of the beam ($P \times y$). The hogging moment leads to a reduction in the total moment in the mid-span of the beam, and thus, enhances the response of the beam. This is illustrated in Figs. 5.14 which show the development of thermal gradient and restraint force for mid-span and support sections in the beam exposed to fire. When the beam is exposed to fire from three sides (top side is unexposed), the bottom-half of the steel section will experience higher temperatures as compared to the top-half of the section. This leads to higher expansion in the bottom-half as compared to the top-half of the section, leading to the development of large axial restraining force (P). This fire induced axial force generates a counter-moment at the support ($P \times d/2$) that opposes the sagging moment ($MGravity + MP\text{-}\ \delta$) at the mid-span of the beam as shown in Fig. 5.14. This leads to a reduction in the total moment in the mid-span, and therefore, enhances the fire resistance of the beam. However, when the deflection of the beam becomes large, the mid-span moment ($MGravity + MP\text{-}\ \delta$) becomes very large (due to increased P-δ effect) as compared to the moment due to fire induced force ($P \times d/2$), therefore, the improvement due to the shift of the axial restraint is diminished.

Local buckling occurs in the bottom flange for the case $y = d/2$, as indicated in Fig. 5.12(b), and this is due to the concentration of stresses in the bottom flange due to restraint effect. The occurrence of local buckling leads to a reduction in fire induced compressive force, but the overall fire response is marginally affected by the occurrence of local buckling.

In the case of the beam with thermal gradients, better improvement in fire response is observed as shown in Fig. 5.13(a). Thermal gradient leads to higher expansion in the bottom-half of the section, as compared to the top-half. Therefore, larger fire induced axial restraining force (P) is generated in the beam for the case of $y = d/2$ as compared to the case of $y = 0$. While thermal gradient caused relatively larger elastic deflection in the beam with $y = 0$, thermal gradient caused an upward "*bowing effect*" for the beam with $y = d/2$, as seen in Fig. 5.13(a). However, due to the development of high compressive stress in the bottom flange (case of $y = d/2$), local buckling occurs at post-yield (Fig. 5.13(b)) and this causes a sudden increase in the midspan deflection with a corresponding drop in the fire induced axial force.

5.4.5 Effect of Thermal Gradient

In order to study the influence of thermal gradient on the fire response of restrained steel beams, thermal gradients are applied on the beam. Two values of thermal gradient were used: zero and 200°C and the average temperature of the beam was maintained constant throughout the analysis The structural parameters of the restrained beam and the results of the analysis are shown in Fig. 5.15.

Results show that that increasing thermal gradient leads to increased elastic deflection of the beam, as shown in Fig. 5.15(a). This can be attributed to the fact that thermal gradient leads to the generation of additional thermal curvature in the beam, and this additional curvature increases the midspan deflection of the beam. Since the average temperature in steel was maintained constant during all the three cases of analysis, small variations in fire induced compressive force were observed, as seen in Fig. 5.15(b).

However, the influence of thermal gradient on the elasto-plastic deflection of the beam is less pronounced. This can be attributed to the fact that once yielding spreads in the beam, the rotational stiffness of the beam will reduce and thus thermal curvature will leads to smaller deflection in the beam.

5.4.6 Effect of Fire Scenario

To study the influence of fire scenario on restrained beam response, three types of fire exposures were selected for analysis, namely: ASTM E119 standard fire, design fire I and design fire II. Typical steel beam, with characteristics shown on Fig. 5.16(b), is subjected to the three fire scenarios whose time-temperature curves are shown in Figure 5.5. The beam has 15 mm spray-applied fire proof insulation and is exposed to fire from 3 sides, with concrete slab on top of the beam. The thermal properties of steel and concrete are assumed to follow Eurocode and the physical and thermal properties of insulation are as presented in Chapter 4. For the structural analysis, high temperature mechanical properties of structural steel as per Poh constitutive model (2001) and ANSYS high temperature creep model are used in the analysis.

Figure 5.16 shows the temperature in steel section due to exposure to the three fire scenarios. The results show that a maximum of 200°C thermal gradient between the top and bottom flanges of the beam had developed in the beam due to the three side fire exposure. Factors affecting the development of such thermal gradients include the depth of the steel beam and the presence of concrete slab which acts as a heat sink for the beam. In the case of a standard fire exposure (Fig. 5.16(a)), the thermal gradient in the beam reduces as fire progresses. This can be attributed to the fact that the steel beam tends towards thermal equilibrium as fire progresses. The plateau that occurs at steel temperature between 750-800°C (Fig. 5.16(a)) is attributed to the phase change that occurs to the structural steel and this process absorbs a considerable amount of heat. In the case of design fires (Fig. 5.16 b and c), the maximum average temperature in steel generally occurs during the cooling phase of the fire. This is mainly attributed to the thermal lag effect and redistribution of heat inside the steel section in addition to the influence of heat stored in the insulation. Thermal gradient reduces after achieving maximum temperature in steel and then it reverses direction. This reversal of thermal gradient can be attributed to many factors including the redistribution of heat due to two dimensional heat conduction in the steel section, the effect of concrete slab, which will supply the top flange with heat as it cools down (reverse of heat flux direction), and the effect of insulation in slowing down the heat dissipation.

The
as n
anal
the
para
resu
scer
but
def
to
Th
sta
la
pr
hi
fi
L
b
g
p
t
s
e

The results of thermal analysis (from each fire scenario individually) were applied as nodal temperatures on the structural mesh of the restrained beam. Structural analysis is carried out to investigate the influence of fire scenario on the response of the restrained. The results of the structural analysis as well as the structural parameters of the analyzed beam are shown in Fig. 5.17. It can be seen that the resulting mid-span deflection and the axial restraint force are dependent on the fire scenario. The restrained beam experiences run away failure under ASTM E119 fire, but no failure occurs in the beam under design fire scenarios. The midspan deflection of the beam is larger under the growth phase of design fire I as compared to the midspan deflection under ASTM E119 or design fire II as seen in Fig. 5.17(a). This is because the growth phase of design fire I is more severe than the ASTM standard fire or design fire II, and this leads to rapid increase in temperature and larger thermal gradients, and thus faster degradation of steel strength and stiffness properties. For a similar reason, the fire induced compressive force in the beam is higher when it is exposed to design fire I as compared to when exposed to design fire II, as shown in Fig. 5.17(b).

Local buckling occurred in all fire exposures, with earlier occurrence of local buckling under design fire I, and this is reasonable because of higher thermal gradient and temperatures under design fire I which leads to earlier spread of plasticity in the beam as compared to exposure to other fire scenarios. While the beam failed under ASTM E119 fire exposure, the beam survived the two design fire scenarios, but with the maximum attained deflection in the beam occurring under exposure to design fire II, as shown in Fig. 5.17(a). This can be attributed to the fact that the beam under design fire II experienced slow cooling as compared to design fire I. By referring to Fig. 5.16(b and c), beam under design fire II sustained an average temperature above 500°C for more 70 minutes (between 40-110 min.), while the beam under design fire II sustained temperature above 500°C for almost 40 minutes (between 30–70 min.). Therefore, in case of exposure to slow heating process (such as design fire II), the spread of plasticity and the influence of high temperature creep have a major effect on the fire response of the restrained steel beams.

The effect of cooling phase in design fire is also shown in Fig. 5.17(b), where the tensile force (due to catenary action) increases when the beam enter the decay phase of design fire, as seen in Figure 5.17(b). This is because steel regains much of its strength upon cooling (as a result of decay phase in design fire I & II), and starts to contract in cooling phase. In the case of ASTM E119 standard fire scenario, deflection continues to increase with temperature due to the absence of decay phase until the beam enters a catenary action phase at around 60 min. into fire exposure (see Fig. 5.17(b)). The tensile force that develops in the beam due to the catenary action results in an improvement in response. However, due to the continuous deterioration of the strength and stiffness properties of steel and due to the increasing influence of high temperature creep, deflection of the beam continues to increase until the full tensile capacity of the beam is exhausted at around 93 min. into fire exposure. In case of a design fire, the tensile force that results from catenary action (that results due to large deflection) leads to improvement of fire response as seen in Fig. 5.17(a and b). Also, fire response of restrained beam is further enhanced due to the tensile force that develops due to the shrinkage of steel in the cooling phase.

5.5 SUMMARY

This chapter presents the influence of various factors on the fire response of restrained steel beams. The studied parameters are: load level, axial and rotational restraint stiffnesses, location of axial restraint force, thermal gradient, and fire scenario. Data from parametric studies indicates that fire scenario, load ratio, and end restraints have significant influence on the fire response of restrained steel beams. Increasing load level leads to earlier deterioration of fire response of steel beams. Axial restraint leads to increased deflection at early stages of fire exposure; however, at later stages of fire exposure, the response of steel beams is significantly improved due to the effect of axial restraint. Increasing rotational restraint leads to improved fire response of a steel beam since rotational restraint helps redistribute the bending moment in the beam. While restrained beams always fail under standard fire exposures, design fires result in recovery of strength, stiffness, and deflection of the restrained beam as a result of the cooling phase, and thus improved fire response. Data from parametric studies also showed that thermal gradient, location of restraint force have a minor effect on the fire response of restrained steel beams. While thermal gradient leads to a slight increase in midspan deflection, the location of axial restraint force leads to a counter bending moment at the support which leads to a slight improvement in fire response. Results from the parametric studies are utilized in Chapters 6 and 7 to develop guidelines for evaluating fire resistance of restrained steel beams.

Table 5.1: Characteristics of the beams used in parametric study of finite element analysis

Parameter	Values	Comments
Load ratio (*LR*)	30%, 50%,70%	$LR = M_{\max} / (F_y Z_x)$
Thermal gradient (ΔT)	0°C, 200°C	$\Delta T = TTF - TBF$
Fire scenario	ASTM E119, Severe (Fire I), Moderate (Fire II)	--
Location of restraint	0, *d/2*	Measured downward form the centroid of the section
Axial restraint ratio (*AR*)	0, 10%, 30%, and infinity	Relative to room-temperature beam stiffnesses
Rotational restraint ratio (*RR*)	0, 10%, 30%, and infinity	

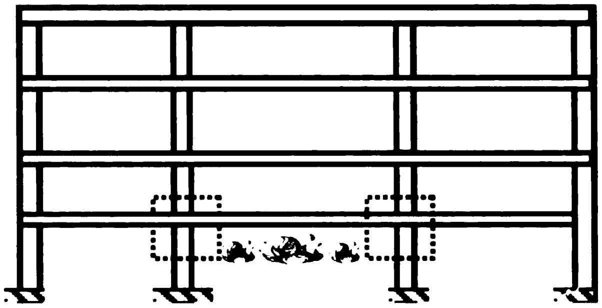

(*a*) Layout of typical Steel frame

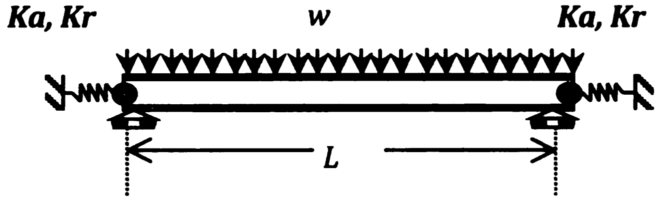

(b) Beam with idealized restraints

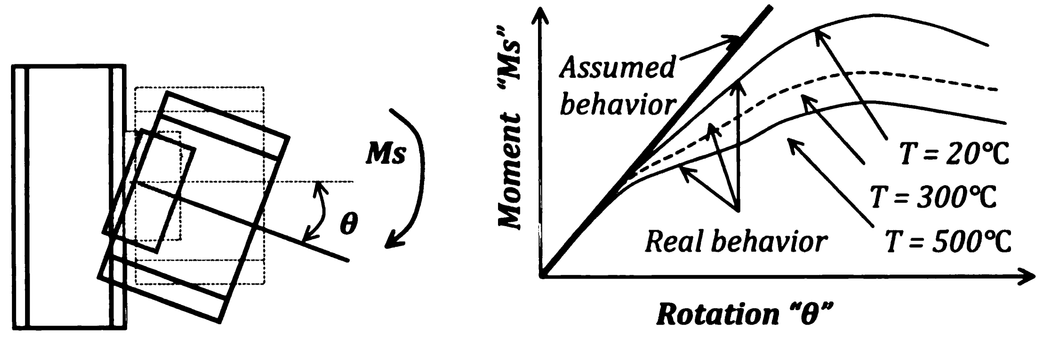

(c) Idealized rotation of connection

(d) Variation of M-θ curves with temperature of connection

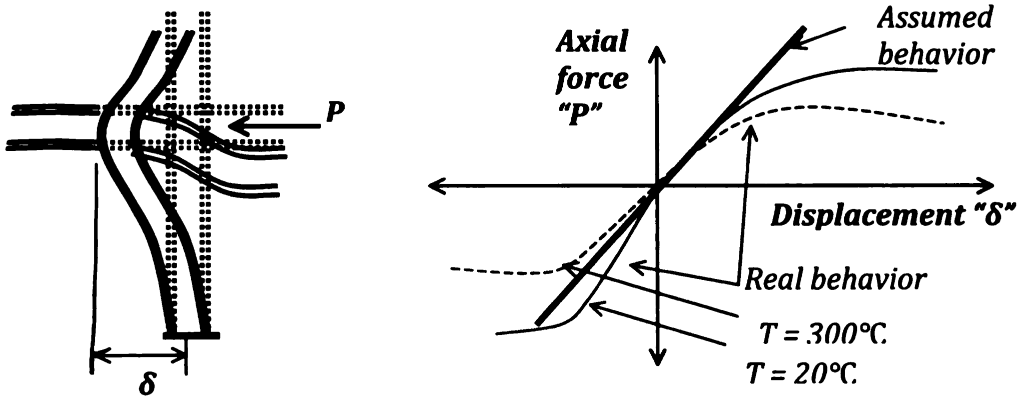

(e) Idealized lateral displacement

(f) Variation of P-δ curves with temperature of adjacent frame

Fig. 5.1: Assumed and real behavior of restraint stiffnesses in restrained beams

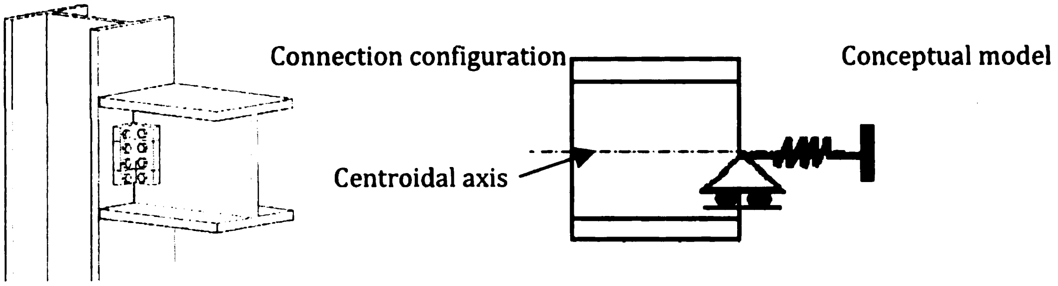

(a) Single plate shear connection.

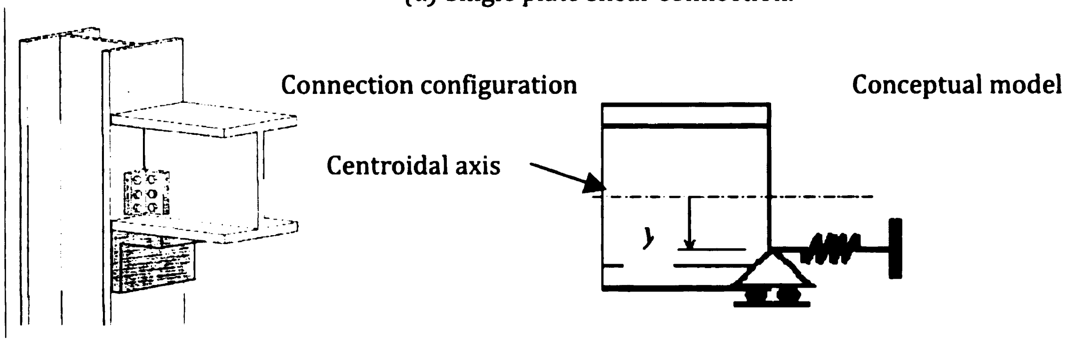

(b) Welded angle seat connection.

Fig. 5.2: Connection types and location of axial restraint in steel beams

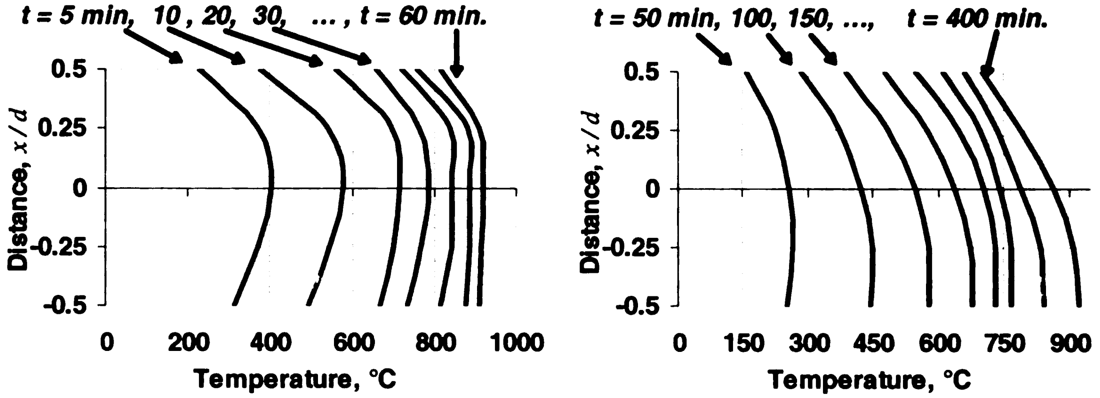

a) Unprotected steel section

(b) 1-inch insulation thickness with concrete slab on top

Nonlinear thermal gradient in the steel section

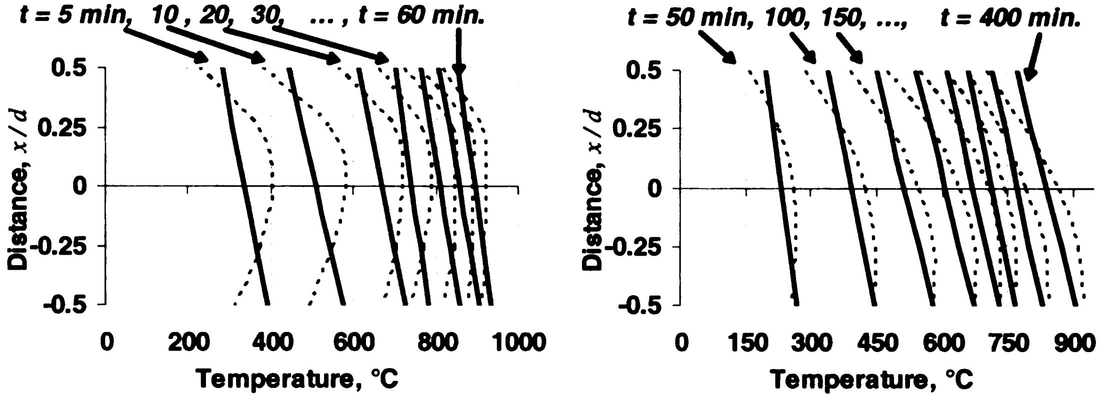

c) Unprotected steel section

(b) 1-inch insulation thickness with concrete slab on top

Linearized thermal gradients for unprotected section

Fig. 5.3: Comparison between nonlinear and linearized thermal gradients in restrained steel beams

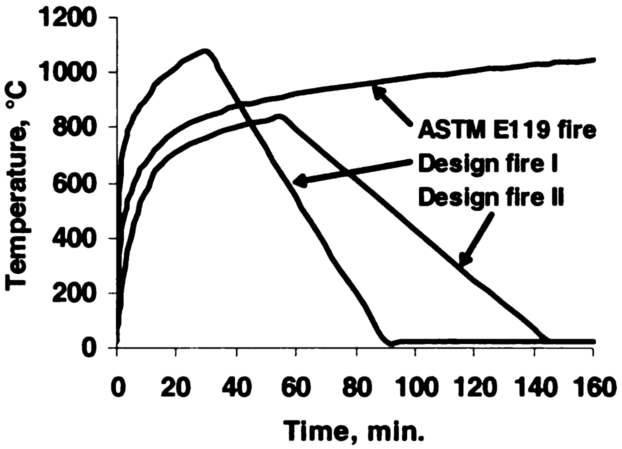

Fig. 5.4: Time-temperature curves for the selected fire scenarios

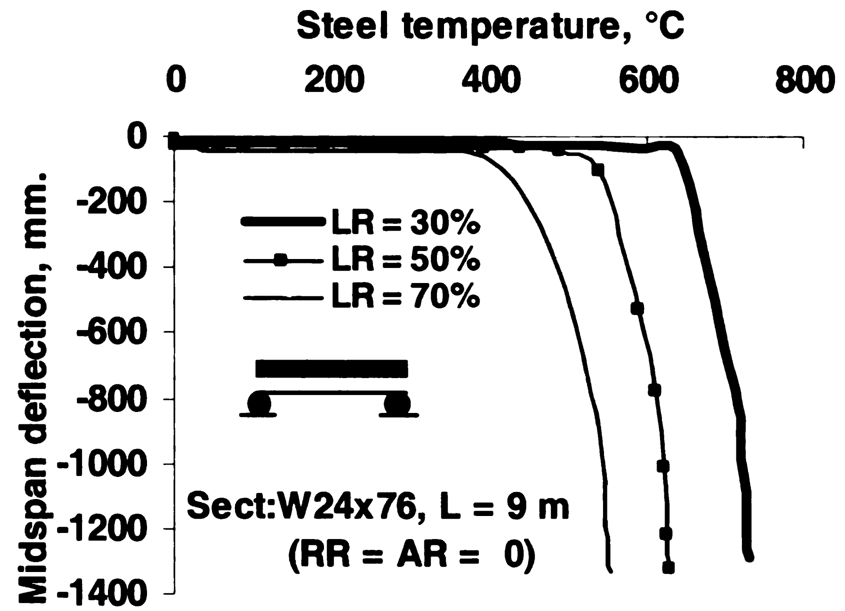

Fig. 5.5: Effect of load ratio on response of simply supported steel beam exposed to uniform heating

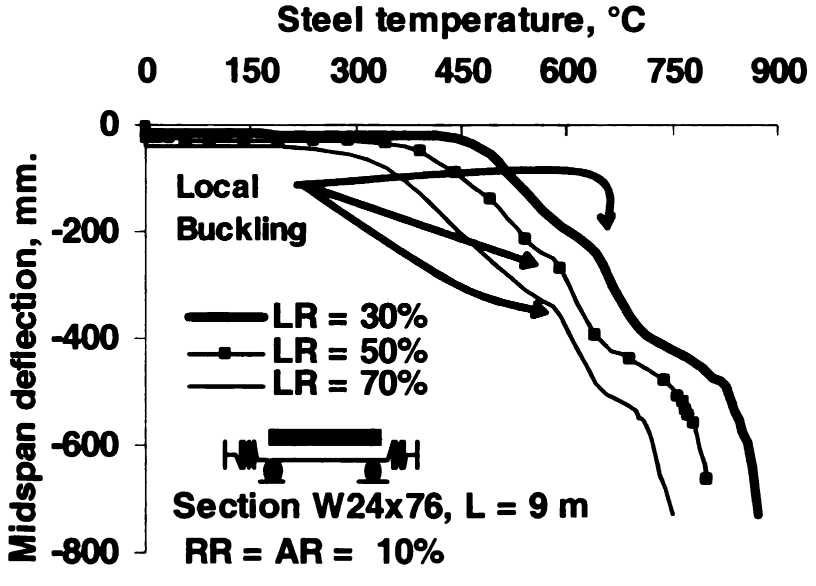

a) Midspan deflection

Fig. 5.6: Effect of load ratio on response of restrained steel beam exposed to uniform heating

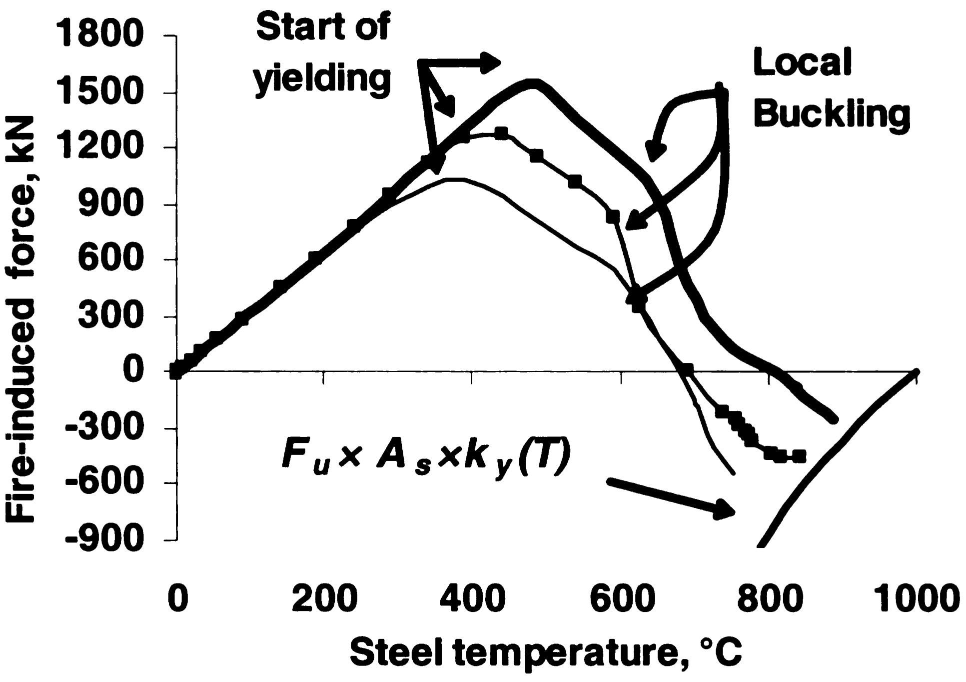

b) Fire-induced axial force

Fig. 5.6: Continued

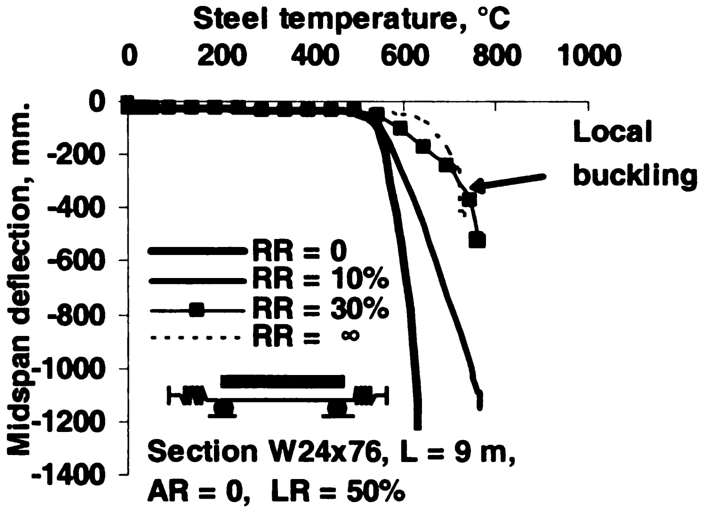

Fig. 5.7: Effect of rotational restraint on response of axially unrestrained beam under uniform heating

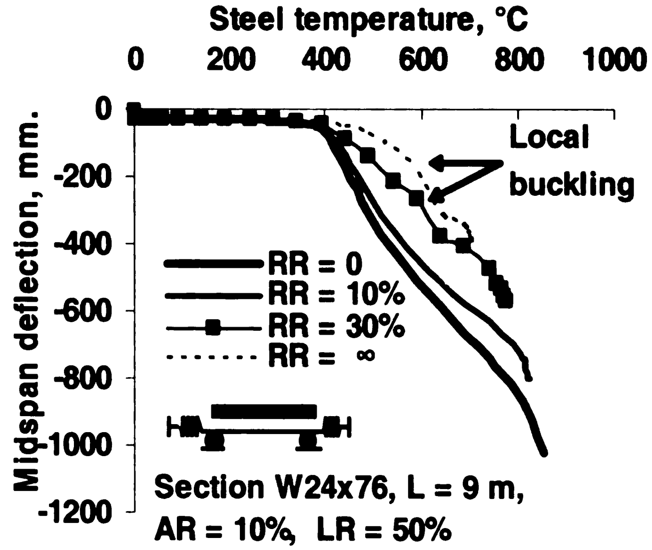

a) Midspan deflection

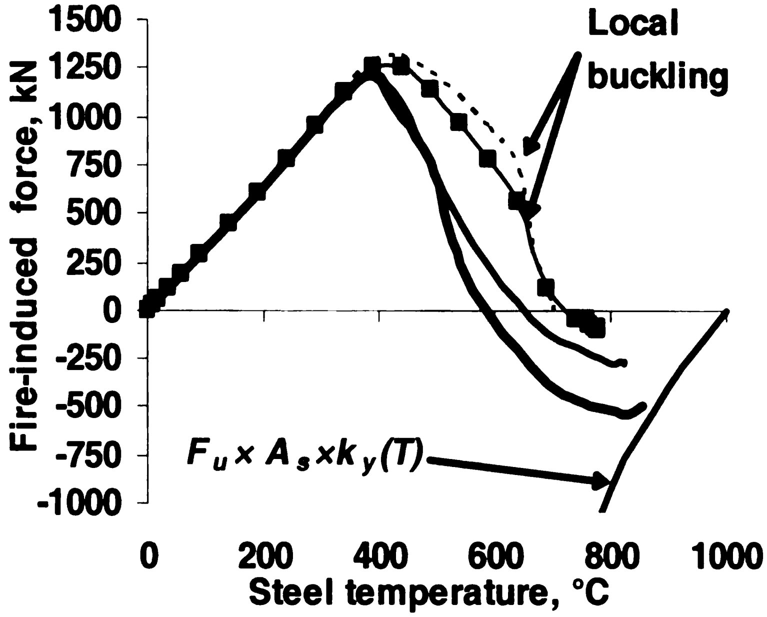

b) Fire induced axial force

Fig. 5.8: Effect of rotational restraint on response of axially restrained beam under uniform heating

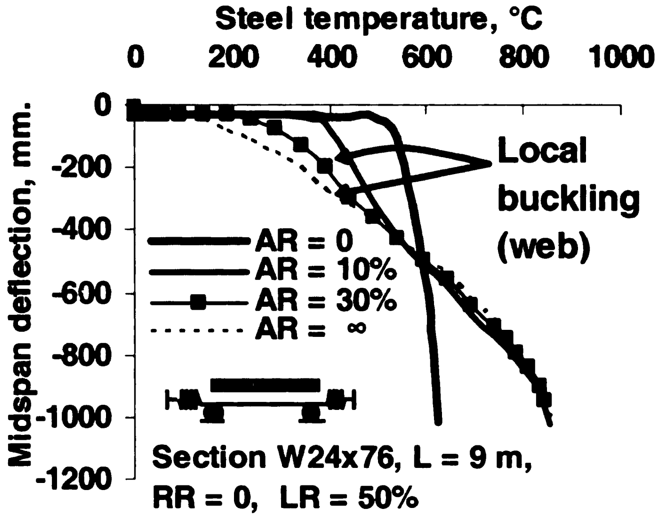

a) Midspan deflection

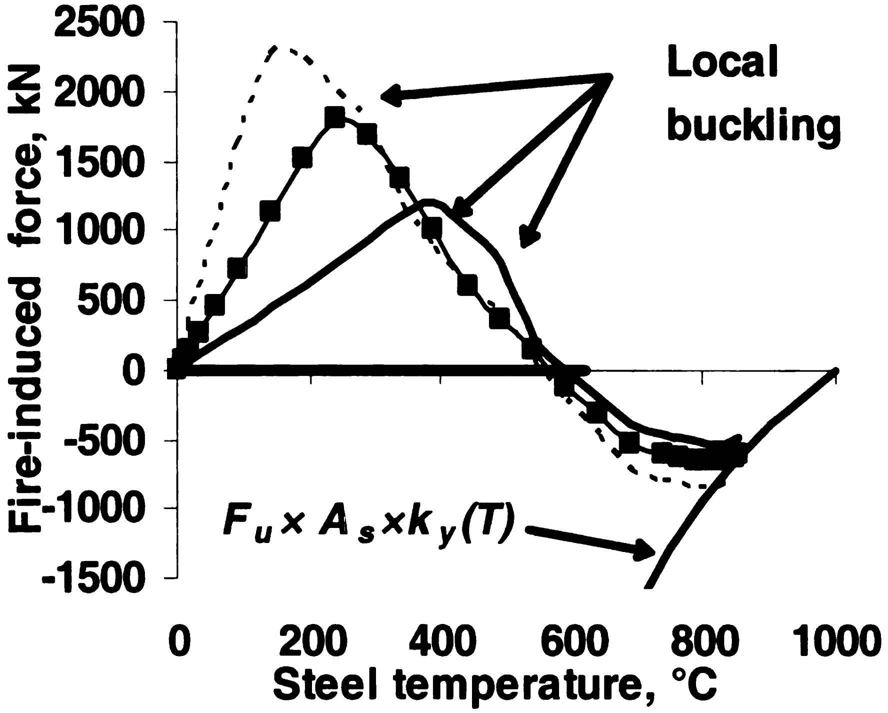

b) Fire induced axial force

Fig. 5.9: Effect of axial restraint on response of rotationally unrestrained steel beam under uniform heating

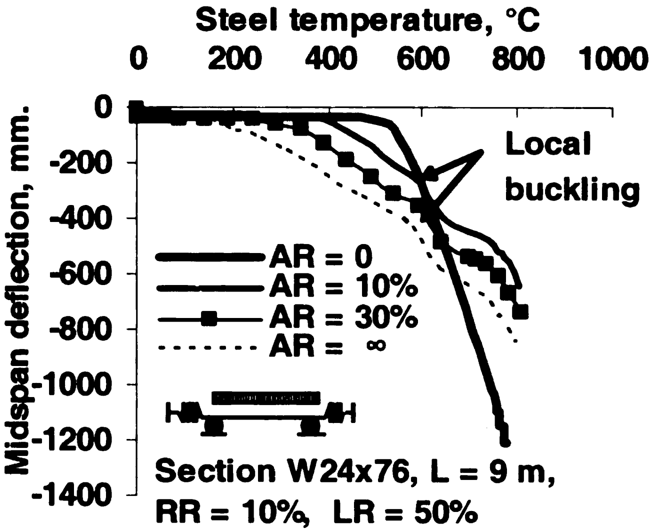

a) Midspan deflection

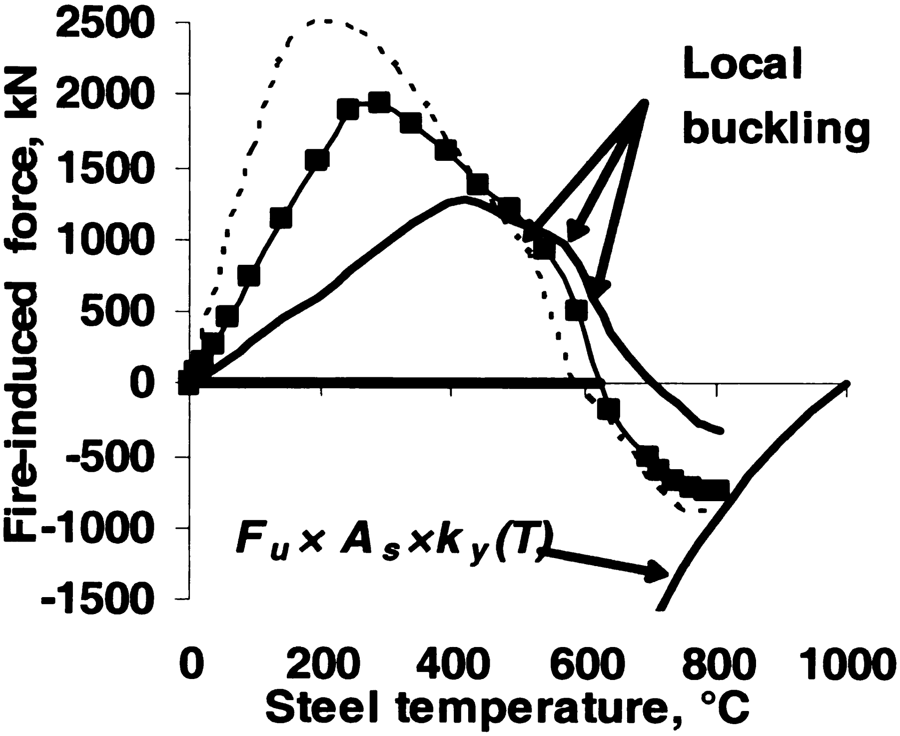

b) Fire induced axial force

Fig. 5.10: Effect of axial restraint on response of rotationally restrained steel beam under uniform heating

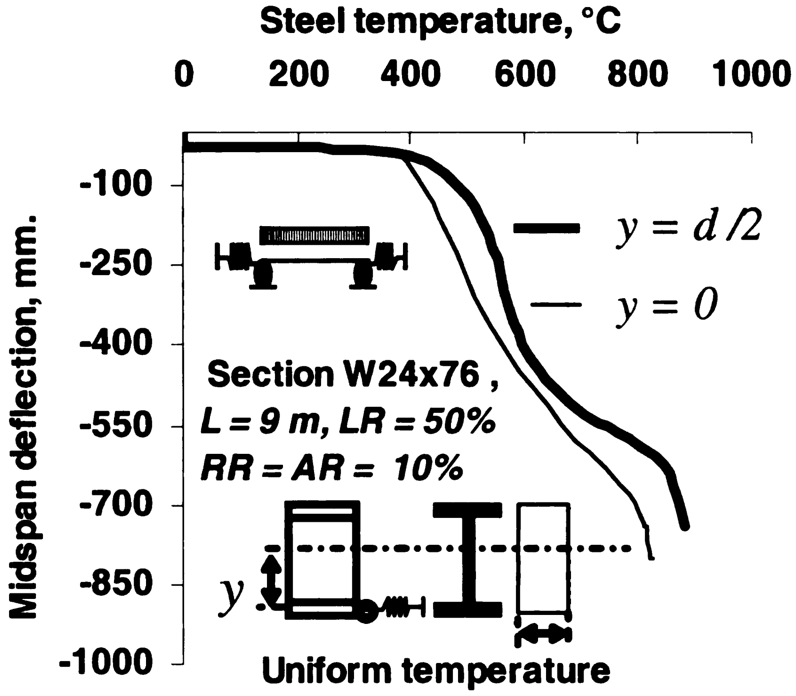

Fig. 5.11: Effect of location of axial restraint on the response of uniformly heated steel beam

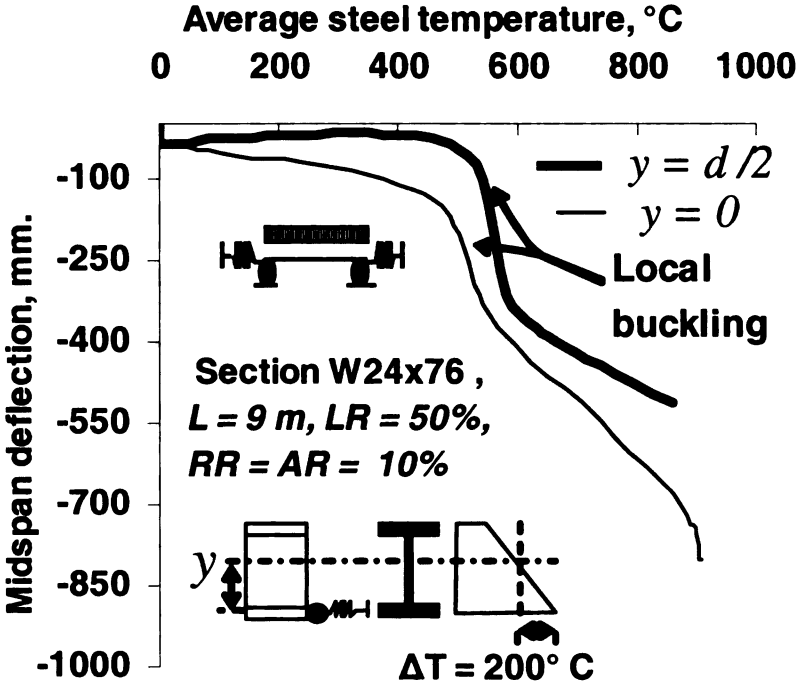

Fig. 5.12: Effect of location of axial restraint on the response of steel beam subjected to thermal gradient

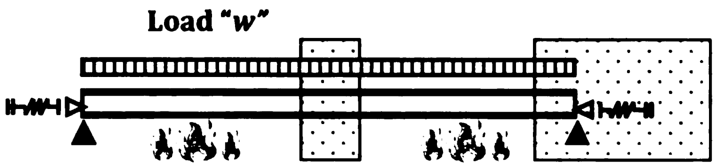

(a) Restrained beam exposed to fire

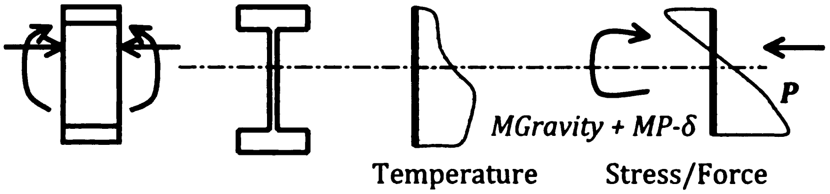

(b) Section at mid-span

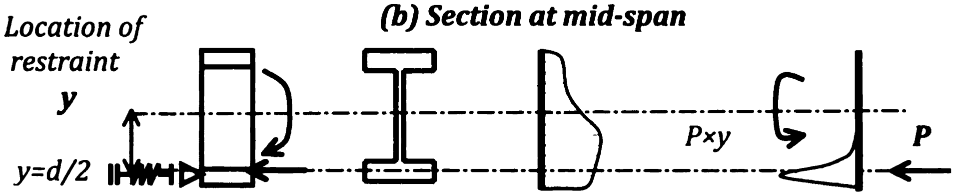

(c) Section at support

Fig. 5.13: Development of fire induced restraint force in a restrained steel beam

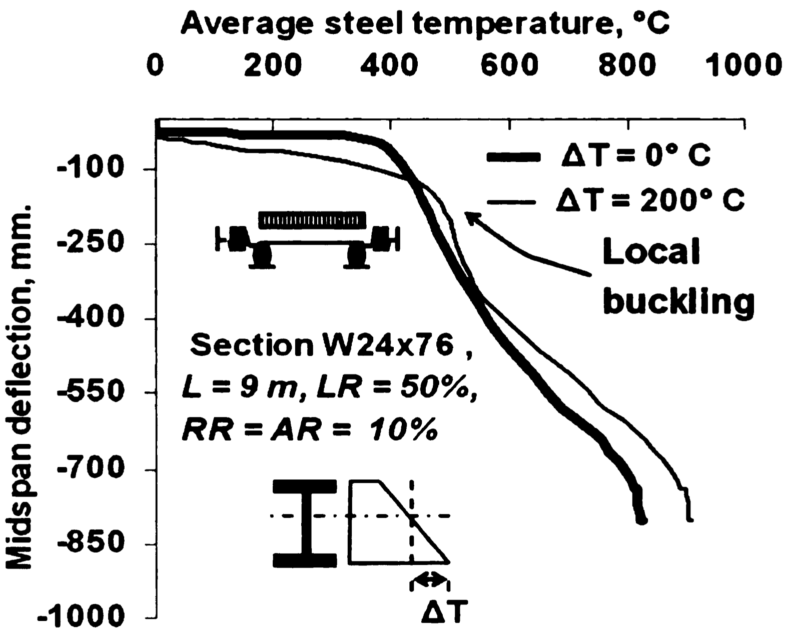

a) Midspan deflection

Fig. 5.14: Effect of thermal gradient on fire response of restrained steel beams

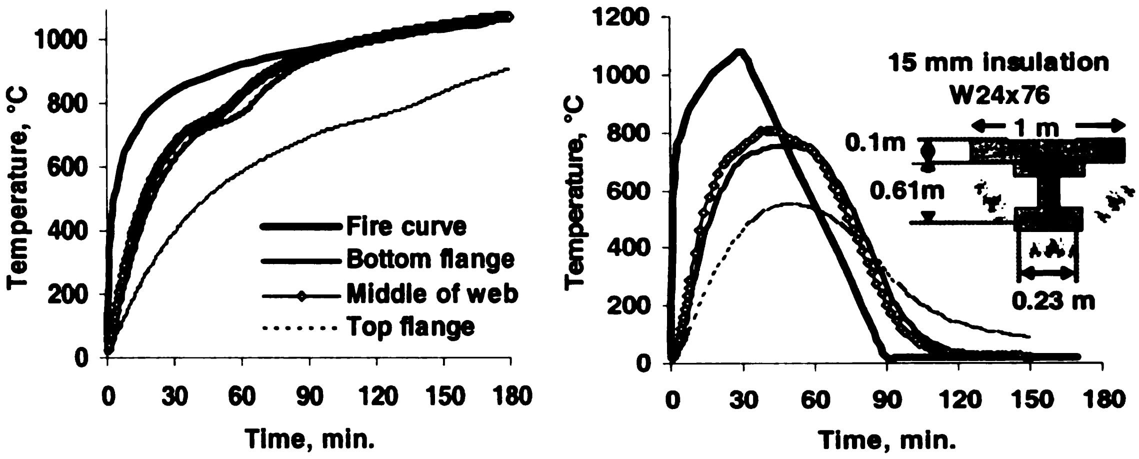

(a) ASTM E119 standard fire

(b) Design fire I

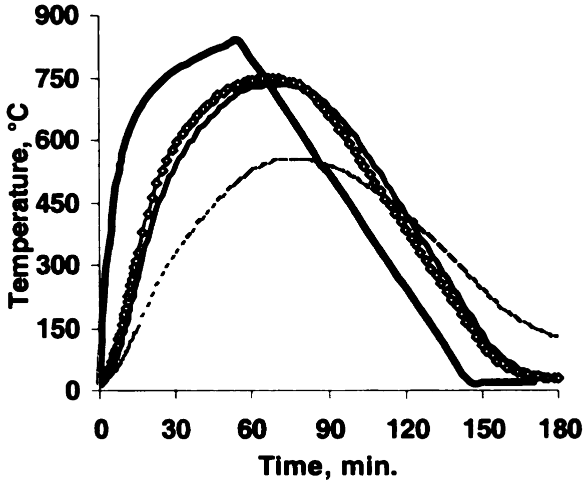

(c) Design fire II

Fig. 5.15: Steel temperature in a restrained steel beam under different fire scenarios

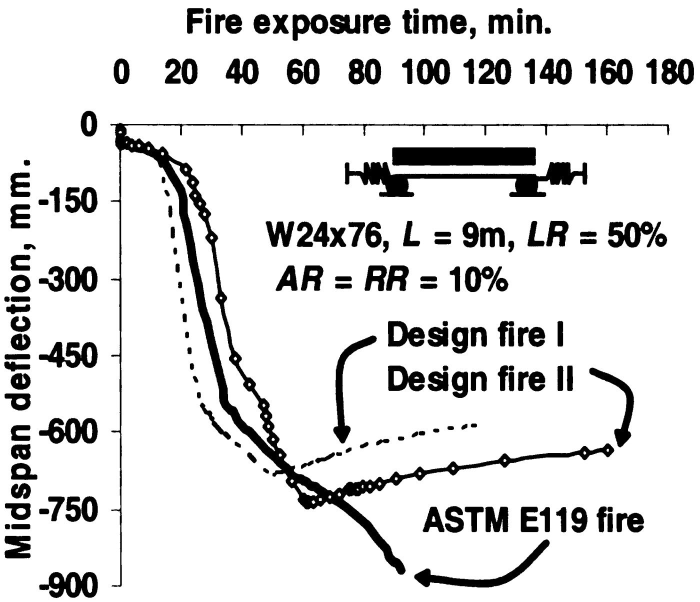

a) Midspan deflection

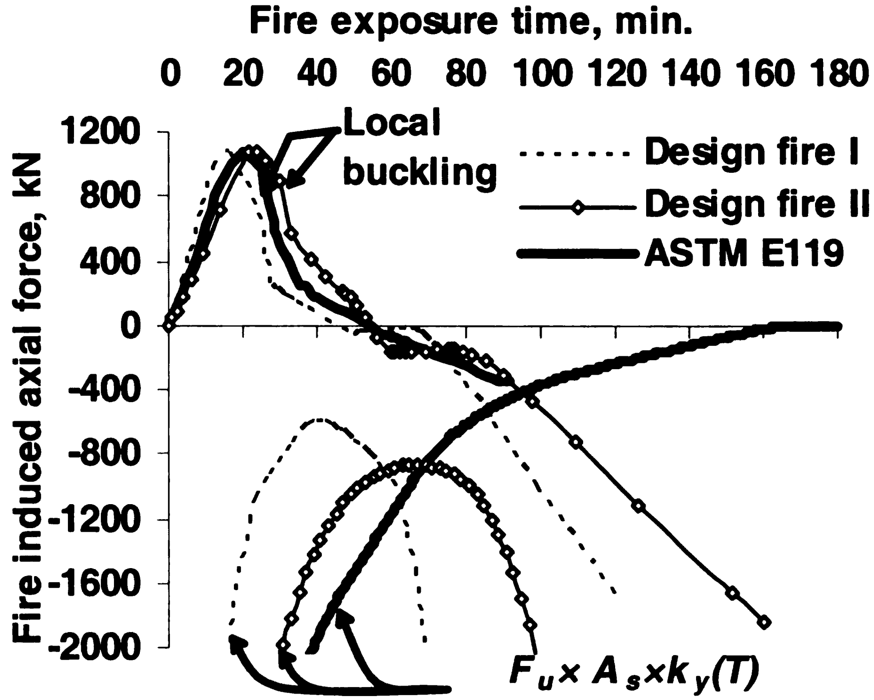

b) Fire induced axial force

Fig. 5.16: Effect of fire scenario on the response of restrained beams

CHAPTER SIX

METHODOLOGY FOR EVALUATING PLASTIC P-M CURVES UNDER THERMAL GRADIENTS

6.1 GENERAL

As illustrated in Chapter 2, there are major drawbacks in the current approaches and code provisions for evaluating fire resistance of steel beam-columns. A rational methodology is proposed in this chapter to overcome some of these drawbacks. The methodology, derived based on heat transfer and structural mechanics principles, takes into consideration the influence of thermal gradients on the plastic P-M diagrams of steel beam-columns. First, the thermal gradient in steel section is quantified and then the plastic P-M diagram of the section is adjusted accordingly. The validity of the proposed approach is established by comparing the fire response predictions from the proposed approach with values obtained from rigorous numerical studies as well as from fire resistance tests (on beam-columns). Also, predictions from the proposed methodology are compared with fire resistance estimates from current codes of practice. The applicability of the proposed approaches to design situations is illustrated through numerical examples.

6.2 EVALUATION OF STEEL TEMPERATURE

In order to quantify fire induced thermal gradient along the depth of the cross section, simplified method for computing temperature in steel section as a function of exposure time is presented. Once the thermal gradient is quantified, it will be used for modifying the shape of the plastic P-M diagrams of the steel cross section. Therefore, this section will present the development of simple equation for predicting temperature in steel.

6.2.1 General

The generalized equation for heat transfer from fire to the structural member can be expressed as (Purkiss 2007):

$$k\nabla^2 T + Q = \rho c \frac{\partial T}{\partial t} \qquad [6.1]$$

in which Q is the total heat flux vector which is comprised of two parts; namely; convective heat flux ($Qcon$) and radiative heat flux (Qr) as follows:

$$Q = Q_{con} + Q_{rad} = h_{con}\left(T - T_f\right) + 4\sigma\varepsilon\left(T^4 - T_f^4\right) \qquad [6.2]$$

The terms in Eqs. [6.1 and 6.2] are defined in Chapter 5. Generally, Eq. [6.1] is simplified into one dimensional problem and then finite difference method is applied for solving the simplified equation. Eurocode 3 (EC3 2005) presents incremental finite difference relations for solving Eq. [6.1] with adjustments made in order to compensate for the simplification. However, since the Eurocode relations are based on finite difference solution, the accuracy of the Eurocode relations is highly dependent on the size of time increment, in addition to them being complex and require intensive use of spreadsheets calculations. Other simpler methods for evaluating steel temperature are totally empirical, such as the "best fit method", and these methods have numerous limitations and also may not yield accurate temperature predictions under wide range of fire scenarios (Buchanan 2002). These limitations can be ascribed to the fact that the best fit method was derived for calculating average steel temperature in proximity to the critical temperature of steel, which corresponds to 538°C for carbon steel. Thus; the temperature predicted by best fit method may not be reliable at temperatures beyond roughly ±25% of critical temperature of steel which is 538°C (Buchanan 2002).

Based on the previous discussion, a simple equation for predicting temperature in steel sections is required. In order to simplify the partial differential equation [6.1], the following assumptions are made (Dwaikat and Kodur 2010a):

- Steel temperature has a uniform distribution, leading to $\nabla^2 T = 0$,
- the radiation problem can be approximately described as an equivalent convection problem,
- temperature in insulation material is assumed to be equal to an average of steel and fire temperatures, i.e. $(Ts + Tf)/m$, where $m = 2$ for linear variation of temperature across the insulation material,
- insulation is thin and thus the volume of the insulation is computed as its thickness (tp) multiplied by the heated perimeter (Fp) of the section, and
- the thermal parameters of steel and insulation materials are assumed to be constant over the temperature range.

Based on the assumptions listed above, Eq. [6.1] can be reduced to the following one dimensional differential equation:

$$\frac{dT_s}{dt} = \frac{\left(F_p / A_s\right)\left(T_f - T_s\right)}{c_s \rho_s \left(1/h_{con} + t_p / k_p\right)\left(1 + \frac{c_p \rho_p}{c_s \rho_s}\frac{F_p}{A_s}\frac{t_p}{m}\right)} - \frac{dT_f / dt}{\left(1 + \frac{c_s \rho_s}{c_p \rho_p}\frac{A_s}{F_p}\frac{m}{t_p}\right)} \qquad [6.3]$$

where *hcon* is the convective heat transfer coefficient, *csρs* and *cpρp* are the heat capacity of steel and insulation, respectively, *kp* is conductivity of the insulation material, and *As* is the cross sectional area of steel section.

Equation [6.3] can be rewritten as

$$\frac{dT_s}{dt} = F_1\left(T_f - T_s\right) - F_2 \frac{dT_f}{dt} \qquad [6.4]$$

with *F1* and *F2* corresponding to the terms in Eq. [6.3].

6.2.2 Exposure to Standard Fire

In order to obtain a simplified solution for Eq. [6.4], the fire time-temperature curve of a standard fire (*Tf*) is fitted by a power function of the form: *Tf* = *atn*. For ISO 834 standard fire *a* = 469.9 and *n* = 0.1677 (*R2* = 0.995), and for ASTM E119 standard fire *a* = 496.5 and *n* = 0.1478 (*R2* = 0.989). Figure 6.1 shows the relative error due to this fitting for both standard fires. It can be seen that the error is less than 2% after the first 10 minutes of fire exposure.

If we assume that the temperature in steel has the following form:

$$T_s(t) = T_f\left(1 - e^{-st}\right) \qquad [6.5]$$

where *s* is a correlation coefficient, then by substituting Eq. [6.5] into Eq. [6.4], dividing by *Tf*, substituting $\frac{dT_f / dt}{T_f} = \frac{n}{t}$, and multiplying by *est* we obtain:

$$\frac{n}{t}\left(e^{st} - 1\right) + s = F_1 - F_2 \frac{n}{t} e^{st} \qquad [6.6]$$

Based on comparison to results from thermal analysis, the value of *s* must be very small (*st* < 1), and thus the exponential function can be approximated as:

$$e^{st} = 1 + st + \frac{(st)^2}{2!} + \frac{(st)^3}{3!} + \ldots \cong 1 + st, \quad \text{for } st < 1 \qquad [6.7]$$

by substituting Eq. [6.7] into Eq. [6.6] and solving for *s* we obtain:

$$s = \frac{F_1 - F_2(n/t)}{n(1 + F_2) + 1} \qquad [6.8]$$

Since *F2* << 1 and the factor *n/t* becomes significantly smaller than 1.0 as *t* increases, we can neglect the second term of the nominator, leading to the following simplified expression for *s*:

$$s = \frac{F_1}{n+1} = \frac{\left(F_p / A_s\right)}{c_s \rho_s \left(1/h + t_p / k_p\right)\left(1 + \frac{c_p \rho_p}{c_s \rho_s} \frac{F_p}{A_s} \frac{t_p}{m}\right)(n+1)} \qquad [6.9]$$

Using *s* from Eq. [6.9], Eq. [6.5] can be used to predict steel temperature at any time step, without the need for incrementing time steps. Equation [6.5] can be applied in one step (no time-steps needed) and this is an advantage over one-dimensional finite different equations (such as those specified in the Eurocode), whose accuracy is highly dependent on the size of time increment used.

6.2.3 Exposure to Design Fire

While the temperature in a standard fire continues to increase indefinitely, the design fire enters a decay phase after reaching a maximum value (Tf,max). A typical design fire can be represented by a parametric fire curve as specified in Eurocode 1. Figure 6.2 (a) illustrates the characteristics of a typical parametric fire scenario. The heating phase of a design fire is specified parametrically in Eurocode 1 in terms of the factor $\mathbf{\Gamma}$ which is dependent on the ventilation characteristics and thermal inertia of fire compartment. For $\mathbf{\Gamma} = 1.0$ the heating phase of a parametric fire represents the ISO 834 standard fire. Heating phase of a design fire can also be fitted using a power function (i.e. $Tf = atn$). For instance, for a parametric fire with $\mathbf{\Gamma} = 0.5$, $a = 312$ and $n = 0.229$ ($R2 = 0.95$), while for parametric fire with $\mathbf{\Gamma} = 1.5$, $a = 474$ and $n = 0.176$ ($R2 = 0.97$). Steel temperature during the heating phase of a design fire can then be computed using Eq. [6.5].

The decay phase of a design fire starts at $t = t1$, as shown in Fig. 6.2. In the parametric fires specified by the Eurocode the decay phase is always linear with a decay rate "*r*" as shown in Fig. 6.2 (b). The fire temperature reduces to room temperature at $t = t2$, however, steel requires more time to cool down to room temperature and this happens at $t = t3$. The maximum temperature in steel occurs at *t2* > *ts,max* > *t1* because in that time interval fire temperature is still greater than average steel temperature, however fire is decaying.

If the rise in steel temperature steel after *t1* (the segment **AB** in Fig. 6.2(b)) is represented by a quadratic function, and if we assume that the maximum steel temperature occurs on the same decay curve of the fire (i.e. point ***B*** is on the fire curve) then the equation for the average steel temperature between *t1* and *ts,max* can be written as:

$$T_s = \alpha t^2 + \beta t + \gamma \qquad [6.10]$$

where α, β, and γ are orientation coefficients. In order to estimate the maximum temperature in steel (*Ts,max*) the following boundary conditions for Eq. [6.10] are utilized:

- at point ***A*** (*t* = *t1*):

  Ts = *Ts1* (using Eq. [6.5] at *t* = *t1*), and *dTs/dt* = slope from Eq. [6.5] at *t* = *t1*,

- and at point ***B*** (*t* = *ts,max*):

  Ts = *Tf*, and *dTs/dt* = 0.

By applying the above four boundary conditions on Eq. [6.10] and solving for *ts,max* and *Ts,max* we obtain:

$$t_{s,\max} = t_1 + \frac{T_{f,\max} - T_{s,1}}{\frac{1}{2}\left.\frac{dT_s}{dt}\right|_{t=t_1} + r} \qquad [6.11]$$

$$T_{s,\max} = \frac{\frac{1}{2} T_{f,\max} \left. \frac{dT_s}{dt} \right|_{t=t_1} + r \times T_{s,1}}{\frac{1}{2} \left. \frac{dT_s}{dt} \right|_{t=t_1} + r} \qquad [6.12]$$

The term $\left. \frac{dT_s}{dt} \right|_{t=t_1}$ can be assumed to be equal to the secant slope of the steel temperature curve, i.e. $\left. \frac{dT_s}{dt} \right|_{t=t_1} = \frac{T_{s,1}}{t_1}$. Substitution back into Eqs. [6.11 and 6.12] gives:

$$t_{s,\max} = t_1 \left(1 + \frac{T_{f,\max} - T_{s,1}}{\frac{1}{2} T_{s,1} + r t_1} \right) \qquad [6.13]$$

$$T_{s,\max} = \frac{T_{f,\max} + 2 t_1 r}{1 + 2 t_1 r / T_{s,1}} \qquad [6.14]$$

As it will be shown through comparison to rigorous finite element analysis, the last two simple equations give a good approximation for both the maximum temperature attained in steel beam during exposure to a design fire scenario and for the corresponding time of attaining that maximum average steel temperature.

6.2.4 Comparison to Finite Element Analysis

In order to verify the proposed equations, results from finite element analysis are compared to the results from the proposed equations. The finite element model developed using ANSYS in Chapter 4 for thermal analysis is used for generating the finite element results. Table 6.1 shows the range of parameters that were used to in the simulations.

A comparison between finite element predictions of steel temperature and those predicted using Eq. [6.5] is shown in Fig. 6.3. The comparison shows that Eq. 6.5 can reasonably predict steel temperatures below 750°C; while steel temperatures are overestimated about 10-12% by Eq. [6.5] for $Ts > 750°C$. This overestimation is because of the phase change that occurs in steel at temperatures between 750°C and 800°C, which is not captured by Eq. [6.5]. Any attempt to make adjustments to Eq. [6.5] in the range of $Ts > 750°C$ will result in a complex equation for predicting steel temperature which departs from the purpose of this study. Thus, Eq. 6.5 is deemed to be acceptable for generating steel temperature conservatively below 750°C and this is the range of temperatures encountered in the failure of beam-columns in most practical situations.

The results of the finite element analysis for the maximum temperature in steel (Ts,max) and the time to reach maximum temperature in steel (ts,max) are compared in Fig. 6.4 and against the predictions using Eqs. [6.13 and 6.14]. The results in Fig. 6.4 indicate that the proposed equations are capable of predicting the maximum temperature attained in steel section when exposed to design fire scenarios.

6.3 PLASTIC P-M DIAGRAMS

6.3.1 General

Current provisions in codes and standards recommend the use of uniform average temperature for establishing the plastic P-M curves at elevated temperatures. This assumption, though adequate for cases where temperature in steel is uniform, such as a column exposed to fire from four sides, may not be valid for columns or beams exposed to fire from 1, 2, or 3 sides since significant thermal gradients develop across the section. These thermal gradients can cause severe distortion in the P-M curves and render the capacity curves based on uniform temperature inadequate for evaluating the strength of such beam-columns. In this section, a simplified approach is proposed for adjusting the uniform temperature plastic P-M curves to account for the shape distortion resulting from fire-induced thermal gradients.

The focus of this study is on the shape of the plastic P-M interaction equations that is influenced by thermal gradients. Therefore, in the generation of the P-M diagrams, the main assumption is that the beam-columns are braced against lateral or torsional buckling. Further, the influence of local buckling is neglected since the beam-column is assumed to be made of a compact section, as required in a design situation. Stability factors (e.g. *KL* for columns) can be achieved independently from the P-M diagrams. This can be done through adjusting both axial and bending capacities (using *Pcr* and *Mcr* instead of plastic capacities *FyAs*, and *FyZx*, respectively), and by amplifying applied moment due to lateral bowing of the member. *Pcr* and *Mcr*, under the influence of thermal gradient, can be computed based on Eurocode recommendations (EC3 2005), or the AISC specifications manual (AISC 2005). In terms of global stability, Eurocode recommends an effective length of *0.5Lo* for columns in intermediate storey and *0.7Lo* for columns in top storey for fire resistance design.

6.3.2 Generation of P-M Diagrams

To generate the plastic beam-column capacity for a section with thermal gradient, each fiber of steel section is subjected to full ultimate stress that corresponds to the temperature in that fiber, i.e. *Fu×ky(Ti).* Fig. 6.5 shows a wide flanged (WF) section with thermal gradient and the corresponding ultimate stress *Fu×ky(Ti)* at each fiber of temperature *Ti.* As shown in Fig. 6.5, the nonlinear thermal gradient is approximated to a linear gradient. The linearization of thermal gradient is illustrated in Section 5.3.4. Temperature in steel is predicted using Eq. [6.5].

The ultimate axial force and bending moment are computed, at any given steel temperature distribution, by direct numerical integration of the ultimate stresses over the cross sectional depth (*d)* using the following algorithms:

$$P = \int F_u dA = \sum \text{sign}(y_i - Y_{NA}) \times F_u \times k_y(T_i) \times b_{eff} \times \Delta y_i \qquad [6.15]$$

$$M_{GC} = \int yF_u dA = \sum \text{sign}(y_i - Y_{NA}) \times (y_i - Y_{GC}) \times F_u \times k_y(T_i) \times b_{eff} \times \Delta y_i \qquad [6.16]$$

where the function "sign(*x*)" is the function that gives the sign of a real number (+1 for *x* > 0 and -1 for *x* < 0) and the positive sign indicates compression. The terms in Eqs. [6.15 and 6.16] are illustrated in Fig. 6.5. The bending moment *MGC* is calculated around the center of geometry (*YGC*) of the section, and the positive sign indicates tension at the top (cooler) fiber. The center of geometry is defined as the geometrical centroid of the section, while the neutral axis (*YNA*) is defined as the axis at which the strain is zero.

Because the section must be in equilibrium, the sum in Eq. [6.15] must equal the externally applied axial force (*P*) acting on the section, while the sum in Eq. [6.16] must equal the externally applied bending moment (*M*). To obtain the entire P-M diagram for the same temperature profile of the section, the location of the neutral axis (*YNA*) is varied along the depth of the section. For each location of the neutral axis, a pair of *P* and *M* values is computed using Eqs. [6.15 and 6.16], respectively. The location of the neutral axis (*YNA*) is varied from zero to *d* in increments of $\Delta yi = 0.001d$. The computations of Eqs. [6.15 and 6.16] are carried out using a MATLAB code for all the cases of sectional geometries and thermal gradients.

Figure 6.6 shows the degradation in strength and stiffness of steel as a function of temperature that is adopted in the calculation of P-M diagrams. These strength-temperature relationships are adopted from the ASCE manual of practice (ASCE 1992).

Preliminary research by Garlock and Quiel (2007) showed that the distortion in the shape of the normalized P-M diagrams does not depend on the relative sizes of the sections; however, the shape critically depends on the axis orientation (i.e. on the direction of thermal gradient). Their study highlighted that the distortion in the P-M diagrams is more severe for the case of thermal gradient in strong direction as compared to the case of weak direction. Therefore, it is proposed here to adjust the P-M diagrams for the case of severe distortion due to thermal gradient in the strong direction, while the shape of P-M diagrams will be maintained for the case of weak direction. The following subsections will present treatment of P-M diagrams for both strong and weak axis orientation.

6.3.2.1 Strong Axis Orientation

The basic features of the distorted plastic P-M diagrams for a WF section with thermal gradient in the strong direction are compared to the case of a uniform temperature in Fig. 6.7. The figure shows that the value of moment capacity under peak axial capacity (point A in Fig. 6.7) moves back and forth (to point ***A'*** in Fig. 6.7) depending on the eccentricity (*e*) between center of stiffness "*CS*" and center of geometry "*GC*" that is caused by the thermal gradient in a WF section. In order to obtain a simple method for deriving the distorted P-M diagrams the following assumptions are made (Dwaikat and Kodur 2010*a,b*):

- The P-M diagram represents a parallelogram with its sides being parallel to the P-M segments derived based on the average temperature of the section. Specifically, we assume that the segments ***AB*** and ***AC*** are parallel to the segments ***A'B'*** and ***A'C'*** respectively, as shown in Fig. 6.7.
- The magnitude of the shift (*MTG*) in the P-M capacity envelope (Fig. 6.7) is assumed to be numerically equal to the ultimate axial capacity (*Pu,Tave*) of the section multiplied by the eccentricity (*e*) between the center of geometry (*GC*) and of the center of stiffness (*CS*) of the section as shown in Fig. 6.10. The ultimate capacity is computed based on the average temperature of the section, i.e:

$$MTG = e \times Pu,Tave = e \times ky(Ts,Ave) \times Fu \times As \qquad [6.17]$$

To compute the eccentricity (*e*) between the *YCS* and *YGC*, the reduction in the elastic modulus of steel is assumed to vary linearly across the depth of the section as shown in Fig. 6.8. Each plate of the section is assumed to have a constant rate of reduction (*kE*) in the elastic modulus depending on its average temperature. The reduction in elastic modulus of the steel in the web is assumed to equal the average of the reductions of both the top (cool) and bottom (hot) flanges. With these assumptions, the eccentricity (*e*) between *YGC* and *YCS* can then be approximated as follows:

$$e = Y_{CS} - Y_{GC} = \frac{\sum A_i \times k_E(T_i) \times y_i}{\sum A_i \times k_E(T_i)} - \frac{d}{2} \qquad [6.18]$$

Substituting for different terms, Eq. [6.18] can be expanded as:

$$e = \frac{B_F t_F k_E(T_{s,CF}) \times d + \left(\frac{k_E(T_{s,CF}) + k_E(T_{s,HF})}{2}\right) t_w d \times \frac{d}{2}}{B_F t_F k_E(T_{s,CF}) + \left(\frac{k_E(T_{s,CF}) + k_E(T_{s,HF})}{2}\right) t_w d + B_F t_F k_E(T_{s,HF})} - \frac{d}{2} \qquad [6.19]$$

$$e = \frac{d}{2}\left(\frac{2B_F t_F}{2B_F t_F + t_w d} \times \frac{k_E(T_{s,CF}) - k_E(T_{s,Ave})}{k_E(T_{s,Ave})}\right) \qquad [6.20]$$

where *BF*, *tF*, *tw*, *d* are dimensions of the section as shown in Fig. 6.8, and *kE(T)* is the reduction factor for elastic modulus at steel temperature *T*. For verifying the validity of Eq. 6.20, the computed value of *MTG* (using Eq. [6.17]) is compared to the actual value obtained from the true P-M interaction curves (via MATLAB code) for sections with different thermal gradients. Fig. 6.9 shows the result of this comparison for different cases of thermal gradients. The figure shows that the eccentricity (*e*) increases more rapidly as the temperature increases. This is because stiffness (*Es*) of steel suffers faster degradation with the increase in temperature. It can be seen in the figure that *MTG* can be reasonably predicted for realistic cases of linear thermal gradients using the simple methodology described above.

With the calculation of *MTG* using Eq. [6.17], an adjustment for the P-M interaction curves can now be proposed. The adjustment of the P-M interaction curves is based on using the average temperature of steel section with a shift *MTG* that occurs as a result of thermal gradient in the section. Fig. 6.10 shows the proposed adjustment for the P-M diagrams to account for the effect of thermal gradients. The adjustment of P-M diagram is aimed at preserving the room-temperature shape of the P-M diagram and only introducing the shift *MTG* to account for the thermal gradient effect. The adjusted equations of the plastic P-M diagrams for wide flange section with linearized thermal gradient in the strong direction can be written as (Dwaikat and Kodur 2010b):

$$\frac{\left|M+M_{TG}\right|}{Z_x F_{u,Ts,ave}}+\frac{P}{A_s F_{u,Ts,ave}} \leq 1.0 \quad \text{and} \quad \frac{\left|M-M_{TG}\right|}{Z_x F_{u,Tave}}-\frac{P}{A_s F_{u,Ts,ave}} \leq 1.0 \qquad [6.21]$$

In order to verify the proposed simple approach for predicting P-M diagrams, two sections with different cases of thermal gradients are analyzed. Figs. 6.11 and 6.12 show the comparison between the true P-M diagrams (solid lines) for these two sections are obtained via MATLAB code that carries out the complex computations using Eqs. [6.15 and 6.16], and the approximated linearized P-M diagrams (dashed lines) that are obtained using Eq.[6.21]. The two sections are W24x76 with relatively thin steel plates and W14x311 with thicker steel plates. These sections were selected to compare the effect of the different steel plate thicknesses on the P-M diagrams. The selected sections (W24x76 and W14x311) were subjected to different thermal gradients along their strong axis, and the resulting P-M diagrams are normalized to the axial (*Pu*) and moment (*Mu*) plastic capacities using average temperatures. It can be seen in Figs. 6.11 and 6.12 that the distortion in the P-M diagrams is well predicted using the proposed simple Eq. [6.21] for both sections. Also, it can be seen in the figures that the distortion is larger for higher temperatures and higher thermal gradients. This is because at higher temperatures (*Ts* > 400°C) the reduction in steel elastic modulus (*Es*) becomes steeper and thus causes larger eccentricity (*e*) between center of stiffness and center of geometry of the non homogenous section. Further, the comparisons in Figs. 6.11 and 6.12 indicate that increasing plate thicknesses has a very small influence on the shape of the P-M diagrams under extreme cases of thermal gradients (case $\Delta T = 225°C$). It can be seen that Eq. [6.21] conservatively predicts the P-M capacity envelopes for realistic cases of thermal gradients.

6.3.2.2 Weak Axis Orientation

In the case of thermal gradient along the weak axis, the distortion in plastic P-M diagrams is smaller as compared to the case of thermal gradient along strong axis. The ensuing analysis shows that for realistic cases of thermal gradients, the effect of thermal gradient on the P-M diagrams can be neglected for weak axis orientation.

Therefore, as shown in Fig. 6.13, the P-M diagram for WF sections with thermal gradients in the weak direction can be constructed by assuming the moment capacity ratio (*M/Mu*) to increase linearly as the axial capacity ratio (*P/Pu*) decreases until the moment capacity ratio (*M/Mu*) reaches its maximum value of 1.0 at *P/Pu* = 0.5, after which the moment capacity remains constant. Based on this assumption, the P-M diagrams for WF sections subjected to thermal gradients in their weak direction can be expressed as (Dwaikat and Kodur 2010a):

$$\begin{aligned} &\text{If } \left|\frac{P}{A_s F_{u,Ts,ave}}\right| \geq \frac{1}{2}, \quad \left|\frac{P}{A_s F_{u,Ts,ave}}\right| + \frac{1}{2}\left|\frac{M}{Z_y F_{u,Ts,ave}}\right| \leq 1.0 \\ &\text{If } \left|\frac{P}{A_s F_{u,Ts,ave}}\right| \leq \frac{1}{2}, \quad \left|\frac{M}{Z_y F_{u,Ts,ave}}\right| \leq 1.0 \end{aligned} \qquad [6.22]$$

Figs. 6.14 and 6.15 show P-M diagrams for two different cross sections with different thermal gradients. The two sections are a W24x76 with relatively thin steel plates and a W14x311 with thicker steel plates. These sections were selected to compare the effect of the different steel plate thicknesses on the P-M diagrams. As seen in Figs. 6.14 and 6.15, the P-M diagrams experience smaller shifts due to the effect of thermal gradient in the weak direction as compared to larger shifts for the case of thermal gradient in strong direction (as seen in Figs. 6.11 and 6.12). The shift in P-M diagrams becomes more noticeable when both the average temperature of the section and the thermal gradient are high (e.g. ΔT = 225°C and *Ts,CF* = 700°C in Figs. 6.14 and 6.15). Such cases of extreme temperatures and thermal gradients are rarely encountered in reality because steel sections tend towards thermal equilibrium as temperature in steel rises with time of exposure. Also, the shape of the P-M diagram seems to be smoother and more rounded for sections with thicker plates. For both cases of sections (thick or thin plates) and the different thermal gradients they are exposed to, Eq. [6.22] seems to provide sufficiently reasonable prediction of the P-M diagrams for WF sections subjected to thermal gradient in the weak direction.

6.3.3 Comparison to Fire Tests

The proposed approach for generating the distorted P-M diagrams induced by thermal gradients is validated by comparing the predictions with measured data in fire resistance tests on beam-columns. For this validation, the same beam-columns (Dwaikat et al. 2009) that were used in the validation of the thermal analysis are used. Beam-columns designated C1-S and C1-W were selected to demonstrate the ability of the simplified approach to predict the distorted P-M envelopes that are induced by non-uniform thermal gradients along strong and weak axes, respectively.

As shown in Fig. 3.3, the tested beam-columns were instrumented with thermocouples to measure steel temperatures, strain gauges to measure bending moment, and LVDT's to measure displacement and rotations. The measured fire induced axial forces and bending moments for the two cases of axis orientations (weak and strong axes) are plotted in Fig.6.16. The generated bending moments were directly computed using the readings of the strain gauges at the base section D-D (see Fig. 3.3 for location of section D-D) which remained cool (below 40°C) during the fire test (Dwaikat et al. 2009). Since the top end of the beam-column was lightly rotationally restrained, it is assumed that the bending moment at section D-D is the maximum and values of the moment at the critical section where plastic hinge developed (at 1930 mm from the based) was interpolated between *MD-D* and zero at the top end (Dwaikat et al. 2009). The pressure recorded in the vertical actuators was also used to directly measure the fire induced axial forces. Fig. 6.16 shows that both the axial force and bending moment increase first and then decrease with fire exposure time. This is because the beam-columns expand non-uniformly under the influence of temperature and thermal gradients until the spread of plasticity in the beam-columns causes a reduction in the axial force.

The recorded temperatures in the two beam-columns in fire resistance experiments are shown in Fig. 3.5. In order to use the simplified approach, the temperature profiles are linearized such that the top flange and average temperatures were assumed to equal the lowest and the average temperatures of the section, respectively. Fig. 6.17 plots the development of the fire-induced P and M in the tested beam-column that had thermal gradient along its strong axis. Also, the P-M envelope as predicted using the simplified approach (Eq. 6.19) for different fire exposure times is also plotted in Fig. 6.17 for the same beam-column at specific times of fire exposure. It is seen in the figure that at different time steps, the beam-columns experience different thermal gradients which cause different shifts in the P-M diagrams. Based on the results in Fig. 6.17, the capacity failure of the beam-column is conservatively predicted at t = 215 min. using Eq. [6.21], compared to the observed failure of the beam-column at t = 220 min. in fire tests. Actual failure in tests is said to occur at the time after which the beam-column is no longer capable of carrying the applied axial load and thus starts to deflect at an accelerated rate. While, the predicted failure is assumed to be the time at which the fire induced *P* and *M* exceed the capacity envelope given in Eq. [6.21].

Figure 6.18 plots the development of fire induced axial force and bending moment for the tested beam-column C1-W, subjected to thermal gradient along its weak axis. The figure also shows the predicted P-M capacity envelope as predicted using Eq. [6.22]. In this case, since the shape of the P-M diagrams is not adjusted, only the P-M diagram at failure is shown in Fig. 6.18. It can be seen that Eq. [6.22] predicts the failure to occur few minutes (t = 212 min.) prior to the observed (actual) failure (at t = 215 min.) of the beam-column in fire resistance experiments.

6.3.4 Design Application

To demonstrate the applicability of the simplified approach in design situations, a numerical example is presented for a beam-column exposed to ASTM E119 standard fire (ASTM 2008). The beam-column is of section W14x176 (Fy = 345 MPa.) and is insulated with 0.5 in. (12.7 mm.) spray applied fire proofing material. Section dimensions are: d = 386 mm, BF = 399 mm, tF = 33.3 mm, tw = 21 mm. The thermal conductivity of insulation is 0.1 W/m.°K. The beam-column is exposed to fire from three sides such that thermal gradient is assumed to develop in the strong direction. Thermal gradients induce thermal bowing which causes additional bending moments to develop in the beam-column. These bending moments include moments resulting from restraining thermal curvature, and from lateral deflection caused by thermal curvature. In both cases, the resulting bending moments need to be accounted for in structural analysis under fire conditions. In this example, the beam-column is braced in both directions in order to ensure fully plastic failure mode.

The plastic P-M capacity envelope for the beam-column will be evaluated for two cases. Case one is for a uniform temperature and case two is with thermal gradient in the section of the beam-column. For the case of uniform temperature, the P-M diagram is evaluated using AISC design specifications (AISC 2005) for the maximum and average temperatures in the section. For the case of thermal gradient, the P-M diagrams will be generated using the simplified approach. For either case, the P-M capacity envelopes will be established at 2 and 3 hours of fire exposure. The temperature in the section will be evaluated using Eq. [6.5].

6.3.4.1 Temperature Calculation

Using the geometric properties of W14x176, section factors (*Ap/V*) were computed for the entire section, top flange, and bottom flange as 54.16, 33.5, and 63.5 m-1, respectively. Table 6.2 shows the calculated temperatures at 2 and 3 hours of fire exposure and compares them to the results of finite element analysis.

Equations [5.4] and [5.5] are used to estimate the linearized thermal gradient in the cross section after 2 and 3 hours of fire exposure. As shown in Table 6.2, linearized thermal gradient (according to proposed approach) increased from 139°C at 2 hours of fire exposure to 180°C at 3 hours of fire exposure. This compares well with finite element predictions, wherein the thermal gradient increased from 193°C to 219°C, at 2 and 3 hours of fire exposure, respectively, as shown in Table 6.2. The reduction factors for *Es* and *Fy* are computed using equations specified in the ASCE manual of practice (ASCE 1992).

6.3.4.2 AISC Specifications

The plastic axial and moment capacities are calculated as per AISC design specifications (AISC 2005) for two cases of uniform temperatures, namely average and maximum section temperatures at 2 and 3 hours of fire exposure. The results of the calculations are presented in Table 6.3.

The plastic P-M diagrams are plotted in Fig. 6.19 for 2 and 3 hours of fire exposure and using maximum and average uniform temperatures in the section. The figure shows that the beam-column experiences significant reduction in capacity between 2 and 3 hours of fire exposure. However, the shape of the P-M diagram does not change despite the change in thermal gradient between the 2-hour and 3-hour fire exposure. This is simply because the AISC procedure does not account for the effect of thermal gradient on the P-M diagrams.

6.3.4.3 Accounting for Thermal Gradient Using the Proposed Approach

The effect of thermal gradient on the P-M diagrams can be included by computing the eccentricity (*e*) between the center of stiffness and the center of geometry at time of fire exposure. Both the eccentricity (*e*) and the shift (*MTG*) in the plastic P-M diagrams are computed at 2-hour and 3-hour fire exposures and are presented in Table 6.4.

The *MTG* is used to adjust the plastic P-M diagrams as per Eq. [6.21] for strong axis direction. The distorted P-M diagrams are plotted in Fig. [6.21] for 2-hour and 3-hour fire exposure. It can be seen that at 2-hour fire exposure, the distortion in P-M diagrams is small, however, at 3-hour of fire exposure, the distortion in P-M diagrams becomes significant. This is because at temperatures above 400°C the reduction in steel young modulus (*Es*) becomes steeper and thus thermal gradients at such elevated temperatures will have higher effect on the plastic capacity of the section. Clearly, the plastic P-M diagrams as per AISC design manual do not account for the shift in the center of stiffness of the section due to thermal gradient, and therefore can be unconservative as seen in Fig. 6.19.

6.5 SUMMARY

The development of simplified approach for evaluating plastic P-M diagrams of steel beam-columns under realistic fire exposure is presented in this chapter. The guidelines are derived based on basic heat transfer and structural mechanics principles and were supported by detailed parametric studies presented in Chapter 5. The proposed guidelines include a method for computing steel temperature and fire induced thermal gradients, and a simplified methodology for adjusting the P-M diagram to account for the influence of fire induced thermal gradient. The validity of the proposed approaches is established by comparing predictions with results from detailed finite element analysis and fire tests. The proposed methodology provides simple and rational approach for generating the plastic P-M interaction diagrams for steel beam-column subjected to thermal gradient under standard or design fire exposures. The applicability of the proposed methodology to a design simulation is illustrated through numerical example.

Table 6.1: The range of parameters used in the simulations

Parameter	Min.	Max.	Step
d (mm)	200	600	200
b (mm)	200	600	200
tf (mm)	10	30	20
tw (mm)	7	14	7
tp (mm)	0	30	10
kp (W/m.°K) @20°C	0.07	0.21	0.14
$\rho \times cp$ (J/m3.°K)@ 20°C	250×900	350×900	150×900
Gamma factor (Γ)	0.5	1.5	0.5
$t1$ (min.)	30	120	30
$t2$ (min.)	$t1 + 30$	$t1 + 150$	60

Table 6.2: Temperatures in W14x176 as predicted by Eq. 6.5 and by detailed finite element analysis

	s	*After 2 hours*				*After 3 hours*			
		Ts(°C) Eq. 6.5	Ts(°C) F.E.	ky	kE	Ts(°C) Eq. 6.5	Ts(°C) F.E.	ky	kE
Cool flange	0.00277	297	314	0.81	0.89	435	429	0.65	0.77
Average	0.00448	436	428	0.65	0.76	615	582	0.35	0.47
Hot flange	0.00526	491	507	0.57	0.69	679	648	0.25	0.35

Table 6.3: Plastic axial and moment capacities calculated as per AISC design manual

	After 2 hours		After 3 hours	
	ΦPn kN	ΦMn kN.m	ΦPn kN	ΦMn kN.m
Average temp.	6759	1060	3622	568
Max. temp.	5922	929	2580	405

Table 6.4: Calculation of eccentricity of center of stiffness and the gradient-induced shift *MTG* as per proposed equations

	ΔT (°C) Eq. 6.5	ΔT (°C) F.E.	*e* (mm) Eq. 6.20	*MTG* (kN.m) Eq. 6.17
After 2 hours	194	193	23.7	160.2
After 3 hours	244	219	90.6	328.35

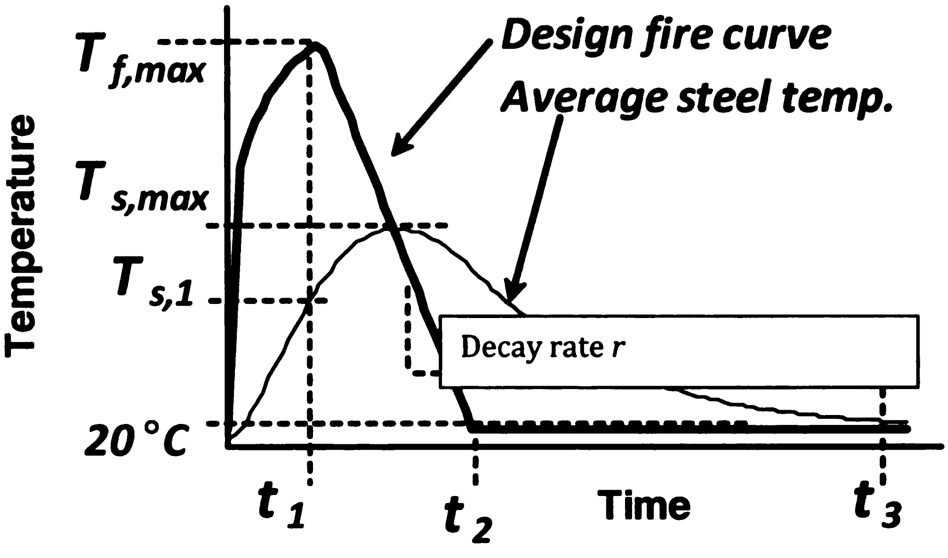

(a) Design fire and steel temperatures

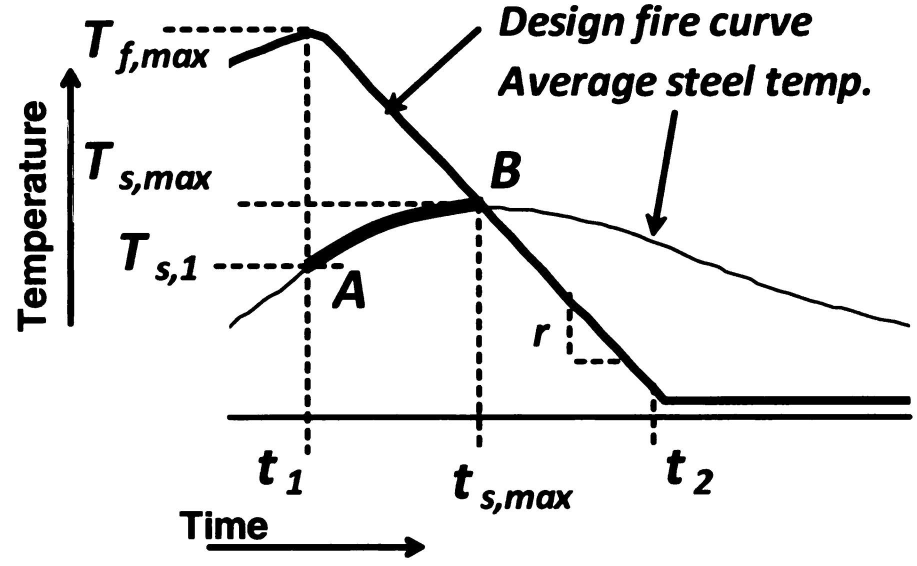

(b) Rise of steel temperature during decay phase

Fig. 6.1 Characteristics of typical parametric fire exposure

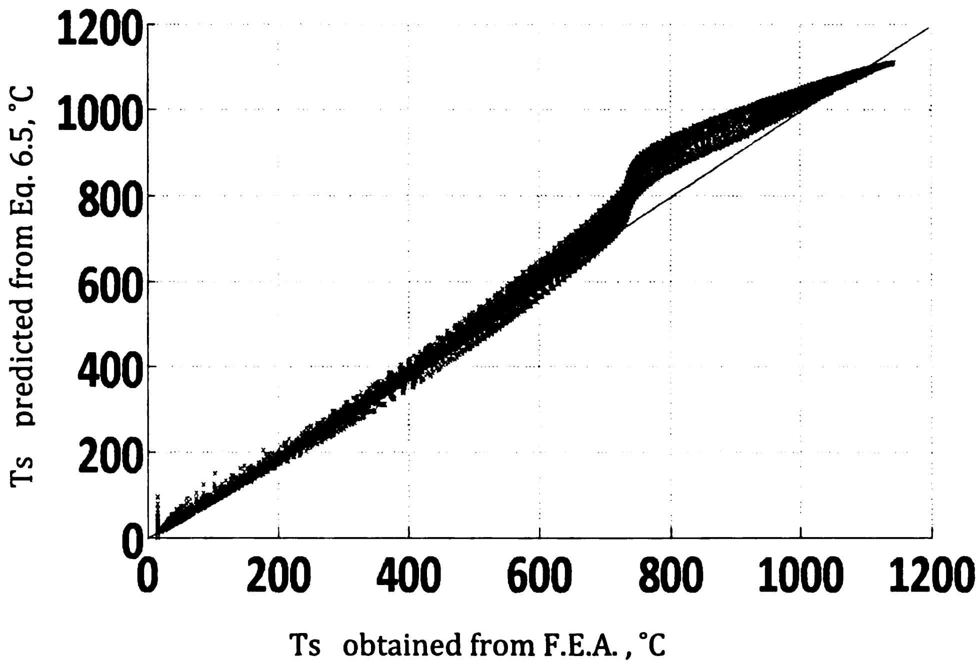

Fig. 6.2: Comparison of steel temperature predicted by Eq. 6.5 with that obtained from finite element analysis

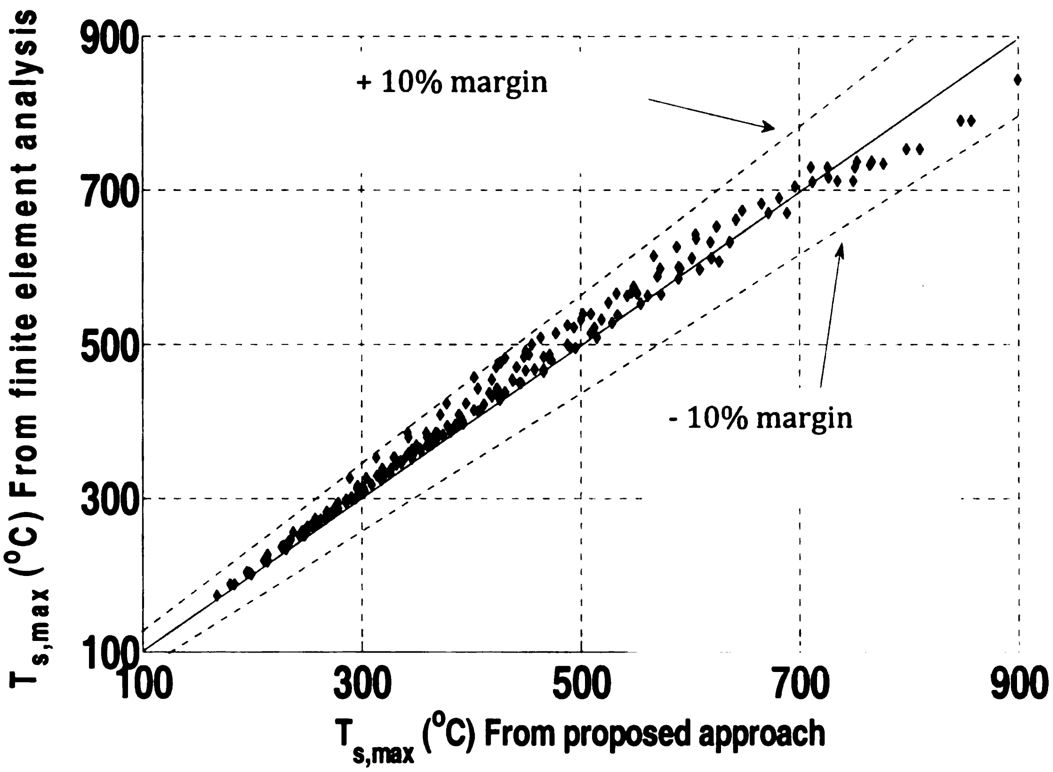

(a) Maximum steel temperature

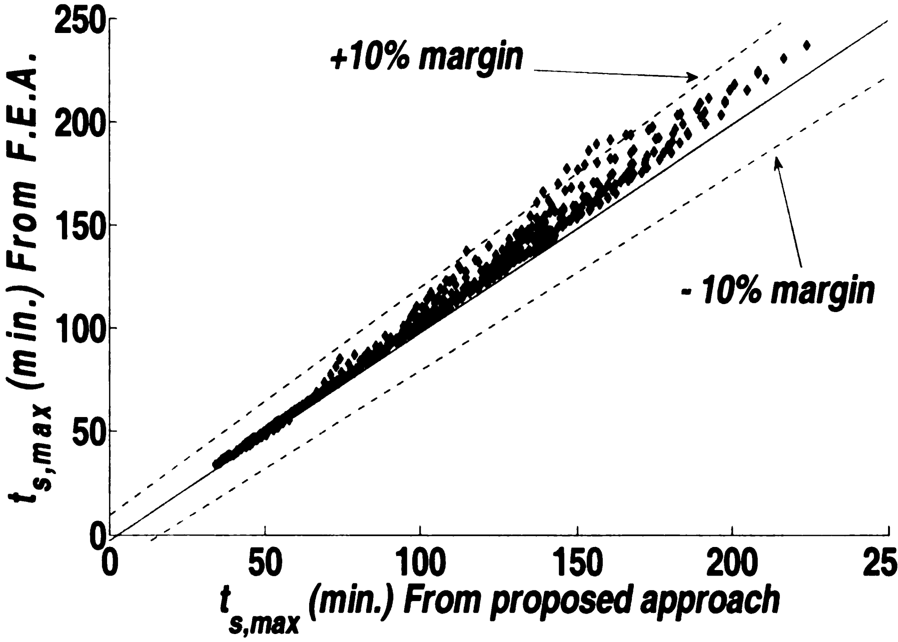

(b) Time for reaching maximum steel temperature

Fig. 6.3: Comparing predictions from proposed equations and from finite element analysis for *Ts,max* and *ts,max*

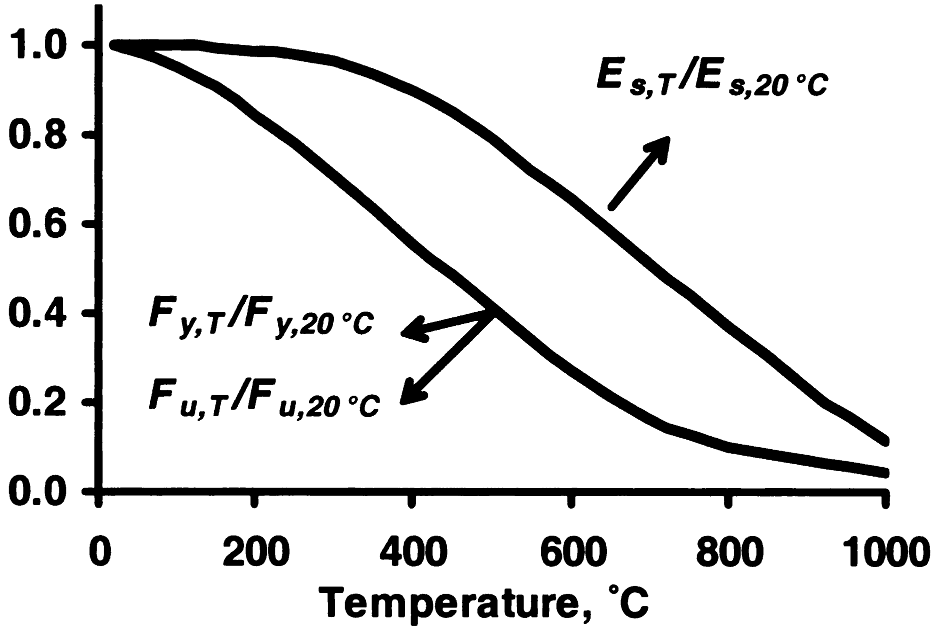

Fig. 6.4: Variation of *Es* and *Fy* as a function of steel temperature

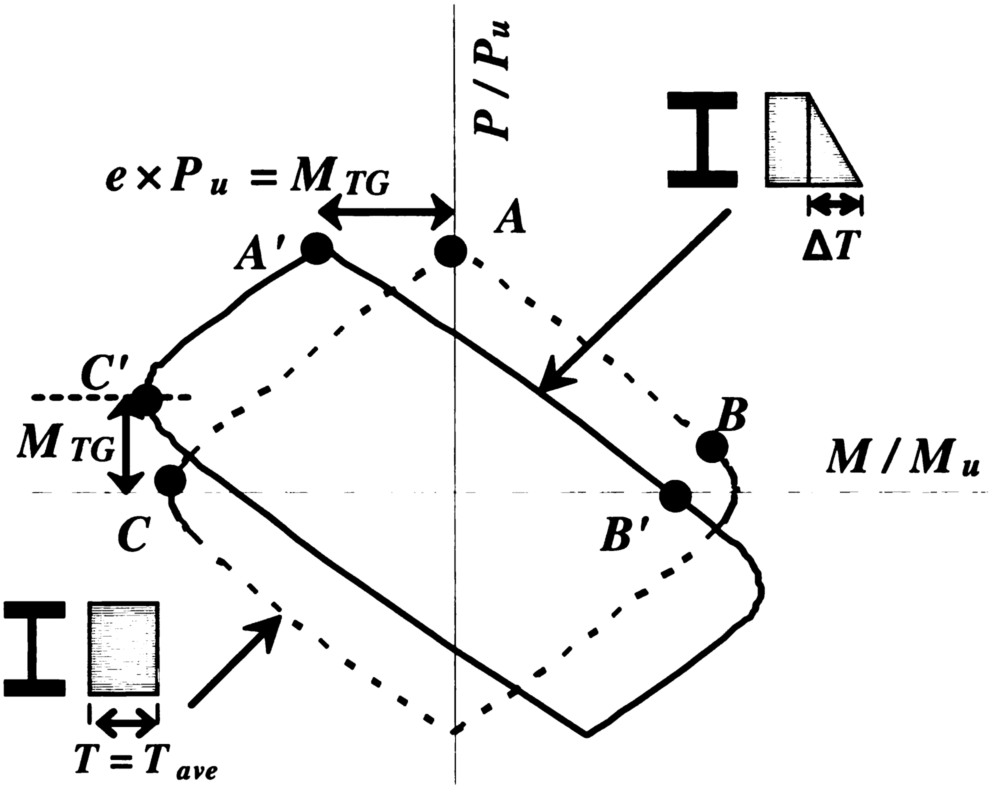

Fig. 6.5: Characterizing P-M diagram for a WF section with thermal gradient in the strong direction

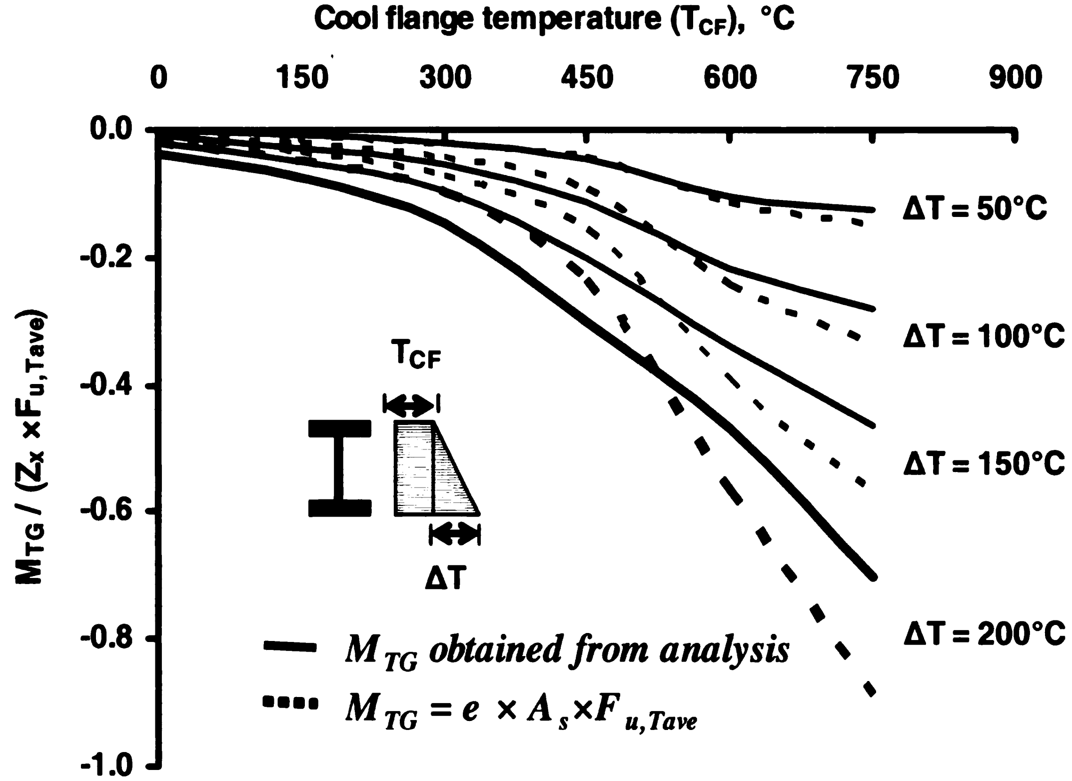

Fig. 6.6: Comparing the shift in moment (*MTG*) as estimated from simplified approach with that obtained from analysis

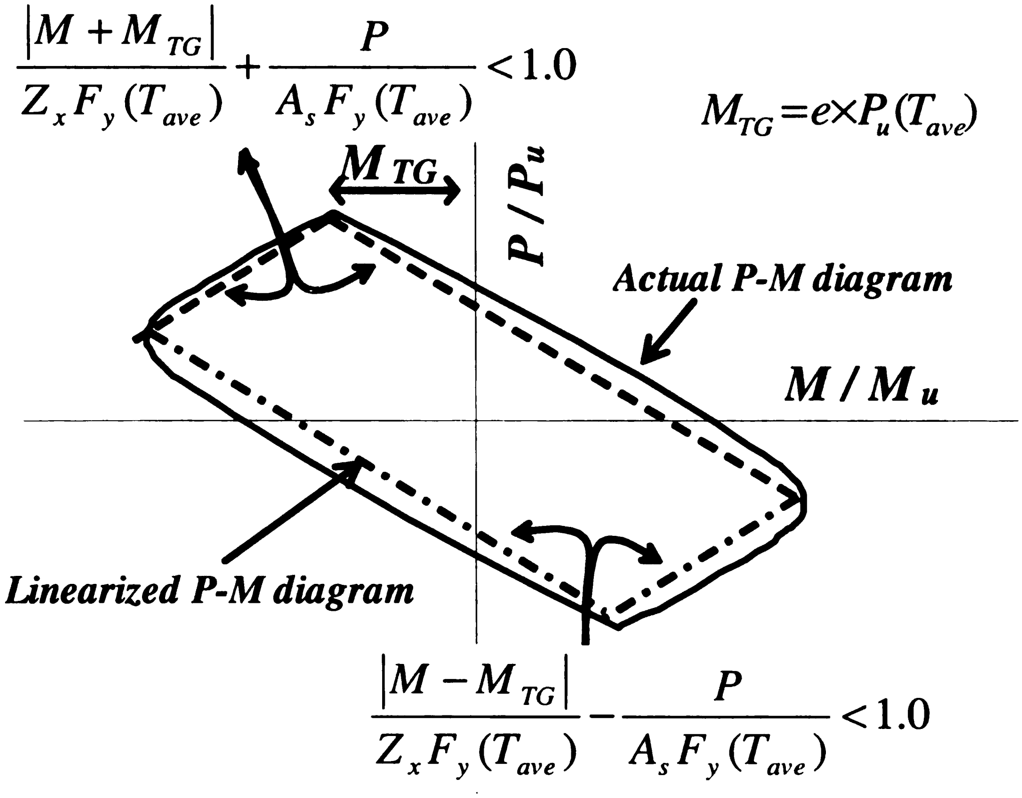

Fig. 6.7: Linearized P-M diagram for WF sections with linear thermal gradient along the strong direction

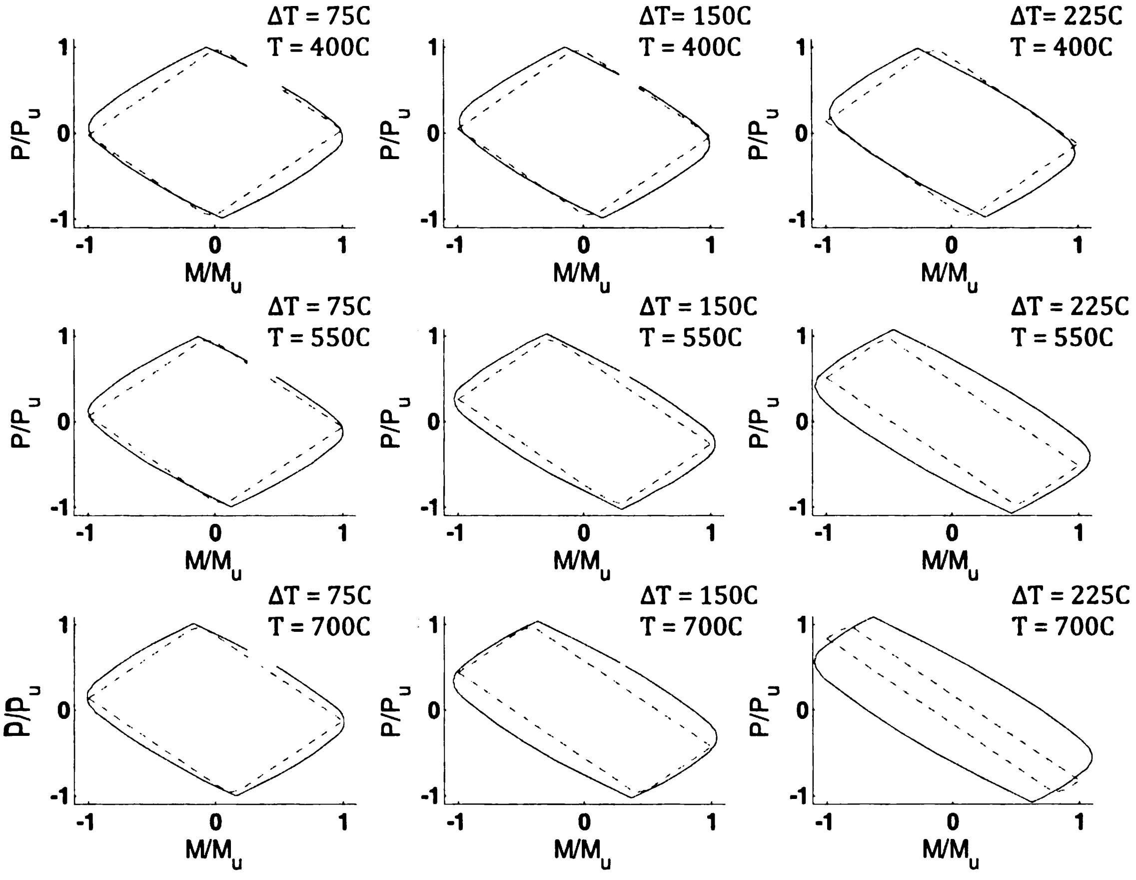

Fig. 6.8: P-M diagrams obtained from analysis (solid curves) and as predicted by Eq. 14 (dashed curves) for W24x76 section with different linear thermal gradients along its strong axis (ΔT=*Ts,HF-Ts,CF*)

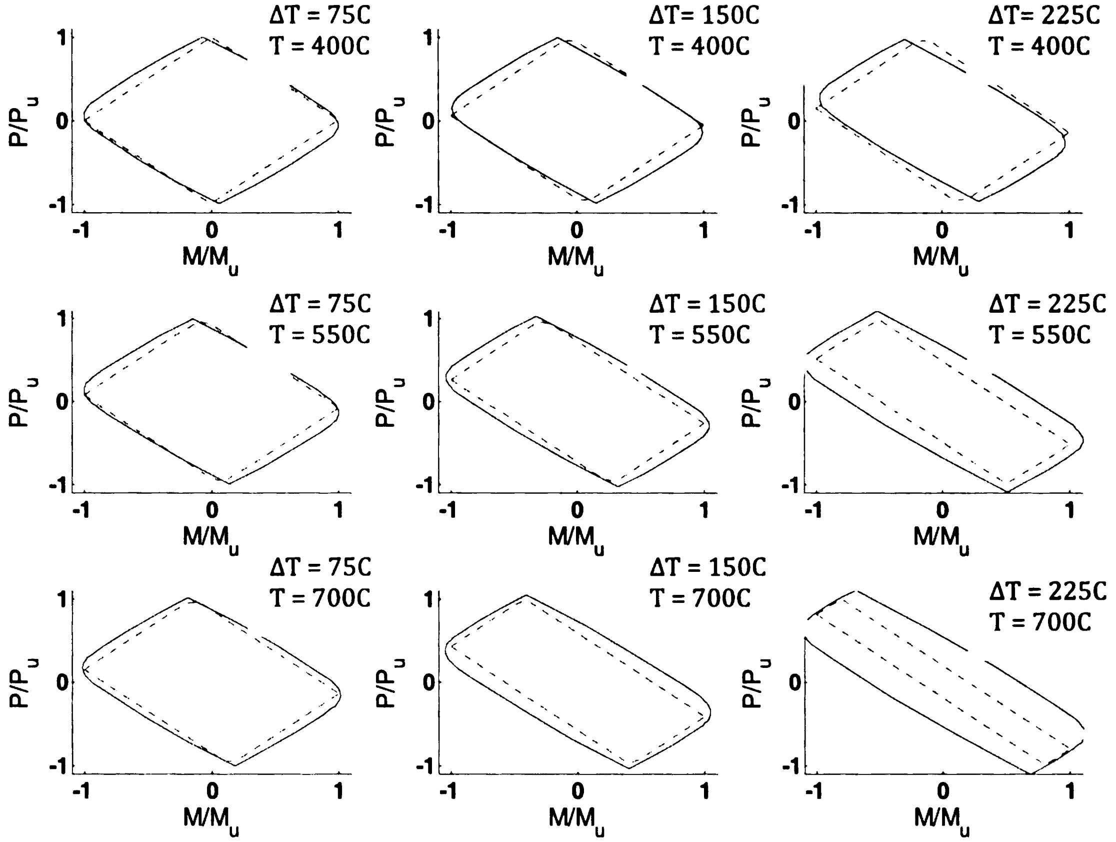

Fig. 6.9: P-M diagrams obtained from analysis (solid curves) and as predicted by Eq. 14 (dashed curves) for W14x311 section with different linear thermal gradients along its strong axis (ΔT=*Ts,HF-Ts,CF*)

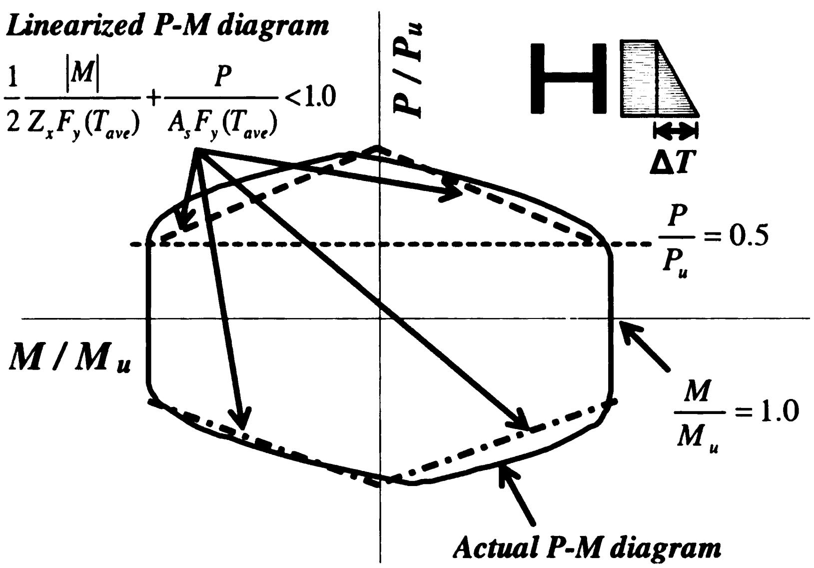

Fig. 6.10: Linearized P-M diagram for a WF section with thermal gradient in weak direction

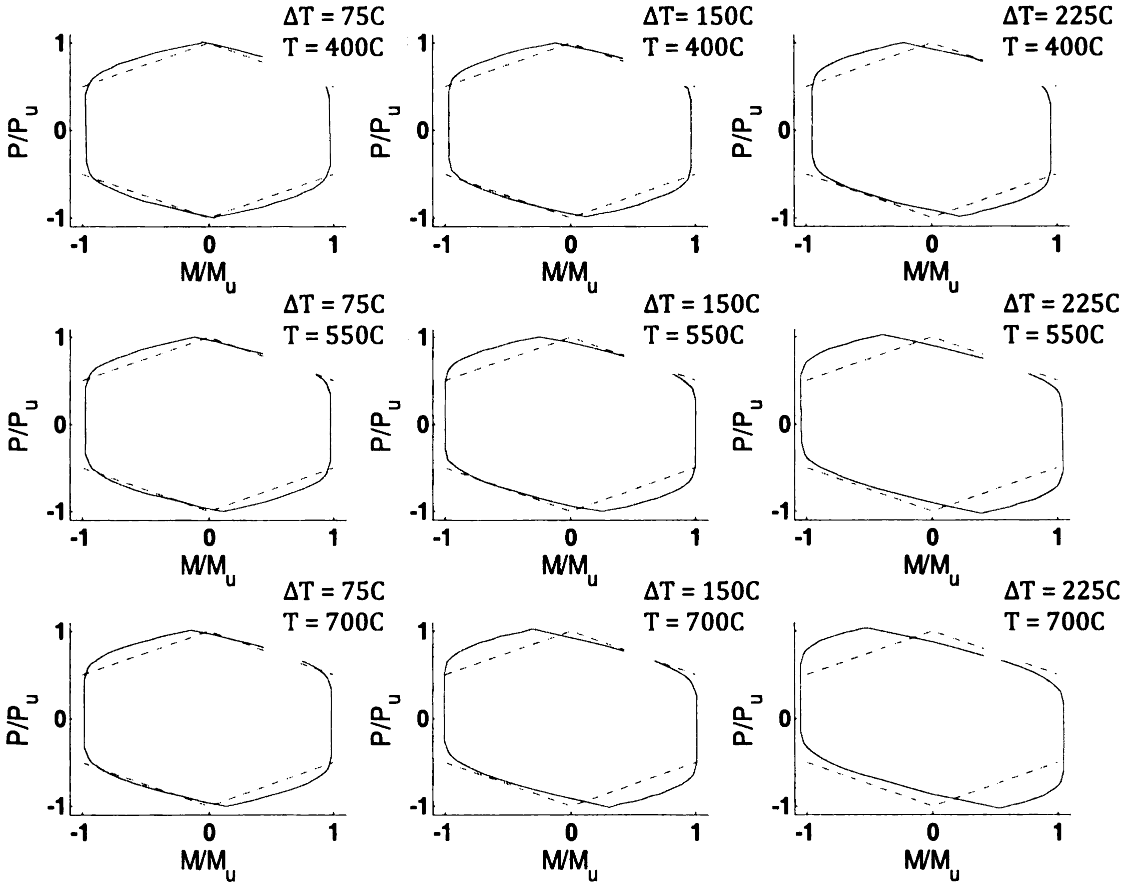

Fig. 6.11: P-M diagrams obtained from analysis (solid curves) and as predicted by Eq. 15 (dashed curves) for W24x76 section with different linear thermal gradients along its weak axis (ΔT=*Ts,HF-Ts,CF*)

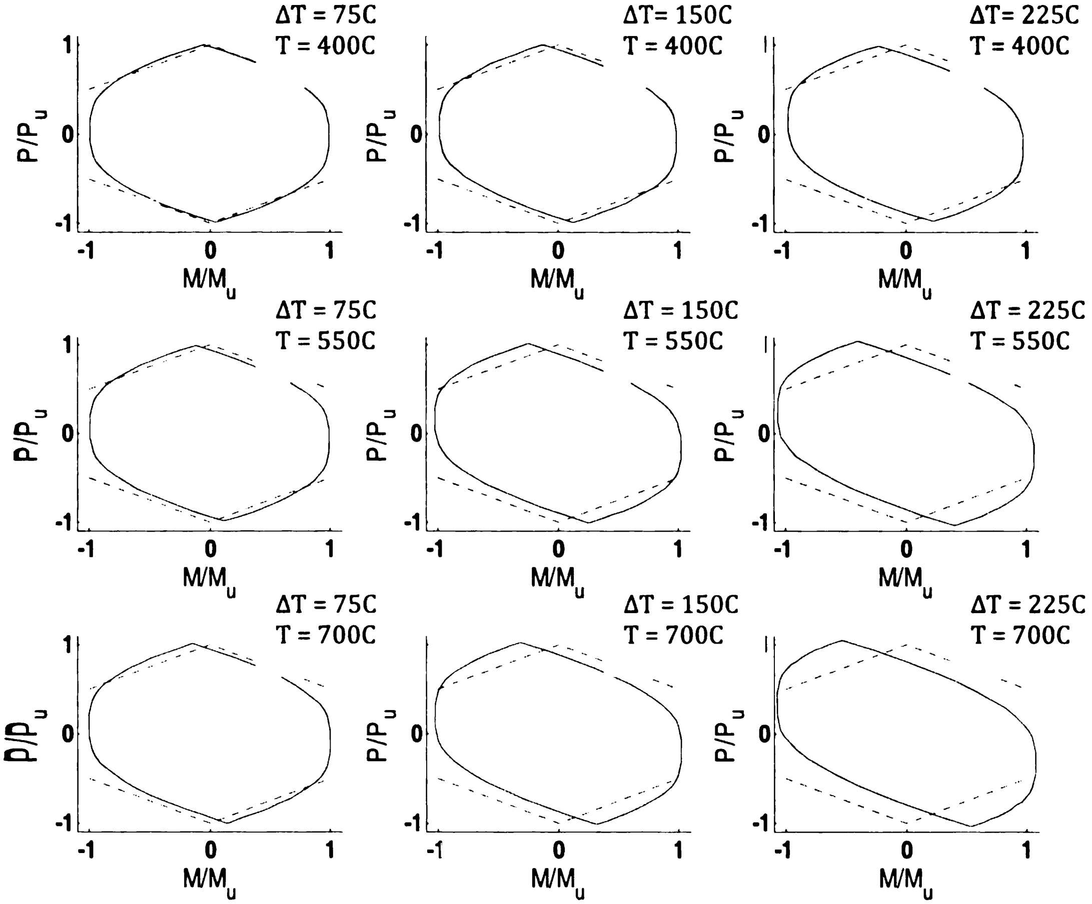

Fig. 6.12: P-M diagrams obtained from analysis (solid curves) and as predicted by Eq. 15 (dashed curves) for W14x311 section with different linear thermal gradients along its weak axis (ΔT=*Ts,HF-Ts,CF*)

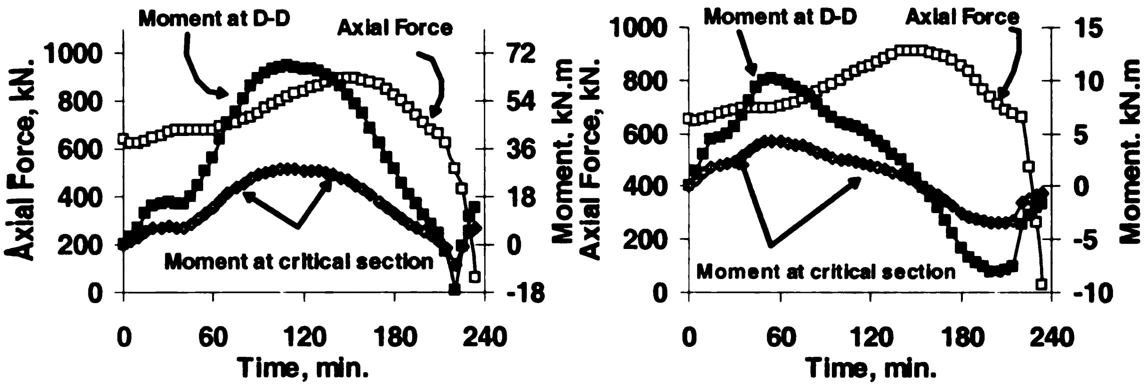

(a) Strong axis (C1-S)

(b) Weak axis (C1-W)

Fig. 6.13: Measured fire induced axial force and bending moment in the tested beam-columns (Refer to Fig. 3.3 for details of tested beam-columns)

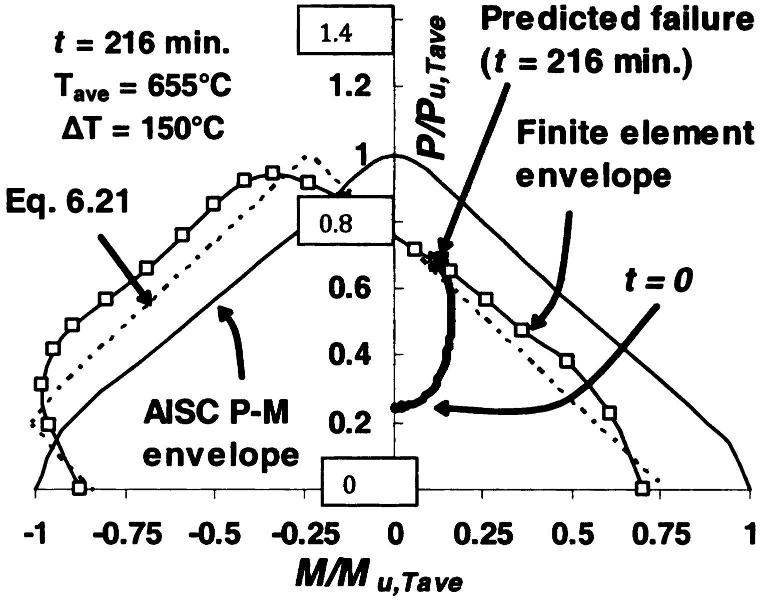

(a) Plastic P-M diagrams at 216 minutes of fire exposure

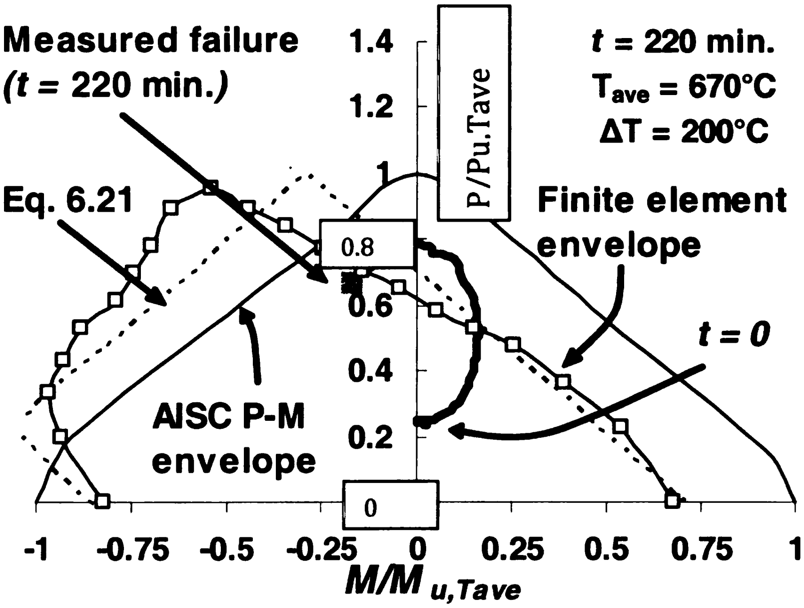

(b) Plastic P-M diagrams at 220 minutes of fire exposure

Fig. 6.14: Predicted P-M capacity envelopes for the tested beam-column C1-S at various fire exposure times

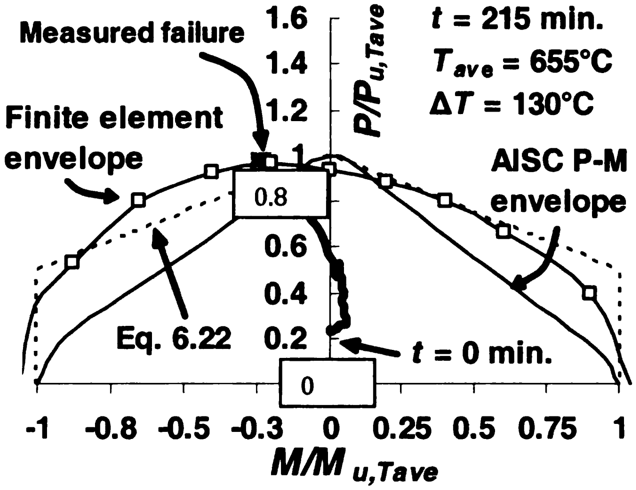

Fig. 6.15: Predicted capacity envelop for the tested beam-column C1-W

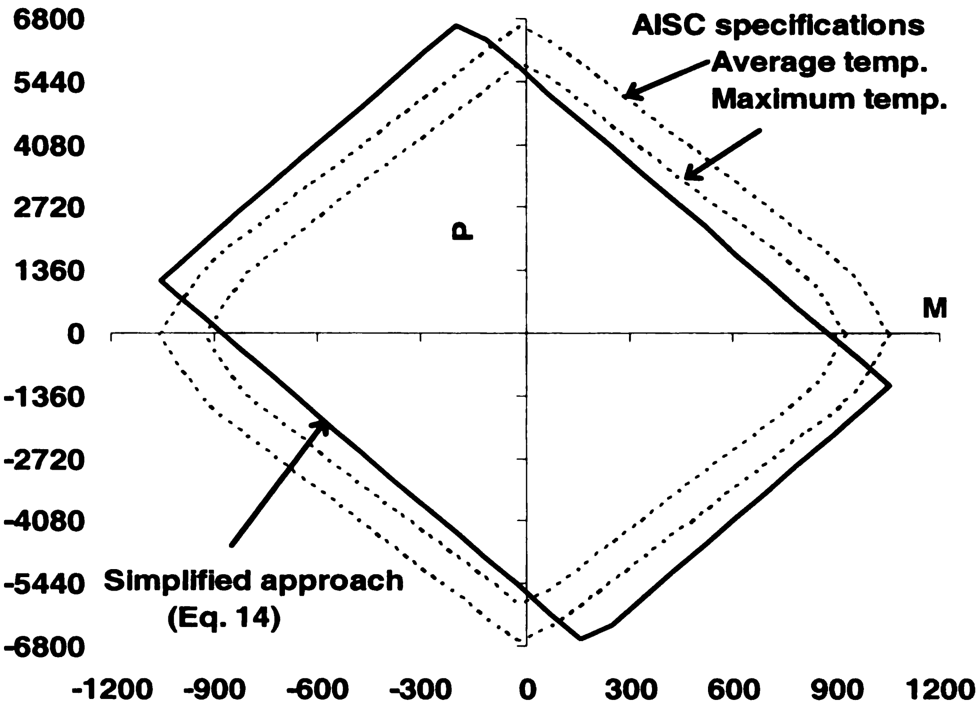

(a) At 2 hours of ISO 834 fire exposure

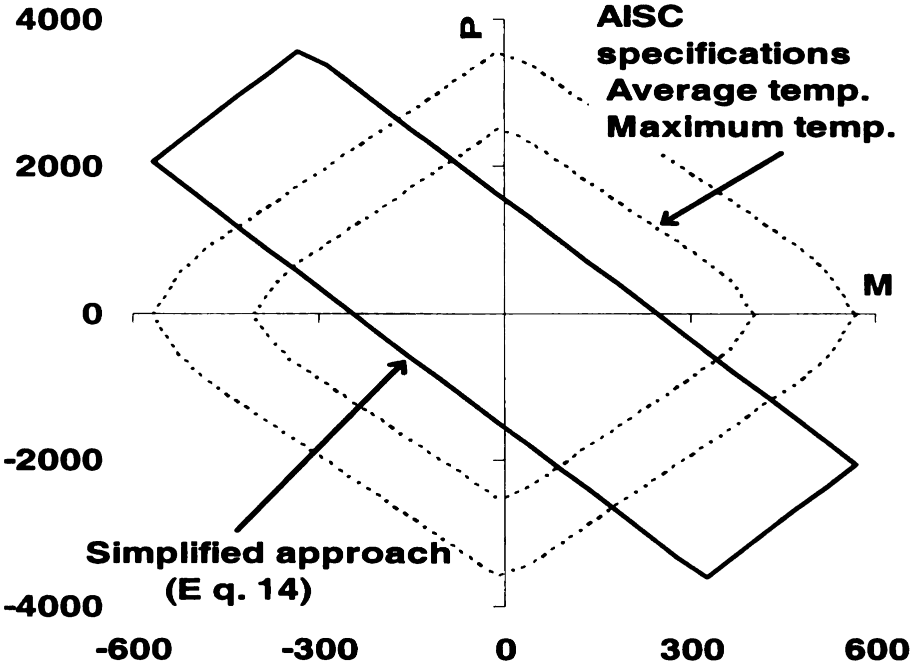

(b) At 3 hours of ISO 834 fire exposure

Fig. 6.16: P-M diagrams for W14x176 using uniform temperature and thermal gradient

CHAPTER SEVEN

METHODOLOGY FOR PREDICTING FIRE RESPONSE OF RESTRAINED STEEL BEAMS

7.1 GENERAL

This chapter presents the development of a simple approach for evaluating fire induced forces and deflections in restrained steel beams at any given fire exposure time. The approach utilizes basic equilibrium and compatibility principles to compute fire-induced forces and deflections in the beam. The validity of the proposed approach is established by comparing fire response predictions with results obtained from rigorous finite element analysis as well as from measured data in fire resistance tests. In addition, predictions from the proposed equations are compared with fire resistance estimates from current codes of practice. The applicability of the proposed approaches to design situations is illustrated through numerical example.

7.2 CHARACTERIZING THE FIRE RESPONSE

A restrained steel beam, shown in Fig. 7.1(a), when exposed to fire, develops significant internal forces (axial force and bending moment) and large deflections due to the effect of restraints and deterioration in steel properties with increasing temperatures. If the beam (shown in Fig. 7.1(a)) is laterally braced, and is made of a compact section (i.e. no local buckling), then the beam undergoes three distinct stages, as shown in Fig. 7.1(b and c) when exposed to fire. In Stage I, elastic response dominates the behavior wherein the beam expands as a result of continuous heating, and compressive axial force and bending moment develop in the beam due to the effect of end-restraints. Fire-induced internal forces and deflections continue to increase until yielding occurs in the beam. Elasto-plastic response dominates the behavior in Stage II, as shown in Fig. 7.1(b). As steel temperature continues to increase with fire exposure time, softening of steel causes larger deflections and rotations until the first plastic hinge develop in the beam. The plastic hinge, which forms at the location of maximum bending moment in the beam, causes sudden increase in deflection as shown in Fig.7.1(c), which leads to reduction and then reversal of the axial force in the beam from compressive to tensile force. The beam enters a catenary phase in Stage III when the fire-induced compressive axial force vanishes as shown in Fig. 7.1(b). In the catenary phase, tensile force develops in the beam and the load bearing mechanism gradually changes form flexural to cable (tensile) until failure occurs by rupture of the beam (or in the connections). When the beam undergoes the above three stages, it is assumed that the connections continue to perform elastically. Therefore, fire-induced forces and rotations in the beam must not exceed the connections capacity.

In the following sections, the response of a restrained steel beam will be traced in temperature domain. The steel beam is assumed to be braced against lateral or torsional buckling. Also, the effect of local buckling is ignored in the development of the proposed approach since in most building applications compact sections are used. It will be shown through comparison with results from finite element analysis (that takes local buckling into consideration) that the occurrence of local buckling has a minor effect on the fire response of restrained steel beams. Under realistic simplifications, expressions for evaluating critical internal forces and deflections are derived based on equilibrium and compatibility principles. These expressions will be derived for monotonic heating with linear thermal gradient through the cross section. The monotonic heating represents temperature in steel that results due to exposure to a standard fire wherein temperature always increases with time. Influence of realistic fires, with cooling phase, will then be introduced. The developed expressions are aimed to serve as a simple, rational, and engineering approach for fire design of restrained steel beams, over a wide range of scenarios.

7.2.1 Fire Induced Forces

As the beam expands with increasing temperature in Stage I, the beam develops significant compressive axial force due to the presence of axial restraints (see Fig. 7.1(b)). At this stage, the response of the beam is in the elastic range but with reduced properties of steel due to increasing temperature. Since the midspan deflection under service load at this stage is very small compared to the beam length ($\Delta e << L$) and can be neglected, the fire-induced axial force can be obtained by applying compatibility principles as:

$$\delta_e = \delta_{th} - \delta_k \Rightarrow \frac{PL}{k_E E_s A_s} = \alpha (T-20) L - 2\left(\frac{P}{K_a}\right) \qquad [7.1]$$

where *δe* and *δth,* are the elastic axial deformation and thermal expansion in the beam, respectively, and *δk* is the elastic deformation in the restraining elements modeled as axial springs with stiffness *Ka* (as shown in Fig. 7.1(a)). *P* is the fire-induced axial force in the beam at steel temperature *T*, *Es* and *α* are the elastic modulus and coefficient of thermal expansion of steel, respectively, *kE* is the temperature-dependent reduction factor for *Es* based on average steel temperature, and *As* is the cross sectional area of the beam.

Solving Eq.[7.1] for *P*, with algebraic manipulation, produces:

$$P = (T - 20)F_A \times F_y A_s \qquad [7.2]$$

where *Fy* is yield strength of steel at ambient temperature, and *FA* is the axial restraint factor defined as:

$$F_A = \frac{\alpha E_s}{F_y}\left(\frac{k_E K_a L/(E_s A_s)}{2k_E + K_a L/(E_s A_s)}\right) \qquad [7.3]$$

Since the beam is most likely to be exposed to fire from three sides, it will develop thermal gradient that causes a thermal bowing in the beam. If we assume that the thermal gradient is linear across the section and uniform along the entire span of the beam, the rotational restraints will restrain the thermal bowing of the beam and thus cause an additional bending moment (*MG*) in the beam as shown in Fig. 7.2(a). If the thermal gradient is linearly approximated as ((*TTF* - *TBF*)/*d*), where *d* is the depth of the section, *TTF* and *TBF* are the temperatures of top and bottom flanges, respectively, then the elastic *MG* can be computed using superposition and compatibility principles as:

$$\theta_e = \theta_{th} - \theta_k \quad \Rightarrow \quad \int_0^{L/2} \frac{M_G}{E_s I}\,dx = \frac{L}{2}\frac{M_G}{k_E E_s I}$$

$$= \alpha\left(\frac{T_{BF} - T_{TF}}{d}\right)\frac{L}{2} - \left(\frac{M_G}{K_r}\right) \qquad [7.3]$$

in which *θe* and *θth,* are the elastic and free thermal rotations in the beam, respectively, and *θk* is the elastic rotation in the restraining elements modeled as rotational springs with rotational stiffness *Kr* (as shown in Fig. 7.1(a)). The reduction in steel elastic modulus (*kE*) is computed based on average steel temperature. *MG* is the bending moment induced by thermal gradient, and *I* is the second moment of area of the section in the direction of thermal gradient.

Solving Eq [7.3] for *MG,* with algebraic manipulation, produces the following:

$$M_G = \left(\frac{\Delta T}{2} F_R\right) F_y S_x \qquad [7.4]$$

where *Sx* is the elastic section modulus, Δ*T* = *TTF* - *TBF,* and the factor *FR* is the rotational restraint coefficient and is defined as follows:

$$F_R = \frac{\alpha E_s}{F_y}\left(\frac{k_E K_r L/(E_s I)}{2k_E + K_r L/(E_s I)}\right) \qquad [7.5]$$

Also, thermal gradient will cause an increase in the curvature of the beam, at midspan. If the beam is not rotationally restrained then the "*free*" thermal curvature that results from a linear thermal gradient will be (*ψth* = α(*TTF* – *TBF*)/*d*). However, since the beam is rotationally restrained, the "*resultant*" thermal curvature *ψth,r* can be obtained by superposition as:

$$\psi_{th,r} = \alpha\frac{\Delta T}{d} - \frac{M_G}{k_E E_s I} = \alpha\frac{\Delta T}{d}\left(1 - \frac{F_y F_R}{\alpha E_s k_E}\right) \qquad [7.6]$$

Fire-induced forces (*P* and *MG*) build up in the beam (as shown in Fig. 7.1(b)) as steel temperature increases until yielding takes place. The increase in elastic stress in the beam, in Stage I, can be used as an indicator for the occurrence of yielding. If the thermal gradient is linear then the mechanical strain is also linear, and thus the build-up of elastic stress in the beam can be evaluated using the following equation:

$$F_{s,\max} = \frac{P}{A_s} + \frac{M_{\max}}{S_x} \qquad [7.7]$$

where *Fs,max* is the maximum stress in the steel section, *Mmax* is the maximum bending moment in the beam. Initially and before yielding, the increase in elastic deflection is small, and thus the slight increase in bending moments due to P-Δ effect in Stage I can be neglected, and Eq. [7.7] can be used until yielding takes place in the section.

Because Eq. [7.7] checks for yielding of steel, *Mmax* is the maximum bending moment at either the support or midspan. Under thermal gradient, additional bending moment (*MG*) is generated if the beam is rotationally restrained. The gradient-induced bending moment (*MG*) will cause compression in the hotter (bottom) fibers of the section. Therefore, as shown in Fig. 7.2(c and d), the midspan bending moment due to gravity load (*Mm*) will be reduced by a magnitude of *MG*, while the bending moment at support (*Ms*) will be increased by a magnitude of *MG*. Also, if the beam-to-column connection is built such that the axial restraint stiffness acts eccentrically to the centroid of the beam, then an additional bending moment ($M = P \times y$) is generated. This is shown in Fig. 7.2(b) where the topology of the beam-to-column connection causes the axial restraint force to be eccentric by a distance y measured from the centroidal axis of the section. Therefore, *Mmax* can be generally computed by accounting for all the previously described bending moments using the following relationship:

$$M_{\max} = \max(M_m - M_G + P \times (\Delta_e - y), M_s + M_G + P \times y) \qquad [7.8]$$

By substituting Eqs [7.2], [7.4], and [7.8] into Eq. [7.7] we obtain:

$$F_A F_y \left(1 \mp \frac{YA_s}{S_x} \right) (T - 20) \mp \frac{\Delta T}{2} \left(F_R F_y \right) = k_y F_y - \frac{M_{\circ}}{S_x} \qquad [7.9]$$

where the positive/negative sign depends on whether *Mo* is either *Ms* or *Mm,* respectively. $Y = \Delta e - y$, where y is the eccentricity of axial restraint force. The elastic deflection (Δe) can be neglected in case of uniform heating, however, in case of thermal gradient; the elastic deflection is significant and must be accounted for. The computation of elastic deflection will be explained in subsequent sections.

Equation [7.9] is nonlinear since all the terms are dependent on steel temperature. In order to solve Eq. [7.9] for the temperature at which yielding occurs in steel (*Ty*), the temperature-dependent factors *FA*, *FR* and *ky* in Eq. [7.9] are approximated as follows.

The variation of *FA* and *FR* with temperature, using ASCE and EC3 high temperature properties of steel, is plotted in Fig 7.3. The trends in the figure show that for temperatures below 550°C, *FA* and *FR* are almost constant for restraint condition (x) less than 100%. Based on this, the temperature-dependent factors *FA* and *FR* can be assumed constant for a given restraint condition based on the temperature reduction factors for the elastic modulus of steel (*kE*) as specified in Eurocode and ASCE manual. This approximation for *FA* and *FR* is reasonable since for typical steel structures exposed to fire, steel yields at temperatures below 550°C. For *T* < 550°C and *x* < 1, where *x* is either *KaL/(EsAs) or KrL/(EsI),* the following approximation is used:

$$F_x = \left(\frac{k_E x}{2k_E + x} \right) \approx \frac{a_1 x}{2a_1 + x} \tag{7.10}$$

The coefficient *a1* in Eq. [7.10] is dependent on the high temperature reduction factors for elastic modulus of structural steel which vary depending on the provisions for steel properties specified in different codes. The coefficient *a1* is obtained by regression through minimizing the "*sum of absolute errors*" for *Fx* in the range *T* < 550°C:

- In case of steel properties as specified in Eurocode 3: *a1* = 0.6.
- In case of steel properties as specified in ASCE manual: *a1* = 0.6829.

The temperature-dependent reduction factor for steel yield strength is approximated as:

$$k_y \approx 1 - a_2 T \tag{7.11}$$

where the coefficient *a2* is also dependent on the material properties as specified in the codes and it is obtained through regression analysis for *ky* in the range of *T* < 600°C as:

- In case of Eurocode 3 steel properties: *a2* = 0.0013.

- In case of steel properties as specified in ASCE manual: *a2* = 0.0008.

By substituting Eqs. [7.10] and [7.11] into Eq. [7.9] the following relationship is obtained for the critical value of *Ty* evaluated at both critical sections (midspan and support sections):

$$T_y = \frac{1 - M_o / M_y - 0.5 F_R \Delta T}{F_A\left(1 + YA_s / S_x\right) + a_2}, \quad Ty < 600°\text{C} \qquad [7.12]$$

In Eq. [7.12], *Mo* is the maximum of *Mm* and *Ms*, *Y* = Δ*e* – *y*, where *y* is the eccentricity of the axial restraint force, *FR* and *FA* are the rotational and axial restraint factors, respectively, and are defined as:

$$F_R = \frac{\alpha E_s}{F_y}\left(\frac{a_1 K_r L/(E_s I)}{2a_1 + K_r L/(E_s I)}\right) \qquad [7.13]$$

$$F_A = \frac{\alpha E_s}{F_y}\left(\frac{a_1 K_a L/(E_s A_s)}{2a_1 + K_a L/(E_s A_s)}\right) \qquad [7.14]$$

The maximum fire-induced compressive force generated in the beam can be computed by substituting *Ty* into Eq. [7.2]:

$$P_{c,\max} = F_y A_s \times F_A\left(T_y - 20\right) \qquad [7.15]$$

As plasticity spreads throughout the section, the axial compressive force reduces until it reaches zero at temperature *Tc* as shown in Fig 7.1(b). The catenary action is initiated at *Tc* upon the development of a first plastic hinge in the restrained beam. Since *P* = 0 at *Tc*, the condition for developing a plastic hinge can be written as:

$$M_{\circ} \mp M_{G} = k_{y}(T_{c})F_{u}Z_{x} \qquad [7.16]$$

where *Fu* is the ultimate tensile strength of steel at ambient temperature, and *Zx* is the plastic sectional modulus. Due to lack of information, the degradation of the ultimate tensile strength of steel (*Fu*) in Eq. [7.16] as a function of steel temperature is implicitly assumed to follow the same degradation (*ky*) as that of yield strength (*Fy*). Using the approximation for *ky* as described earlier, the temperature at catenary action can be computed as:

$$T_{c} = \frac{1}{a_{2}}\left(1 - \frac{M_{\circ}}{M_{u}} - \frac{M_{y}}{M_{u}}\frac{F_{R}\Delta T}{2}\right) \qquad [7.17]$$

where *Mo* is the maximum of *Mm* and *Ms*, *Mu* = *FuZx* and *My* = *FySx*. Assuming no local buckling, and knowing that *P* = 0 at *T* = *Tc*, then using the room temperature values of midspan and support moments (*Mo* = max(*Mm* and *Ms*)) in Eq. [7.17] can provide a reasonable approximation for the steel temperature at catenary point (*Tc*). It will further be shown through comparison to results from rigorous finite element analysis that the error in computing *Tc* does not severely affect the evaluation of deflection.

At Stage III, the tensile force in the beam increases until it reaches a maximum value at which full plasticity is achieved at the two sections (at midspan and at support). After that, the tensile force drops in the beam following the same trend as that of the degradation of the steel yield strength with temperature. This is illustrated in Fig. 7.4 which shows the development of tensile force in the restrained beam during catenary phase. If the connections can sustain the tensile force, then we can obtain a conservative approximation for the maximum tensile force in the beam through extending a line between the point of maximum compressive force (*Ty, Pc,max*) and the point of catenary (*Tc, P* = 0), as shown in Fig. 7.4. Using this approach, the temperature at which maximum catenary force occurs in the beam is the temperature *T* that satisfies the following relation:

$$P_{c,\max} - P_{c,\max}\left(\frac{T - T_y}{T_c - T_y}\right) = -k_y(T)F_yA_s \qquad [7.18]$$

*Pc,*max is the maximum compressive force in the beam computed using Eq.[7.15] at steel temperature *Ty*. Since the maximum tensile catenary action force is expected to occur at temperatures beyond 500°C, the yield reduction factor (*ky*) can be approximated as:

$$k_y \approx a_3 - a_4 T, \qquad 500^\circ\mathrm{C} \le T \le 900^\circ\mathrm{C} \qquad [7.19]$$

where *a3* and *a4* are regression coefficients that are dependent on steel properties:

- For steel properties as specified in Eurocode 3: *a3* = 1.139; *a4* = 0.0013
- For steel properties as specified in ASCE manual; *a3* = 1.329; *a4* = 0.0014

By direct substitution, an expression for estimating the temperature at which the catenary force is maximum is obtained as:

$$T_{ten,\max} = \frac{T_c T_y F_A + a_1 a_3 \left(T_c - T_y\right)}{T_y F_A + a_1 a_4 \left(T_c - T_y\right)} \qquad [7.20]$$

The temperature obtained from Eq. [7.20] is used to compute the maximum tensile catenary force as:

$$P_{ten,\max} = F_y A_s \left(a_3 - a_4 T_{ten,\max}\right), \qquad 500^\circ\mathrm{C} \le T_{ten,\max} \le 900^\circ\mathrm{C} \qquad [7.21]$$

7.2.2 Fire Induced Deflection

Elastic deflection at $T = Ty$ can be obtained using conventional room-temperature deflection expressions found in structural analysis textbooks [19], but the revised steel elastic properties, reduced as a function of temperature, are to be substituted in place of room-temperature steel properties. Influence of thermal gradient on elastic deflection can be quite significant, and can be incorporated by direct integration of the "*resultant*" thermal curvature in Eq. [7.6]. For restrained beam with uniformly distributed load, subjected to linear thermal gradient along the depth of the cross section, the total elastic midspan deflection is:

$$\Delta_e = \left(\frac{5wL^4}{384 k_E E_s I} + \alpha \frac{L^2}{8} \frac{\Delta T}{d} \right) \left(1 - \frac{F_R}{a_1} \frac{F_y}{\alpha E_s} \right) \qquad [7.22]$$

where the reduction in elastic modulus (*kE*) is computed based on the average steel temperature. The second order effect on the elastic deflection can be neglected since the total elastic deflection is generally small.

Elasto-plastic temperature-deflection history of the restrained beam can be conservatively evaluated based on linear interpolation between the deflection at the end of elastic phase (at $T = Ty$) and at the point of catenary action of the beam (at $T = Tc$), as shown in Fig. 7.6.

For evaluating the deflection at point of catenary action (Δc), the condition $P = 0$ at $T = Tc$ is utilized. Fig. 7.5 shows a schematic of approximating the deflected shape of the beam, only half of the beam is shown due to symmetry. When the beam expands under the influence of temperature, it compresses the axial spring by a magnitude of $\delta = P/Ka$. However, when the axial force $P = 0$, the value of δ is zero. Using this information, a compatibility equation can be written (see Fig. 7.5) as:

$$\Delta_c^2 = \left[\left(\frac{L}{2}\right)'\right]^2 - \left[\frac{L}{2} + \delta\right]^2 = \left(\frac{L}{2} + \alpha\frac{L}{2}(T_c - 20) - \delta_{pl}\right)^2 - \left(\frac{L}{2}\right)^2 \qquad [7.23]$$

where (*L*/2) is half the deformed length of the beam. The plastic permanent shortening (δpl) in the beam length (due to compression) is small and can be neglected as compared to the thermal expansion of the beam. Solving for Δc and neglecting second order terms we obtain:

$$\Delta_c = \frac{L}{2}\sqrt{2\alpha(T_c - 20)} \qquad [7.24]$$

Using linear interpolation, as shown in Fig 6, the deflection between *Ty* and *Tc* can be obtained as:

$$\Delta = \Delta_y + \frac{\Delta_c - \Delta_y}{T_c - T_y}\left(T - T_y\right), \quad Ty < T < Tc \qquad [7.25]$$

Using Eq. [7.25], a limiting temperature based on a deflection limiting criterion Δ = *LF* can be obtained as:

$$T_{DLS} = T_y + \frac{\left(L_F - \Delta_y\right)\left(T_c - T_y\right)}{\left(\Delta_c - \Delta_y\right)} \qquad [7.26]$$

where *TDLS* is steel temperature at deflection limit state, *LF* is the deflection limit state and is usually taken as $\left(\frac{1}{30} - \frac{1}{20}\right)L$. It will be shown through a design example that Eq. [7.26] can effectively be used as a guideline for fire design of restrained beam based on deflection criteria.

7.2.3 Influence of Fire Scenario

The temperature rise in steel, as a function of fire exposure time, depends on section geometry, insulation, and fire scenario. Generally, from a structural fire design point of view, fire scenarios are classified into two types, namely; standard and design or "*realistic*" fire scenarios. Examples of standard and typical design fires with resulting average steel temperatures are compared in Fig. 7.7.

In case of a standard fire exposure, the fire and steel temperatures increase continually with time, as shown in Fig. 7.7. However, because of depletion of fuel and/or oxygen, a realistic fire (also known as design fire) in buildings undergoes a decay (cooling) phase after achieving a maximum value of $T_{f,max}$ at $t = t1$ as shown in Fig. 7.7. In the early stages of the cooling phase, the temperature of the fire is still higher than the average temperature of the steel in the beam (due to lag effect) and therefore steel temperature continues to increase for a little while during the cooling phase of fire until steel temperature reaches a maximum value of $T_{s,max}$ at $t = t_{s,max}$, as shown in Fig. 7.7, after which, the steel temperature starts to decline gradually.

The computation of steel temperature as a function of fire exposure time is beyond the scope of this study. Eurocode 3 provides simple expressions for calculating steel temperature at small time increments [2] both under standard and design fires. These incremental expressions are the finite difference solutions of the approximated one-dimensional heat transfer differential equation (assuming constant steel temperature) for protected and unprotected steel sections. The methods specified in the Eurocode can be used to evaluate the time-temperature history in fire exposed steel sections.

While under standard fire steel properties continue to deteriorate due to increasing temperature, the decay phase of a design fire leads to a recovery of strength and stiffness in steel as a result of decreasing temperature in steel. Also, the decay phase of a design fire leads to cooling and contracting of steel and this contraction causes an increase in tensile stresses in the beam and thus leads to recovery of some deformations in the beam. The total recovered deformation in the beam depends on the stress state of steel prior to the start of cooling of the beam. There is a lack of information on the behavior of steel in the cooling phase under realistic fires. Generally, it is conservative to assume that the elastic deflection of steel (Δy) is recovered by the end of the decay phase of a design fire.

In order to evaluate the tensile force that results due to the shrinkage of steel, Fig. 7.8 compares the deflected shape of the beam prior to fire exposure and after cooling of steel. In Fig. 7.8, the half length of the beam prior to start of the cooling of steel (at $t = ts,max$) is denoted as $(L/2)$ and is equal to the original half length plus the change in length due to the effects of thermal expansion and plastic shortening. For typical cases of design, plastic shortening δpl can be neglected as compared to the thermal expansion experienced by the beam. For the approximation depicted in Fig. 7.8, the following compatibility relationship can be written after the complete cooling of steel:

$$\left(\frac{L}{2}+\alpha\frac{L}{2}(T_{s,\max}-20)-\delta_{pl}\right)^2-(\Delta_{\max}-\Delta_{rec})^2=\left(\frac{L}{2}-\frac{P_{sh}}{2K_a}\right)^2 \qquad [7.27]$$

The maximum tensile force that results due to the shrinkage of steel (*Psh*) at the end of the decay phase can be obtained by solving Eq. [7.27] and neglecting squared terms as they tend to be very small:

$$P_{sh}=\left(\alpha L(T_{s,\max}-20)-\frac{2}{L}(\Delta_{\max}-\Delta_{rec})^2\right)K_a \qquad [7.28]$$

Δmax is the maximum deflection achieved in the beam and can be computed using Eq. [7.25] at *Ts* = *Ts,max*, and Δrec is the recovered deflection due to the cooling of steel, and can be assumed to be equal to the total elastic deflection Δy.

7.3 COMPARISON TO TEST RESULTS

The proposed approach for evaluating fire induced restraint force and deflection in restrained beams is compared against the results of a fire test. Unprotected restrained beam, tested under a design fire by Li and Guo (2008), was selected for the validation of the proposed approach. The tested beam, made of mild steel (*Fy* = 275 MPa), section H250x250x8x12, and length 4500mm, was loaded by two-point load with 130kN each (70% of its plastic bending capacity), and then was subjected to a design fire from four sides with the top flange protected using ceramic insulation to simulate 3-side exposure. Details of the fire test are presented in Chapter 4.

The axial and rotational restraint stiffnesses are estimated as *Ka* = 39.5kN/mm and *Kr* = 54 kN.m/milirad, respectively. The recorded fire induced deflection and axial force are plotted in Fig. 9(a and b). Average steel temperature and thermal gradient obtained from the fire test are used in the analysis. Equation [7.25] was used to predict midspan deflection, while Eqs [7.15] and [7.28] are used to predict the fire induced forces during growth phase and decay phase of the fire test. The fire induced deflection and axial force predicted using the proposed approach is also plotted in Fig. 7.9(a and b). The elasto-plastic deflection is conservatively captured by the proposed approach as shown in Fig. 7.9(a). Also, the proposed approach predicts catenary action to occur at 16 min. of fire exposure, and this compares very well with the recorded time of 15 min for catenary action in the test. However, because the proposed approach uses linear interpolation of the deflection, the maximum midspan deflection (Δmax) is conservatively overestimated by 20% as shown in Fig. 7.9(a). In Fig. 7.9(c), the proposed approach predicts the fire-induced axial force fairly well before the catenary point (at 15 min.). However, in the decay phase, the proposed approach slightly underestimates the tensile force that is due to the shrinkage of steel. Slight differences between the predictions from the proposed approach and results of the fire test can be attributed to the differences in material properties, uncertainties in the stiffness values of end restraints (*Ka* and *Kr*), and to the simplifying assumptions of the proposed approach. The occurrence of local buckling in the actual test had a minor influence on the fire response. This is due to the fact that in restrained beams, tensile force develops in the beam and this tensile force alleviates the effect of local buckling. Based on the comparison shown in Fig. 7.9(a), Eq. [7.25] can be used to conservatively predict deflection of the restrained beam, and thus can be used to design the beam based on a deflection limit state.

7.4 COMPARISON TO FINITE ELEMENT ANALYSIS

Since there is a lack of fire test data on restrained steel beams under fire, predictions from the proposed approach are compared with results from finite element analysis. The finite element model developed using ANSYS in Chapter 4 for fire resistance analysis is used for generating the finite element results. The characteristics of the beam used in the finite element analysis are shown in Table 7.1. In the following sections the proposed equations for predicting fire-induced forces and deflection are verified by comparing its predictions against finite element analysis results.

7.4.1 Fire-Induced Forces

Figure 7.10 compares maximum compressive axial force obtained from finite element analysis to that obtained via Eq. [7.15]. The axial force is normalized to the plastic axial capacity at the temperature of yielding ($Py = ky(Ty) \times Fy \times \mathrm{As}$). The temperature at yielding (Ty) is computed using Eq. [7.12] for the proposed approach, but for finite element analysis results, Ty is obtained from ANSYS output as the temperature at which the compressive force is maximal.

Results plotted in Fig. 7.10 shows that the proposed approach produces conservative estimates of the maximum compressive force. The slightly conservative predictions are due to the presence of thermal gradient. The proposed approach accounts for thermal gradient by assuming that, in the elastic range, the mechanical strain distribution remains linear under linear thermal gradient. Obviously, this assumption might deviate slightly since the relation between temperature and the reduction in steel elastic modulus is slightly nonlinear. However, this assumption may be justified for the purpose of simplicity.

The temperatures at yield (*Ty*) and at catenary point (*Tc*), as obtained from finite element analysis and from proposed approach, are presented in Fig. 7.11(a and b) for all the combinations of parameters in Table 7.1. Slight differences between the finite element analysis results and those obtained by the proposed approach are mainly attributed to the idealizations and simplifying assumptions. Since *Tc* is used to compute midspan deflection (Δc) at catenary point, conservative values of *Tc* will lead to conservative values of Δc. Further, since Δc is written as a square root function of *Tc* (Eq. [7.24]), the effect of change in *Tc* on the value of Δc will be proportional to the reciprocal of the square root function. In numerical terms, a change in *Tcat* from 500°C to 600°C will affect Δc by 10%, and from 700°C to 800°C will affect Δc by 6%. Using this argument, the slight deviation in estimating *Tc* by the proposed approach can be justified.

7.4.2 Mid-span Deflection

Deflections obtained from the proposed approach are compared to those obtained from finite element analysis for beams with varying parameters specified in Table 7.1. Influence of axial restraint is shown in Fig. 7.12, which plots the midspan deflection of steel beams with zero rotational restraint (*Kr* = 0) but with different axial restraint stiffnesses (*Ka* = 0 and 10% *EsA/L*) under uniform temperature. It is evident in the figure that in most cases, the proposed approach provides conservative estimates of the midspan deflection until the catenary point is reached (the points when the predictions intersect the deflection obtained from finite element analysis). In cases where local buckling occurs (*L:12m, LR:30% and LR:50%*) the proposed approach becomes slightly unconservative just prior the catenary point. However, it stays conservative beyond the catenary point. The influence of local buckling on the deflection of the beam is not pronounced since local buckling generally occurs in Stage II wherein the beam deflection is already increasing due to the spread of plasticity. Slight variations between the proposed approach and the finite element analysis results can be attributed to the simplifying assumptions made in this study, such as linear interpolation of deflection between yield and catenary points, in addition to the slight discrepancies in calculation of the temperature at catenary point (*Tc*).

The effect of rotational restraint is shown in Fig. 7.13 which compares the deflection for the same beams as those shown in Fig. 7.12 but with rotational restraint $Kr = EsI/L$ imposed on the beams. The rotational restraint caused local buckling to occur in post-yield stage (Stage II) which caused convergence problems in the finite element analysis (especially for the cases of *L:6m*). However, the proposed approach remained conservative for most cases of the restrained beams.

Figure 7.14 compares the influence of thermal gradient on the midspan deflection as predicted by the proposed approach and by finite element analysis. The beams in Fig. 7.14 are axially and rotationally restrained and loaded uniformly. The results indicate that thermal gradients greatly influence the elastic deflection of the beam. Figure 7.14 also shows that the proposed approach is capable of capturing the effect of thermal gradient on the elastic deflection. In the elasto-plastic range, the applied thermal gradient (ΔT = 200°) caused local buckling in the bottom flange of the beam near the supports, which caused convergence problems in the finite element analysis for case of *L:6m*. However, the predicted deflections in the elasto-plastic range are in good agreement for cases of low to moderate slenderness ratios (*L:6m* and *9m*) which are typical spans of beams used in building applications where fire resistance is an issue.

Figure 7.15 compares the effect of location of axial restraint on the fire response of restrained beams. For the analyzed beams in Fig. 7.15, the location of axial restraint (y) was varied from the geometric centroid (y = 0) to the bottom flange (y = d/2). Axial and rotational restraint and thermal gradient for different span lengths and load ratios are considered in the analysis. The results in Fig. 7.15 indicate that shifting the location of axial restraint to the bottom flange leads to reduced midspan deflection, and thus enhances the fire response of the restrained beams. This is because when the axial restraint is located at the bottom flange, a counter bending moment is generated at the supports. This counter bending moment at the supports leads to a reduction in the bending moment at midspan by a magnitude of ($P \times y$), where P is the fire-induced axial force in the beam.

Figure 7.15 also indicates that the influence of shifting the location of axial restraint is well predicted by the proposed approach. For the cases of short beams (*L:6m*) and (y = $d/2$), local buckling occurred in the bottom flange simultaneously with the occurrence of yielding. This is because of the high concentration of the stresses in the bottom flange. However, the occurrence of local buckling did not significantly change the fire response of the restrained beams. This is because after the occurrence of local buckling, the beams entered the catenary phase, and tensile stresses started to develop in the beams, and thus gradually changing the bearing mechanism from flexural to cable.

Overall, the predictions from the proposed approach are in good agreement with results from finite element analysis on the fire response of restrained beams. Thus, the proposed approach can be applied to compute fire-induced forces and deflections, which in turn can be used to estimate realistic failure under both strength and deflection limit states.

7.4.3 Deflection Limit State

The proposed approach can be used to predict the limiting temperature under different deflection limit states. The limiting temperature is the temperature at which a deflection limit state is achieved. Figure 7.16 compares the results from the proposed approach (Eq. [7.26]) to results from finite element analysis on all the combinations of beams with characteristic shown in Table 7.1. Two deflection criteria were used, *LF* = *L/20* and *LF* = *L/30*. These deflection criteria are commonly used in fire tests (BS 1987) and are chosen for comparison. As shown in Fig. 7.16, the approach predicts the temperature at deflection limit state (*TDLS*) within 10% margin of error. The approach conservatively underestimates *TDLS* when the deflection criteria is *LF* = *L/30*. This is because the midspan deflection is interpolated linearly and the resulting deflection is generally greater than the actual deflection obtained from finite element analysis in the temperature range $T < Tc$. This is shown in Fig. 7.6 which illustrates the linear interpolation of the midspan deflection. Based on Fig. 7.6, Eq. [7.26] for predicting *TDLS* is conservative when the deflection limit state (*LF*) is less than Δc. For the cases when *LF* is greater than Δc, the predicted *TDLS* can be reduced by 10% to remain on the conservative side.

7.5 DESIGN APPLICABILITY

The proposed simplified approach for predicting fire response of restrained steel beams can be applied in fire design. An example is presented here to demonstrate the applicability and rationality of the proposed approach. Step-by step design procedure in analyzing a typical restrained beam (shown in Fig. 7.17) under fire is presented below:

Problem:

- Design the beam for 2 hours of fire exposure under ASTM E119 standard and specified design fire. Use deflection limit state of $LF = L/30$.

Beam characteristics:

- Beam length and section: 7000 mm, W24x76.
- Loading: uniformly distributed dead and live service loads: wD = 35 kN/m, wL = 70 kN/m.
- Axial restraint stiffness (Ka): 41.3 kN/mm ($\approx 0.1EsAs/L$).
- Rotational restraint stiffness (Kr): 50 kN.m/milirad ($\approx 2.0EsI/L$)
- Initial thermal gradient (ΔT) = 150°C.
- Steel properties: Grade 50 steel; Fy = 355 MPa and Fu = 445 MPa.
- High temperature properties: as per ASCE specified temperature-dependent reduction factors (ASCE 1992).

Response parameters:

- Load combination under fire (ASCE-07 2005)

$wf = 1.0\,wD + 0.5wL = 70$ kN/m. (≈ 30% of ultimate load capacity at 20°C)

- Axial and rotational restraint factors (as per Eqs. [7.13 and 7.14])

$$F_A = \frac{\alpha E_s}{F_y}\left(\frac{a_1 K_a L/(E_s A_s)}{2a_1 + K_a L/(E_s A_s)}\right)$$

$$= \frac{14\times 10^{-6}\times 2\times 10^5}{355}\left(\frac{0.6829\times 0.1}{2\times 0.6829 + 0.1}\right) = 0.00037$$

$$F_R = \frac{\alpha E_s}{F_y}\left(\frac{a_1 K_r L/(E_s I)}{2a_1 + K_r L/(E_s I)}\right)$$

$$= \frac{14\times 10^{-6}\times 2\times 10^5}{355}\left(\frac{0.6829\times 2}{2\times 0.6829 + 2}\right) = 0.0032$$

- Yield temperature (as per Eq. [7.12] and using $Mo = \max(Ms, Mm) = 285.8$ kN.m)

$$T_y = \frac{1 - M_o/M_y - 0.5F_R\Delta T}{F_A + a_2}$$

$$= \frac{1 - 285.8/1023.8 - 0.5\times 0.0032\times 150}{0.00037 + 0.0008} = 411^\circ\text{C}$$

- Catenary temperature (as per Eq.[7.17])

$$T_c = \frac{1}{a_2}\left(1 - \frac{M_\circ}{M_u} - \frac{M_y}{M_u}\frac{F_R\Delta T}{2}\right)$$

$$= \frac{1}{0.0008}\left(1 - \frac{285.8}{1308.9} - \frac{1023.8}{1308.9}\times\frac{0.0032\times 150}{2}\right) = 878.8^\circ\text{C}$$

- Deflection at onset of yielding (as per Eq. [7.25])

$$\Delta_y = \left(\frac{5wL^4}{384 k_E E_s I} + \alpha \frac{L^2}{8} \frac{\Delta T}{d} \right) \left(1 - \frac{F_R}{a_1} \frac{F_y}{\alpha E_s} \right)$$

$$= \left(\frac{5 \times 70 \times 7^4}{384 \times 0.79 \times 2 \times 10^5 \times 8.7 \times 10^{-4}} + 14 \times 10^{-6} \times \frac{7^2}{8} \times \frac{150}{0.61} \right) \times$$

$$\left(1 - \frac{0.0032}{0.6829} \times \frac{355}{14 \times 10^{-6} \times 2 \times 10^5} \right) = 15 \text{ mm}$$

- Deflection at catenary point (as per Eq. [7.24])

$$\Delta_c = \frac{L}{2} \sqrt{2 \times \alpha (T_c - 20)} = \frac{7000}{2} \sqrt{2 \times 14 \times 10^{-6} (878.8 - 20)} = 542 \text{ mm}$$

- Temperature at deflection limit state (as per Eq. [7.26])

$$T_{DLS} = T_y + \frac{(L_F - \Delta_y)(T_c - T_y)}{(\Delta_c - \Delta_y)} = 411 + \frac{(7000/30 - 15)(878.8 - 411)}{(542 - 15)} = 605^\circ\text{C}$$

- Temperature at ultimate strength failure (tensile capacity)

$$T_f = \frac{T_c T_y F_A + a_1 a_3 (T_c - T_y)}{T_y F_A + a_1 a_4 (T_c - T_y)}$$

$$= \frac{878.8 \times 411 \times 0.00037 + 0.6829 \times 1.329 \times (878.8 - 411)}{411 \times 0.00037 + 0.6829 \times 0.0014 \times (878.8 - 411)} = 931^\circ C$$

Design for standard fire exposure

After computing the limiting temperature (*TDLS*) based on deflection limit state, the fire resistance duration can be computed Eq. [6.5]. The insulation material is assumed to have thermal conductivity of 0.1 W/m.oC and heat capacity of 375 kJ/m3/°C. The insulation thickness is increased and the average steel temperature is calculated using Eq. [6.5] at t = 120 min. of fire exposure until the $Ts \approx TDLS$. This occurred when an insulation thickness of 25 mm is used. For the same insulation thickness, the limiting temperature based on strength failure (Tf) is reached at 218 min. of standard fire exposure

Design for design fire exposure

If the beam is exposed to a design fire scenario shown in Fig. 7.18(a), then the maximum temperature attained in steel (Ts,max) should not exceed the limiting temperature based on deflection limit state ($TDLS$ = 605°C). Using Equations 6.13 and 6.14, the required insulation thickness at which $Ts,max \approx TDLS$ is 15 mm, for which the maximum steel temperature under fire is Ts,max = 597°C < $TDLS$ = 605°C (at 90 min. of fire exposure). The average steel temperature as a function of exposure time is plotted in Fig. 7.18(a) with the applied insulation thickness of 15 mm.

Fire resistance using code provisions

In the current code provisions, the critical temperature is computed based on specified semi-empirical equations. First, the load ratio under fire conditions (r) is computed as: $r = Mo/Mp$ = 285.8/1308.9 = 0.21. Second, the critical temperature is computed as per Eqs. [2.5a - 2.5c]:

$$T_{cr}^{EC3} = 717^\circ C,\ T_{cr}^{SNZ} = 760^\circ C \text{ and } T_{cr}^{JBC} = 621^\circ C$$

By using Eq. [6.5] for computing steel temperature and assuming insulation thickness of 25 mm, the following fire resistances are obtained for each critical temperatures computed above:

$$t^{EC3} = 160\text{min.}, \; t^{SNZ} = 170\text{min.} \text{ and } t^{JBC} = 132\text{min.}$$

The computed values above illustrate the discrepancies between the critical temperature relationships specified in codes and standards. A comparison for the fire resistances computed using proposed approach and using equations specified in codes and standards is shown in Table 7.2. The relationship specified in the Japanese Building Code for evaluating critical temperature gave 132 min. of fire resistance for the designed beam. The New Zealand and Eurocode relationships overestimated the fire resistance by 50 min and 40 min., respectively, and thus, a design according to these relationships would have resulted in an unconservative prediction of insulation thickness (less than 25 mm.).

Finite element analysis

The solution developed above using the proposed simplified approach is verified against results of finite element analysis on the beam with the computed insulation thicknesses under both standard and design fire scenarios. The temperature attained in steel section is computed through heat transfer analysis. The details of finite element modeling for heat transfer analysis are presented in Chapter 4. The analysis is carried out by subjecting the beam, with the specified boundary conditions above, to the uniformly distributed load until room-temperature response is obtained. To apply the fire scenario, steel nodal temperatures obtained from the heat transfer analysis are applied, at each time step, at the corresponding nodal locations of the structural model. The midspan deflection of the beam under standard and design fires is plotted in Fig. 7.18(b).

While the midspan deflection continues to increase in the case of standard fire exposure, as shown in Fig. 7.18(b), a recovery of deflection occurs in beam in the case of design fire exposure, and this is attributed to the cooling phase of design fire, as shown in Fig. 7.18(a). The sudden increase in midspan deflection at the128th minute of standard fire exposure (Fig. 7.18(b)) is attributed to the occurrence of local buckling in the bottom flange of the beam near the support. The stiffened response of the beam after the 150th minute into standard fire exposure is attributed to the catenary action wherein tensile force develops in the beam until complete ultimate rupture occurs after 202 minutes into standard fire exposure.

It is worth mentioning that the fire design in this example is based on deflection limit state, which is more realistic than strength failure criteria. Applying the proposed approach resulted in a conservative fire design of the restrained beam, as shown in Fig. 7.18. Under standard fire exposure, ultimate strength failure is achieved at 200 minutes as seen in Fig 7.18(b), and the fire induced deflection prior to ultimate failure was very large. However, under design fire exposure, no strength failure occurs in the beam, although deflection in the beam did reach large values, as shown in Fig. 7.18(b). Therefore, the proposed approach for fire design based on limiting deflection provides a realistic assessment of fire resistance of beams as compared to strength design criteria.

Table 7.2 compares the fire resistances computed using proposed approach, relations specified in codes and standards, and obtained form finite element analysis under different limit states. The fire resistances computed using the proposed approach are close to the fire resistances predicted using finite element analysis for deflection and strength limit states. However, the fire resistances computed using relations specified in codes and standards are scattered and do not distinguish between deflection or strength limit states. This is because the relations specified in codes and standard for computing fire resistance are mainly based on evaluating critical temperature, which is does not reflect the realistic performance of the beam.

7.6 SUMMARY

A simplified methodology for evaluating fire response of restrained steel beams is developed in this chapter. The methodology is derived based on utilizing compatibility and equilibrium principles. The approach developed in this chapter accounts for various parameters that have a significant influence on the fire resistance of restrained steel beams such as fire scenario, load ratio, thermal gradient, and restrained conditions. The validity of the proposed approaches is established by comparing predictions with results from detailed finite element analysis and fire tests. The proposed methods provides simple, engineering approach for computing the fire resistance of restrained steel beams exposed to standard or design fire scenarios. The approach facilitates a rational fire design of restrained beams under various parameters such as sectional size, length, load, insulation thickness and material properties. The applicability of the proposed approach in a design simulation is illustrated through a numerical example. The proposed methodology is compared against relations specified in codes and standards, and it is shown that the approach provides better assessment of fire resistance based on different limit states.

Table 7.1: Characteristics of the beams used in finite element analysis for comparison with proposed approach

Parameter	Values	Comments
Span length (*L*)	6m, 9m, 12m	Total length
Load ratio (*LR*)	30%, 50%,70%	$LR = M_{\max} / \left(F_y Z_x\right)$
Thermal gradient (ΔT)	0°C, 100°C, 200°C	$\Delta T = TTF - TBF$
Location of restraint	0, *d/2*	Measured downward form the centroid of the section
Axial stiffness (*Ka*)	0, 0.1, 0.3*EsAs/L* and infinity	Relative to room-temperature beam stiffnesses
Rotational stiffness (*Kr*)	0, 0.1, 0.3*EsI/L* and infinity	

Table 7.2: Fire resistance predicted using proposed approach and provisions in codes and standards under different limit states

	Fire resistance (minutes)	
	Deflection limit state (L/30)	Strength limit state
Proposed approach	120	218
Japanese Building Code	132	132
Eurocode 3	160	160
New Zealand Standard	170	170
Finite element analysis	128	202

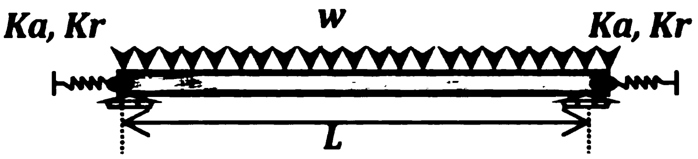

a) Layout of restrained steel beam

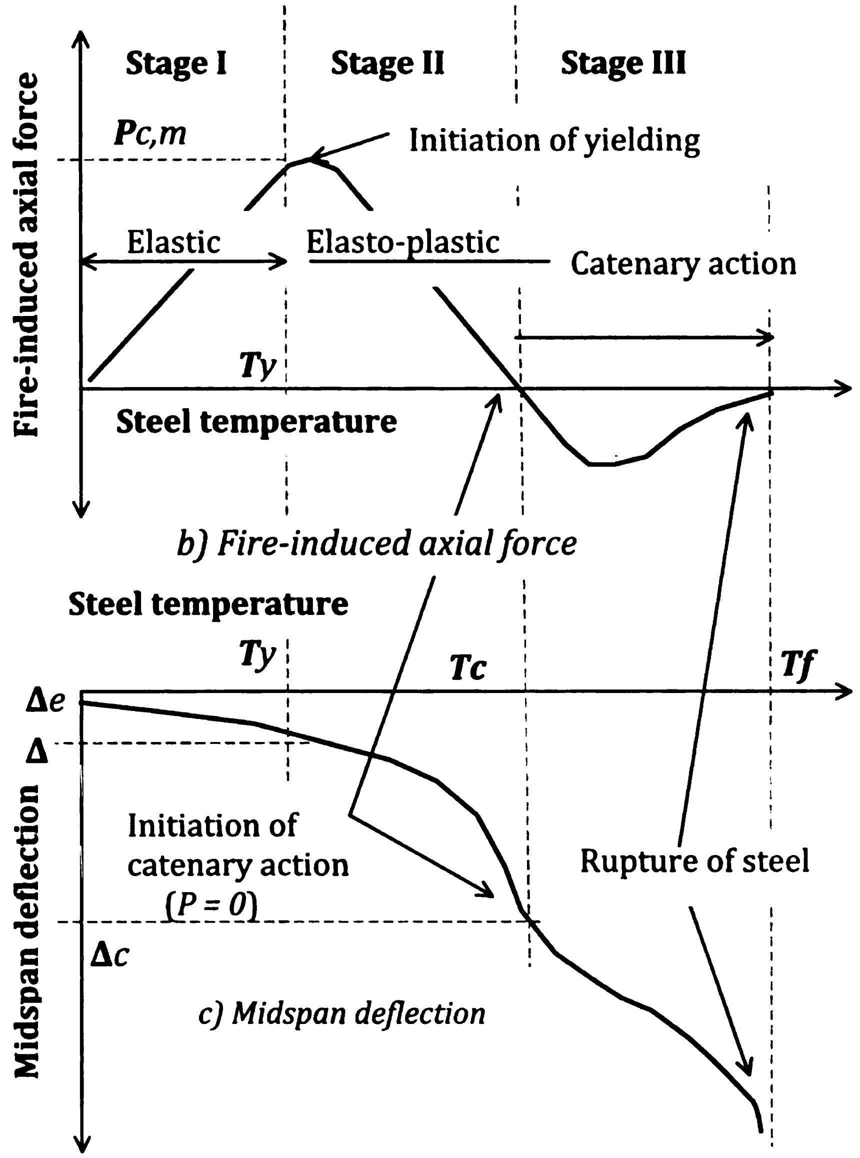

b) Fire-induced axial force

c) Midspan deflection

Fig. 7.1: Typical fire response of a restrained steel beam that fails by yielding

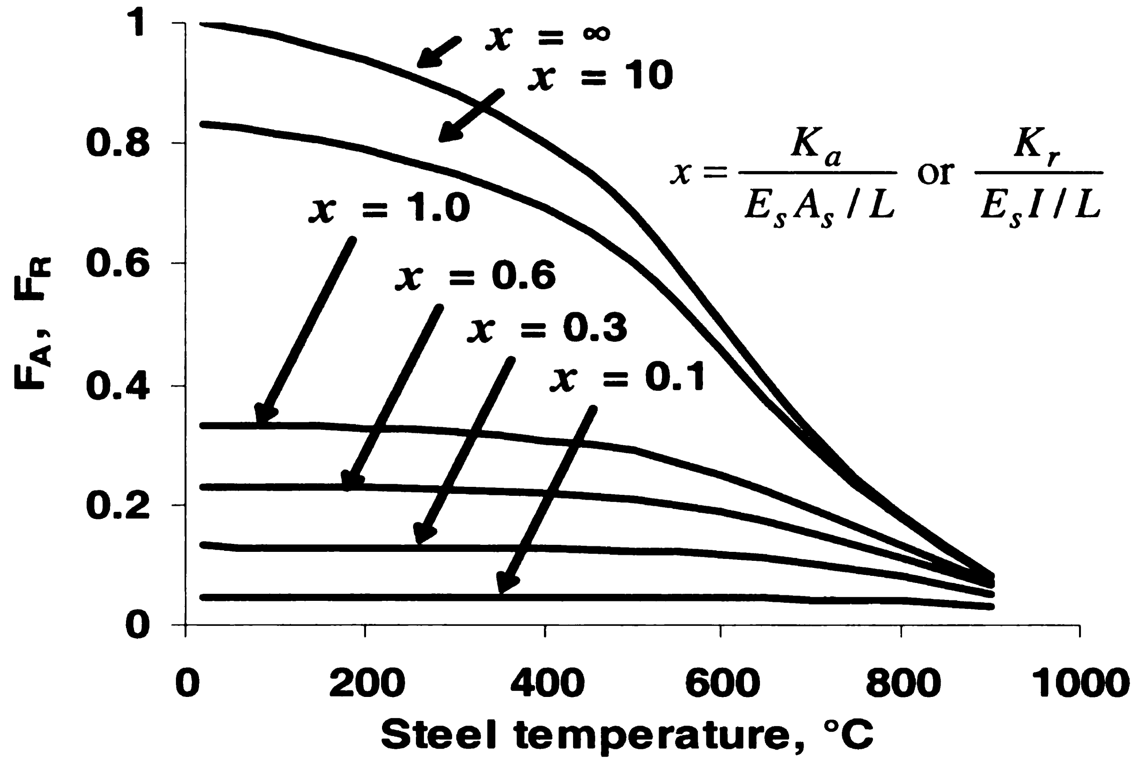

a) ASCE high temp. steel properties

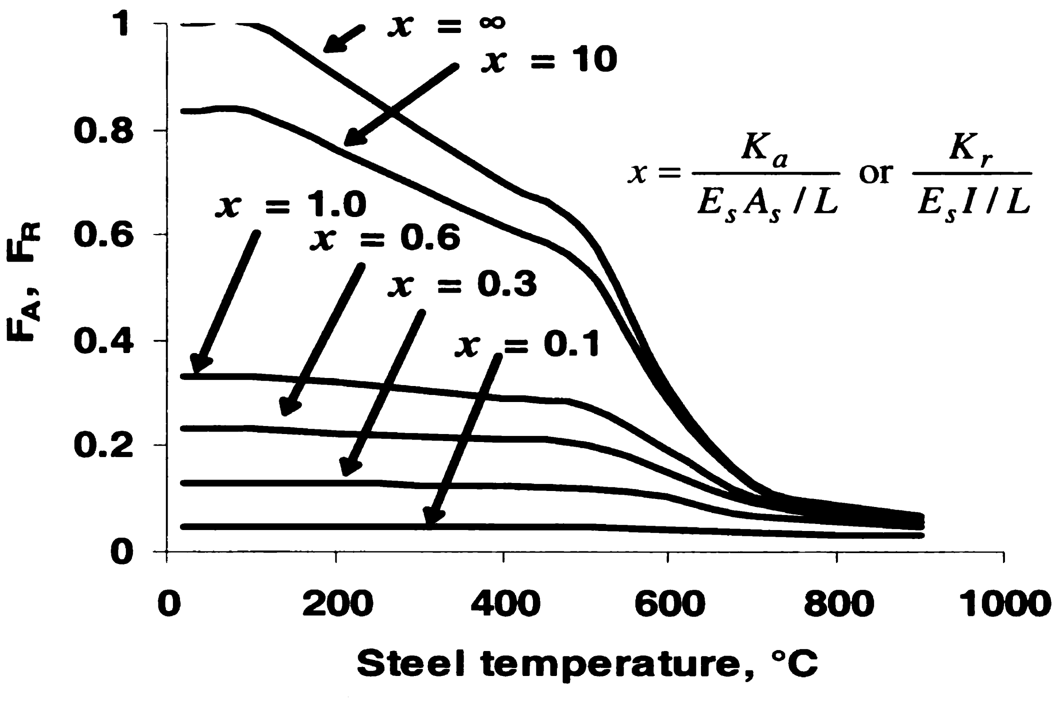

b) Eurocode 3 high temp. steel properties

Fig. 7.2: Variation of the restraint factors (*FA and FR*) as a function of end restraint ratio (*x*) and temperature using ASCE and Eurocode steel high temperature properties

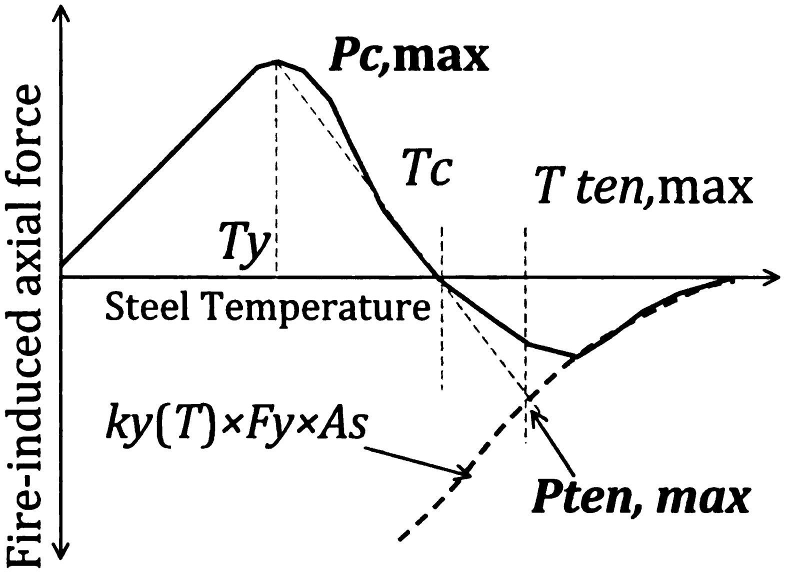

Fig. 7.3: Development of tensile catenary force in restrained beam

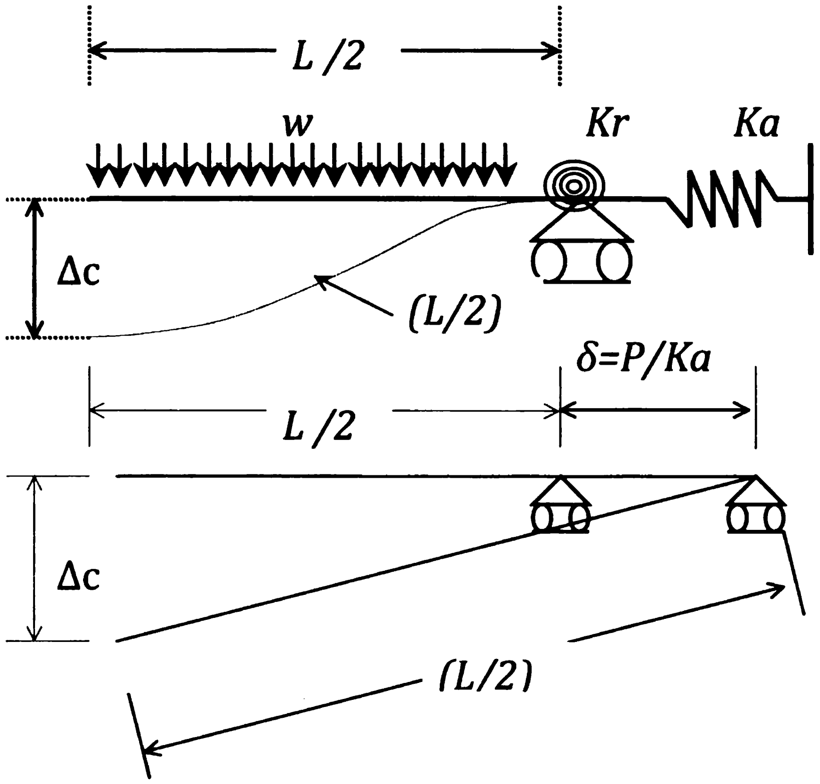

Fig. 7.4: Approximated deflection profile at the catenary point

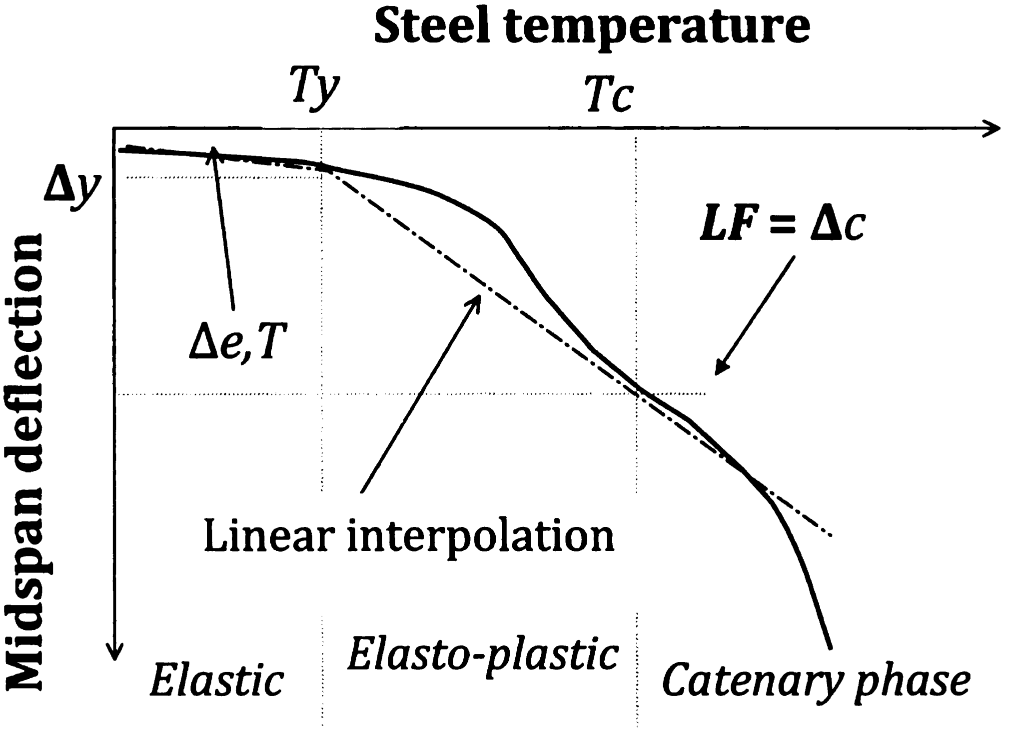

Fig. 7.5: Interpolating deflection between catenary point and point of initiation of yielding

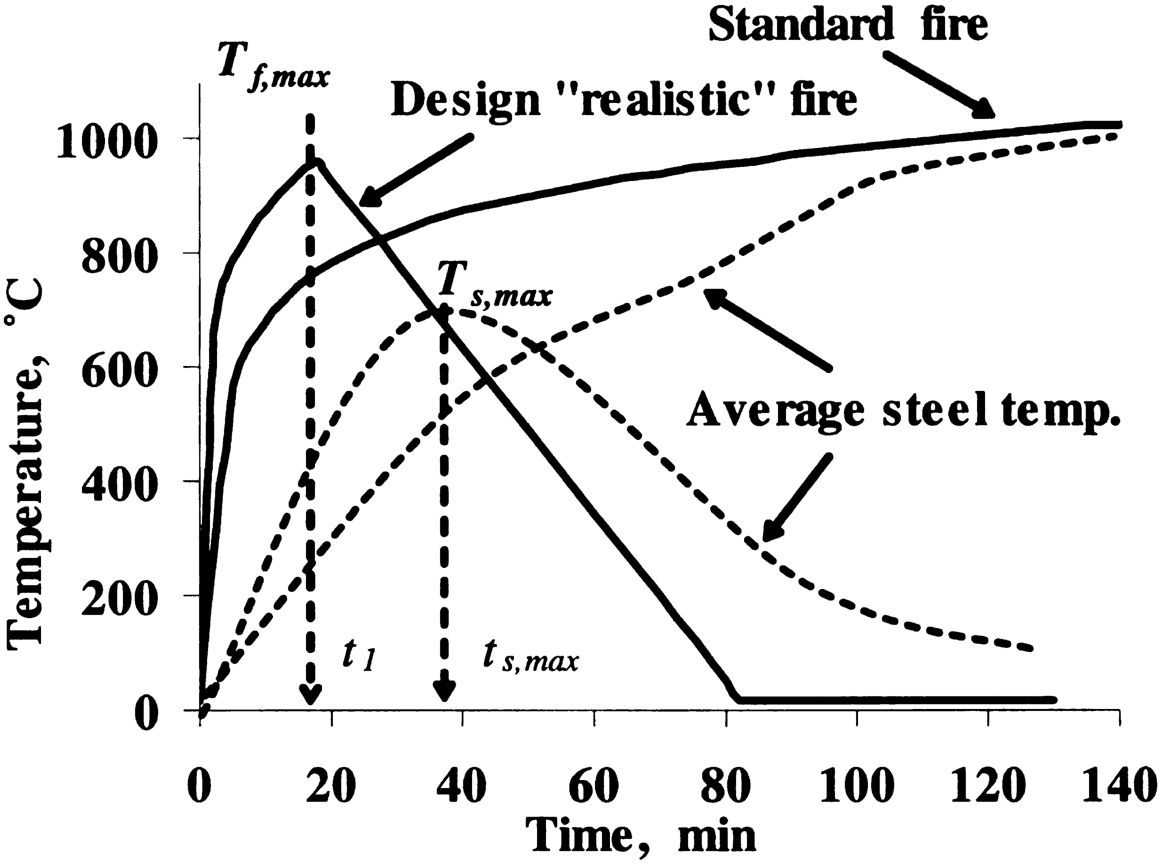

Fig. 7.6: Standard and design (realistic) fire scenarios

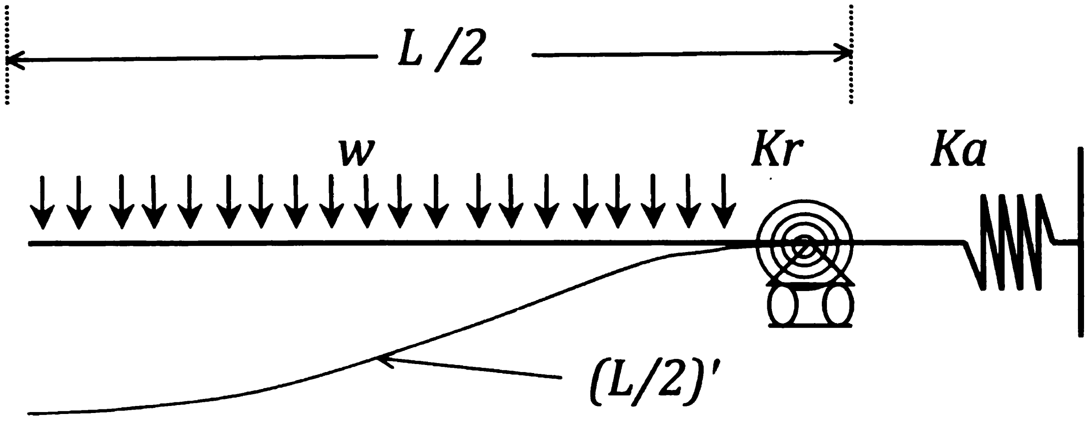

(a) Equilibrium position before fire exposure

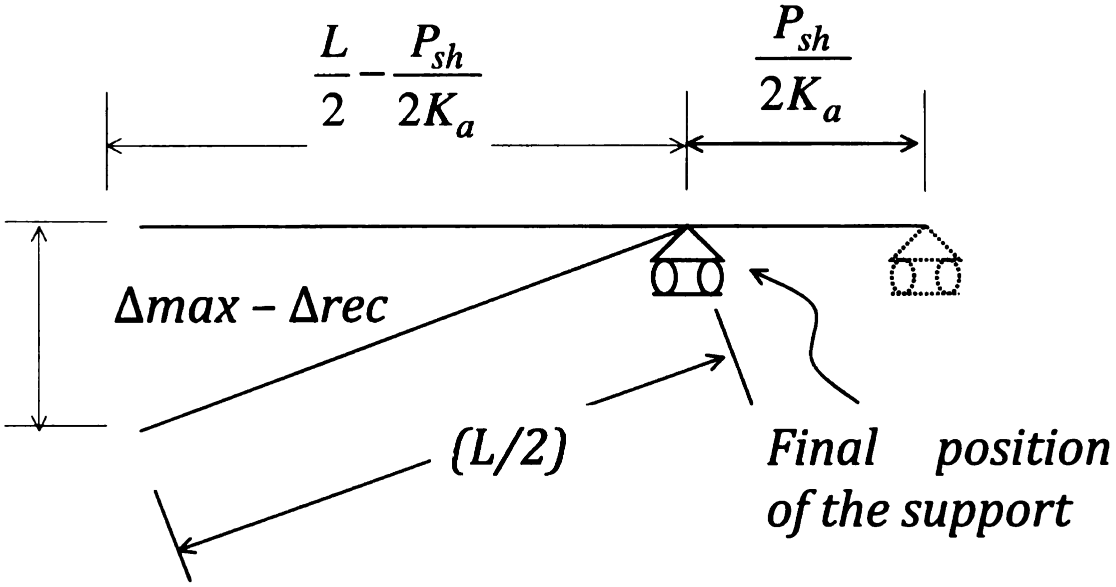

(b) Equilibrium position after cooling

Fig. 7.7: Approximated deflection profile after cooling of steel

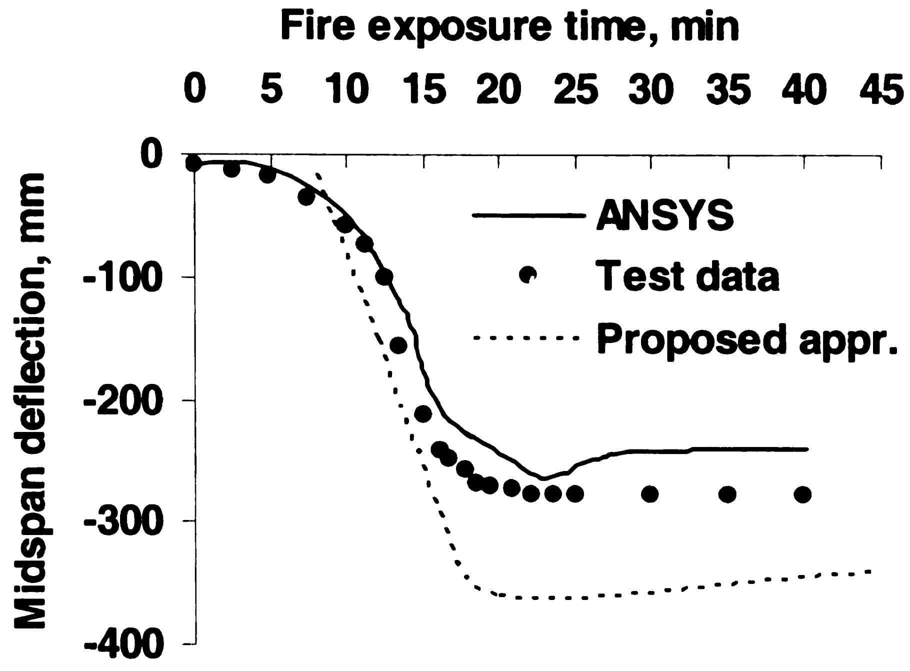

(a) Predicted and measured deflection

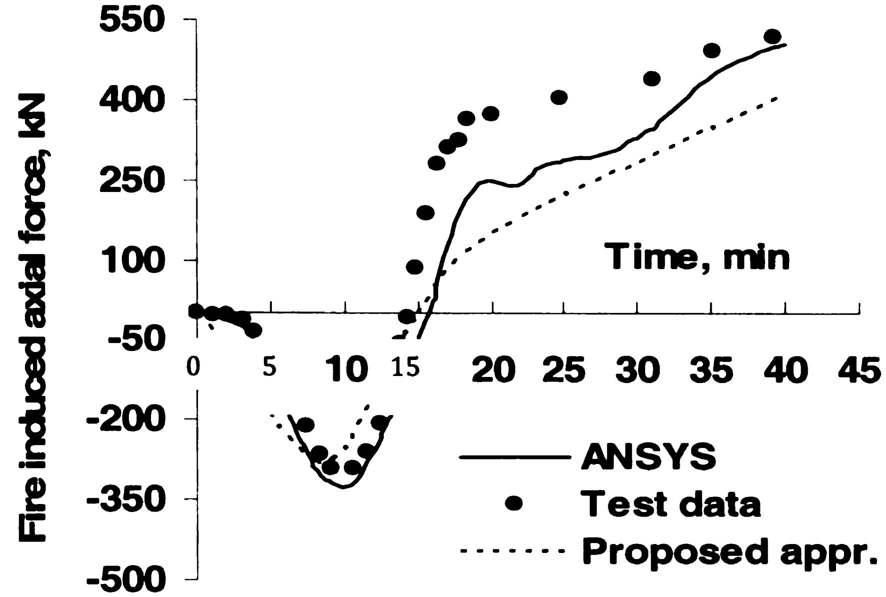

(c) Predicted and measured fire-induced axial force

Fig. 7.8: Comparison of fire response predictions from the proposed approach with results from finite element analysis and from fire test

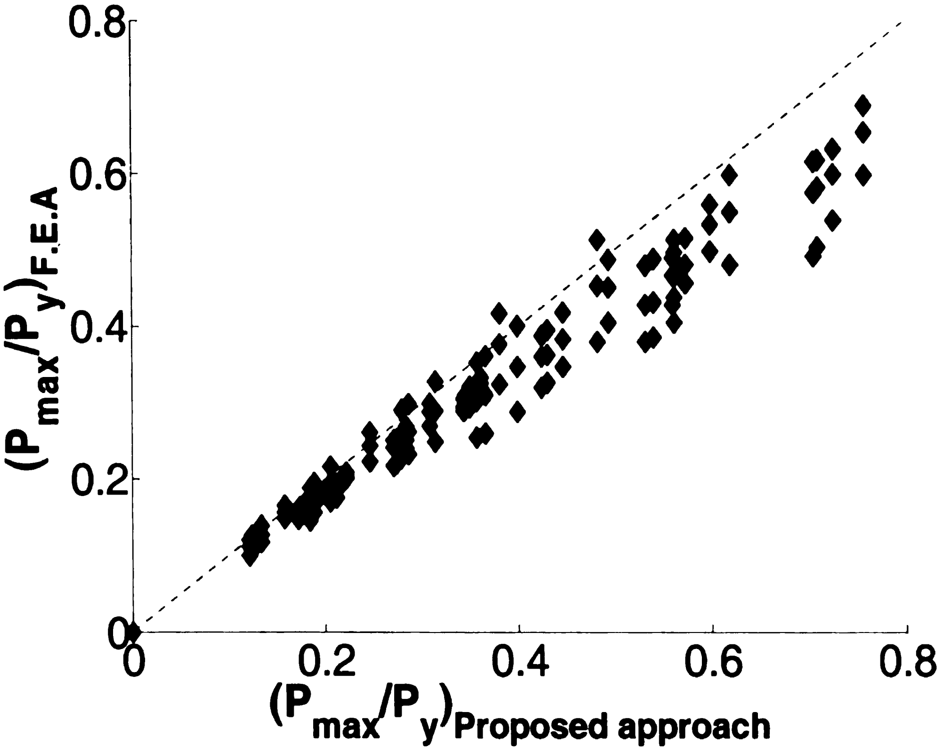

Fig. 7.9: Comparison of maximum compressive fire-induced axial force as obtained from the proposed approach and finite element analysis

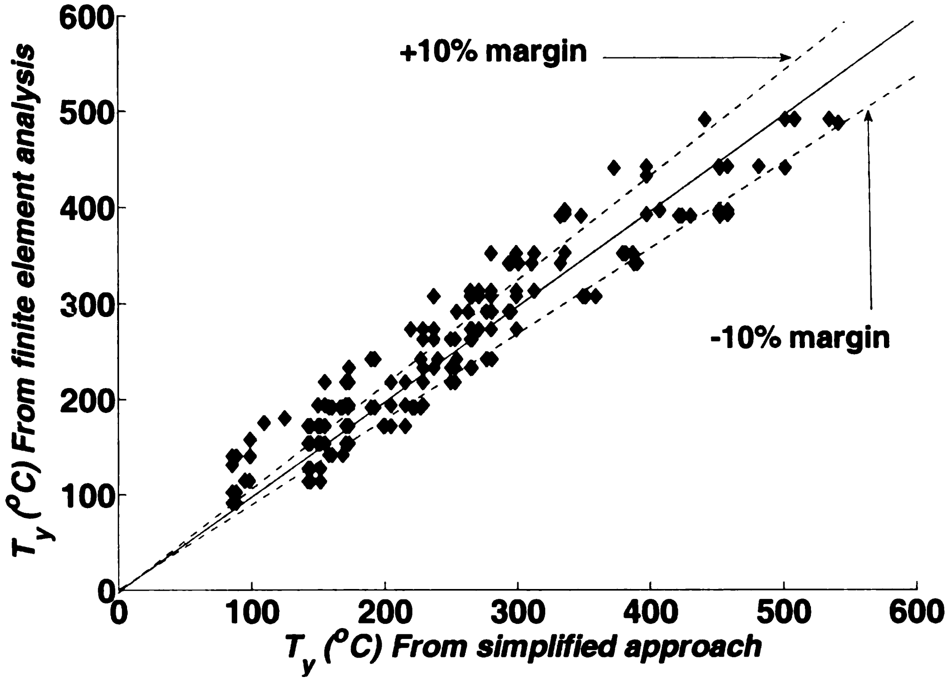

a) Temperature at yield (Ty)

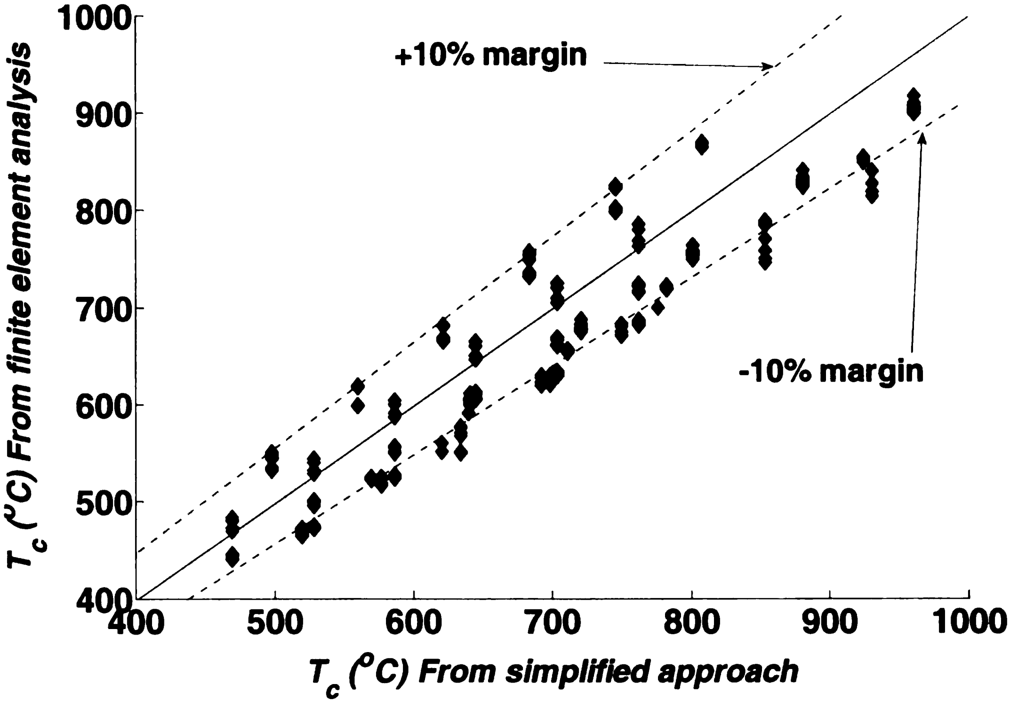

b) Temperature at catenary point (Tc)

Fig. 7.10: Comparison of predictions from proposed approach with results from finite element analysis for *Ty* and *Tc*

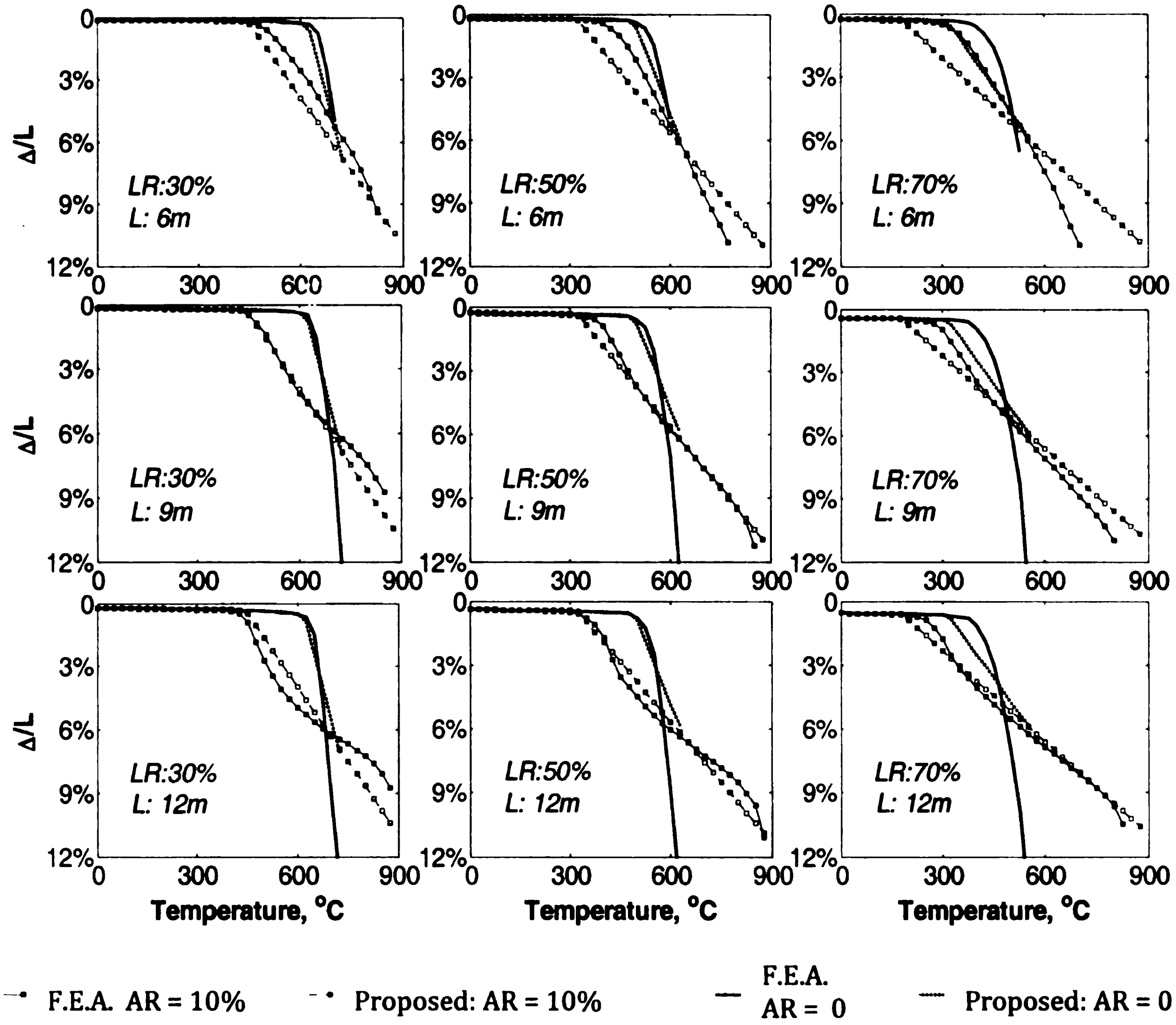

Fig. 7.11: Midspan deflections as obtained from proposed approach and finite element analysis for W24x76 laterally-braced beam under different axial restraints (*Kr* = 0)

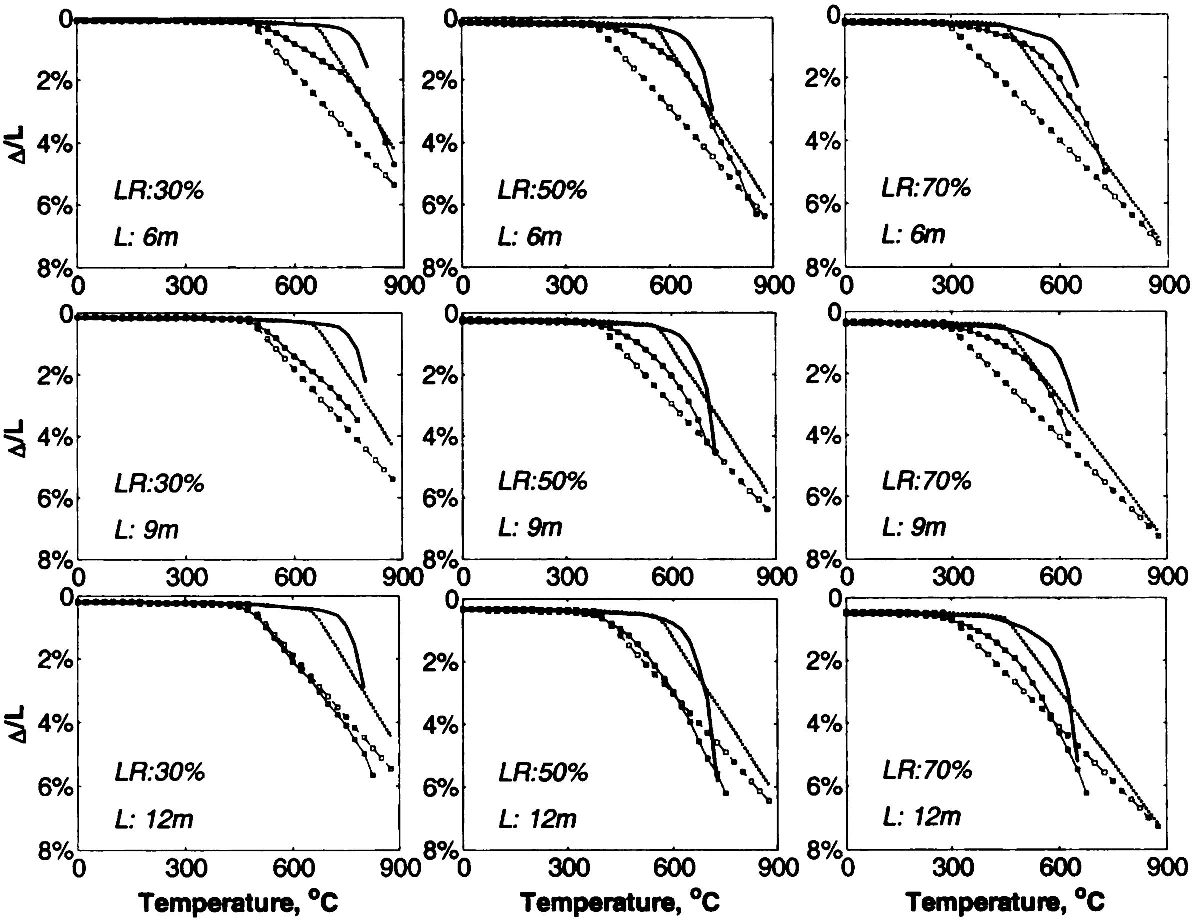

Fig. 7.12: Midspan deflections as obtained from proposed approach and finite element analysis for W24x76 laterally-braced beam under different axial restraints (*Kr* = 100% *EsI/L*) (symbols for lines are like previous figure)

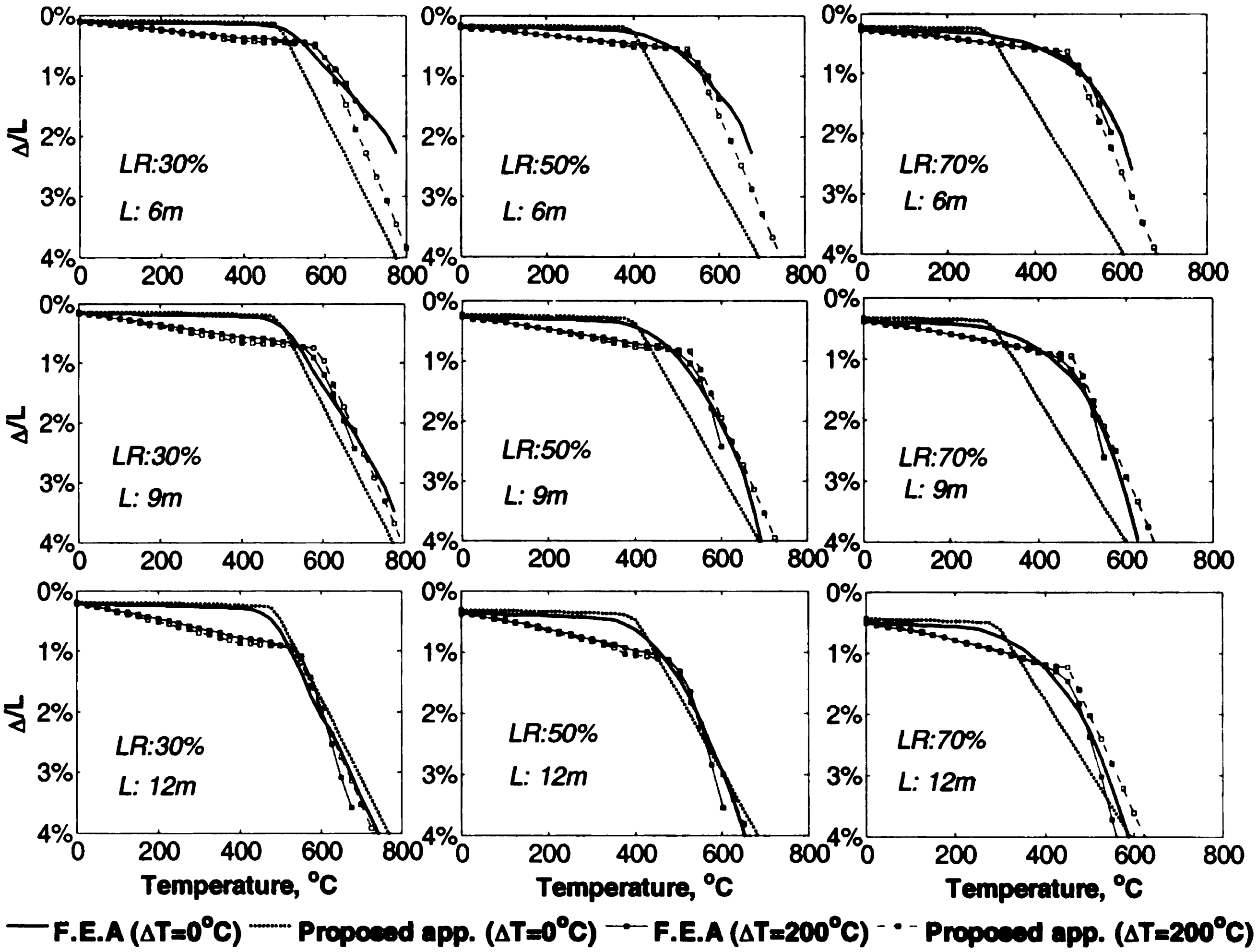

Fig. 7.13: Midspan deflections as obtained from proposed approach and finite element analysis for W24x76 laterally-braced beam under different thermal gradients (*Kr = 100% EsI/L, Ka = 10%EsA/L*)

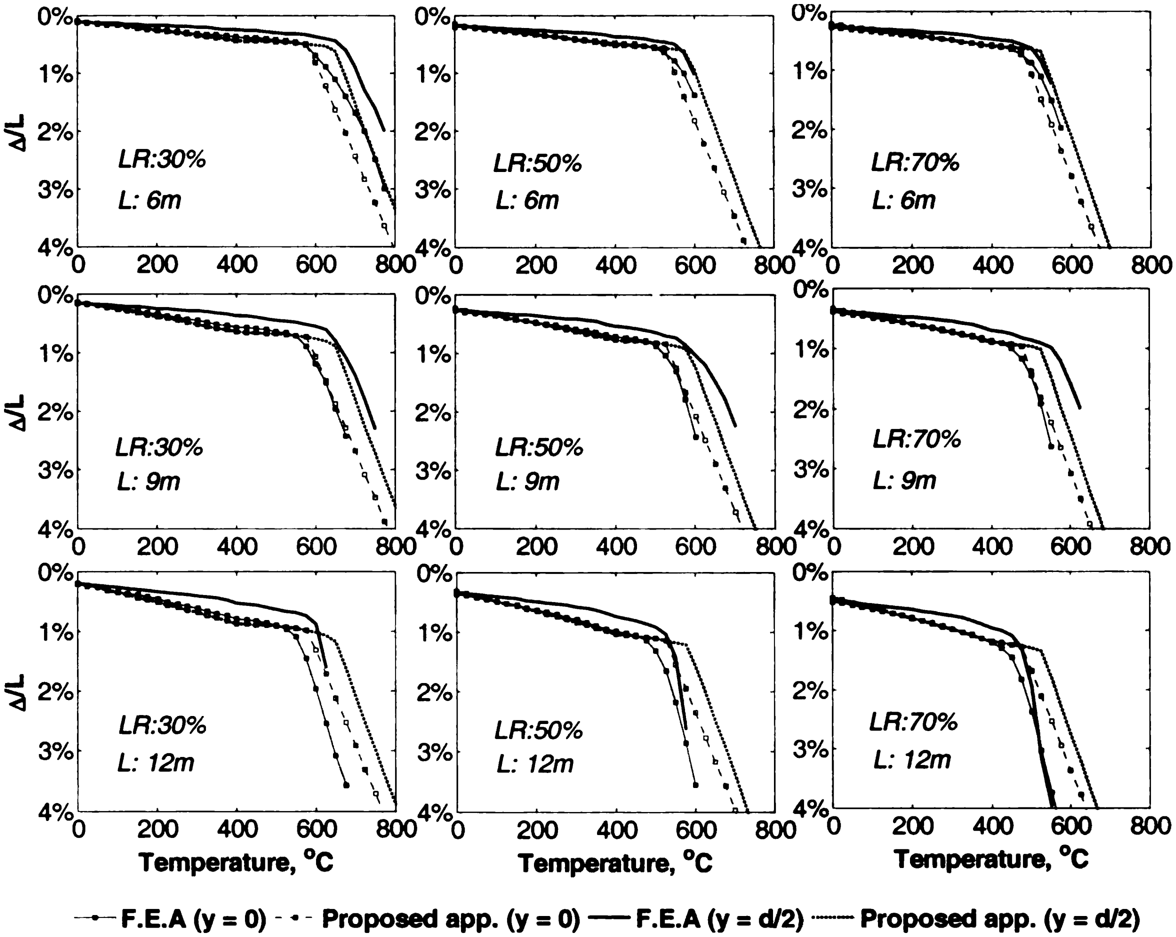

Fig. 7.14: Midspan deflections as obtained from proposed approach and finite element analysis for W24x76 braced beam with different locations of axial restraint (*Kr = 100% EsI/L, Ka = 10%EsA/L*, *ΔT* = 200°C)

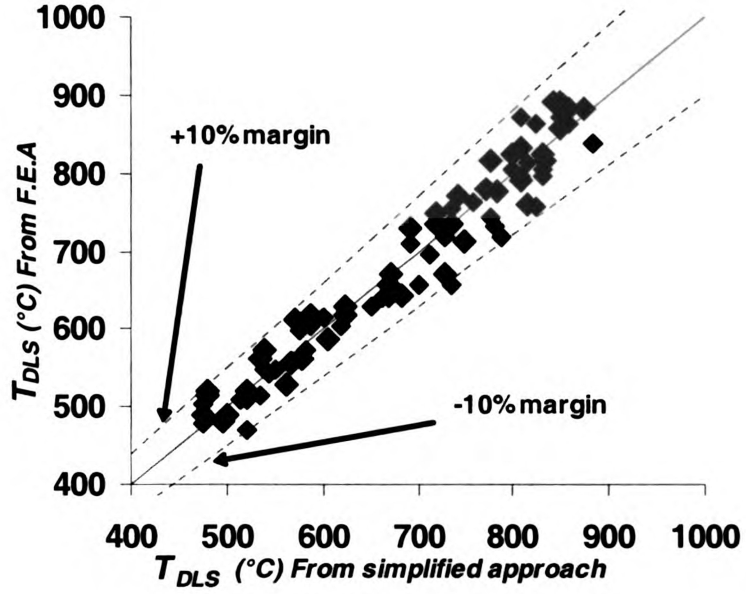

a) Deflection limit state (LF) = L/20

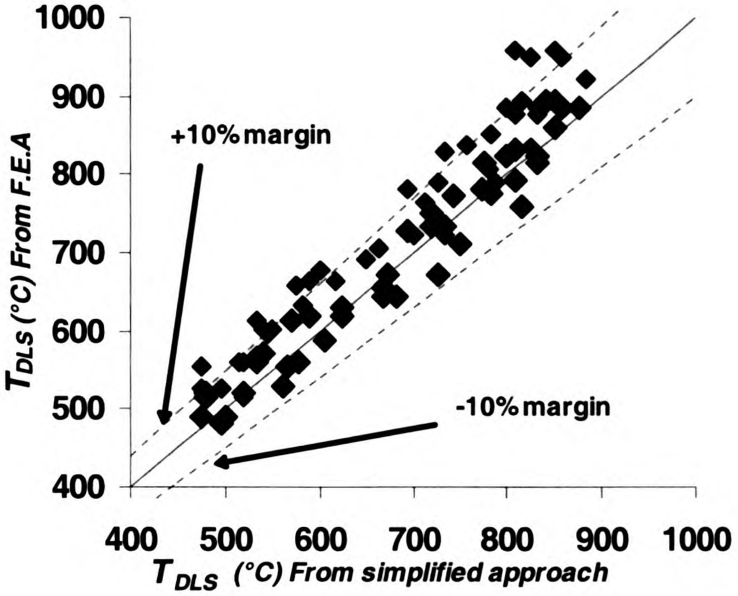

b) Deflection limit state (LF) = L/30

Fig. 7.15: Comparison of predicted temperatures at deflection limit state as predicted by proposed Eq. 7.26 for *LF = L/20* and *L/30* with results from finite element analysis

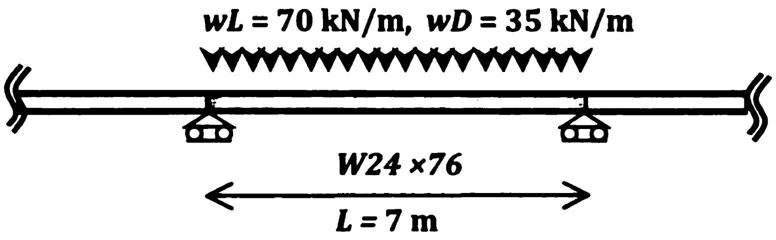

a) Beam loading and properties

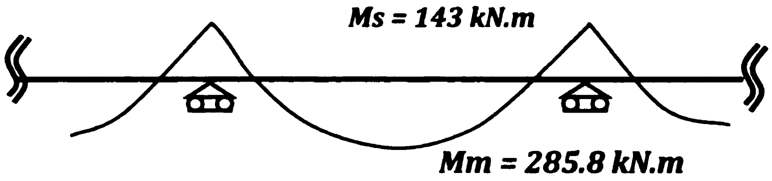

b) Bending moment diagram under fire load

Fig. 7.16: Properties of the continuous beam used in the design example

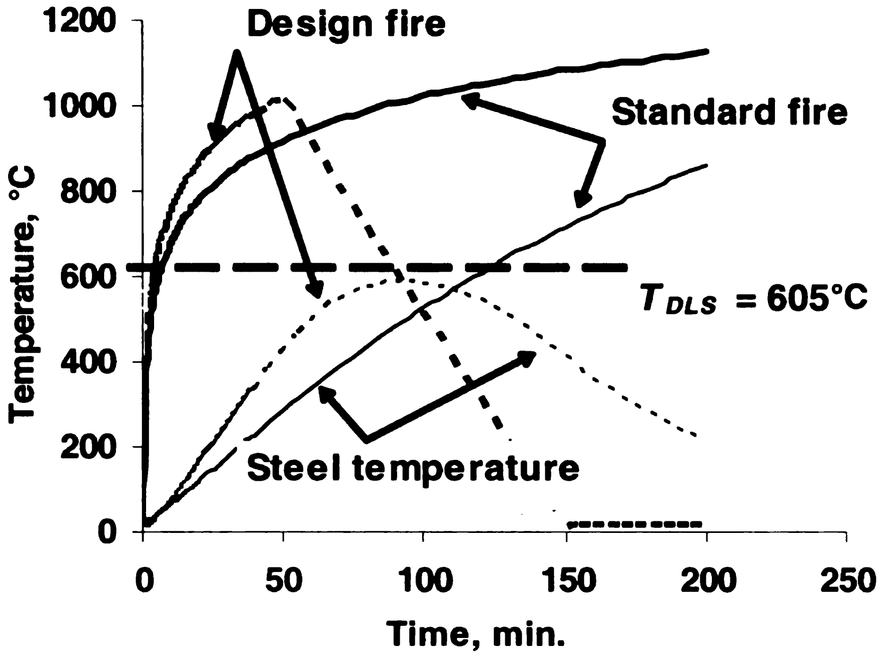

(a) Steel temperature

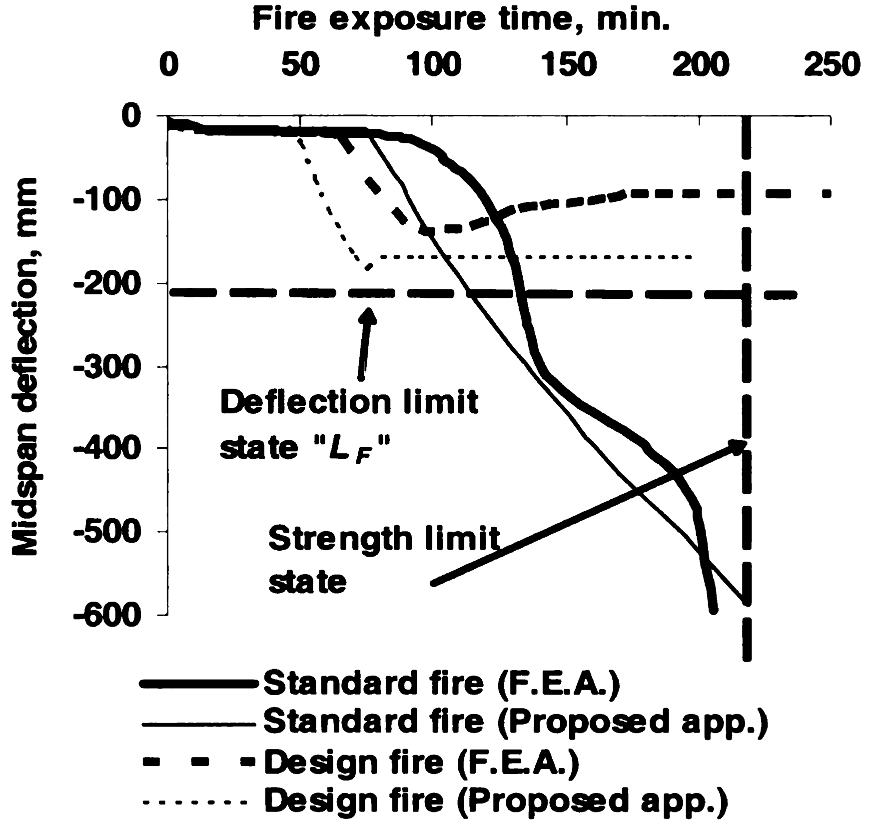

(b) Midspan deflection

Fig. 7.17: Steel temperature and midspan deflection as a function of fire exposure time for restrained beam

CHAPTER EIGHT

CONCLUSIONS AND RECOMMENDATIONS

8.1 SUMMARY

The thermal and structural response of steel beam-columns exposed to fire conditions was investigated as part of this study. Both the plastic axial force (*P*) - moment (*M*) behavior and the global response of steel beams under fire induced thermal gradient and restraint conditions were studied. As part of experimental studies, fire resistance tests were carried out on four steel beam-columns to obtain data on the plastic P-M behavior of beam-columns under realistic fire conditions. The parameters that were varied in the fire tests included load ratio, fire scenario, insulation thickness and magnitude and orientation of thermal gradient.

Data from the fire resistance tests, in addition to available test data from literature, were used to validate finite element models that were created using ANSYS. In the analysis, all the critical factors, namely high temperature material properties, fire induced restraints and thermal gradients, and the different strain components (including high temperature creep) that have significant influence on the fire response of steel beam-columns were incorporated in the models. The finite element models were applied to conduct a set of parametric studies to quantify the influence of various factors on the fire response of steel beam-columns. Results from fire tests and parametric studies were utilized to develop two methodologies for evaluating response of beam-columns under fire conditions at sectional and global levels. At the sectional level, a simple methodology for generating plastic P-M diagrams was derived by accounting for the effect of thermal gradients. At global level, a simplified approach was developed for evaluating fire induced axial force and deflection in restraint steel beams at any given time. The proposed approaches take into consideration the influence of various factors governing the fire response, including fire scenario, end restraints, connection configuration (location of axial restraint force), thermal gradient, load level, beam geometry, and failure criteria. The applicability of the proposed methods to design situations is illustrated through numerical examples. It is shown that the proposed design guidelines require minimal computational effort, and thus are attractive for incorporation in codes and standards.

8.2 KEY FINDINGS

Based on the information presented in this study, the following key conclusions are drawn:

- There is very limited information on the fire performance of steel beam-columns, especially under realistic fire scenarios and restraint conditions. The current provisions, developed based on limited fire tests under "standard fire scenarios", are prescriptive and do not facilitate a rational approach for evaluating the fire resistance. Also, to date, there are no engineering calculation methodologies for evaluating the response of restrained steel beams under thermal gradients.

- The fire resistance tests on four steel beam-columns provided unique data on the behavior of steel beam-columns under realistic fire, load, and restraint scenarios.
- Data from fire resistance tests show that fire induced thermal gradient causes a shift in the plastic P-M diagrams of steel beam-columns made of wide flanged sections. This shift in plastic P-M diagrams is more significant when thermal gradient is in the strong direction of the cross section.
- Results from parametric studies, as well as data from fire resistance experiments, indicate that fire scenario, load ratio, thermal gradient, magnitude and location of axial restraint and rotational restraint have a significant influence on the fire response of steel beam-columns, specifically:
    - A higher load level has an adverse effect on the fire response of steel beam-columns.
    - A higher axial restraint ratio leads to higher fire induced restraint force and larger mid-span deflection.
    - Fire resistance is higher when the axial restraint is shifted downward below, the centroidal axis of the beam.
    - Fire resistance decreases with increased axial restraint stiffness under deflection limit state; however, fire resistance increases with increased axial restraint stiffness under strength failure criteria.
    - Increased rotational restraint stiffness leads to improved fire response in restrained steel beams.

  - Higher fire induced thermal gradients lead to larger elastic midspan deflection in steel beams.
  - The type of fire exposure has a significant effect on the fire resistance of restrained steel beams and these beams can survive burn-out conditions under most design fire scenarios.
- The proposed methodology for adjusting the plastic P-M diagrams provides a simple and rational approach for generating P-M diagrams for steel beam-columns. The approach accounts for to thermal gradients generated under 1-, 2-, or 3-side exposure to either standard or design fire scenarios.
- The proposed methodology for tracing the fire response of restrained steel beams, derived based on equilibrium and compatibility principles, accounts for realistic load, boundary conditions, thermal gradient, and fire scenarios. The approach can be applied for evaluating fire resistance of restrained beams under standard or design fire exposures and utilizing strength or deflection limit states.
- The proposed approach provides, for the first time, simple design tools for fire design of restrained steel beams. The approach requires minimal computational effort, and provides better fire resistance predictions than those obtained from current codes provisions. Therefore, it can be integrated into structural design processes and substantially improve the fire safety of the structures designed.

8.3 RECOMMENDATIONS FOR FUTURE RESEARCH

While this study has developed fundamental understanding of the fire response of steel beam-columns, further research is required to extend the principles to other practical situations that are present in typical steel framed buildings. The following are some of the key recommendations for further research in this area:

- The influence of thermal gradients on plastic P-M diagrams was presented here for wide flanged (WF) sections. Further research is required to quantify the effect of thermal gradient on other types of steel sections such as boxed sections and concrete-filled steel tube sections.
- The research presented here can be extended to include the effect of composite action between steel beams and concrete slabs. Current provisions of fire design of composite beams do not take into consideration the effect of end restraint and fire scenario.
- In the current study, the end restraints were idealized with constant and elastic axial and rotational stiffnesses. Also, to-date, there is no information on how to quantify the temperature-dependent variation of axial and rotational restraint stiffnesses (*Ka* and *Kr*) acting on the boundaries of restrained steel beams. Further research is required to account for the more realistic nonlinear behavior of end restraints (*Ka* and *Kr*).
- In this study, the steel beam-columns were assumed to have a zero effective length (*KLo*), i.e., fully braced beam-column with plastic failure mode. This research can be extended to account for the variation of the effective length of restrained steel columns under fire conditions.
- The current constitutive models for high temperature material properties of steel (including high temperature creep strain), particularly in the cooling phase, are not sufficiently accurate. Improvements in such constitutive

models will help to enhance the accuracy of the model predictions under design fire scenarios.

8.4 RESEARCH IMPACT

The current approaches for evaluating fire resistance through standard fire tests on full-scale steel members are expensive, time consuming and have a number of drawbacks. An alternative is to use calculation methods for predicting fire resistance. However, such calculation methods are not widely available at present. Further, the current fire resistance provisions in codes and standards (ASCE 1992, EC3 2005) are prescriptive and do not account for realistic conditions such as end restraint, loading and fire scenarios. Thus, the current design approaches may not be fully applicable for undertaking performance-based design which provides rational and cost-effective fire safety solutions.

The proposed design approach provides a convenient way of obtaining fire response and fire resistance of restrained steel beams, and thus can be used for estimating fire resistance in lieu of full-scale standard fire resistance tests. The proposed design approach can be applied to evaluate fire resistance under realistic fire, loading and restraint scenarios. The proposed equations express fire resistance in terms of structural parameters, and thus the approach is attractive for incorporation in codes and standards. In summary, the use of the proposed approach will facilitate a rational fire design under a performance-based code environment. Such a rational design approach will contribute to reduced loss of life and property damage in fire incidents.

APPENDIX

This research has produced the following papers:

Peer-Reviewed Journal Papers

1. Dwaikat, M.M.S, and Kodur V.K.R, (2010) "Effect of Location of Restraint on Fire Response of Steel Beams", Journal of Fire Technology, (46)1, pp. 109-128.
2. Dwaikat, M.M.S and Kodur, V.K.R. (2009) "A Simplified Approach for Evaluating Plastic Axial and Moment Capacity Curves for Beam-Columns with Non-uniform Thermal Gradients", Engineering Structures, 32, pp.1423-1436
3. Kodur V.K.R. and Dwaikat M.M.S. (2009), "Response of Steel Beam–Columns Exposed to Fire", Engineering Structures, (31), pp. 369-379.
4. Kodur V.K.R, Dwaikat M. M. S., and Dwaikat M. B. (2008), "High-Temperature Properties of Concrete for Fire Resistance Modelling of Structures", ACI Material Journal, 105(5), pp. 517-527.
5. Kodur, V.K.R., Dwaikat, M.M.S, and Fike R., (2009) "High-Temperature Properties of Steel for Fire Resistance Modelling of Structures", In Press, Journal of Materials in Civil Engineering- ASCE.
6. Kodur, V.K.R., and Dwaikat, M.M.S, (2009) "Effect of High Temperature Creep on the Fire Response of Restrained Steel Beams". In Press, Materials & Structures Journal.

Conference Proceedings

1. Dwaikat, M.M.S. and Kodur, V.K.R. (2010) "Performance based design approach for evaluating fire resistance of restrained steel beams", Proceedings of the Sixth International Conference on Structures in Fire (SiF'10), East Lansing.
2. Dwaikat, M.M.S. and Kodur, V.K.R. (2010) "Lateral-Torsional Buckling of Steel Beam-Columns under Fire Exposure", SSRC Annual Stability Conference, Orlando, Florida.
3. Dwaikat, M.M.S., and Kodur, V.R., (2009) "Effect of Fire Induced Restraint on the Fire Response of Steel Beams", 5th International Symposium on Steel Structures: ISSS '09, Seoul, Korea.
4. Dwaikat, M.M.S., and Kodur, V.K.R, (2009) "Effect of Restraint Force Location on the Response of Steel Beams Exposed to Fire", Structures Congress Conference '09, ACSE, Austin, TX
5. Dwaikat, M.M.S., and Kodur, V.R., (2008) "Fire Performance of Steel Beam-Columns under Design Fire Exposures", Proceedings of the Fifth International Conference on Structures in Fire (SiF'08), Singapore.
6. Dwaikat, M.M.S., and Kodur, V.R., (2008) "Effect of High Temperature Creep and Fire Scenario on the Response of Steel Beam-Columns", BFRL Fire Conference, NIST/BFRL, Gaithersburg, MD.
7. Kodur, V.R, Garlock, M.E, Dwaikat, M.S, Quiel, S.,(2009) "Collaborative Research: Fire Engineering Guidelines for the Design of Steel Beam-

Columns", Proceedings of 2009 NSF Engineering Research and Innovation Conference, Honolulu, Hawaii.

8. Iqbal, S., Dwaikat, M.M.S., and Harichandran R. S., (2009) "Simple Approach for Calculating Inelastic Deflections of Simply Support Steel Beams under Fire." Structures Congress Conference '09, ACSE, Austin, TX.

REFERENCES

1. AISC (2005), "Steel Construction Manual 3rd Edition", American Institute of Steel Construction, Chicago, Illinois.

2. Ali, F. and O'Connor, D., (2001) "Structural performance of rotationally restrained steel columns in fire." Fire Safety Journal, Vol. 36, No. 7, pp. 679-691.

3. Ali, F., Shepherd, P., Randall, M., Simms, I.W., O'Connor, D.J., Burgess, I.W. (1988) "The effect of axial restraint on the fire resistance of steel columns." Journal of Constructional Steel Research, Vol. 46, No. 1-3, pp. 305-306(2).

4. Al-Jabri K.S., Burgess I.W., Lennon T., Plank R.J. (2005) "Moment-rotation-temperature curves for semi-rigid joints", Journal of Constructional Steel Research, 61, pp. 281–303.

5. Anderberg Y., (1988), "Modeling Steel Behavior." Fire Safety Journal, 13, pp.17-26.

6. ANSYS, (2007), "ANSYS Multiphysics", version 11.0 SP1 ANSYS Inc.

7. ASCE, (1992) "Structural Fire Protection", manual No.78,, ASCE committee on fire protection, structural division, American Society of Civil Engineers, New York.

8. ASCE-07 (2005), "Minimum Design Loads for Buildings and Other Structures", American Society of Civil Engineers, Reston, VA.

9. ASTM E119a (2008), "Standard Methods of Fire Test of Building Construction and Materials", American Society for Testing and Materials, West Conshohocken, PA.

10. Bailey, C.G., Lennon, T., Moore, D.B. (1999). "The behaviour of full-scale steel-framed buildings subjected to compartment fires." The Struct. Eng., 77(8), 15-21.

11. Banovic, S.W., McCowan, C.N., Luecke, W.E, (2005) "NIST NCSTAR 1-3E: Physical Properties of Structural Steel". Federal Building and Fire Safety Investigation of the World Trade Center Disaster. Gaithersburg, MD: National Institute of Standards and Technology (NIST).

12. Bentz D. P. and Prasad K. R., (2007), "Thermal Performance of Fire Resistive Materials I. Characterization with Respect to Thermal Performance Models." Report BFRL - NIST 7401. Gaithersburg, MD.

13. Bletzacker, R. W., (1966) "Effect of Structural Restraint on the Fire Resistance of Protected Steel Beam Floor and Roof Assemblies", Final Report. EES 246/266. Ohio State University, Columbus, Ohio.

14. BS 476-3:1987 (1987), "Fire Tests on Building Materials and Structures – Part 20: Method fro Determination of the Fire Resistance of Elements of Construction (General Principles) ", BSi, UK.

15. Buchanan A.H. (2002), Structural Design for Fire Safety, John Wiley & Sons Ltd., Chichester, England.

16. Chen J., and Young B., (2008), "Design of High Strength Steel Columns at Elevated Temperatures." Journal of Constructional Steel Research, 64 (6), pp. 689-703.

17. Chen, J., Young, B., Uy, B., (2006), "Behavior of High Strength Structural Steel at Elevated Temperatures." Journal of structural engineering, pp. 132-12.

18. Clark, C.L. (1953), "High-temperature alloys". Pitman, NY.

19. Cooke G.M.E., (1988), "An Introduction to the Mechanical Properties of Structural Steel at Elevated Temperatures", Fire Safety Journal, 13 (1), pp.45-54.

20. Dever, D.J. (1972), "Temperature dependence of the elastic constants in a-Iron single crystals: relationships to spin order and diffusion anomalies", Journal of Applied Physics, 43(8), pp. 3293-3301.

21. Dorn, J. E. (1954), "Some fundamental experiments on high temperature creep." Journal of Mechanical Physics and Solids, 3, 85-116.

22. Dwaikat, M.M.S, and Kodur V.K.R, (2010a) "Effect of Location of Restraint on Fire Response of Steel Beams", Journal of Fire Technology, (46)1, pp. 109-128.

23. Dwaikat, M.M.S and Kodur, V.K.R. (2010b) "A Simplified Approach for Evaluating Plastic Axial and Moment Capacity Curves for Beam-Columns with Non-uniform Thermal Gradients", In Press, Engineering Structures.

24. Dwaikat, M.M.S and Kodur, V.K.R. (2009a) "An Engineering Approach for Predicting Fire Response of Restrained Steel Beams." Submitted, Journal of Engineering Mechanics, ASCE.

25. Dwaikat, M.M.S and Kodur, V.K.R. (2009b) "A performance-based methodology for fire design of restrained steel beams", Submitted, Computers & Structures Journal.

26. Dwaikat, M.M.S., Kodur, V.K.R., Quiel, S.E., Garlock, M.E.M. (2009) "Experimental Behaviour of Steel Beam-Columns Subjected to Fire-Induced Thermal Gradients", Submitted, Journal of Structural Engineering, ASCE.

27. EC1 (2002), "EN 1991-1-2: Actions on Structures. Part 1-2: General Actions - Actions on Structures Exposed to Fire", European Committee for Standardization, Brussels, Belgium.

28. EC3 (2005), "EN 1993-1-2: Design of Steel Structures. Part 1-2: General Rules - Structural Fire Design", European Committee for Standardization, Brussels, Belgium.

29. Garlock, M.E.M. and Quiel, S.E. (2007) "Mechanics of Wide-Flanged Steel Sections with Thermal Gradients Due to Fire Exposure," International Journal of Steel Structures, Korean Society of Steel Construction, 7(3), 153-162.

30. Garlock, M.E.M. and Quiel, S.E., (2008) "Plastic Axial Load - Moment Interaction Curves for Fire-Exposed Steel Sections with Thermal Gradients", Journal of Structural Engineering, ASCE 134(6).

31. Ghali, A., Neville, A.M., and Brown, T.G. (2003) "Structural analysis – A unified classical and matrix approach." 5th Ed., Spon Press, Abingdon, Oxon, U.K.

32. Gumen V., ul Haq A., Illyas B., and Maqsood A. (2001) "High-Temperature Thermal Conductivity of Ceramic Fibers" Journal of Materials Engineering and Performance, 10(4), pp. 475–478

33. Harada K., Ohmiya Y., Natori A., and Nakamichi A., (2004) "Technical basis on structural fire resistance design in building standards law of Japan", Fire and Materials, 28, pp. 323–341.

34. Harmathy, T. (1967) "A comprehensive creep model", Journal of Basic Engineering, 89(D-3): pp. 496-502.

35. Harmathy, T. and W. Stanzak, (1970) "Elevated-temperature tensile and creep properites of some structural and prestressing steels. American society for testing and material", special publication, p. 186-208.

36. Huang Z-F, Tan K-H, and Ting S-K, (2006), "Heating Rate and Boundary Restraint Effects on Fire Resistance of Steel Columns with Creep." Engineering Structures 28, pp. 805–817.

37. Huang, Z. F., and Tan, K. H. (2003). "Analytical Fire Resistance of Axially Restrained Steel Columns." Journal of Structural Engineering, 129(11), 1531-1537.

38. IBC, (2000), "International Building Code", International Code Council, Inc. (ICC), Falls, Church, VA.

39. Iding, R. H., Bresler, B., and Dawson, S. P., (1988) "Fire Endurance of Steel Beam-Slab Assemblies under Different Conditions of Restraint", Final Report to American Iron and Steel Institute, Wiss, Janney, Elstner Associates, Inc.

40. ISO 834 (1975), "Fire resistance tests - elements of building construction. International Organization for Standardization".

41. Isolatek International (2008), "CAFCO 300 Guide Specifications", Stanhope, NJ: <http://www.cafco.com/pdfs/CAFCO%20300%20Brochure.pdf>.

42. Kirby, B. R. (1997) "Large scale fire tests: the British Steel European collaborative research programme on the BRE 8-storey frame. Proceedings of the Fifth International Symposium of Fire Safety Science, Melbourne, Australia, pp. 1129-1140.

43. Kirby, B. R., and Preston, R. R. (1988), "High temperature properties of hot-rolled, structural steels for use in fire engineering design studies." Fire Safety Journal, 13, 27-37.

44. Kodur V.K.R. and Dwaikat M.M.S, (2009a), "Response of Steel Beam–Columns Exposed to Fire". Engineering Structures, (31), pp. 369-379.

45. Kodur, V.K.R., and Dwaikat, M.M.S, (2009b) "Effect of High Temperature Creep on the Fire Response of Restrained Steel Beams". In Press, Materials & Structures Journal.

46. Kodur V.R. (1999), "Performance based fire resistance design of concrete-filled steel columns", Journal of Constructional Steel Research Institute, 51, pp. 21-36.

47. Kodur, V.K.R., and Dwaikat, M.M.S and Fike R., (2009) "High-Temperature Properties of Steel for Fire Resistance Modelling of Structures", Journal of Materials in Civil Engineering- ASCE, Accepted.

48. Kodur, V.K.R., and Harmathy, T.Z. (2002) "Properties of Building Materials", SFPE Handbook of Fire Protection Engineering, 3rd Edition. P.J. DiNenno, National Fire Protection Agency, Quincy, MA.

49. Li G-Q, Jiang S-C, Yin Y-Z, Chen K., and Li M-F, (2003), "Experimental Studies on the Properties of Constructional Steel at Elevated Temperatures." Journal of Structural Engineering, 129 (12), pp. 1717-1721.

50. Li, G.Q., He, J.L., and Jiang, S.C. (2000) "Fire-resistant experiment and theoretical calculation of a steel beam", China Civil Engineering Journal 32 (4), pp. 23–26.

51. Li, G-Q. and Guo, S-X. (2006) "Analysis of restrained heated steel beams during cooling phase", 4th SiF'06 international workshop, Proceedings, pp. 41-51, Aveiro, Portugal.

52. Li, G-Q. and Guo, S-X. (2008) "Experiment on restrained steel beams subjected to heating and cooling." Journal of Constructional Steel Research, Vol. 64, pp. 268-274.

53. Liu, T.C.H., Fahad, M.K., Davies, J.M. (2002). "Experimental investigation of behaviour of axially restrained steel beams in fire." J. Constr. Steel Res., 58, 1211-1230.

54. Meacham B.J., and Custer R.L.P. (1992), "Performance-Based Fire Safety Engineering: an Introduction of Basic Concepts", Journal of Fire Protection Engineering, 7(2), pp. 35-54.

55. Newman, G. (1999) "The Cardington Fire Tests", Proceedings, North American Steel Construction Conference, New Orleans, LA, American Institute of Steel Construction, Chicago, IL.

56. Newman, G. M., Robinson, J. T. and Bailey, C.G. Fire safety design: a new approach to multi-storey steel framed buildings. SCI Publications P288, The Steel Construction Institute, 2000.

57. NIST (2005). "NCSTAR 1: Final report of the National Construction Safety Team on the collapse of the World Trade Center Twin Towers". National Institute of Standards and Technology (NIST). Gaithersburg, MD.

58. NKK. (1989) "Fire-Resistant Steel for Building Structural Use." Nippon Steel Corporation, Tokyo. 8p.

59. Outinen J., Kesti J., and Mäkeläinen P., (1997), "Fire design model for structural steel S355 based upon transient state tensile test results", Journal of Constructional Steel Research, 42(3), pp. 161-169.

60. Outinen, J., (2007), "Mechanical properties of structural steels at high temperatures and after cooling down", Helsinki University of Technology Laboratory of Steel Structures Publications 32, Doctoral Dissertation.

61. Outinen, J., Mäkeläinen, P., (2004), "Mechanical Properties of Structural Steel at Elevated Temperatures and After Cooling Down." Fire and Materials, 28, pp.237-251.

62. Poh, K.W., (1995) "General stress-strain equation", Journal of Materials in Civil Engineering, 9(4), pp. 214-217.

63. Poh, K.W., (2001) "Stress-strain-temperature relationship for structural steel", Journal of Materials in Civil Engineering, 13(5), pp. 371-379.

64. Powel R.W and Tye R.P. (1960), "High alloy steels for use as a thermal conductivity standard", British Journal of Applied Physics, vol 11, pp. 195-198.

65. Purkiss J. A. (2007) "Fire safety engineering design of structures." 2nd Ed., Butterworth-Heinemann, Linacre House, Jordan Hill, Oxford OX2 8DP, UK.

66. Quiel, S.E., Garlock M.E.M., Dwaikat, M.M.S., Kodur, V.K.R., (2009) "Computational Studies of Steel Beam-Columns with Thermal Gradients." Fire Safety Journal, submitted for publication.

67. Rempe J.L., Knudson D.L., (2008), "High Temperature Thermal Properties for Metals Used in LWR Vessels." Journal of Nuclear Materials, 372(2-3), pp. 350-357.

68. Rodrigues, J.P.C., Neves, I.C., Valente, J.C. (2000) "Experimental research on the critical temperature of compressed steel elements with restrained thermal elongation." Fire Safety Journal, Vol. 35, No. 2, pp. 77-98.

69. Skowronski, W. (1988). "A study of the steel beam deformations during fire." Building and Environment, 23(2); pp.159-167.

70. Skowronski, W. (1990). "Load capacity and deflection of fire-resistant steel beams." Fire Technology, pp. 310-328.

71. SNZ (1997), "Steel Structures Standard. NZS 3404: Part 1 & Part 2", New Zealand, Wellington.

72. Stirland C., (1980), "Steel properties at elevated temperatures for use in fire engineering calculations", Document ISO/TC92/WG15, No. 14, British Steel Corporation, Teeside Laboratories, U.K.

73. Tan, K.H. and Z.F. Huang, (2005) "Structural responses of axially restrained steel beams with semirigid moment connection in fire". Journal of Structural Engineering. 131(4): pp. 541-551.

74. Tan, K.-H., Toh, W.-S., Huang, Z.-F., Phng, G.-H. (2007) "Structural responses of restrained steel columns at elevated temperatures. Part 1: Experiments." Engineering Structures, Vol. 29, No. 8, pp. 1641-1652.

75. Thor, J. (1973). "Deformations and critical loads of steel beams under fire exposure conditions." Report No. D16:1973, National Swedish Building Research Summaries, Stockholm

76. Touloukian, Y., (1972), "Thermal Radiative Properties for Non Metallic Solids," Thermal Physical Properties, Vol. 8, pp. 142.

77. Twilt L., (1991), "Stress-strain relationships of structural steel at elevated temperatures: Analysis of various options and European proposal -Part F: mechanical properties", TNO-rapport BI-91-015, Delft.

78. Usmani, A.S., et al. (2001) "Fundamental principles of structural behaviour under thermal effects". Fire Safety Journal, 36(8): p. 721-744.

79. Wainman, D, E. and Kirby, B.R., (1988), "Compendium of U.K. Standard Fire Test Data on Unprotected Structural Steel–1." British Steel Corporation RS/RSC/S10328/1/87/B.

80. Wainman, D, E. and Kirby, B.R., (1989), "Compendium of U.K. Standard Fire Test Data on Unprotected Structural Steel–2." British Steel Technical RS/R/S1199/8/88/B. Rotherham.

81. Wang Y.C. (2002) "Steel and composite structures, behavior and design for fire safety." Spon Press, London, UK.

82. Wang, Y. C. and Kodur, V.K.R. (2000) "Research towards use of unprotected steel structures." ASCE Journal of Structural Engineering, 126(12), pp. 1442-1450.

83. Wang, Y.C. and Davies, J.M., (2003) "Fire test of non-sway loaded and rotationally restrained steel column assemblies." Journal of Constructional Steel Research, Vol. 59, pp. 359-383.

84. Wang, Y.C. and Y.Z. Yin, (2006) "A simplified analysis of catenary action in steel beams in fire and implications on fire resistant design", Steel and Composite Structures,. 6(5): pp. 367-386.

85. Wang. Y. C. (2000) "An analysis of the global structural behaviour of the Cardington steel-framed building during the two BRE fire tests." Engineering Structures, 22, pp. 401-412.

86. Williams-Leir, G., (1983) "Creep of structural steel in fire: Analytical expressions", Fire and Materials, 7(2), pp. 73-80.

87. Yang, K.-C., Lee, H.-H., Chan, O. (2006) "Performance of steel H columns loaded under uniform temperature." Journal of Constructional Steel Research, Vol. 62, pp. 262-270.

88. Yawata Iron and Steel Co. (1969), "WEL-TEN 80 material datasheet", Japan, pp. 142-164.

89. Yin, Y.Z. and Y.C. Wang, (2003) "Numerical simulations of the effects of non-uniform temperature distributions on lateral torsional buckling resistance of steel I-beam", Journal of Constructional Steel Research,. 59: pp. 1009-1033.

90. Zienkiewicz, O. C. and Cormeau, I. C., (1974) "Visco-plasticity - Plasticity and Creep in Elastic Solids - A Unified Numerical Solution Approach", International Journal for Numerical Methods in Engineering, Vol. 8, pp. 821-845.